It's just a phase!
Signals from exoplanets in the optical and infrared regime

Inaugural dissertation
of the Faculty of Science,
University of Bern

presented by

Kathryn D. Jones

Supervisor of the doctoral thesis:
Prof. Dr. Kevin Heng
University of Munich

source: https://doi.org/10.48549/5781 | downloaded: 4.3.2025

WISSEN
SCHAFFT
WERT.

WISSEN
SCHAFFT
WERT.

It's just a phase!
Signals from exoplanets in the optical and infrared regime

Inaugural dissertation
of the Faculty of Science,
University of Bern

presented by

Kathryn D. Jones

Supervisor of the doctoral thesis:
Prof. Dr. Kevin Heng
University of Munich

Accepted by the Faculty of Science.

Bern, 13th December 2024

The Dean
Prof. Dr. Jean-Louis Reymond

This work is licensed under a Creative Commons Attribution 4.0 International License
https://creativecommons.org/licenses/by/4.0/

WISSEN
SCHAFFT
WERT.

WISSEN
SCHAFFT
WERT.

Abstract

In this thesis, we explore exoplanet climates using space-based observations, with a particular focus on hot Jupiters. These giant, gas-rich planets, which orbit close to their stars, offer unique opportunities to study extreme atmospheric conditions. By combining new data from missions like CHEOPS and TESS with advanced theoretical and numerical models, this work provides critical insights into the atmospheric dynamics of these worlds. We investigate how light interacts with exoplanet atmospheres—through reflection, transmission, and emission—unveiling the underlying physical and chemical processes in action. A major contribution of this thesis is the development and application of the `catwoman` transit model, which interprets asymmetric light curves shaped by the complex limb structures of exoplanets. By utilising full-phase curve models, including transit models, we extract two-dimensional thermal and scattering properties of planetary atmospheres while precisely constraining key system parameters. Additionally, this research breaks new ground by modelling the opposition surge effect on exoplanets, using Solar System objects as analogues to enhance our understanding of how light interacts with different planetary surfaces and atmospheres. This work continues to expand the limits of both observational and modelling techniques, advancing our ability to study the climates of Earth-like planets and moving us closer to answering profound questions about habitability in our Universe.

Have a little patience.

Take That

I would like to dedicate this thesis to Mum and Dad, Iwan, Grandma and Grandad, and Beauty and George Jones.

List of publications

1. *The Effect of Atmospheric Chemistry on the Optical Geometric Albedos of Hot Jupiters*

   Jones, K. D., Morris, B. M. & Heng, K., 2024, submitted, A&A

2. *Hot Rocks Survey I : A shallow eclipse for LHS 1478 b*

   August, P. C., Buchhave, L. A., Diamond-Lowe, H., ..., **Jones, K. D.**, et al., submitted, A&A

3. *Enceladus and Jupiter as exoplanets: the opposition surge effect*

   Jones, K. D., Morris, B. M. & Heng, K., 2024, in review, A&A

4. *Sulfur dioxide in the mid-infrared transmission spectrum of WASP-39b*

   Powell, D., Feinstein, A. D., Lee, E. K. H., ..., **Jones, K. D.**, et al., 2024, Nature, 626, 8001, doi: 10.1038/s41586-024-07040-9

5. *Investigating the visible phase-curve variability of 55 Cnc e*

   Meier Valdés, E. A., Morris, B. M., Demory, B. -O., ..., **Jones, K. D.**, et al., 2023, A&A, 677, A112, doi: 10.1051/0004-6361/202346050

6. *The Mantis Network. III. Expanding the limits of chemical searches within ultra-hot Jupiters: New detections of Ca I, V I, Ti I, Cr I, Ni I, Sr II, Ba II, and Tb II in KELT-9 b*

   Borsato, N. W., Hoeijmakers, H. J., Prinoth, B., ..., **Jones, K. D.**, et al., 2023, A&A, 673, A158, doi: 10.1051/0004-6361/202245121

7. *Examining the orbital decay targets KELT-9 b, KELT-16 b, and WASP-4b, and the transit-timing variations of HD 97658 b*

   Harre, J. -V., Smith, A. M. S., Barros, S. C. C., ..., **Jones, K. D.**, et al., 2023, A&A, 669, A124, doi: 10.1051/0004-6361/202244529

8. *The stable climate of KELT-9b*

   Jones, K. D., Morris, B. M., Demory, B. -O., et al., 2022, A&A, 666, A118, doi: 10.1051/0004-6361/202243823

9. *Physically-motivated basis functions for temperature maps of exoplanets*

   Morris, B. M., Heng, K., **Jones, K. D.**, et al., 2022, A&A, 660, A123, doi: 10.1051/0004-6361/202142135

10. *Spi-OPS: Spitzer and CHEOPS confirm the near-polar orbit of MASCARA-1 b and reveal a hint of dayside reflection*

    Hooton, M. J., Hoyer, S., Kitzmann, D., ..., **Jones, K. D.**, et al., 2022, A&A, 658, A75, doi: 10.1051/0004-6361/202141645

11. *Constraining Mornings and Evenings on Distant Worlds: A new Semianalytical Approach and Prospects with Transmission Spectroscopy*

    Espinoza, N. & **Jones, K. D.**, 2021, AJ, 162, 4, doi: 10.3847/1538-3881/ac134d

12. *catwoman: A transit modelling Python package for asymmetric light curves*

    Jones, K. D. & Espinoza, N., 2020, JOSS, 5, 55 doi: 10.21105/joss.02382

Contents

List of Figures

List of Tables

Chapter 1

Introduction

1.1 Exoplanets

An exoplanet (or extra-solar planet) is a planet orbiting a star outside of our Solar System. To date, over 5,700 planets have been detected, using a variety of different methods. The first official exoplanet detection was in 1992 around the pulsar PSR1257 +12 (Wolszczan & Frail, 1992). The exoplanet in this system was detected through measuring perturbations from the expected time of the pulsar signal. The first exoplanet that was detected around a main-sequence star was 51 Pegasi b in 1995 (Mayor & Queloz, 1995). They observed a change in radial velocity of the star through lines in its emission spectrum and found a signal characteristic of a Jupiter-like planet orbiting the star. Since then, thousands more exoplanetary systems have been discovered using this method, as well as other, newer techniques.

1.2 Exoplanet Detection Methods

Figure 1.1 shows a list of confirmed exoplanets plotted with their masses as a function of orbital period, colour-coded by their method of detection. It is clear that different detection methods find planets in specific parameter spaces.

[1] https://exoplanetarchive.ipac.caltech.edu/index.html

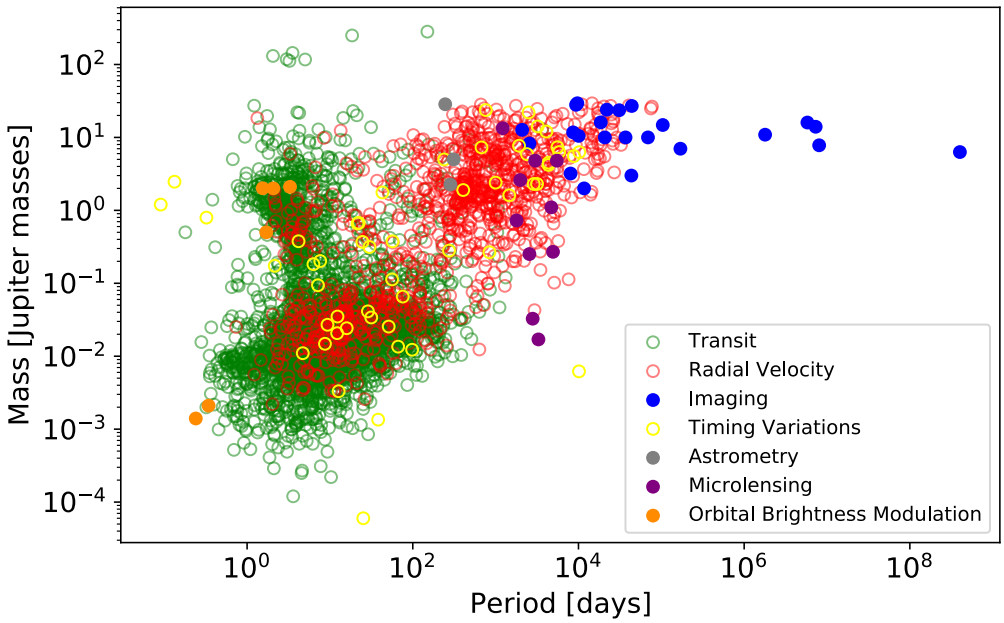

Figure 1.1 | All confirmed exoplanets, as of 4th July 2024, plotted with their mass as a function of orbital period. The colour and labels show the detection methods used. It is clear from this plot that different methods find planets in specific parameter spaces. Some confirmed planets do not have a precise-enough mass measurement and so they are not visible here. Data from the the NASA Exoplanet Archive[1].

1.2.1 Transits

To date, the majority of exoplanets have been detected using the 'transit' method. This is when the plane of the planetary orbit is such that we can observe the planet periodically eclipsing the central star. Due to the distances involved, we can only observe the overall 'brightness' of the planet-star system. The system flux as a function of time is called a *lightcurve*, demonstrated in Figure 1.2. The transit depth, δ, is given by the ratio of the area of the stellar disk to the planetary disk:

$$\delta = \left(\frac{R_p}{R_*}\right)^2, \tag{1.1}$$

where R_p is the planetary radius and R_* the stellar radius. There are certain caveats to this equation, primarily the complication of limb darkening, which is an observed effect where the limbs of the star appear dimmer than the centre. This changes the shape of the transit to appear deeper in the middle of the transit and shallower at the edges, and must be taken into account in our transit models (see, e.g. Csizmadia et al., 2013, Espinoza & Jordán, 2015). Another large caveat is planetary atmospheres, which will be discussed in Section 1.4. The time between transits directly gives us the planetary orbital period (P), and using Kepler's Third Law of Planetary Motion (Kepler, 1619) we can estimate the planetary orbital radius (a) by:

$$a = \left(\frac{GM_*P^2}{4\pi^2}\right)^{(1/3)}, \tag{1.2}$$

where G is the Gravitational constant and M_* is the mass of the host star, where we have assumed a circular planetary orbit.

This method was first used to observe transits of the hot Jupiter HD 209458b in 2000 (Charbonneau et al., 2000), which was initially discovered using radial-velocity measurements (see Section 1.2.2). The first exoplanet actually discovered using the transit method was OGLE-TR-56b, another hot Jupiter, by Torres et al. (2003). It is not coincidental that the first exoplanets discovered using this method are all large Jupiter-size planets with short orbital periods. For a given stellar radius, larger exoplanets produce deeper transits which, given a specific noise minimum of the observations, are detected at a higher significance. Furthermore, a shorter period transiting exoplanet is more likely to transit when you happen to be observing the system. This is evident in the population of exoplanets detected by the transit method in Figure 1.1 occupying the low-period regime.

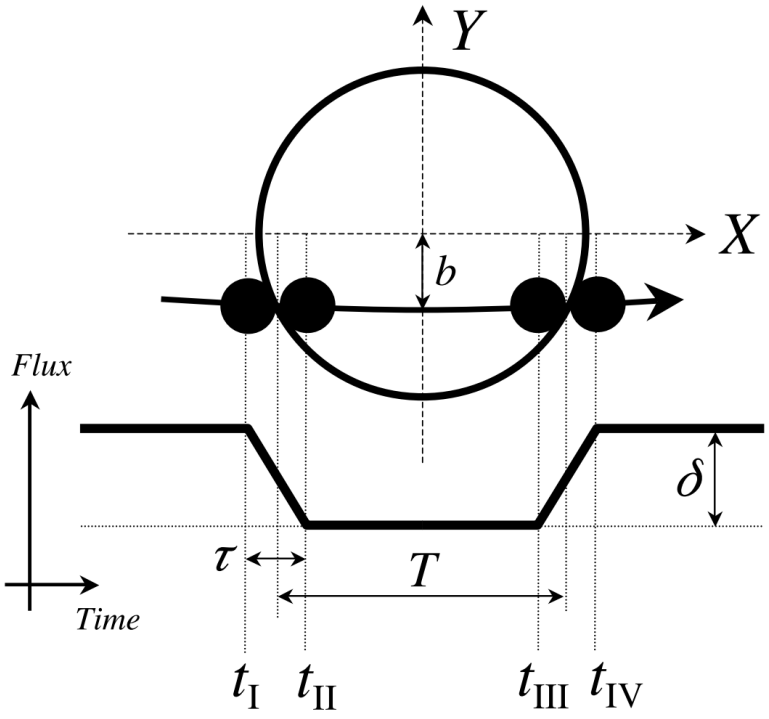

Figure 1.2 | Schematic from Winn (2010). When a planet passes in front of its host star, it blocks some of the light from the star, decreasing the overall system flux. This flux decrease has a characteristic shape depending on the orbital period, planet radius and impact parameter (b). t_I to t_{II} is known as the ingress and t_{III} to t_{IV} is the egress. T is defined as the transit duration and δ is the transit depth.

1.2.2 Radial Velocity

As previously stated, the first exoplanet discovered around a main-sequence star was detected using the radial velocity method. Following the laws of classical mechanics, both the planet and its host star orbit a point in space that corresponds to their centre of mass. Due to the large mass difference, this is always inside the star itself, however, not exactly at its centre. Therefore, the star will move slightly. This small movement can be detected by observing the change in wavelength of the observed stellar light due to the Doppler effect (see Figure 1.3). The Doppler effect is the change in observed wavelength due to a moving emitting light source (Doppler, 1842).

As the star orbits the centre of mass of the planet-star system, and if the system is orientated such that the star has a radial velocity component along the line-of-sight of the observer, the stellar emission spectrum will appear to periodically shift to bluer and then to redder wavelengths. Using

$$v_s = \frac{c\Delta\lambda_o}{\lambda}, \tag{1.3}$$

where v_s is the radial velocity of the star, c is the speed of light, $\Delta\lambda_o$ is the observed change in wavelength and λ is the wavelength in rest frame of source, it is possible to construct a plot of the radial velocity of the star as a function of time (see Figure 1.4).

From the amplitude and period of this radial velocity curve, you can deduce the mass of the planet by first using this period, P, in Kepler's Third Law (Equation 1.2) and then inserting the semi-major axis, a, into

$$v_p = \frac{2\pi a}{P}, \tag{1.4}$$

assuming a circular orbit. From here we use the conservation of momentum to derive the planetary mass:

$$M_p = \frac{M_* v_*}{v_p}, \tag{1.5}$$

where v_* comes from the amplitude of the radial velocity curve and M_* is the mass of the star. Generally, this technique is biased towards finding more massive exoplanets slightly further away from their stars than the transit method. It is also biased towards planets around low-mass stars, as both scenarios increase the amplitude of the radial velocity signal.

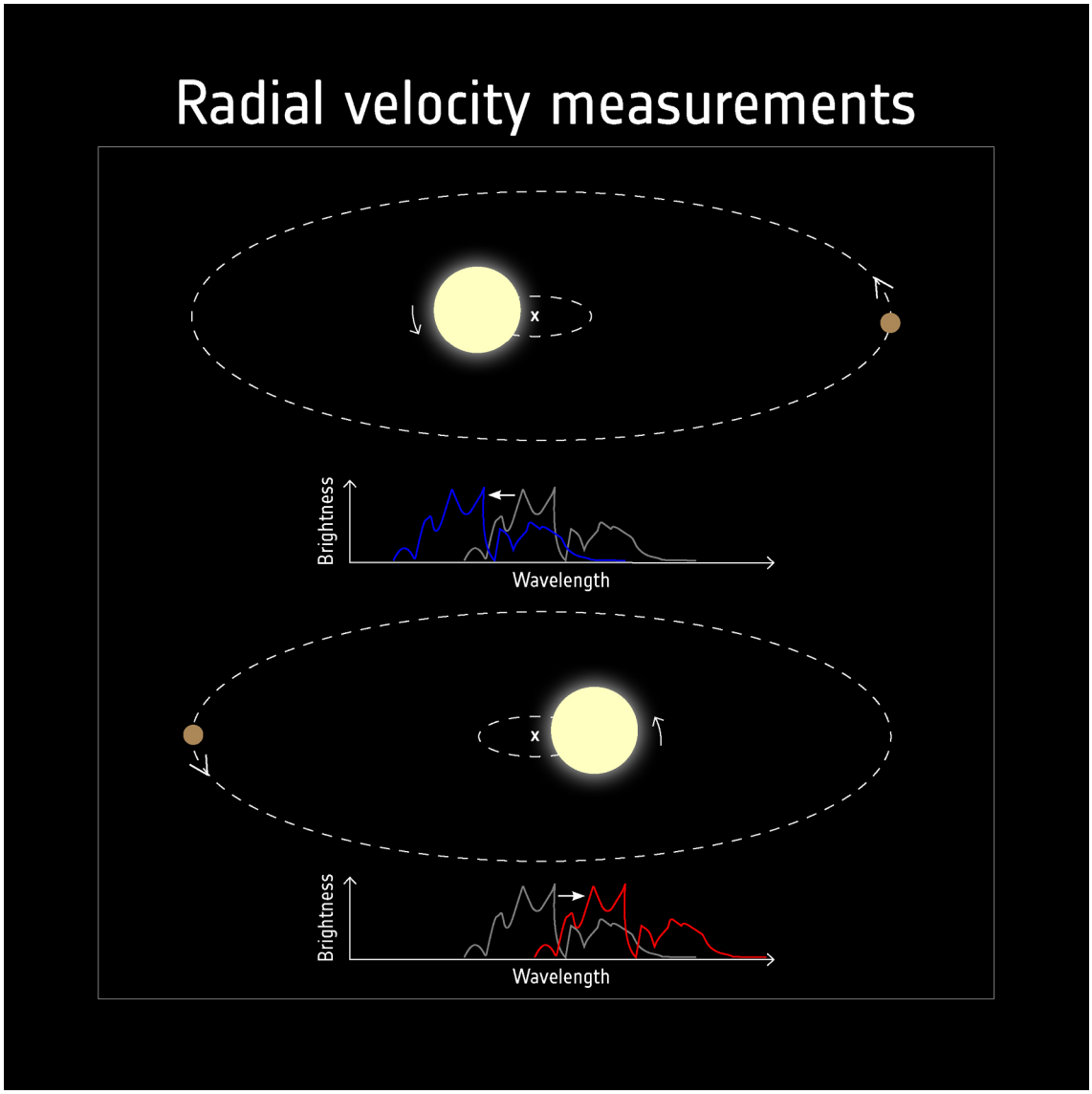

Figure 1.3 | Diagram: ©ESA. In reality, due to the laws of classical mechanics, a planet does not orbit its star, but both the star and planet orbit a point in space that corresponds to their combined centre of mass. When the star is moving radially towards the observer, due to the Doppler Effect, its emission spectrum is observed at bluer wavelengths (blue-shifted), whereas when it is moving in the opposite direction, the stellar spectrum is red-shifted. The inferred stellar radial velocity and the period of this blue and red-shift cycle gives you the mass of the planetary body (assuming you know the stellar mass).

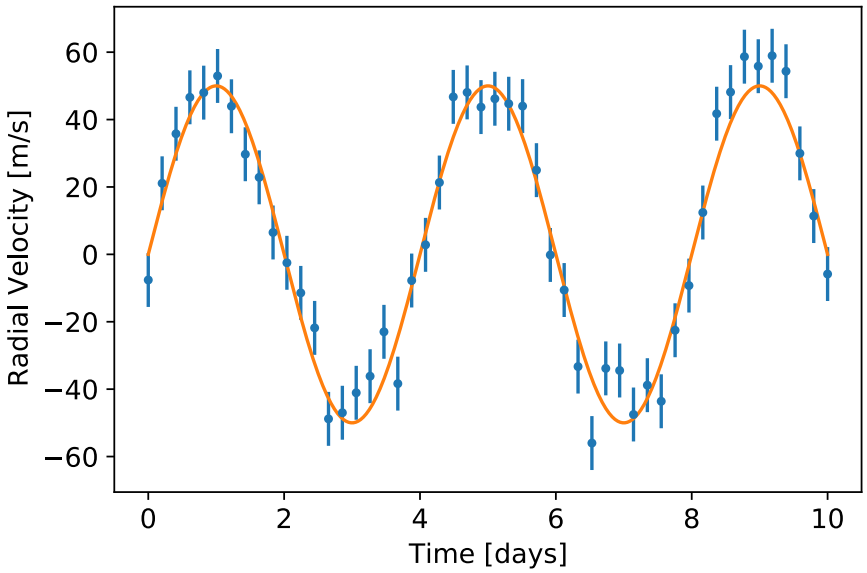

Figure 1.4 | Mock radial velocity curve showing how the star moves with respect to the observer. The period, amplitude and shape of this curve constrains the planetary mass, period and eccentricity. The uncertainty of these data points depends on how confidently we can track the shift in wavelength of the stellar emission spectrum.

1.2.3 Direct Imaging

An increasingly-popular technique for exoplanet detection is to directly image the planet-star system. Due to the brightness of the host star, this requires highly sophisticated optics, including the use of a coronagraph to block out the stellar light. Nulling interferometry is also being used in some operating instruments (e.g. The Large Binocular Telescope Interferometer, LBTI, Ertel et al., 2020). This creates spaces on the image where the incoming light destructively or constructively interferes in order to reduce the stellar signal and boost the planetary signal. From the image, it is possible to obtain the orbital separation of the planet and, from the brightness of the planet, a rough estimate of its temperature can be obtained. If images are taken over a long enough time, it is possible to see the path of the planet and therefore estimate its orbital period (see, e.g. Zurlo et al., 2022).

The first exoplanet candidate directly imaged was 2M1207b in 2004 by Chauvin et al. (2004). It is a Jupiter-sized exoplanet orbiting a Brown Dwarf with a calculated separation of 42^{+19}_{-2} au (Ricci et al., 2017) and an effective temperature of 1300 K (Luhman et al., 2023). Since then, around 80 more exoplanets have been discovered with this method.

An advantage of direct imaging is that planets with much larger periods (e.g. years to hundreds of years) can be detected, expanding the parameter space of the exoplanet sample, and reaching more 'Solar-System-like' systems. This is because planets too close to their host star cannot be resolved and so this technique requires a certain amount of spatial separation between exoplanet and star. However, often a long baseline (e.g. decades) is required to model the orbit of a planet and confirm it is a companion to the host star and not just a background object.

1.2.4 Other Methods

Alternative exoplanet detection methods include tracking timing variations, for example the timing of a planet's transits. An outer second planet in the same system can gravitationally influence the orbit of the transiting inner planet, perturbing the measurable transit timings. From these variations, the mass and period of the outer planet can be determined (see, e.g. Wittrock et al., 2023, Yahalomi et al., 2024).

Gravitational microlensing is another increasingly-popular detection technique (see, e.g. Beaulieu et al., 2006, Cassan et al., 2012). This technique monitors the brightness of a background star over time. If, by chance, another star closer to the observer becomes aligned, or almost aligned, with the background star, due to the gravity of the foreground star, it acts like a lens for the background star, magnifying the observed brightness. If the foreground star hosts a planet, then this planet will also magnify the background star, for a shorter time, imprinting an additional signal over the normal signal, which can be detected.

1.3 Exoplanet Types

The (roughly) 5,700 detected exoplanets are distributed across 4,300 planetary systems. 970 systems (about 23%) have more than one planet and, of those, only 13 have been found to have more than 5 planets. This includes the most studied exoplanet system, TRAPPIST-1 (Gillon et al., 2017), which has 7 Earth-sized planets, including 4 planets within the 'Habitable Zone' (Kopparapu et al., 2013, O'Malley-James & Kaltenegger, 2017). This makes the Solar System, with its eight planets (and Pluto) seem rather rare. However, due to observational biases, not all types of systems and planets can be detected

with equal probability (see, e.g. Burke et al., 2015, Batalha, 2014, Winn & Fabrycky, 2015, for a review on planet occurrence rates from observations). The predicted system populations can also be modelled using planet formation simulations (see, e.g. Mordasini, 2018, for a review on occurrence rates from planet formation models). The sample of known exoplanets has grown dramatically in recent years due to exoplanet surveys such as Kepler (Borucki et al., 2010) and TESS (Ricker et al., 2015).

When studying exoplanet types, we see structure in the distribution of planet masses, radii, composition, climate and more. Here, and throughout this thesis, **we define climate as the physical and chemical conditions in planet's atmosphere**. Looking again at Figure 1.1, we can divide them into categories, based on their mass, radius and orbital period. Planets with at least 0.5 Jupiter masses and periods less than $\sim$ 10 days are known as hot Jupiters; hot giant gaseous planets. Planets with masses from around 10^{-2} to 10^{-1} Jupiter masses (roughly 2 to 30 Earth-masses) are known as super-Earths, these are expected to be rocky or even lava-worlds (e.g. Chao et al., 2021, Meier et al., 2021). Less-massive planets are therefore called Earth-like planets. It is not possible with our current technology to detect planets much smaller than this. In between these categories are other planet types, such as Saturn-like planets and mini-Neptunes. Since the work in this thesis is mostly focussed on hot Jupiters and super-Earths, we give more details about these planet types in the next two subsections.

1.3.1 Hot (and Ultra-hot) Jupiters

Hot Jupiters are giant gaseous planets with large hydrogen-helium envelopes that orbit very close to their host stars and have equilibrium temperatures above $\sim$ 1200 K, although this is not a strict boundary. The origins of such a system, and how such a massive planet can get so close to its star, is still a dynamic topic of research. Many theories, including disk migration, in-situ formation, high-eccentricity tidal decay and planet-planet interactions are all still up for debate, and it is generally accepted that more than one of them could be the cause (see, e.g. Dawson & Johnson, 2018).

The first discovered exoplanet around a main-sequence star was a hot Jupiter: 51 Pegasi b (Mayor & Queloz, 1995), using the radial velocity method. However, it wasn't until Charbonneau et al. (2000), when the first transit of hot Jupiter HD 209458b was observed, which allowed its radii to be measured (see Equation 1.1). From radial velocity

and transit surveys, it is calculated that around 1% of Sun-like stars harbour a hot Jupiter (Howard et al., 2012, Wright et al., 2012), which is around 10% of the occurrence rate of all giant planets (Cumming et al., 2008). With a mass and a radius, the bulk-density and predicted 'surface' gravity can be calculated, giving us constraints on the structure and composition of the planet (see, e.g. Fortney et al., 2010, for a review).

Due to their very small orbital radii, hot Jupiters are expected to be tidally locked, where the same hemisphere of the planet faces the star at all times. This creates a large thermal and chemical dichotomy within the atmosphere of the planet, where there is a permanent, hot 'dayside' and a cool 'nightside' which never receives direct stellar radiation.

Ultra-hot Jupiters are a special class of hot Jupiters with equilibrium temperatures above ~ 2500 K. These are highly irradiated and very extreme worlds, where dissociated atoms and ions exist in the atmosphere and extreme day-to-night winds drive heat transport around the planet. Their atmospheres and temperature structures are very important to study as they have been shown to be distinct from cooler hot Jupiter atmospheres (Baxter et al., 2020), and can be used to test the limits of and improve our chemical models and GCMs (General Circulation Models). They also exhibit unique chemical processes, such as hydrogen dissociation and recombination, which will be covered in Chapter 2. Furthermore, as they are so hot, their thermal emission flux is very high in the optical and near-infrared bands, opening up the possibility of using a large range of ground and space-based telescopes to observe them with.

1.3.2 Super-Earths

With the James Webb Space Telescope (JWST, Gardner et al., 2006) now online, we have the precision and access to infrared wavelengths that allow us to probe the atmospheres of super-Earth exoplanets. With around 50% of all Sun-like stars predicted to have exoplanets smaller than Neptune (see, e.g. Howard et al., 2012), they are very abundant. They are mostly presumed to be rocky with differing envelope fractions or secondary (i.e. not from the protoplanetary disk) atmospheres. However, other surfaces, such as lava, oceans or ice may also be possible. These types of planets are very interesting to study as we do not have any super-Earth analogues in the Solar-System. Furthermore, with their larger radii we can detect them more easily than smaller Earth-like planets, and so they are our

first glimpse into (potentially) rocky worlds.

As orbital period significantly affects the observability of an exoplanet, the known super-Earths to-date have extremely low periods and therefore are very hot due to their proximity to the host stars. A lot of work has been done to study the atmospheres of some of the brightest super-Earth targets, including 55 Cnc e (see, e.g. McArthur et al., 2004, Demory et al., 2011a, Meier Valdés et al., 2023, Hu et al., 2024, Patel et al., 2024) and K2-141b (see, e.g. Barragán et al., 2018, Zieba et al., 2022). However, due to their small atmospheric scale heights and radii compared to hot Jupiters, their signals are much smaller and harder to characterise. It is therefore important that we understand our instruments and models, by testing them on more optimal targets (e.g. hot Jupiters) before applying them to super-Earths, in order to extract the most reliable information.

1.4 Exoplanet characterisation

Once an exoplanet has been detected, depending on the detection method, the mass, radius and orbital period are usually known. However, this is only the beginning. Astrophysicists now aim to answer important questions, including but not limited to:

- Are there habitable exoplanets?
- What causes the variation we observe in exoplanet climates?

These two questions are intrinsically linked, since they both rely on having a deep and complete understanding of exoplanet atmospheres. For this to be achieved, exoplanet observations and physical models must work hand-in-hand to extract the most reliable information and, more importantly, contextualise the information to improve our understanding of these topics. Luckily, exoplanet atmospheres imprint detectable signatures on the light which we receive from the system (see Section 1.4.1), compared to other characteristics of a planet, such as its interior structure or origins, which must be studied through less direct means. **This thesis will focus on the question of understanding exoplanet climates (i.e. the physical and chemical conditions in a planet's atmosphere), using models to extract as much information as possible from the light we receive from the exoplanet-star systems.**

To answer the question of exoplanet habitability, we need to learn more about exoplanet climates, i.e. atmospheric conditions (if an atmosphere exists at all). Tackling this

systematically, the easiest parameter to derive is the equilibrium temperature, $T_{\rm eq}$. From the known effective temperature of the host star, T_*, the semi-major axis, a, and the radius of the star, R_*, and assuming the planet absorbs all of the incoming stellar radiation and then re-emits it uniformly across its entire surface,

$$T_{\rm eq} = T_* \sqrt{\frac{R_*}{2a}}. \tag{1.6}$$

This parameter, together with the planetary mass and radius, provides the first indication of the kind of climate present on the planet. However, this is not conclusive. For example, the equilibrium temperature of the Earth is around 255 K (−18°C), but due to the greenhouse gases in our atmosphere, some of the outgoing radiation is trapped and acts to additionally warm the planet. To go from the equilibrium temperature to atmospheric conditions, we need more information.

1.4.1 Spectral signatures

Every atom and molecule in the Universe absorbs and emits radiation at specific wavelengths according to the possible energy levels their electrons can occupy. Larger molecules can also absorb and emit light in specific continuums due to changes in their rotational or vibrational energies. For example, when we look at the light from the Sun and separate it into individual wavelengths (a spectrum), we see dark gaps at certain wavelengths. This was first investigated by Joseph von Fraunhofer in 1814 (Fraunhofer, 1814). The lines that he first identified are today known as the *Fraunhofer Lines* (see, e.g. Smith, 1987). These are the result of molecular and atomic species in the Sun's photosphere which absorb specific wavelengths of the solar light as it passes through the photosphere towards Earth. Therefore, obtaining a spectrum like this of an exoplanet's atmosphere contains precious information about the chemical composition and abundances of species present. Unlike the Solar System objects where we can visit and take direct measurements of their atmospheres, exoplanets are too far away. Therefore, the light that we receive is our only tool to understand the chemical composition of planets (and stars) in our Galaxy.

1.4.2 Introduction to opacity

Determining which chemicals are present in an exoplanet atmosphere requires understanding the signals they produce and how they do this. The study of how radiation travels through a medium with a specific chemical composition and temperature-pressure profile is known as *radiative transfer*. One of the most important parameters in radiative transfer is the optical depth, a measure of how opaque the medium is to radiation, given by

$$\tau(\lambda) \equiv \int n\sigma(\lambda)\, dx, \tag{1.7}$$

where n is the number density, σ is the cross section, λ is the wavelength of radiation being considered and x is the length or, in the context atmospheres, the vertical distance. The number density is the density of particles of the chemical species of interest and the cross section is the 'effective size' of a particle in the context of interactions. When a photon travels through a medium (or atmosphere), it can be approximated that it will travel a distance x equivalent to $\tau \sim 1$ before being scattered or absorbed. Therefore, light coming from the surface of an exoplanet will only exit into space (and travel towards us) when it travels less than 1 optical depth. This specific distance into the atmosphere is known as the *surface of last absorption*. For a variety of uses, instead of using n and σ to calculate the optical depth, it is sometimes written as

$$\tau(\lambda) \equiv \int \kappa(\lambda)\rho\, dx, \tag{1.8}$$

where $\kappa = \sigma/m$ and is known as the opacity, and $\rho = nm$ is the species mass density.

The opacity of a chemical species is a complex combination of its scattering and absorption properties, and is very dependent on the size of the particle relative to the wavelength. The parameter that reflects how likely the particle will scatter when there is an interaction is given by the single-scattering albedo:

$$\omega \equiv \frac{\sigma_s}{\sigma_s + \sigma_a}, \tag{1.9}$$

where σ_s is the scattering cross section and σ_a is the absorption cross section. As the cross sections all depend on wavelength, so does ω.

Another important quantity related to scattering of individual particles is the scattering phase function, $p(\alpha)$. It describes the probability that a photon is scattered through some angle, α, and is normalised to unity. Depending on the composition, size and shape

of the particle, the scattering phase function can change significantly (see, e.g. Lodge et al., 2024). The overall behaviour of the scattering phase function can be characterised using the so-called asymmetry parameter, g. This parameter is essentially the mean of the cosine of the scattering angle and describes the overall shape of the phase function. An asymmetry parameter of $g \sim 1$ implies dominant for forward scattering (i.e. in the same direction as the incoming light). Whereas $g \sim -1$ implies that the photons are mostly back-scattered. A phase function with $g = 0$ is symmetric, but not necessarily isotropic. In general, particles much larger than the considered wavelength tend to have scattering phase functions with a strong forward-scattering peak, yielding asymmetry parameters close to 1. The phase function of particles much smaller than the wavelength of the photon, on the other hand, approach the limit of Rayleigh scattering, and therefore have asymmetry parameters close to 0 (see, e.g. Bohren & Huffman, 1983, van de Hulst, 1957).

The combined scattering and absorption properties of all chemical species present in an exoplanet atmosphere dictates how reflective the planet is, and what kind of radiation is transmitted from and through the atmosphere.

1.4.3 Transit spectroscopy

For exoplanets, due to the presence of a host star, there are two ways to obtain an atmospheric spectrum. The first is by obtaining a *transmission spectrum*. During a planetary transit, a small fraction of the stellar light will pass through the planet's atmosphere (assuming it has one). As we have discussed in Section 1.4.2, the light will only pass through a maximum atmospheric thickness where the optical depth $\tau = 1$. As is demonstrated in Figure 1.5, this will correspond to a specific transit radius. If we observe the transit at a wavelength where the atmosphere has a high opacity, the light will be able to pass through less atmosphere and so the transit will appear deeper and we will derive a larger planetary radius (see Equation 1.1). However, if we observe at a wavelength where the atmosphere is not absorbing at all, then the stellar light will just pass straight through and only the surface of the planet will block the star during transit. Therefore, we will derive a smaller radius. If we do this for a range of wavelengths, we obtain a spectrum of transit depths: i.e. a transmission spectrum (Seager & Sasselov, 2000, Brown, 2001, Hubbard et al., 2001). The strength of the transmission spectrum signals is proportional to the atmospheric *scale*

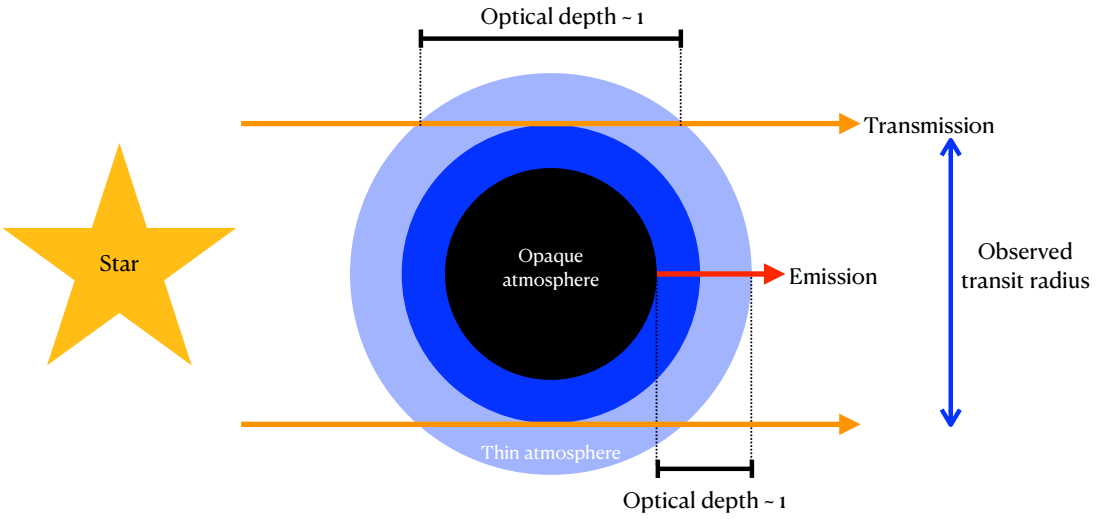

Figure 1.5 | Diagram demonstrating how we obtain a transmission spectrum. Depending on the wavelength and the opacity of the planetary atmosphere, we will observe different transit depths. The spectrum of transit depths will contain information about the chemical species present in the atmosphere. The spectrum will also weakly depend on the temperature-pressure profile of the atmosphere. However, this is only a weak correlation and it is much more informative to obtain the temperature from an emission spectrum instead (see Section 1.4.4).

height, H:

$$H = \frac{k_B T}{mg}, \tag{1.10}$$

where k_B is the Boltzmann constant, T is the mean atmospheric temperature, m is the mean molecular mass and g is the acceleration due to gravity (Winn, 2010).

For example, Figure 1.6 shows a transmission spectrum of the hot Saturn-like exoplanet WASP-39b, using data published and made publicly available in Powell et al. (2024). This was one of the first exoplanets observed with the new James Webb Space Telescope (JWST, Gardner et al., 2023, see Section 1.5.2). The increase in transit depth around 7.5 μm and a non-decrease around 9 μm is attributed to the presence of sodium oxide in the atmosphere of this planet. This was an exciting confirmation of previously tentative detections made by the JWST Early-Release Science Team (see, e.g. Rustamkulov et al., 2023, Alderson et al., 2023, Ahrer et al., 2023, Feinstein et al., 2023). Sodium oxide was a breakthrough finding as its presence suggests that photochemistry is an important process in hot Jupiter atmospheres (Tsai et al., 2023).

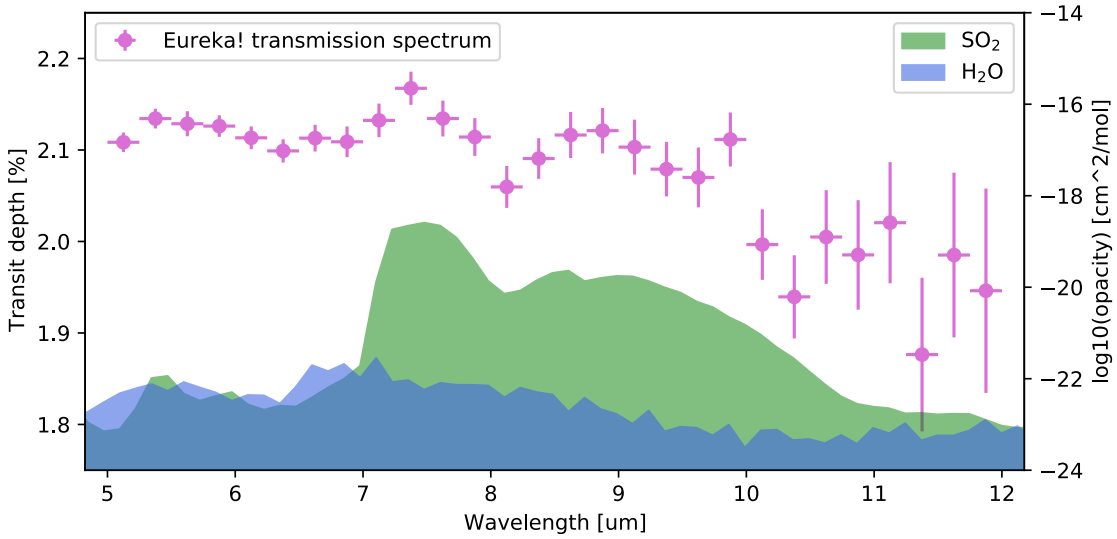

Figure 1.6 | Data from Powell et al. (2024). In pink is the transmission spectrum of WASP-39b derived with the `Eureka!` python package (Bell et al., 2022). The increase in transit depth around 7.5 μm and a non-decrease around 9 μm is attributed to the presence of sodium oxide in the atmosphere of this planet. The blue and green shaded regions show the opacity functions of sodium oxide and water to highlight the different signal origins in the transmission spectrum.

1.4.4 Emission spectroscopy

The second type of atmospheric spectrum is an *emission spectrum*, and it involves observing the radiation emitted from the planet itself. To understand this, we must first introduce a few key observables. In Section 1.2.1, we introduced a transit, however, this represents just one small portion of the entire orbit of the exoplanet.

If the planet is orbiting in a plane that produces a transit as seen from Earth, it will also be eclipsed by the star at approximately half a orbital period later (depending on the eccentricity of the orbit). Provided that there is sufficient detectable planetary flux in the observation bandpass, when the planet disappears behind the star the overall flux of the system will decrease (see Figure 1.7).

Here the phrase ‘planetary flux’ is intentionally ambiguous. This is because the origin of this flux can be separated into two parts:

- thermal emission
- reflected light.

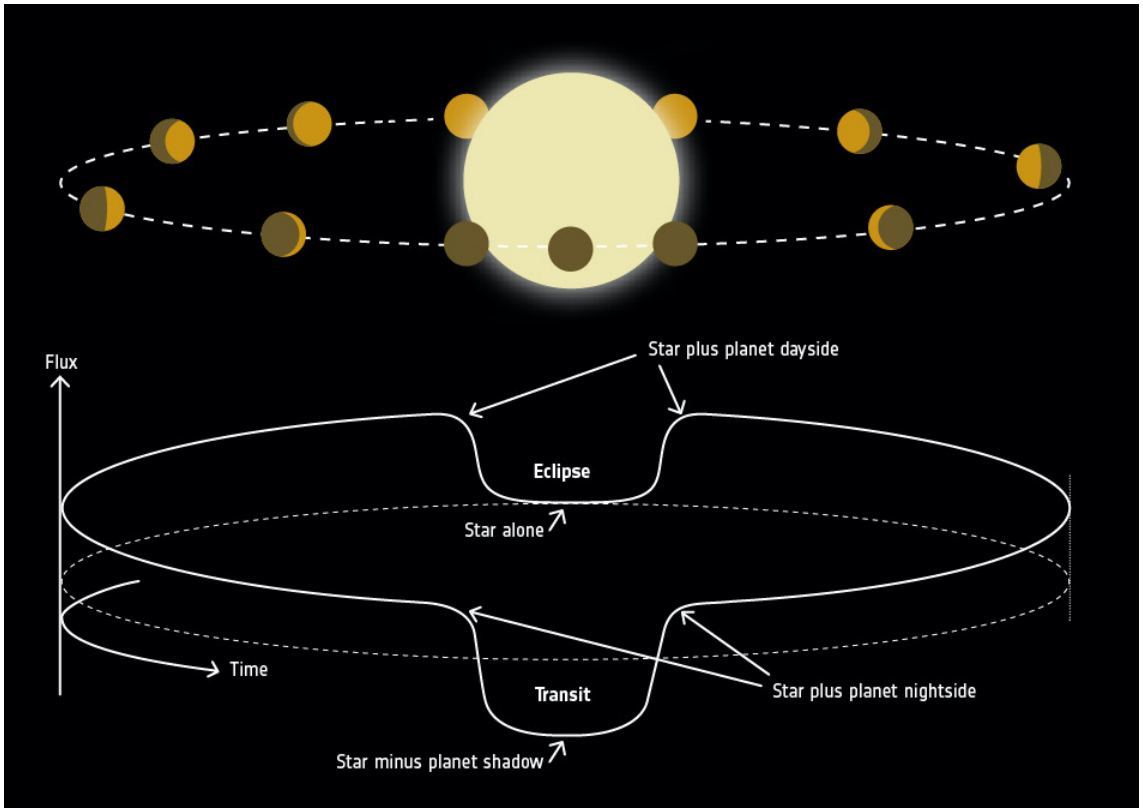

Figure 1.7 | Diagram: ©ESA. The combined planet and star system flux as a function of time is called a lightcurve. When a planet orbits its host star, like phases of the Moon, different fractions of its dayside are visible to us at different stages of its orbit. We can extract this signal to obtain information about the planet's dayside and nightside temperature and how reflective it is. The maximum planetary flux occurs mid-eclipse (however it is blocked by the star), whilst the minimum is seen during transit. Modelling all elements of the phase curve, including the transit and eclipse, is crucial to accurately determine the planetary signal.

Reflected light, perhaps trivially, is the light from the host star reflected off the planet (either atmosphere or surface, or both) back towards the observer. We will explore this phenomenon in more detail in Section 1.4.5. Thermal emission describes the radiation being emitted from the planet itself by virtue of its temperature.

Any object with a non-zero temperature will emit radiation. A perfectly opaque and non-reflective object in thermal equilibrium with its surroundings is called a blackbody, and emits a continuum of radiation with a radiance, B, given by

$$B(\lambda, T) = \frac{2hc^2}{\lambda^5} \frac{1}{e^{hc/\lambda k_B T} - 1}, \tag{1.11}$$

where $B(\lambda, T)$ is a measure of power per unit emitting area per unit wavelength per solid angle. T is the temperature of the body, λ is the specific wavelength, h is the Planck constant, c, the speed of light, and k_B, the Boltzmann constant. Due to the Lambert cosine law (Lambert, 1892), the intensity of light observed from a blackbody or other homogeneously reflecting/emitting body is directly proportional to the cosine of the angle, θ, between the normal to the body surface and the observer's line of sight. Therefore, the radiance with respect to an area normal to the propagation direction is $B(\lambda, T)\cos\theta$. Integrating this over the whole solid angle of a hemisphere, we obtain the emitted spectral flux, i.e. power per unit area per unit wavelength (note that this assumes $B(\lambda, T)$ is independent of emitting angle) :

$$\begin{aligned} F_\lambda(\lambda, T) &= \pi B(\lambda, T), \\ &= \frac{2\pi hc^2}{\lambda^5} \frac{1}{e^{hc/\lambda k_B T} - 1}, \end{aligned} \tag{1.12}$$

where the only difference from Equation 1.11 is the factor of π. As it will be used later, we can take this a step further and integrate over all wavelengths to obtain the flux (power per unit area):

$$\begin{aligned} F(T) &= \int_0^\infty \frac{2\pi hc^2}{\lambda^5} \frac{1}{e^{hc/\lambda k_B T} - 1} \, d\lambda \,, \\ &= \sigma T^4, \end{aligned} \tag{1.13}$$

where $\sigma = \frac{2\pi^5 k_B^4}{15c^2h^3}$ and is known as the Stefan-Boltzmann constant.

Assuming there is no reflected light, an eclipse depth (D) that we measure is equal to the ratio of the planetary flux to the stellar flux, at the point of observation:

$$\begin{aligned} D_{\text{thermal}} &= \frac{4\pi R_p^2}{4\pi a^2} F_p \div \frac{4\pi R_*^2}{4\pi a^2} F_*, \\ &= \left(\frac{R_p}{R_*}\right)^2 \frac{F_p}{F_*}, \end{aligned} \tag{1.14}$$

where F_p and F_* are the planetary and stellar fluxes respectively, integrated over the bandpass that the eclipse is observed in. This is a crucial point because the ratio of the planetary to stellar flux will change depending on the wavelength due to the planet and the star having distinct temperatures. Putting this equation in terms of the spectral fluxes:

$$D_{\text{thermal}} = \left(\frac{R_p}{R_*}\right)^2 \frac{\int \tau(\lambda) F_{p,\lambda}(\lambda, T_p)\, d\lambda}{\int \tau(\lambda) F_{*,\lambda}(\lambda, T_*)\, d\lambda}, \tag{1.15}$$

where $\tau(\lambda)$ is the bandpass transmission function. This is necessary because, due to hardware constraints, bandpasses are not entirely uniform and so we need to weight each wavelength differently, as determined by the instrument. Depending on the units of τ, sometimes an additional factor of λ/hc needs to be added to both the numerator and denominator. This is because the eclipse depth is usually recorded as a ratio of electron counts, instead of energy, and so to convert between energy and number of photons, we need this additional factor.

Of course, using the real stellar spectrum is ideal for F_*, however, most of the time this is not available. We must approximate by either assuming a blackbody and using Equation 1.12, or by using synthetic stellar spectra (see, e.g. Husser et al., 2013). These spectra are generated from model stellar atmospheres, and are usually much better approximations than a blackbody. They are generally available for a wide range of stellar temperatures and masses.

Using Equation 1.15, we can use numerical methods to solve for the planetary flux, however, we must assume a functional form for $F_{p,\lambda}(\lambda, T_p)$. The simplest choice is a blackbody, where we insert Equation 1.12 in place of the planet's spectral flux. This leaves us with only 1 free parameter, the blackbody temperature of the planet. This is often called the *brightness temperature*, which defines the temperature of a blackbody needed to produce the bandpass-integrated flux necessary for a secondary eclipse with the measured depth.

If we measure an eclipse depth across a range of bandpasses or wavelengths, then we will obtain a 'spectrum' of brightness temperatures, i.e. an emission spectrum. The brightness temperature will vary as a function of wavelength. This is due to the emitted radiation coming from the surface of last absorption (Section 1.4.2) and is illustrated in Figure 1.5. As planets are not known to be isothermal (none of the Solar System planets are), radiation originating from different atmospheric depths (due to changes in

the atmosphere's opacity) will be emitted at different temperatures.

Figure 1.5 shows how there are differences between emission and transmission spectroscopy. In emission, the light is coming perpendicular from the surface of the planet, whereas, in transmission, the light passes through a chord of the atmosphere. Due to the geometry, for the same 'thickness' of atmosphere, the emitted light often comes from deeper in the atmosphere than the transmitted light can probe. Also, emission spectroscopy can generally give tighter constraints on the planet's temperature-pressure profile, as this directly effects the observed flux. However, for transmission, the T-P profile has less of a direct effect. This is more of an advantage than a problem, as these two techniques combined can give us even more spectroscopic and thermal profile information about a planet's atmosphere.

1.4.5 Reflected Light

Let us now consider how reflected light changes a planet's eclipse depth. Firstly, we need to introduce a few macroscopic properties of reflection. The brightness (in reflected light only) of a planet compared to an isotropically scattering disk is given by A_g, the geometric albedo. If the atmosphere preferentially scatters in the direction of the observer, then this value can be greater than 1. We can show how this relates to the eclipse depth by consider the amount of stellar flux reaching the planet and then how much is reflected. The reflected planetary flux is therefore:

$$\begin{aligned} F_p &= A_g \frac{4\pi R_*^2}{4\pi a^2} F_*, \\ &= A_g \frac{R_*^2 F_*}{a^2}. \end{aligned} \tag{1.16}$$

Substituting this into Equation 1.14, we find that

$$D_{\text{reflected}} = A_g \left(\frac{R_p}{a}\right)^2. \tag{1.17}$$

Therefore, when both reflected light and thermal emission are present, the eclipse depth can be expressed as:

$$D_{\text{total}} = \left(\frac{R_p}{R_*}\right)^2 \frac{\int \tau(\lambda) F_{p,\lambda}(\lambda, T_p)\, d\lambda}{\int \tau(\lambda) F_{*,\lambda}(\lambda, T_*)\, d\lambda} + A_g \left(\frac{R_p}{a}\right)^2. \tag{1.18}$$

In order to accurately determine the planet's brightness temperature from the secondary eclipse, the contribution from the reflected light needs to be removed. This will be explored in more detail in Chapter 5.

1.4.6 Phase curves

To go even further, we can observe a planet throughout its entire orbit to obtain a *phase curve*, allowing us to collect three-dimensional information about its atmosphere. Assuming the planet is transiting, the phase curve will include a transit, occultation and the additional signal from the planet as it goes around the host star. As shown in Figure 1.7, similar to phases of the Moon, different fractions of the dayside of the exoplanet will be visible to us (the observer) at different times in its orbit. The amplitude, shape and phase offset of this signal gives us very important longitudinal information about the planet's emission.

Planets receive the most stellar irradiation at their substellar point. If there is no redistribution of heat then the planet's phase curve should peak exactly during secondary eclipse (although it is blocked by the star). However, if there are dynamic processes happening in the atmosphere, such as day-to-nightside winds, this 'hotspot' can shift and the phase curve peak will have a *phase offset*. We also get information about the nightside temperature of the planet by observing the phase curve signal at its minimum (i.e. during transit - for circular orbits). For planets with a rotation period significantly less than their orbital period, it could be assumed that the planet would absorb the light from the star and then re-radiate it as thermal emission relatively uniformly across the entire surface. However, for tidally locked planets, where the same hemisphere is always facing the star, the heat from the star may not be so evenly distributed between the constant dayside hemisphere and the nightside hemisphere. The level of this 'heat redistribution' can provide insights into the dynamics and chemistry of the planet's atmosphere. This topic is explored in more detail in Chapter 2.

Phase curves are crucial to our understanding of the 3D structure of exoplanets. However, in order to extract this information, we need accurate phase curve models. Some of the simplest solutions are analytic, for example, the basic solution would be to describe the phase curve as a sine function, i.e,

$$F = A \sin(\phi + \xi), \tag{1.19}$$

where A is the phase curve amplitude, ϕ is the phase and ξ is the phase offset. $\phi = 0$ is defined as the secondary eclipse and $\phi = [-\pi, \pi]$ is the transit. This is straightforward to model, however, not the most physical (i.e. not derived from physical principles). We

can go a step further and assume the planet is a Lambertian Sphere (i.e. an isotropically emitting or scattering sphere). In this case, the phase curve flux, F, can be described as

$$F = A(\sin|\phi| + (\pi - |\phi|)\cos|\phi|). \tag{1.20}$$

There are also variations of this by Hu et al. (2015), called a 'piece-wise Lambertian', which allows reflection/emission within two longitude boundaries, and negligible flux elsewhere.

We know, not only from the planets in our own Solar System, but also phase curves from hot Jupiters, that exoplanets are generally not isotropically emitting spheres. General Circulation Models (GCMs) have also predicted this (Showman et al., 2009, Rauscher & Menou, 2013). Specifically for hot Jupiters, we expect a non-symmetric hot spot and a 2D temperature structure dependent on thermal flows and winds in the atmosphere (see, e.g. Roth et al., 2024, Tan & Komacek, 2019, Amundsen et al., 2016). Clouds are also expected to be very influential in the observed emission and reflective properties of an exoplanet atmosphere (see, e.g. Parmentier et al., 2016, Powell et al., 2018), especially if they do not cover the planet uniformly (see Chapter 3) or are variable in time.

In Morris et al. (2022), we created and tested a 2D temperature map model for hot Jupiters that uses modified-spherical harmonics as the basis functions for the map (see Figure 1.8). From these maps, we integrate longitudinally to obtain a phase curve that can be compared to observations. Once we obtain the best-fit global temperature map of the planet, we can calculate properties such as the Bond albedo (ratio of the total reflected stellar flux to the incoming stellar flux, i.e., the geometric albedo integrated over all phase angles and wavelengths) and the heat redistribution efficiency (dayside flux to nightside flux ratio) – areas which I specifically contributed to.

There are other physically-motivated phase curve models such as `starry` (Luger et al., 2019), which uses normal spherical harmonics and a special mathematical framework to allow for fast-computing, and `TauREx3 PhaseCurve` (Changeat & Al-Refaie, 2020), a '1.5D' phase curve model which splits up the planetary atmosphere into three distinct sections corresponding to the dayside, nightside and terminator. Each section then contributes to the overall transmission spectrum.

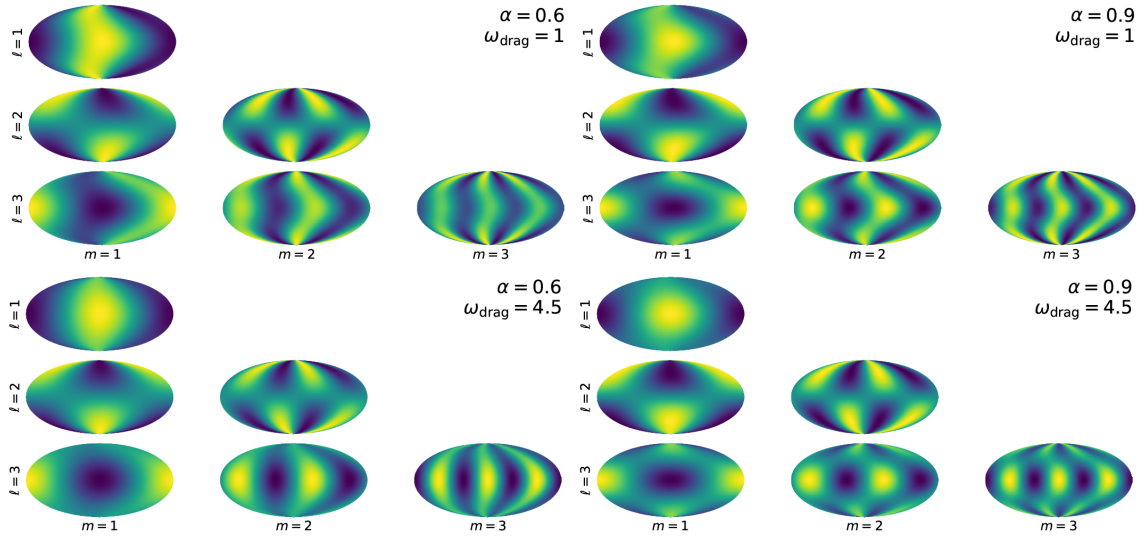

Figure 1.8 | The different modes of the modified spherical harmonics we used in Morris et al. (2022) to model the thermal phase curves of hot Jupiters. The two sides show how the parameters α and ω_{drag} change the shape of the functions.

1.5 Observations

The robustness of our atmospheric models rely on having the observations to compare them to. With recent technological advances in precision photometric (broad-band) and spectroscopic instruments, the level of precision we can achieve in our light curve observations have improved dramatically. For example, with ground-based observations it was realistic to expect a noise floor no lower than ~ 200 ppm (i.e. 0.02%), however, now with space-based observations from CHEOPS, TESS and JWST, we can get down to 10's of ppm precision (or $< 0.001\%$). For context, depending on the observed bandpass, the transit depth of most Jupiter-sized exoplanets is of the order of 1000 ppm, whilst their eclipse depths are usually of the order of 10 to 100 ppm. What these lower noise floors mean is that we can now probe exciting regimes including the dayside emission and reflection of super-Earths and the nightside of hot Jupiters.

The precision of our light curves also highly depends on the cadence (i.e. time between data points) with which we observe. This is very important when observing a transit, since most of the information about the impact parameter and shape of the limbs of the exoplanet (see Chapter 3) are encoded in the ingress and egress which, most of the time, have very short durations compared to the transit overall.

In the next few subsections we give further details about the telescopes and instru-

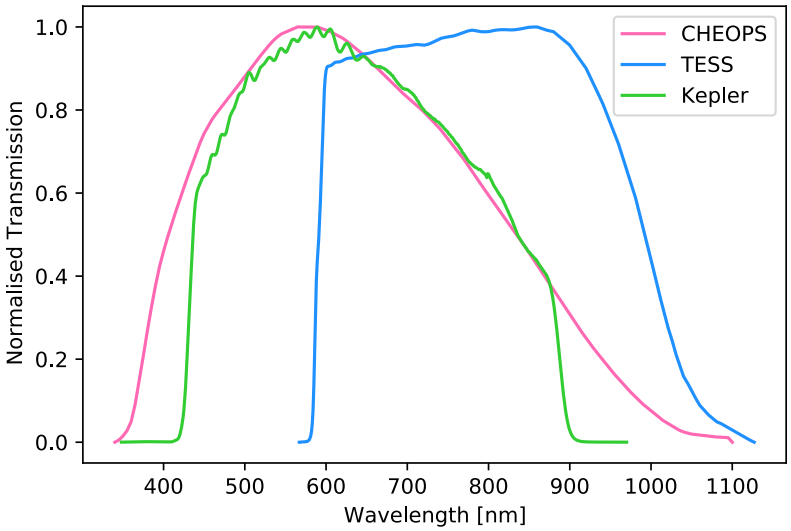

Figure 1.9 | Normalised telescope transmission functions for CHEOPS, TESS and Kepler plotted as a function of wavelength. Data from the SVO Filter Profile Service (Rodrigo & Solano, 2020).

ments used in this thesis and how they have impacted the field of exoplanet atmospheres so far.

1.5.1 CHEOPS

The CHaracterising ExOPlanet Satellite (CHEOPS) mission is a 30 cm space telescope in a low-Earth orbit, and has been operational since the beginning of 2020 (Benz et al., 2021). CHEOPS has now finished its 3.5-year nominal mission and has been granted an extended mission until 2026. A major component of the guaranteed time observations performed in the nominal mission involved thorough atmospheric classification of a wide range of transiting exoplanets, using precise full-phase curve and occultation observations. CHEOPS is a photometric instrument, with a bandpass overlapping and slightly bluer than TESS (Ricker et al., 2015) (see Figure 1.9 for a comparison of the instrument transmission functions).

Notable results from using CHEOPS include observing a hot dayside atmosphere and asymmetric transit of WASP-189b caused by gravity darkening (Lendl et al., 2020, Deline et al., 2022), a six-planet system in a Laplace resonance chain (TOI-178, Leleu et al., 2021), the transit of ν^2 Lupi d, a planet on a 109 day orbit (Delrez et al., 2021, Ehrenreich

et al., 2023), and the detection of tidal-deformation of a hot Jupiter (Barros et al., 2022). One of the largest observation campaigns of the program was observing phase curves (29 in total) of the super-Earth 55 Cnc e, where we detected significant atmospheric variability and showed that it could not be attributed to a circumstellar torus of dust (Meier Valdés et al., 2023, Morris et al., 2021). Since CHEOPS scheduling is more flexible than the whole-sky survey telescope TESS, it has often been used to follow-up promising targets from TESS and track down their orbital periods (see, e.g. Luque et al., 2023).

Another large study using CHEOPS was to observe and analyse high-precision phase curves of hot Jupiters to determine their day (and some nightside) temperatures and geometric albedos. This includes my work on KELT-9b, the hottest known exoplanet, detailed in Chapter 2.

1.5.2 JWST

The James Webb Space Telescope (JWST) is part of the new generation of space telescopes. It was launched on Christmas Day 2021 and started its science operations at its home at Lagrange-point Two (Euler, 1767) in July 2022. It aims to study and advance the science of a wide range of astrophysics sub-fields, including exoplanets. The reason it is so important for exoplanet research is due to its four instruments which can take spectroscopic measurements in the infrared (NIRISS, NIRSpec, NIRCam and MIRI). This allows us to peer into the atmospheres of smaller and cooler planets (by either transit or eclipse spectroscopy, or phase curve spectroscopy).

First results from JWST revealed the ability to capture a wide and precise transmission spectrum of hot Jupiter WASP-39b from all four instruments (Rustamkulov et al., 2023, Ahrer et al., 2023, Alderson et al., 2023, Feinstein et al., 2023). Further observations of this target revealed the first detections of sodium oxide in the atmosphere (see, e.g. Tsai et al., 2023, Powell et al., 2024). Other notable results have been the detections of methane and carbon dioxide in the atmosphere of K2-18b (Madhusudhan et al., 2023), which, they argued, could be due to the planet being a so-called 'Hycean world' - a temperate ocean-covered world with a H_2-rich atmosphere with the potential to harbour life (Madhusudhan et al., 2021). However, as of now, Hycean worlds are not yet widely accepted as a planet type due to their complicated origins and degenerate observations (see, e.g. Wogan et al., 2024). Another recent result from JWST has been the spectral

variability of 55 Cnc e (McArthur et al., 2004). Firstly, Hu et al. (2024) published a tentative detection of a CO_2 secondary atmosphere (i.e. not from the primordial disk). Using two different instruments (NIRCam and MIRI) in spectroscopic modes, they found this kind of atmosphere was preferred with a confidence of 2-3 σ. However, Patel et al. (2024) observed four more occultations using NIRCam, and found wild variation in the eclipse depths, not only in time but also in wavelength, putting Hu et al. (2024)'s claims into question. This aperiodic and seemingly random variability was also observed with CHEOPS, as mentioned in Section 1.5.1.

1.5.3 Future Missions

Even as JWST has only just started its nominal mission, astronomers are already turning their thoughts to what is next. Mission planning takes decades so it is important for the community to support the development of new technology and telescopes to invest in the future of their respective fields.

For exoplanets, we remain in very exciting and dynamic times. There are three major upcoming missions on the near-horizon that will have large impacts on exoplanet science. The first is PLATO (PLAnetary Transits and Oscillations of stars, Rauer et al., 2024), an ESA mission which will have 26 cameras staring at a singular patch of sky for a number of years in order to discover longer-period exoplanets and characterise planet host stars signals and variability.

The second is The Nancy Grace Roman Space Telescope (Spergel et al., 2013), a NASA-lead mission aimed to utilise its large field-of-view and high mirror sensitivity to not only study distant galaxies, but search for habitable exoplanets using visible to infrared cameras and spectrographs. They will perform wide-field surveys, in contrast to JWST and CHEOPS, including searching for planets using the microlensing method (see Section 1.2.4).

The third is ARIEL (Atmospheric Remote-sensing Infrared Exoplanet Large-survey, Tinetti et al., 2021), another ESA-lead mission planned to launch in 2029. It will observe exoplanets using the transit method with both visible and infrared images and an infrared spectrograph. Unlike PLATO, ARIEL is focussed on characterising previously-discovered planets.

To look beyond the horizon is uncertain, however, there are mission concepts already

in place. For exoplanets, there is the Habitable Worlds Observatory (Dressing et al., 2024), a large UV/optical/NIR space observatory focussing on all aspects of astrophysics and cosmology. It is imagined to obtain near-flyby quality observations of objects in our Solar System and measure spectra of 25 habitable-zone exoplanets. Mostly driven by Switzerland, there is also LIFE (Large Interferometer For Exoplanets, Quanz et al., 2022), a space mission being designed to search for and characterise dozens of temperate Earth-like exoplanets and investigate signs of habitability.

Chapter 2

The Stable Climate of KELT-9b

This chapter has been published in A&A as **Jones, K. D.**, Morris, B. M., Demory, B. -O., Heng, K., Hooton, M. J. and the CHEOPS consortium 2022, A&A, 666, A118, doi: 10.1051/0004-6361/202243823, *The stable climate of KELT-9b*.

For its whole existence, an exoplanet is irradiated by its host star. What happens to this radiation and how it drives the thermal dynamics and structure of the planet is one of the most important aspects of understanding exoplanet atmospheres. As mentioned in Section 1.4, investigating the temperature structure and heat exchange processes in the atmosphere is a crucial step to understand the climate of an exoplanet.

A full exoplanet phase curve encodes vast amounts of information about the planet and its atmosphere/surface. However in order to reliably extract that information, accurate and physically-motivated models are needed for all the different elements that make up a phase curve (see Section 1.4.6). Hot Jupiters are excellent laboratories to test our methods; due to their tidally-locked orbits they often have extreme longitudinal temperature contrasts. The larger this contrast (and therefore the larger the phase curve amplitude), the higher the signal-to-noise ratio which allows us to extract more precise model parameters from a model fit. They also have short orbital periods, and so observing (often multiple) full phase curves of hot Jupiters is currently feasible with even the largest and most time-expensive space telescopes.

To investigate models that look at the 3D temperature structure of a hot Jupiter, KELT-9b is an ideal candidate. As the hottest-known exoplanet with a measured dayside temperature above 4500 K, it is hotter than most K-type stars. These temperatures mean that the blackbody peak of the planet reaches a maximum in the optical regime. The depth of an

eclipse does also depend on the stellar temperature, however the planet's temperature is a satisfactory indicator of achieving high signal-to-noise observations in the wavelength range of interest. Additionally, these temperatures are high enough to thermally dissociate most molecules, so we can assume the atmosphere of KELT-9b is cloud-free. As clouds often mask the true temperature profile and chemical composition of a planetary atmosphere, this makes modelling the signals from KELT-9b much less complex and degenerate.

Abstract

Even among the most irradiated gas giants, so-called ultra-hot Jupiters, KELT-9b stands out as the hottest planet thus far discovered with a dayside temperature of over 4500 K. At these extreme irradiation levels, we expect an increase in heat redistribution efficiency and a low Bond albedo owed to an extended atmosphere with molecular hydrogen dissociation occurring on the planetary dayside. We present new photometric observations of the KELT-9 system throughout 4 full orbits and 9 separate occultations obtained by the 30 cm space telescope CHEOPS. The CHEOPS bandpass, located at optical wavelengths, captures the peak of the thermal emission spectrum of KELT-9b. In this work we simultaneously analyse CHEOPS phase curves along with public phase curves from TESS and *Spitzer* to infer joint constraints on the phase curve variation, gravity-darkened transits, and occultation depth in three bandpasses, as well as derive 2D temperature maps of the atmosphere at three different depths. We find a day-night heat redistribution efficiency of ~ 0.3 which confirms expectations of enhanced energy transfer to the planetary nightside due to dissociation and recombination of molecular hydrogen. We also calculate a Bond albedo consistent with zero. We find no evidence of variability of the brightness temperature of the planet, excluding variability greater than 1% (1σ).

2.1 Introduction

Understanding the climate of an exoplanet involves quantifying its global thermal and chemical structure. To date there have been a plethora of methods used to aid in this characterisation, including observing a phase curve. This is a lightcurve of the system taken as the planet orbits the star. The planet can add to the total flux of the system with either thermal emission or reflected light from the star. Similar to phases of the Moon, different fractions of the dayside of the exoplanet will be visible to us at different times in its orbit. There are three main observables within a phase curve: phase curve amplitude and shape, the occultation depth (when the planet goes behind the star) and the planet's hotspot phase offset (from the substellar point). From this information, one can derive 2D temperature maps of the planet's photosphere. For planets with a rotation period significantly less than its orbital period, it could be assumed that the planet would absorb the light from the star and then re-radiate it as thermal emission relatively uniformly

across the entire surface. However, for tidally locked planets, where a single hemisphere is always facing the star, it can be seen that the heat from the star is not so evenly distributed. The level of this 'heat redistribution' can provide insights into the dynamics and chemistry of the planet's atmosphere.

Ultra-hot Jupiters (UHJs) are a newly emerging class of short-period exoplanets with temperatures exceeding ~2500 K. Crucially, several chemical properties distinguish them from regular hot Jupiters. Firstly, their dayside atmospheres are hot enough that hydrogen is predicted to exist in its atomic form (Bell & Cowan, 2018). The photon energies involved in H^- opacities become the dominant source of the spectral continuum over Rayleigh scattering (Arcangeli et al., 2018), resulting in a low optical geometric albedo. As these planets are tidally locked with their host star, the hydrogen will recombine to molecular hydrogen at cooler longitudes, assisting with the heat transport around the planet. The prediction of higher heat redistribution in UHJs as opposed to moderately hot Jupiters follows this (Bell & Cowan, 2018). Secondly, the high dayside temperatures result in the thermal dissociation of most molecules, leaving only water and carbon monoxide as the main opacity sources (see also, e.g. Lothringer et al., 2018, Kitzmann et al., 2018, Parmentier et al., 2018). Following this, metals are predicted to exist in their atomic form rather than being bound in molecules, a prediction that has been observationally verified for KELT-9b (Hoeijmakers et al., 2018; 2019, Pino et al., 2020, Bello-Arufe et al., 2022). Due to the high levels of irradiation, UHJs are expected to have extended atmospheres which also lends itself to hydrogen atmospheric escape, a phenomenon also detected for KELT-9b (Yan & Henning, 2018, Wyttenbach et al., 2020). Chemically, UHJs are objects in between gas-giant exoplanets and stars.

Not only is it important to characterise the thermal and reflective properties of a planet, but also any transient departures from the mean global state (weather). Observed variability may be caused by dynamical processes in the atmosphere of the exoplanet (see review by Heng & Showman, 2015); for example, baroclinic instabilities in the Earth's atmosphere occur on timescales of 3 to 7 days (Peixóto & Oort, 1984). To date, quantifying the climate of an exoplanet and any associated transient phenomena has only been attempted for hot Jupiters. This is due to their short orbital periods (which facilitate repeated observations) and large atmospheric pressure scale heights (due to their hot, hydrogen-dominated atmospheres). Armstrong et al. (2016) claimed variability from HAT-P-7b in

the form of a shift in the peak offset of its Kepler phase curve from either side of the substellar point. However this was reassessed in Lally & Vanderburg (2022) and they concluded that the apparent variations were artefacts most likely caused by stellar super-granulation. Furthermore, Agol et al. (2010) analysed 7 transits and 7 secondary eclipses of HD 189733b, measured by the *Spitzer* Space Telescope, and set an upper limit of 2.7% on the variability of flux from its dayside. In addition, Owens et al. (2021) scrutinised 27 days of TESS data and found no detectable variability from WASP-12b (another UHJ). Other works focussed on the aspects of a climate that can be probed with phase curves include Kreidberg et al. (2018), who used Hubble-WFC3 and *Spitzer* phase curves of the UHJ WASP-103b to infer inefficient dayside-to-nightside heat redistribution, an absence of water and a carbon-to-oxygen ratio less than 0.9. Arcangeli et al. (2019) used Hubble-WFC3 phase curves of the UHJ WASP-18b to find that atmospheric drag is needed to explain the observed dayside-nightside flux contrast and they speculated that this drag may be magnetic in nature.

KELT-9b is the hottest known exoplanet and the most extreme member of the UHJ class with an equilibrium temperature of 4050 ± 180 K (Gaudi et al., 2017). It has a near-polar, 1.48-day orbit around a rapidly rotating A0B9 star ($T_{\rm eff} = 10170$ K) (Gaudi et al., 2017). Its dayside brightness temperature has been measured to be 4600 K in both the z-band (Gaudi et al., 2017) and the TESS bandpass (Wong et al., 2020b), making the dayside of KELT-9b as hot as the photosphere of a K4 star. This dayside brightness temperature implies a peak blackbody emission wavelength of 0.63 μm, which sits in the centre of the CHEOPS bandpass. In Hooton et al. (2018), they found a near-ultraviolet geometric albedo upper limit of < 0.14 (3σ) and in Sudarsky et al. (2000) at wavelengths applicable to CHEOPS, they predict a geometric albedo around 0.05, which corresponds to a percentage of reflected light in the CHEOPS bandpass of $\lesssim 8\%$ of the total dayside flux (thermal emission plus reflected light). These properties imply that the CHEOPS space telescope is well-positioned to monitor the thermal flux of KELT-9b.

The CHaracterising ExOPlanet Satellite (CHEOPS) mission is a 30 cm space telescope in a low-Earth orbit since December 2019 (Benz et al., 2021). A major component of the guaranteed-time observations planned in the nominal mission involve a thorough atmospheric classification of a wide range of transiting exoplanets, using precise full-phase curve and occultation observations. Published detections include a hot dayside

atmosphere for the UHJ WASP-189b (Lendl et al., 2020, Deline et al., 2022) variations in the phase curve of the super-Earth 55 Cnc e (Morris et al., 2021), and a hint of day-side reflection for another UHJ, MASCARA-1b (Hooton et al., 2022). In this work, we embark on a comprehensive observational campaign to quantify the climate and variability of KELT-9b. Using the CHEOPS space telescope, we observed 9 secondary eclipses and 4 full phase curves. Additionally, we re-analyse the 4.5 μm *Spitzer* and TESS phase curves of KELT-9b. We interpret the CHEOPS, TESS, and *Spitzer* phase curve variation jointly using `kelp`, a recently published framework that describes a 2D temperature map using parabolic cylinder functions (Morris et al., 2022).

In Section 2.2 we detail the technical aspects of the CHEOPS, TESS, and *Spitzer* observations and include a description of the CHEOPS space telescope and its data reduction pipeline. Section 2.3 explains the different sections of the data analysis and includes a detailed description of the models used to model the phase curves in each bandpass and the CHEOPS occultations. In Section 2.4, we report the results of our phase curve fit and occultation eclipse depths. Within this section, in Section 2.4.1 and 2.4.2 we show the bandpass-dependent 2D thermal maps derived from the best-fit phase curve parameters and discuss the resulting day and nightside integrated temperatures. The results of the CHEOPS occultation analysis is detailed in Section 2.4.3 and in Section 2.4.4 we report the Bond albedo and heat redistribution efficiency. Finally in Section 2.4.5 we compare our results with previous results using the same datasets. A discussion of the impact and importance of this work for the study of the climate on UHJs and future multi-wavelength JWST phase curves can be found in Section 4.5.

2.2 Observations

2.2.1 CHEOPS observations

CHEOPS is an on-axis Ritchey-Chrétien telescope (Benz et al., 2021). Its nadir-locked orientation keeps the bottom of the spacecraft pointed towards Earth throughout each orbit, causing the field of view of CHEOPS to rotate during science observations. This frequently results in systematic noise in phase with the spacecraft roll angle, as neighbouring stars contribute varying levels of contamination into the CHEOPS aperture over one spacecraft orbit (e.g, Lendl et al., 2020). Detailed systematic investigations have re-

vealed that CHEOPS observations occasionally contain a ramp feature whereby the flux of the first few orbits can show a significant correlation with the temperature fluctuations of the telescope assembly and is most likely caused by the change in temperature of the telescope as it adjusts to a new pointing position (Morris et al., 2021).

CHEOPS observed nine occultations of KELT-9 between 25 July 2020 and 24 July 2021 and four phase curves; observed on 31 August 2020, 10 September 2020, 31 July 2021 and 22 August 2021, each observation lasting around 2.4 days. The individual occultation observations lasted between 5.9 and 6.9 hours, distributed over 4 to 5 CHEOPS orbits. Further details of the individual observations can be found in Table 2.1.

CHEOPS data is automatically processed by the CHEOPS Data Reduction Pipeline (DRP, Hoyer et al., 2020). The CHEOPS DRP performs the basic calibration of the science images (i.e. bias, dark, flat-field corrections) and also performs background correction, cosmic-rays hits removal, correction of bright stars' smear trail contamination and provide estimations of the flux contamination of background stars (see details in Hoyer et al., 2020). Finally, the DRP extracts the photometric signal of the target in 3 standard apertures called `RINF`, `DEFAULT` and `RSUP` (at radius of R=21.5", 25" and 30"), in addition to the `OPTIMAL` aperture with a radius set to minimise the effect of the contamination by close-by background stars. In the case of KELT-9 observations this aperture was set at R=40". In our analysis we use the light curves obtained with the `DEFAULT` aperture.

2.2.2 TESS observations

The TESS satellite (Ricker et al., 2015) observed more than 20 phase curves of KELT-9 during Sector 14 and 15 of the telescope's operation (months of July and August 2019). These observations were first published in Wong et al. (2020b) using their own reduction techniques. For our analysis we used the PDCSAP flux measurements at 2 minutes cadence (pre-reduced using the TESS SPOC pipeline to remove long-term trends and systematics) (Jenkins et al., 2016). We downloaded the data and stitched the light curves into a single array using `lightkurve` (Lightkurve Collaboration et al., 2018).

2.2.3 *Spitzer* observations

In this work, we analyse the *Spitzer* archival data of KELT-9 b that have already been published (Mansfield et al., 2020). We downloaded KELT-9 b archival IRAC data from

Date Start [UT]	Date Stop [UT]	File Key	Duration [dd:hh:mm]	Exposure Time [s]	Exposures per stack	Efficiency %
2020-07-25 07:15	2020-07-25 14:05	CH_PR100036_TG001201_V0200	00:06:50	36.7	3 (×12.2 s)	61
2020-08-04 16:02	2020-08-04 21:52	CH_PR100036_TG001202_V0200	00:05:50	36.7	3 (×12.2 s)	66
2020-08-17 23:54	2020-08-18 05:49	CH_PR100036_TG001203_V0200	00:05:55	36.7	3 (×12.2 s)	73
2020-08-20 23:28	2020-08-21 05:57	CH_PR100036_TG001204_V0200	00:06:28	36.7	3 (×12.2 s)	65
2020-08-23 23:20	2020-08-24 05:21	CH_PR100036_TG001205_V0200	00:06:00	36.7	3 (×12.2 s)	72
2020-08-28 10:32	2020-08-28 16:30	CH_PR100036_TG001206_V0200	00:05:58	36.7	3 (×12.2 s)	71
2020-09-03 08:19	2020-09-03 14:17	CH_PR100036_TG001207_V0200	00:05:58	36.7	3 (×12.2 s)	72
2020-09-13 16:15	2020-09-13 22:44	CH_PR100036_TG001208_V0200	00:06:28	36.7	3 (×12.2 s)	50
2021-07-24 15:45	2021-07-24 21:37	CH_PR100036_TG001209_V0200	00:05:52	36.7	3 (×12.2 s)	69
2020-08-31 13:29	2020-09-03 00:53	CH_PR100036_TG001001_V0200	02:11:24	36.7	3 (×12.2 s)	61
2020-09-10 03:31	2020-09-12 14:11	CH_PR100036_TG001002_V0200	02:10:39	36.7	3 (×12.2 s)	59
2021-07-31 04:25	2021-08-02 15:06	CH_PR100036_TG000901_V0200	02:10:40	36.7	3 (×12.2 s)	63
2021-08-22 11:04	2021-08-24 22:15	CH_PR100036_TG000902_V0200	02:11:10	36.7	3 (×12.2 s)	62

Table 2.1 | CHEOPS observation logs, corresponding to the occultation-only observations in the first 9 rows and the phase curve observations in the last 4 rows. The File Key is useful for uniquely identifying the visits used in this work.

the *Spitzer* Heritage Archive[1]. The data consist of one full phase curve at 4.5μm split in two Astronomical Observation Requests (AORs) obtained under program ID 14059 (PI J. Bean). The reduction and analysis of these datasets are similar to Demory et al. (2016a). We model the correlated noise associated with IRAC intra-pixel sensitivity (Ingalls et al., 2016) using a modified implementation of the BLISS (BiLinearly Interpolated Sub-pixel Sensitivity) mapping algorithm (Stevenson et al., 2012).

In addition to the BLISS mapping, our baseline model includes a linear function of the Point Response Function (PRF) Full Width at Half-Maximum (FWHM) along the x and y axes, which significantly reduces the level of correlated noise as shown in previous studies (see, e.g.: Lanotte et al., 2014, Demory et al., 2016b;a, Gillon et al., 2017, Mendonça et al., 2018). Our baseline model does not include time-dependent parameters. Our implementation of this baseline model is included in a Markov Chain Monte Carlo (MCMC) framework already presented in the literature (Gillon et al., 2012). We run two chains of 200,000 steps each to determine the phase curve properties at 4.5 μm based on the entire dataset described above. From our BLISS mapping+FWHM baseline model, we obtain a median RMS of 723 ppm per 23s integration time for that dataset.

[1] http://sha.ipac.caltech.edu

2.2.4 Stellar parameters

As a key stellar prior in our analysis, we determine the stellar radius of KELT-9 using a Markov-Chain Monte Carlo (MCMC) modified infrared flux method (IRFM; Blackwell & Shallis 1977, Schanche et al. 2020). To achieve this, we compute synthetic fluxes from constructed spectral energy distributions (SEDs). These were built from stellar atmospheric models and stellar parameters derived via the spectral analysis in Borsa et al. (2019) that were integrated over bandpasses of interest with the SED attenuated to determine the extinction within the model fitting. We compared these fluxes to observed broadband photometry retrieved from the most recent data releases for the following bandpasses; *Gaia* G, G_{BP}, and G_{RP}, 2MASS J, H, and K, and *WISE* W1 and W2 (Gaia Collaboration et al., 2021, Skrutskie et al., 2006, Wright et al., 2010) to calculate the apparent bolometric flux, and hence the stellar angular diameter and effective temperature. In our analysis we use stellar atmospheric models from the ATLAS Catalogues (Castelli & Kurucz, 2003). By converting the angular diameter to the stellar radius using the offset-corrected *Gaia* EDR3 parallax (Lindegren et al., 2021), we obtain $R_\star = 2.379 \pm 0.038\,R_\odot$.

The stellar radius $R_\star$ together with the effective temperature $T_{\rm eff}$ and the metallicity [Fe/H] constitute the input set to determine the isochronal age $t_\star$ and mass $M_\star$. To make the derivation process more robust we employed two different stellar evolutionary models, namely PARSEC v1.2S[2] (Marigo et al., 2017) and CLES (Code Liègeois d'Évolution Stellaire, Scuflaire et al., 2008). In detail, we used the capability of the isochrone placement technique (Bonfanti et al., 2015; 2016) to fit the input parameters within pre-computed PARSEC grids of tracks and isochrones so to retrieve a first pair of age and mass estimates. A second pair of age and mass values, instead, was directly computed by the CLES code which generates the best evolutionary track that is compatible with the input parameters following a Levenberg-Marquadt minimisation scheme (see Salmon et al., 2021, for further details). After checking the mutual consistency of the two respective pairs through a χ^2-based criterion, we finally merged our outcomes as described in Bonfanti et al. (2021) and we obtained $t_\star = 0.3 \pm 0.1$ Gyr and $M_\star = 2.45^{+0.19}_{-0.17}\,M_\odot$.

[2] *PA*dova and T*R*ieste *S*tellar *E*volutionary *C*ode: http://stev.oapd.inaf.it/cgi-bin/cmd

Table 2.2 | Stellar parameters used to derive the stellar radius and mass used in this paper. This table also includes these calculated parameter values.

Stellar parameter	Unit	Value
Metallicity	dex	0.14 ± 0.30
Surface gravity	dex	4.1 ± 0.3
Radius	$R_\odot$	2.379 ± 0.038
Mass	$M_\odot$	$2.45^{+0.19}_{-0.17}$
Age	Gyr	0.3 ± 0.1

2.3 Analysis

2.3.1 Phase curves

Over its first and second year, CHEOPS has observed 4 full phase curves of KELT-9; TESS has observed over 20 and *Spitzer* has observed 1. We present here a joint analysis of all these observations.

As already discussed in Section 2.1, KELT-9b is the hottest known exoplanet with a dayside temperature of ~4600 K and a thermal emission peak in the CHEOPS bandpass as well as efficient optical absorbers. We therefore assume that all phase curves are completely dominated by thermal emission, an assumption justified in Schwartz et al. (2017) and Morris et al. (2022).

We fit each instrument's observations with a self-consistent transit, eclipse and thermal phase curve model. Table 2.3 shows the parameters common to all phase curves and Table 2.4 shows parameters that are instrument-specific. In the following subsections, we detail the different components of the model used in the fitting procedure, along with the detrending and other models specific to each bandpass.

To fit our global model, we used an affine-invariant ensemble sampling to estimate the parameter posterior distributions with 900 walkers, 5000 burn-in steps and then 80000 steps (Foreman-Mackey et al., 2013). We confirmed that the chains converged by analysing the autocorrelation time. The integration length is 50 times the number of samples.

2.3.1.1 Gravity-darkened transit model

Gravity can darken stellar photospheres due to rapid rotation, shaping the star into an oblate spheroid. von Zeipel (1924) showed that this oblateness causes a temperature gradient across the surface of the star and consequently reduces the emitted flux near the equator. Depending on the geometry of the star-planet system, this causes significant deviations from a simple symmetric transit light curve (Barnes, 2009). This effect is in addition to limb darkening (Claret, 2017). We must accurately model the transits in our observations in order to calculate the planetary radius and model the phase curve amplitude accurately, which in turn gives us information about the temperature map of the planet.

We model the transit of KELT-9b with `pytransit` (version 2.5.17, Parviainen, 2015), an open-source Python package which implements a gravity-darkened transit model based on Barnes (2009). For describing this model we will use the same notation as in Hooton et al. (2022). The model is characterised by

- R_*, the stellar radius
- R_p, the planetary radius (in units of stellar radii, R_*)
- P, planetary orbital period
- ρ, the stellar density
- a, the semi-major axis in units of R_*
- i, the planetary orbital inclination
- e, orbital eccentricity
- ω, argument of periastron
- P_{rot}, the rotation period of the star
- T_{pole}, the stellar temperature at its pole
- λ, the sky-projected spin orbit angle (the sky-projected angle between the planetary orbital plane and the stellar equatorial plane)
- i^*, stellar inclination, defined as the angle between the observer's line of sight and the stellar rotation axis. This is related to the stellar obliquity ϕ, specified in Ahlers et al. (2020), by $i^* = 90° - \phi$. We note this is not the same $\Delta\phi$ that we use to describe the thermal phase curve model.
- β, the gravity-darkening coefficient (defines how strong the temperature gradient

is), defined in von Zeipel (1924).

- u_1 and u_2, the quadratic limb-darkening coefficients, which we reparametrise as q_1 and q_2 (Kipping, 2013)
- t_0, the time of mid-transit
- f_0, transit scaling factor (scales the out-of-transit baseline)
- $filter$, the telescope's bandpass transmission efficiency
- stellar spectrum

We fixed $T_{\rm pole} = 10170\,\mathrm{K}$, $e = 0$ and $\omega = 90°$. We also fixed $R_* = 2.379\,R_\odot$ (see Section 2.2.4). For CHEOPS and TESS we use a PHOENIX model stellar spectrum (Husser et al., 2013), and for *Spitzer* we use a blackbody spectrum.

Due to the large degeneracy between the limb darkening and gravity darkening parameters, we had to use previous studies to inform our priors, instead of just letting them all float freely - something we tested and found no clear unique solution. Therefore we used results from previous doppler tomography studies (Gaudi et al., 2017, Borsa et al., 2019) to inform priors on b, λ and $v \sin i^*$ (where v is the rotational velocity of the star), and theoretical limb-darkening tables in Claret & Bloemen (2011), Claret (2017; 2021) to inform priors on q_1 and q_2. We also used Claret (2016) to inform priors on β. See Table 2.3 and 2.4 for the priors used for all the gravity-darkened model parameters.

Using the information obtained from the transit fit we can calculate the true 3D spin-orbit angle (Ψ), given by the equation:

$$\cos\Psi = \sin i^* \cos i + \cos i^* \sin i \cos\lambda. \tag{2.1}$$

Gravity-darkened transits have also been analysed in other CHEOPS work (see, e.g.: Lendl et al., 2020, Hooton et al., 2022, Deline et al., 2022).

2.3.1.2 Thermal phase curve model

To model the shape of the thermal phase curve we use `kelp` (Morris et al., 2022), a Python package that models the surface temperature of the planet as a 2D thermal map constructed by modified spherical harmonics (parabolic cylinder functions) (Heng & Workman, 2014), given by equation (1) of Morris et al. (2022):

$$T(\theta,\phi) = \bar{T}\left(1 + \sum_{m,\ell}^{\ell_{\rm max}} h_{m\ell}(\theta,\phi)\right), \tag{2.2}$$

where θ and ϕ are latitude and longitude. $\bar{T}$ is a background temperature upon which 2D perturbations exist and are quantified by the "alphabet" or basis functions $h_{m\ell}$ as defined by equation (258) of Heng & Workman (2014). These functions are also dependent on the dimensionless parameters α and $\omega_{\rm drag}$. The dimensionless fluid number α is constructed from the Rossby, Reynolds and Prandtl numbers; it quantifies the competition between stellar heating (forcing) and sources of friction (drag). The normalised drag frequency $\omega_{\rm drag}$ quantifies the strength of friction. In practice, we find that it is sufficient to truncate the series in the preceding equation at $l_{\rm max} = 1$ (Morris et al., 2022). The entire temperature map may be shifted back and forth in longitude by $\Delta\phi$, which effectively fits for the hotspot offset if $\omega_{\rm drag} \gtrsim 3$ (Morris et al., 2022). Full details of the theoretical formalism may be found in Section 2 of Morris et al. (2022), which we will not repeat here.

Overall, our thermal phase curve model is parametrised by the following variables:

- $\Delta\phi$, hotspot offset
- α, dimensionless fluid number
- $\omega_{\rm drag}$, dimensionless drag frequency
- $C_{m\ell}$, the power of individual harmonic modes
- $\ell_{\rm max}$, describes the highest spherical harmonic mode in the model
- planetary parameters including a, R_p, $T_{\rm pole}$
- telescope bandpass transmission efficiency
- $\bar{T}$, scaling term of the mean temperature field

`kelp` integrates over the passband-weighted thermal map visible at a specific time in its orbit and converts the map into a flux measurement using the following equation from Cowan & Agol (2011), which can be compared to the observed phase curve:

$$\frac{F_p}{F_\star} = \frac{1}{\pi I_\star}\left(\frac{R_p}{R_\star}\right)^2 \int_0^{\pi} \int_{-\xi-\pi/2}^{-\xi+\pi/2} I_p(\theta,\phi)\cos(\phi+\xi)\sin^2(\theta)\, d\phi\, d\theta, \tag{2.3}$$

where I, the intensity, is defined by

$$I = \int \lambda \mathcal{F}_\lambda \mathcal{B}_\lambda(T(\theta,\phi))d\lambda, \tag{2.4}$$

where $\mathcal{F}_\lambda$ is the instrument-specific filter response function and $\mathcal{B}_\lambda(T(\theta,\phi))$ is the Planck function of each temperature element $T(\theta,\phi)$.

The initialisation of this model at every time-step required is a bottleneck in the joint MCMC fit for the phase curves. To increase the speed we evaluated the model at 200 orbital phases, spaced equally between -π and π. We then linearly interpolated the model flux values back to the original time resolution. We investigated the effect of increasing the number of samples on the fitted parameters and found that the median parameter values converged to a constant value at around 150, and so we choose 200 samples to increase the speed of the code whilst not decreasing the accuracy of the phase curve fit.

In the joint fit, we followed Morris et al. (2022) and set $\alpha = 0.6$, $\omega_{drag} = 4.5$ and $\ell_{max} = 1$, since latitudinal variations in temperature and flux are not constrained by thermal phase curves and it was shown in that study that it is sufficient to describe the temperature map only with the first mode. We also set all $C_{m\ell} = 0$ apart from C_{11} which is a free parameter. See Table 2.3 for the priors of the phase curve model.

2.3.1.3 Secondary eclipse model

The `batman` package models the flux decrement as the planet is occulted by the star (Kreidberg, 2015). We multiply this normalised model (where the planetary flux is null during the eclipse) by the thermal phase curve model to produce the full phase curve model.

2.3.1.4 Stellar pulsation model

After examining the residuals of an initial CHEOPS phase curve fit, without any stellar pulsation model, it was clear that there was a periodic signal present in the phase curves at a period of around 7.5 hours (see Figure 2.1). This signal was identical to the one observed in Wong et al. (2020b) and Mansfield et al. (2020) and has been attributed to stellar pulsations. In Wyttenbach et al. (2020), they analysed these pulsations and concluded that they are compatible with p-mode oscillations present in a δ Scuti-type star.

To correct for this signal we used a Gaussian process with a simple harmonic oscillator (SHO) kernel implemented by `celerite2` (Foreman-Mackey et al., 2017, Foreman-Mackey, 2018). We fixed the amplitude (100 ppm) and the damping timescale, τ, to 2x the gaussian process period (GP period), which is a fitted parameter. This damping timescale provides coherence of pulsations over several cycles while allowing for evolution of the pulsation signal on longer timescales. Because of this we calculate the Q value of this

SHO kernel to be 6.

We found evidence of the same stellar pulsations in the TESS phase curves as well. Although the PDCSAP flux light curves have already been corrected for long-term trends, there were still significant trends present in the KELT-9 light curve which we believe to be of instrument systematic origin. Therefore we implemented the same kernel described above for these TESS phase curves, along with an additional Matérn 3/2 kernel with an amplitude of 200ppm and a timescale of 12 days to remove the long-term trends in this data.

The pulsations are also detectable in the *Spitzer* data, albeit at less than 10% of the total amplitude of the phase curve (a lower percentage than in the other two bandpasses). After further analysis showed modelling the pulsations within this dataset had a non-trivial impact on the phase curve parameters, we extended the GP to also include the *Spitzer* phase curve. The amplitude of the pulsations in the *Spitzer* data was also around 100ppm so this hyperparameter could remain the constant. We decided to use the same kernels in both CHEOPS, TESS, and *Spitzer* to jointly infer the free kernel hyperparameters.

2.3.1.5 CHEOPS

The composite transit, eclipse and thermal phase curve model we use to fit the CHEOPS observations is composed of

- gravity-darkened transit model
- planet thermal phase curve model
- eclipse model
- stellar pulsation model
- systematics model

Data clipping and systematics model: For each phase curve, before stitching them together with the other datasets, we sigma-clipped outliers of the centroid position of the target star at 4.5σ and masked out individual points with anomalously high levels of background or low temperature readings. As discussed in Section 2.2.1, these telescope assembly temperatures have been shown to coincide with a systematic "ramp" feature in the CHEOPS light curves, most likely caused by the change in temperature of the telescope as it adjusts to a new pointing position (Morris et al., 2022). We also masked

out the first few hours of data in the second, third and fourth phase curve, as they coincided with a strong, non-linear increase in the telescope temperature. We mask on average 16% of datapoints from each phase curve.

We used a linear detrending model including vectors proportional to the temperature, temperature^2 and roll angle in our fit to detrend against the correlated noise sources. We chose these basis vectors based on the analysis performed in Morris et al. (2022) which used the BIC minimisation to find the parameters that contributed the most to the model without overfitting.

2.3.1.6 TESS

The TESS phase curves model is a linear combination of:

- gravity-darkened transit model
- planet thermal phase curve model
- eclipse model
- stellar pulsation model

Data clipping: As described in Section 2.2.2, we use the TESS PDCSAP light curves from the SPOC pipeline. Before the fit we also masked out sections of the phase curves that clearly had strong systematics and that were also removed in the analysis performed in Wong et al. (2020b). These usually affected the data points shortly before or after a gap in the TESS observations. In total we mask out 5% of the datapoints.

2.3.1.7 *Spitzer*

The *Spitzer* phase curve model is a linear combination of:

- gravity-darkened transit model
- planet thermal phase curve model
- eclipse model
- stellar pulsation model

Pre-fit conditioning and systematics model: See Section 2.2.3 for a description of the detrending applied to the *Spitzer* dataset. From the BLISS mapping detrending rou-

tine, we obtain a detrended lightcurve, which we use for our joint phase curve fit. Observations are also available at 3.6 μm, which will be the subject of a forthcoming paper by Beatty et al. (in prep.).

2.3.1.8 On ellipsoidal variations

To include an ellipsoidal variation model (see, e.g.: Welsh et al., 2010, Gai & Knuth, 2018), we initially fit the first two CHEOPS phase curves separately using the Wong et al. (2020b) sinusoidal model for the stellar pulsations and ellipsoidal variations, leaving the phase and amplitude of both sinusoids as free parameters. The resulting ellipsoidal phase and amplitude were not consistent between each phase curve. We then fit the combined set of CHEOPS phase curves and the chains converged on solutions with ellipsoidal variation amplitudes of <10 ppm. The theoretical expectation is reported as 44 ± 6 ppm in Wong et al. (2020b), therefore this fitted amplitude is over 5σ lower than the theoretical value. We suggest that the variability on the $P/2$ timescale may not be ellipsoidal because it has an unexpected and evolving phase and appears incoherent over 4 orbital timescales (from the first to second phase curve observations).

Carrying out the same test with only the GP stellar pulsation model instead of the pure sinusoids, we found that both models agreed on the amplitude of the stellar pulsations as well as other planetary parameters. As a result of this analysis, we conclude that the GP stellar pulsation model is flexible enough to capture the stellar signals without absorbing the planetary ones.

2.3.2 CHEOPS occultations

As well as the 9 occultation-only CHEOPS observations, 5 eclipses were observed within the 4 CHEOPS phase curves (2 of the 5 eclipses were observed within the same phase curve). To increase our occultation sample size, we added these to the set of occultations, clipping them so that they each had a similar number of CHEOPS orbits to the rest of the occultations. Therefore, there are thirteen occultations in total.

Each occultation was then fitted independently with a model containing a linear combination of:

- eclipse model

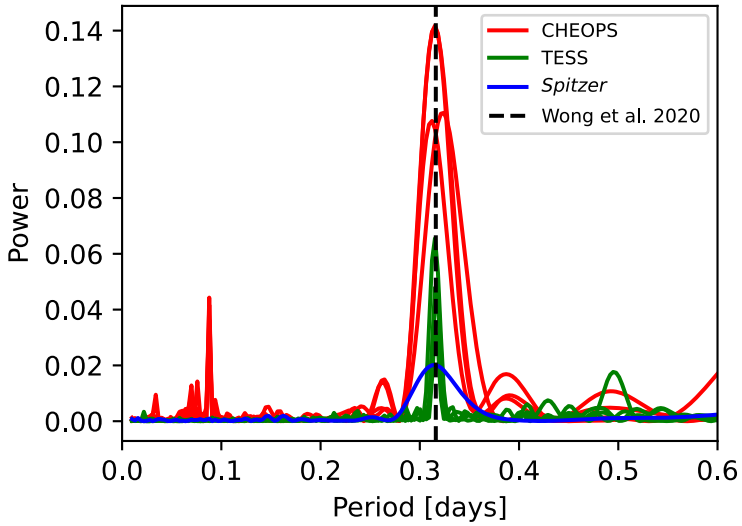

Figure 2.1 | Periodograms reveal the presence of stellar pulsations in the residuals of the phase curve fitting. In red are the four CHEOPS phase curves, in green are the TESS phase curves and in blue is the *Spitzer* phase curve. It is clear the stellar pulsation period (near 0.3 days) is present in all phase curves and matches that signal seen also in Wong et al. (2020b) and Mansfield et al. (2020) (dashed black line). The short period peaks are only present in CHEOPS but not TESS or *Spitzer* so we assume they are CHEOPS systematics and disregard the signal.

- stellar pulsation model
- systematics model

We carried out the fit of the occultations with `PyMC3` (Salvatier et al., 2016), which uses a gradient-based Hamiltonian Monte Carlo (HMC) method to integrate for parameter posteriors.

Data clipping and systematics model: Similarly to the phase curves, the occultations were sigma-clipped to remove outliers in the target centroid-space and flux values (both by 3σ), and points with anomalously large background or temperature readings were masked out. The data points were also flux sigma-clipped. After clipping, 4-14% of points were removed from each observation.

Since the observation duration for each occultation is short (4-5 CHEOPS orbits), we risk fitting a model that is too complex. To investigate the minimum complexity model needed to reproduce the light curve without over-fitting, we used Leave-One-Out cross-validation (Vehtari et al., 2015) to compare the predictive power for each model containing different basis vectors in the systematics model. The basis vectors we tested included a flux constant, sin (roll angle), cos (roll angle), time, time^2, temperature (from the *thermFront2* sensor) and background. These have been shown in a previous study (Morris et al., 2022) to be the most influential basis vectors on the light curves.

Overall, the preferred systematic model included every basis vector except the background, however other combinations were preferred by nine of the other occulations. After fitting, we investigated whether there was a trend between the fitted eclipse depth and the number of basis vectors chosen for each occultation. We found no correlation.

2.3.2.1 Stellar pulsation model

As detailed in Section 2.3.1.5, We observed a stellar pulsation signal in the phase curves with an amplitude of around 100 ppm and a timescale of 7.5 hours. Assuming it is continuous and also present in the occultation observations, the occultations are taken over a long enough timescale that this signal would vary significantly within a single visit. However as the baseline of the occultations is so short, it is impossible to uniquely infer the phase and amplitude of the pulsations in each observation. Therefore we included a sinusoid in the occultation models with a period fixed at 7.5 hours, with the phase of

this signal free to vary independently between each occultation. In order to avoid biasing the prior, we implemented a hierarchical Bayesian technique where the prior of the amplitude was set to $\mathcal{N}(100, \sigma)$ ppm, and truncated at zero so that the amplitude is always positive, and the standard deviation σ became a fitted parameter and was allowed to vary as $\mathcal{U}(10, 1000)$ ppm.

2.3.2.2 Eclipse model

We used the `batman` package to create a basic secondary eclipse model for the occultations. The out-of-eclipse observations contain a hint of the shape of the phase curve of KELT-9, which peaks near secondary eclipse. We used the best-fit posteriors from the full phase curve fit to produce a phase curve model from `kelp`. This model is used to scale the out-of-eclipse sections of the basic `batman` model. This model was characterised by the following parameters:

- t_0, the time of transit centre*
- R_p, the planetary radius (in units of stellar radii, R_*)
- b, the impact parameter
- P, the planetary orbital period*
- ρ, the stellar density

where we fixed starred (*) values and and fit for unstarred ones.

2.4 Results

Figure 2.2 shows the phase folded CHEOPS, TESS, and *Spitzer* phase curves respectively, with the stellar pulsations and other systematic trends removed, and overplotted with the best-fit phase curve, transit and eclipse model. The fitted parameter posteriors are detailed in Table 2.3 for global variables and Table 2.4 for bandpass-dependent variables. A clearer view of the transit fits can be seen in Appendix 2.A. The results of the occultation depth analysis are shown in Figure 2.8.

In the phase curve analysis we included both year 1 and year 2 CHEOPS phase curves. We analysed these years of phase curves separately and we saw no evidence of variability from one CHEOPS year to the next. The change in parameter values from using only year

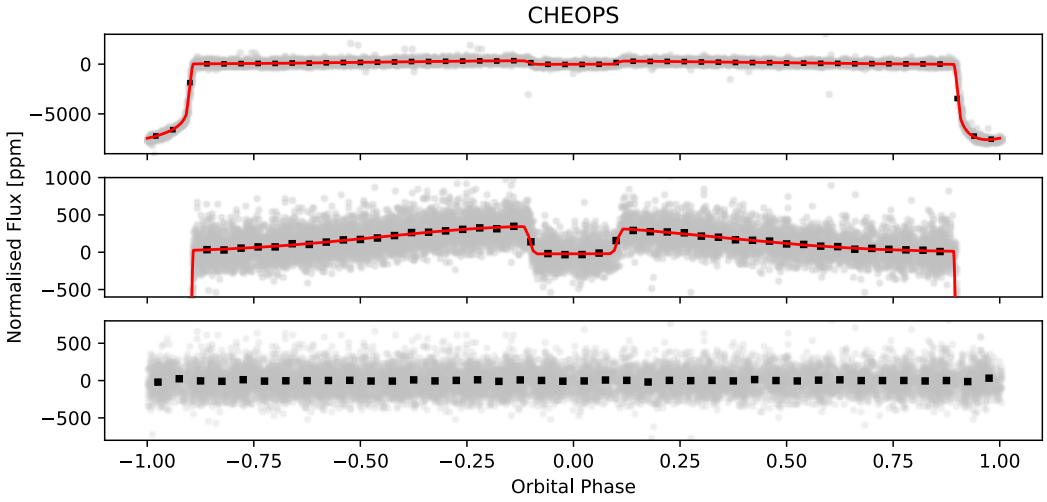

(a) CHEOPS phase-folded and detrended phase curves (first 2 panels, 2nd panel is a zoomed-in view of the 1st). 3rd panel shows residuals of the fit.

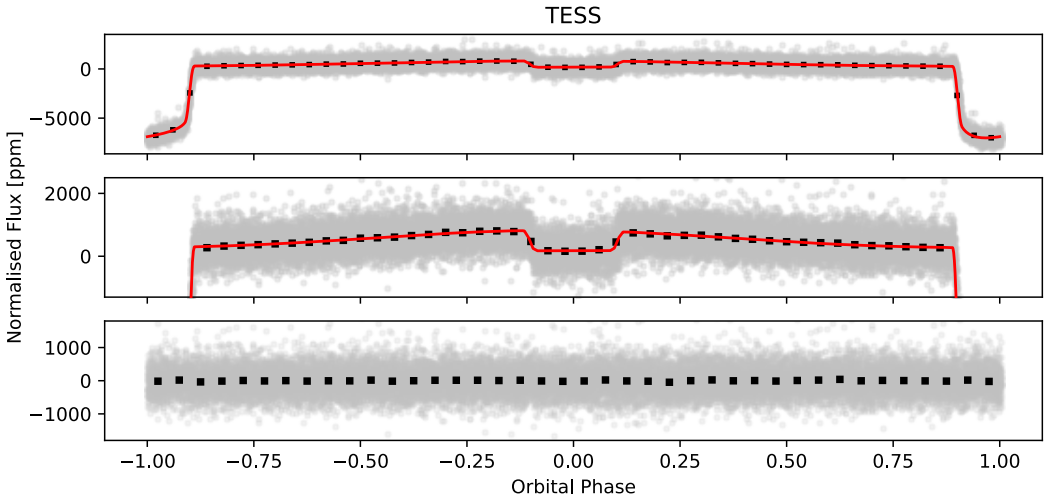

(b) TESS phase-folded and detrended phase curves (first 2 panels, 2nd panel is a zoomed-in view of the 1st). 3rd panel shows residuals of the fit.

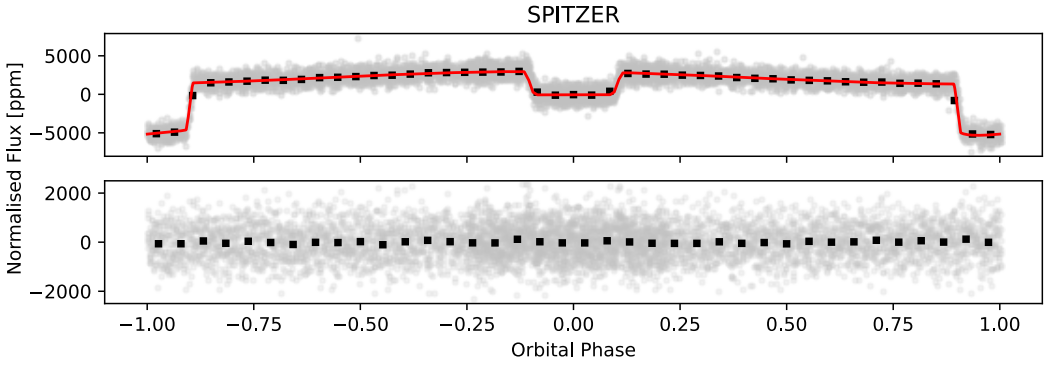

(c) *Spitzer* phase-folded and detrended phase curve (first panel). 2nd panel shows residuals of the fit.

Figure 2.2 | CHEOPS, TESS, and *Spitzer* phase-folded and detrended (stellar pulsations and other systematic trends removed) phase curves, overplotted with the best-fit phase curve model, transit model and eclipse model (in red). In black are the binned grey datapoints, with error bars that are smaller than the point size in all panels so they are not visible.

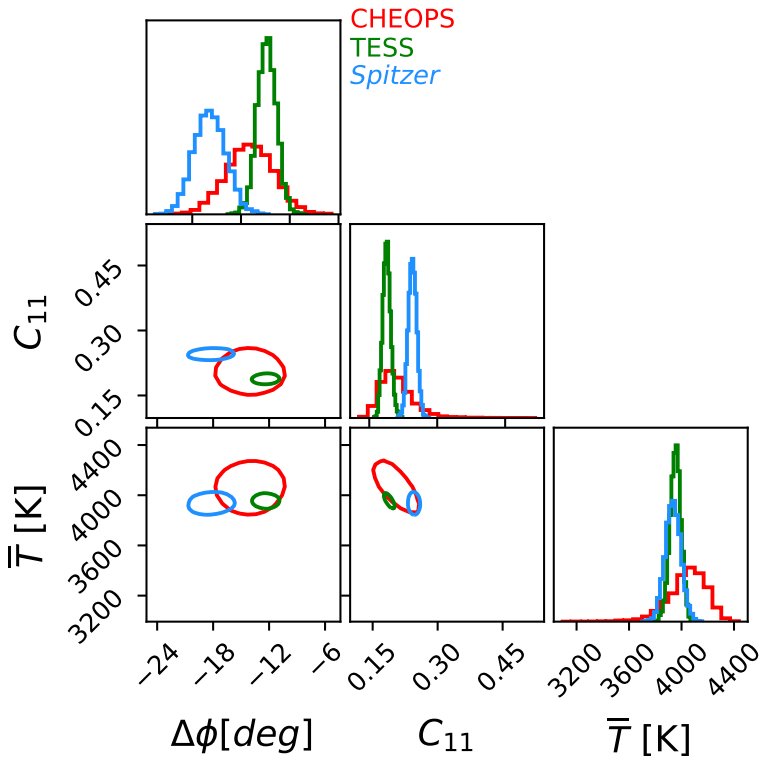

Figure 2.3 | Posteriors of the phase curve parameters across the three bandpasses showing 1σ-confidence contours. Red is CHEOPS, green is TESS and blue is *Spitzer*.

1 to including both year 1 and 2 was, for the majority of parameters, within 1σ and the rest was within 2σ. This justified our decision to use the same parameters in the fitting procedure for all CHEOPS phase curves.

2.4.1 Thermal map of KELT-9b

As described in Section 2.3.1.2, we use a generalised spherical harmonic temperature map to fit the thermal phase curve variation in the light curves. To a good first-approximation, there are only three free variables that can describe most hot-Jupiter phase curves: $\Delta\phi$ (hotspot offset), $C_{1,1}$ ($C_{m\ell}$ power coefficient) and $\bar{T}$ (mean background temperature). As each instrument observes in a different bandpass, they are probing different atmospheric depths of KELT-9b and so we used an independent phase curve model for each bandpass. Although Hooton et al. (2022) used spherical harmonic temperature maps in a similar way to fit the phase variations in CHEOPS and *Spitzer* light curves for MASCARA-1b, they used a single set of the same three parameters for bandpasses due to the limited phase coverage of the CHEOPS observations. Figure 2.4 shows the temperature maps derived

Table 2.3 | Global priors and best-fit values for the model and detrending parameters as described in Section 2.3, along with the derived parameters. The reported errors are the 16$^{\text{th}}$ and 84$^{\text{th}}$ percentile interval for every parameter. * is for parameters that are only shared between CHEOPS and TESS. When priors are based on previous results, the citation is included.

Parameter		Unit	Prior	Best-fit value
Global				
Fitted parameters				
Period	P	days	$\mathcal{N}(1.4811235, 0.0000011)$[a]	$1.48111949 \pm 0.00000034$
Transit duration	T_{14}	days	$\mathcal{U}(0.13, 0.2)$[a]	$0.16552^{+0.00016}_{-0.00015}$
Impact parameter	b		$\mathcal{N}(0.168, 0.017)$[b]	$0.195^{+0.016}_{-0.015}$
Sky-projected spin orbit angle	λ	deg	$\mathcal{N}(-85.78, 0.46)$[b]	$-85.67^{+0.46}_{-0.45}$
Gravity-darkening coefficient	β		$\mathcal{U}(0.01, \infty)$, $\mathcal{N}(0.237, 0.01)$[e]	$0.2270^{+0.0077}_{-0.0080}$
GP periodic timescale* (SHO)	ρ_{SHO}	days	$\mathcal{U}(0.2, 0.4)$	$0.3386^{+0.0037}_{-0.0036}$
Stellar inclination	i^*	deg	$\mathcal{U}(0, 180)$	47.1 ± 1.1
Derived parameters				
Semi major axis	a	$R_\star$		$3.0914^{+0.0090}_{-0.0100}$
Orbital inclination	i	deg		$86.38^{0.29}_{0.30}$
Stellar density	ρ	g cm^{-3}	$\mathcal{N}(0.256, 0.33)$[d]	$0.2548^{+0.0022}_{-0.0025}$
GP damping timescale* (SHO)	τ_{SHO}	days		$0.6772^{+0.0074}_{0.0072}$
Stellar rotational period	P_{rot}	hrs	$\mathcal{U}(4.61, \infty)$[f]	18.96 ± 0.34
True spin orbit angle	Ψ	deg		$84.36^{+0.37}_{-0.38}$
Fixed parameters			Source	Value
Stellar radius	$R_\star$	$R_\odot$	This work (Section 2.2.4)	2.379
Effective/polar stellar temperature	T_{eff}	K	Gaudi et al. (2017)	10170
Projected rotational velocity	$v \sin i^*$	km s^{-1}	Borsa et al. (2019)	111.8
Eccentricity	e		assumed	0
Argument of periastron	ω	deg	assumed	90
Fluid number	α		Morris et al. (2022)	0.6
Drag frequency	ω_{drag}		Morris et al. (2022)	4.5
Highest present spherical mode	l_{max}		Morris et al. (2022)	1
GP Amplitude* (SHO)	σ_{SHO}	ppm		100
GP Amplitude* (Matérn)	σ_{Matern}	ppm		200
GP timescale* (Matérn)	ρ_{Matern}	days		12

[a] Wong et al. (2020b)
[b] Borsa et al. (2019)
[c] Ahlers et al. (2020)
[d] This work (See Section 2.2.4)
[e] Claret (2016)
[f] Restricted by break-up velocity

Table 2.4 | Bandpass-specific priors and best-fit values for the model and detrending parameters as described in Section 2.3, along with the derived parameters. The reported errors are the 16$^{\text{th}}$ and 84$^{\text{th}}$ percentile interval for every parameter.

Parameter		Unit	Prior	Best-fit value
CHEOPS				
Fitted parameters				
Zero transit epoch	t_0	BJD time - 2459095.2	$\mathcal{U}$(-0.01, 0.01)	$-0.003751^{+0.000060}_{-0.000059}$
Transit depth	*depth*		$\mathcal{U}$(0.0049, 1)	$0.006212^{+0.000019}_{-0.000020}$
Transit scaling factor	f_0		$\mathcal{U}$(0.9, 1.1)	$0.99998^{+0.00012}_{-0.00011}$
1st quadratic limb darkening component	q_1		$\mathcal{N}$(0.34052, 0.01)[a]	$0.3299^{+0.0078}_{-0.0074}$
2nd quadratic limb darkening component	q_2		$\mathcal{N}$(0.22030, 0.01)[a]	$0.2210^{+0.0086}_{-0.0087}$
Hotspot offset	$\Delta\phi$	deg	$\mathcal{U}$(-180, 29)	-14.1 ± 2.4
$C_{m\ell}$ power coefficient	$C_{1,1}$		$\mathcal{U}$(0, 1)	$0.205^{+0.039}_{-0.028}$
Mean background temperature	$\bar{T}$	K	$\mathcal{U}$(2890, 5780)[d]	4060^{+120}_{-150}
Derived parameters				
Planetary radius	R_p	$R_\star$		$0.07882^{+0.00012}_{-0.00013}$
1st quadratic limb darkening component	u_1			$0.2541^{+0.0094}_{-0.0097}$
2nd quadratic limb darkening component	u_2			0.320 ± 0.012
TESS				
Fitted parameters				
Zero transit epoch	t_0	BJD time - 2458693.8	$\mathcal{U}$(-0.01, 0.01)	$0.013185^{+0.000044}_{-0.000045}$
Transit depth	*depth*		$\mathcal{U}$(0.0049, 1)	0.006263 ± 0.000016
Transit scaling factor	f_0		$\mathcal{U}$(0.9, 1.1)	1.00017 ± 0.00012
1st quadratic limb darkening component	q_1		$\mathcal{N}$(0.1690, 0.01)[b]	$0.1541^{+0.0062}_{-0.0064}$
2nd quadratic limb darkening component	q_2		$\mathcal{N}$(0.2082, 0.01)[b]	$0.2175^{+0.0094}_{-0.0097}$
Hotspot offset	$\Delta\phi$	deg	$\mathcal{U}$(-180, 29)	-12.32 ± 0.97
$C_{m\ell}$ power coefficient	$C_{1,1}$		$\mathcal{U}$(0, 1)	$0.1884^{+0.0088}_{-0.0083}$
Mean background temperature	$\bar{T}$	K	$\mathcal{U}$(2890, 5780)[d]	3955^{+40}_{-42}
Derived parameters				
Planetary radius	R_p	$R_\star$		0.079142 ± 0.000099
1st quadratic limb darkening component	u_1			$0.1705^{+0.0076}_{-0.0075}$
2nd quadratic limb darkening component	u_2			0.2216 ± 0.0096
Spitzer				
Fitted parameters				
Zero transit epoch	t_0	BJD time - 2458415.36	$\mathcal{U}$(-0.01, 0.01)	0.00206 ± 0.00015
Transit depth	*depth*		$\mathcal{U}$(0.0049, 1)	0.006152 ± 0.000068
Transit scaling factor	f_0		$\mathcal{U}$(0.9, 1.1)	0.99993 ± 0.00020
1st quadratic limb darkening component	q_1		$\mathcal{N}$(0.0097, 0.01)[c]	$0.0118^{+0.0065}_{-0.0054}$
2nd quadratic limb darkening component	q_2		$\mathcal{N}$(0.1463, 0.01)[c]	$0.1464^{+0.0099}_{-0.0101}$
Hotspot offset	$\Delta\phi$	deg	$\mathcal{U}$(-180, 29)	$-18.2^{+1.7}_{-1.6}$
$C_{m\ell}$ power coefficient	$C_{1,1}$		$\mathcal{U}$(0, 1)	0.2453 ± 0.0092
Mean background temperature	$\bar{T}$	K	$\mathcal{U}$(2890, 5780)[d]	3934^{+54}_{-58}
Derived parameters				
Planetary radius	R_p	$R_\star$		0.07843 ± 0.00043
1st quadratic limb darkening component	u_1			$0.0318^{+0.0082}_{-0.0084}$
2nd quadratic limb darkening component	u_2			$0.077^{+0.019}_{-0.020}$

[a] Claret (2021)
[b] Claret (2017)
[c] Claret & Bloemen (2011)
[d] Morris et al. (2022)

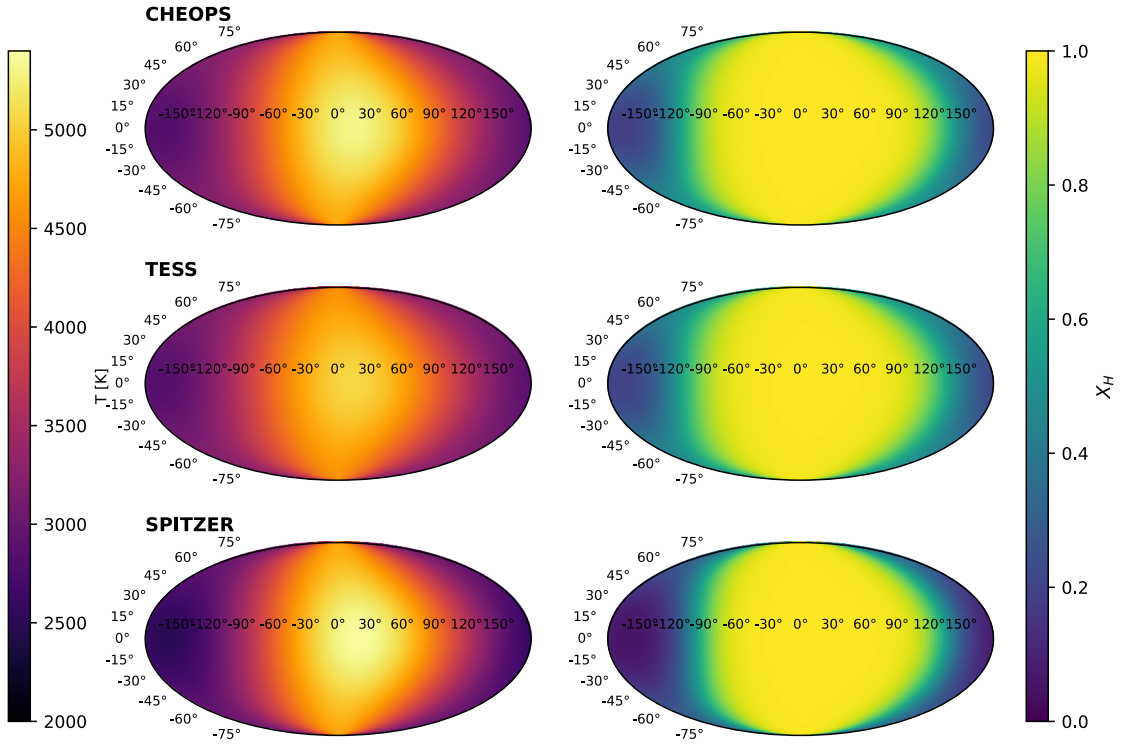

Figure 2.4 | 2D thermal temperature maps (left column and colour bar) and maps showing ratio of atomic to molecular hydrogen, assuming chemical equilibrium, that would be present given the temperature maps (right column and colour bar) of KELT-9b in each bandpass. The hottest temperature is reached near the substellar point and is just over 5000 K whereas the lowest temperature is reached in the *Spitzer* bandpass at just under 2500 K. On all three maps, the dayside is mostly atomic hydrogen-saturated while across the terminator and over to the nightside, the ratio falls to near zero at the antistellar point.

from the best-fit phase curve models for each instrument. Similar to other hot Jupiters, the result in all three bandpasses is a hotspot slightly offset to the east. Furthermore, the minimum nightside temperature remains above 2000 K in all bandpasses, further evidence for significant heat-redistribution in the atmosphere. It is also apparent that in the TESS data, there is a smaller temperature contrast between the maximum and minimum temperature than the other datasets.

In Figure 2.3 we illustrate the fitted posteriors of the three free variables in these phase curve models. Table 2.4 details the best-fit values of these parameters along with the other bandpass-dependent parameters. It is clear that these parameters change significantly as we probe different depths of KELT-9b's atmosphere.

The CHEOPS nightside posteriors are considerably broader than those of TESS and *Spitzer*. The TESS data has around 50 days of photometry compared to the ~10 days of CHEOPS, which contributes to narrower TESS posteriors. The CHEOPS nightside flux (in ppm) is also lower in the CHEOPS observations and so is detected at at lower significance than the other instruments. Furthermore, *Spitzer* observes a larger planet-to-star contrast than the other two instruments and also other factors such as a larger collecting area and the longer observing durations all contribute to the narrower posteriors. This may also be related to the fact that we detrend the CHEOPS data simultaneously in the fitting procedure but not the TESS and Spitzer data. However, we try to account for this by fitting for an additional white noise term to each individual data set, modifying the uncertainties based on the standard deviation of the flux values.

In the second column of Figure 2.4 we show the ratio of atomic hydrogen to molecular hydrogen in the atmosphere of KELT-9b, assuming equilibrium chemistry and using the method and equations described in Heng et al. (2016). This supports the theory that the dissociation from atomic to molecular hydrogen occurs near the day-night terminator for the wavelengths observed.

2.4.2 Dayside and nightside brightness temperatures

Although our work reveals 2D information regarding the planet's temperature profile, we believe it is useful to still report the dayside and nightside brightness temperatures that we infer directly from two single ('1D') measurements: the eclipse depth and the flux at half an orbital period away from the centre of the eclipse. Assuming a model spectrum

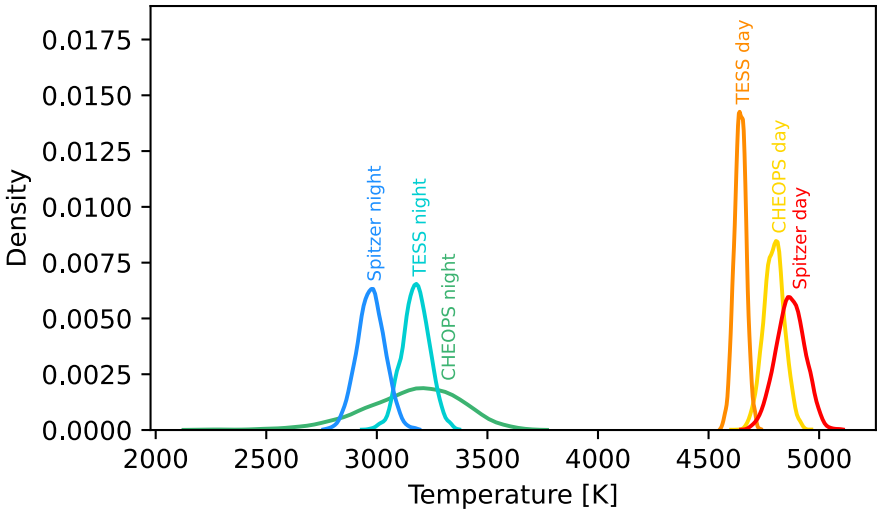

Figure 2.5 | Posteriors of the brightness day and nightside temperatures from the different bandpasses.

Table 2.5 | Fitted eclipse depths and night fluxes derived directly from the phase curve fitting procedure for each of the three different bandpasses. The last two columns show the corresponding dayside and nightside brightness temperatures, derived using a PHOENIX model for KELT-9 and the respective bandpass filter functions.

	Eclipse Depth [ppm]	Night Flux [ppm]	Dayside Temp [K]	Nightside Temp [K]
CHEOPS	367 ± 17	37^{+16}_{-14}	4796 ± 46	3180^{+190}_{-230}
TESS	645 ± 15	105^{+11}_{-11}	4643 ± 26	3177^{+60}_{-61}
Spitzer	3007^{+57}_{-55}	1440^{+53}_{-49}	4870^{+67}_{-65}	2973^{+66}_{-62}

for the star, a black body for the planet and by using each instrument's filter function, these brightness temperatures can be calculated. Although this is not the main focus of this paper, it is useful to report these temperatures due to the wide understanding of this temperature statistic in the community, along with the opportunity for direct comparison to previous work.

We obtain a dayside brightness temperature of CHEOPS, TESS, and *Spitzer* of 4796 ± 46 K, 4643 ± 26 K and 4870^{+67}_{-65} K respectively. We found the nightside brightness temperatures of the three bandpasses (in the same order) to be 3180^{+190}_{-230} K, 3177^{+60}_{-61} K and 2973^{+66}_{-62} K. Figure 2.5 shows the posteriors of these wavelength-dependent temperatures (derived from the posteriors of the thermal phase curve parameters). It is clear that the highest average dayside temperature is observed in the *Spitzer* bandpass, followed by CHEOPS and then TESS. Generally, the nightside temperatures also have wider posteriors as the lower nightside flux is detected at a lower significance.

Our TESS dayside brightness temperature is consistent with the Wong et al. (2020b) value of 4600 ± 100 K and our TESS nightside temperature is also consistent with their nightside temperature of 3040 ± 100 K. This is an encouraging test of our full phase curve model as both of these studies used the same TESS data. For our *Spitzer* dayside temperature, our results are consistent within 2σ to the dayside brightness temperature reported in Mansfield et al. (2020), 4566^{+140}_{-136} K. However our nightside temperature is not consistent with their nightside brightness temperature of 2556^{+101}_{-97} K (difference of over 3σ). This could in part be due to the different detrending method applied to *Spitzer* data in this study compared to the Mansfield et al. (2020) study.

Figure 2.6 shows the nightside temperatures of the most extreme hot Jupiters plotted against their equilibrium temperatures and Figure 2.7 shows the dayside temperature of these planets against equilibrium temperature. We define the equilibrium temperature as $T_{eq} = T_* \sqrt{R_*/2a}$. It has been reported in Keating et al. (2019) that due to the presence of clouds the nightside temperature of most hot Jupiters is around 1100 K, with the caveat that clouds would disperse for hotter planets, and therefore the nightside temperature may increase again proportionally to the amount of stellar irradiation. KELT-9b supports this caveat as it is clearly an exception to the pattern of constant nightside temperature, having a nightside temperature exceeding 2900 K.

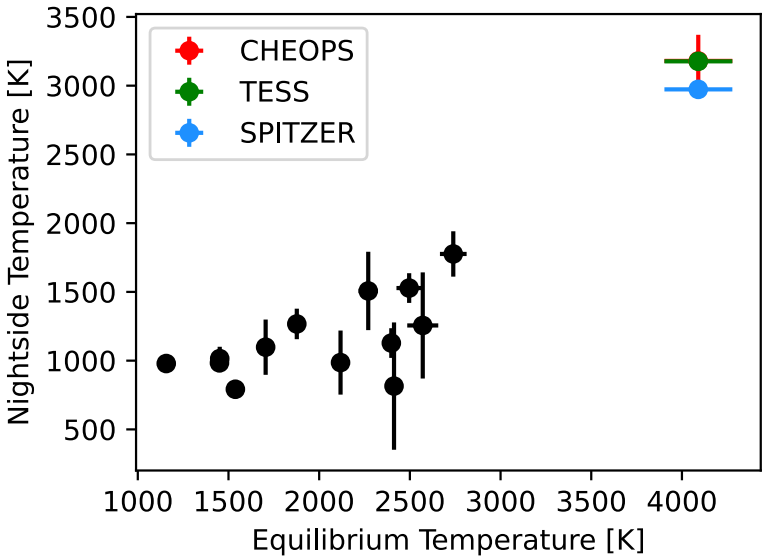

Figure 2.6 | Nightside integrated temperatures of hot Jupiters plotted against their equilibrium temperatures (Keating et al., 2019). The coloured points show the KELT-9b temperatures derived in this study.

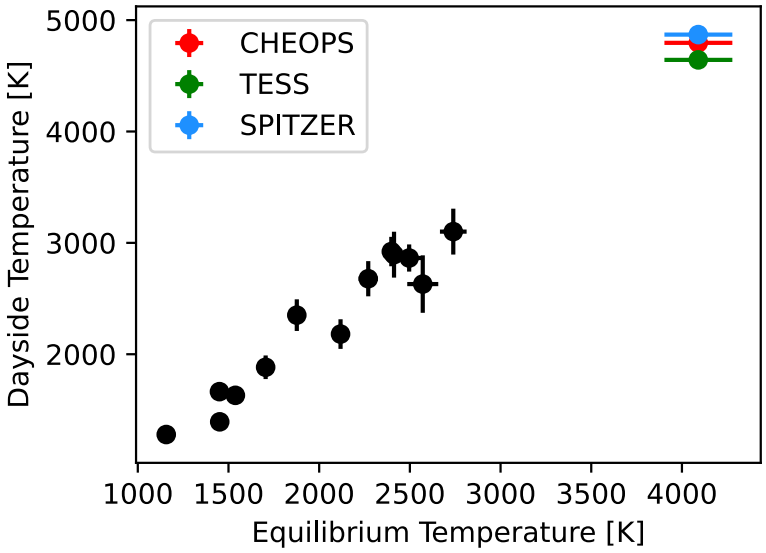

Figure 2.7 | Dayside integrated temperatures of hot Jupiters plotted against their equilibrium temperatures (Keating et al., 2019). The coloured points show the KELT-9b temperatures derived in this study.

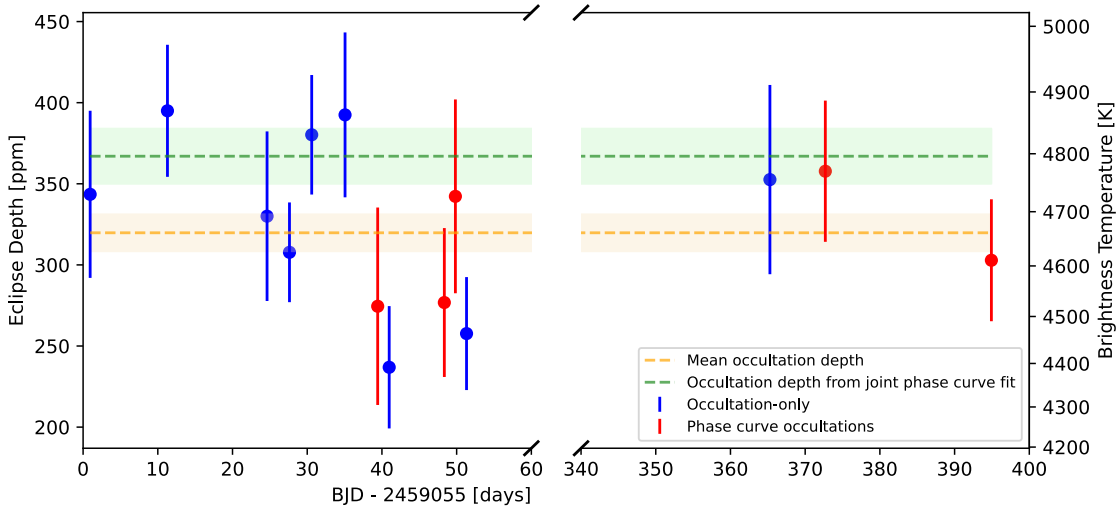

Figure 2.8 | Fitted eclipse depths from the 9 CHEOPS occultation observations (in blue) and 5 CHEOPS occultations extracted from the phase curves (in red). The eclipse depth derived from the joint CHEOPS phase curve fit is shown in green (367 ± 17 ppm, with 1σ shaded) and the mean value of these 14 occultations (320 ± 11 ppm) is shown in orange (with 1σ shaded). These two mean eclipse depths are consistent with each other by just over 2σ. The right-hand y-axis shows how the eclipse depths convert to dayside brightness temperatures, assuming the dayside hemisphere is a blackbody and radiates at a uniform temperature.

2.4.3 Eclipse depths

Figure 2.8 shows the eclipse depths fitted from the CHEOPS occultation observations. As explained in Section 2.3.2, this dataset includes 9 occultation-only observations and four occultations cut-out from the four CHEOPS phase curves. Together they have a mean eclipse depth of 320 ± 11 ppm. This is consistent within 2.3σ of the eclipse depth found from the full phase curve fit of the four CHEOPS phase curves which was 367 ± 17 ppm. The mean eclipse depth variation (from the occultations) corresponds to a brightness temperature change of around ±33 K.

To validate our eclipse model uncertainties, we fit the same size error bar to each eclipse depth datapoint at the same time as performing a straight-line fit to the eclipse depths. This fitted error bar amplitude was similar to the average of our occultation fit error bars, therefore we suggest that the error bars are appropriate to justify our results.

As described in Section 2.3.2, fitting the eclipses is particularly challenging due to

lack of data out-of-eclipse. This makes finding the correct phase and amplitude of the stellar variations, which we know are present from the CHEOPS, TESS, and *Spitzer* phase curves, very difficult. As the amplitude and half-period of these variations are on the same order as the eclipse depth and duration, this inflates the uncertainty in the eclipse depth measurements, and including them in the eclipse depth fit allows the reported error bars to reflect this uncertainty. This may also be an explanation as to why the mean occultation depth is less than the estimated occultation depth from the full phase curve-only fits, as the stellar pulsations being fitted can mimic the dip of the eclipse and produce a good fit with an anomalously low eclipse depth. It is worth noting that this difference is probably not due to the difference in modelling of the out-of-eclipse flux between the occultation-only observations and the occultations within the phase curves as we used a phase curve model in the occultation-only analysis as well (see Section 2.3.2.2). In models without this stellar pulsation model, the eclipse depths we retrieve are very different from one another and from the analysis with the pulsation model, and the errors reported were considerably smaller than the scatter in the depths. In this case it is clear that phase curve observations have been vital for informing the priors and model of the occultation-only observations. In future CHEOPS projects, one must be extremely cautious when working with occultations from variable and pulsating stars. Phase curves are essential in this case to constrain this stellar source of variability, due to the very limited baseline of occultation observations.

These eclipse depths, especially with the addition of the three occultations observed a year later, suggests a lack of significant variability in the atmosphere of KELT-9b. The variation in eclipse depths is roughly consistent with the error bar of the mean depth. Therefore we set an upper limit of temperature variability of KELT-9b at 1% of the mean brightness temperature ($\sim 1\sigma$). This observation is consistent with the lack of variability observed by *Spitzer* for HD 189733 b by Agol et al. (2010), for HD 189733 b and HD 209458 b by Kilpatrick et al. (2020), and with theoretical expectations by, for example, Showman et al. (2009) and Komacek & Showman (2020).

2.4.4 Albedo and heat redistribution

A thermal phase curve constrains the global dayside and nightside brightness temperatures. If the atmosphere radiates like a perfect blackbody, then the brightness temperature

is equal to the real temperature, despite the thermal phase curve being observed only within a limited range of wavelengths. The traditional approach is to then use a 0D 'box model' to convert these temperatures into the Bond albedo and heat redistribution efficiency, e.g., equations (4) and (5) of Cowan & Agol (2011). We do not expect KELT-9b to radiate like a perfect blackbody, but our approach for converting the temperature map to fluxes assumes a Planck function (Morris et al., 2022). Generally, the CHEOPS, TESS, and *Spitzer* thermal phase curves are probing different atmospheric layers (across radial distance or atmospheric pressure), which are described by different temperature maps.

We utilise the method described in Morris et al. (2022) to use the entire 2D temperature maps derived from the phase curve fitting to calculate these values. Following this, the Bond albedo is defined as

$$A_{\rm B} = 1 - \left(\frac{a}{R_\star}\right)^2 \frac{\int_{-\pi}^{\pi}\int_{0}^{\pi} F_p(\theta,\phi)\sin\theta\, d\theta\, d\phi}{\pi\sigma T_\star^4}, \tag{2.5}$$

where σ is the Stefan-Boltzmann constant and $F_p(\theta,\phi)$ is the flux from the planet derived from the temperature map. We must note here that the Bond albedo is a wavelength-independent quantity, however in this paper we quote three Bond albedos, one derived from each temperature map. We do this by assuming that each temperature element from the temperature map behaves like a blackbody. For each temperature element the flux of that element is estimated to be equal to $F_p(\theta,\phi) = \sigma T_p^4(\theta,\phi)$. This is not a perfect assumption, and so the Bond albedos reported from each temperature map may vary slightly (and can go negative) due to non-blackbody behaviour of the atmosphere. For example, if, at a certain wavelength, we are observing a strong absorption feature, then the estimated bolometric flux and brightness temperature may be less than the actual bolometric flux, as we assume that the small wavelength-band we observe is representative of the entire spectrum. The Bond albedos reported using the temperature map from each bandpass are reported in Table 2.6.

Considering the Bond albedo reported from each temperature map, there is strong evidence to suggest it is consistent with zero. This result is expected due to the extreme level of irradiation on the planet, which would contribute to a highly extended atmosphere where light entering from the direction of the star would have a very low probability of escaping before being absorbed. This therefore implies KELT-9b predictably, behaves similar to a blackbody.

The heat redistribution parameter of the atmosphere is defined as the ratio of the night-

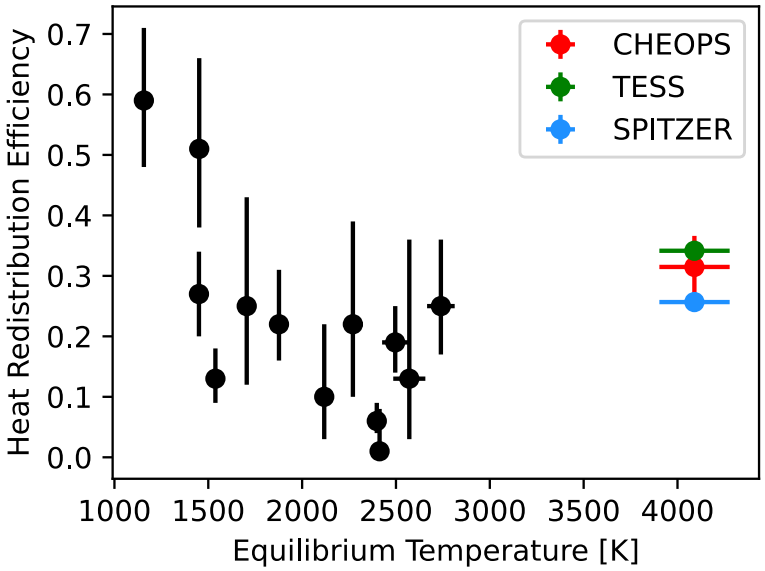

Figure 2.9 | Heat redistribution efficiency of hot Jupiters plotted against their equilibrium temperatures. The coloured points show the KELT-9b efficiency, ε, derived in this study.

side flux to the dayside flux and describes the extent to which heat is transported around the planet. As KELT-9b is tidally locked, this parameter is entirely dependent on the dynamics and chemistry of the atmosphere. It is also derived using information from the entire temperature map using the equation from Morris et al. (2022):

$$\varepsilon = \frac{\int_{\pi/2}^{\pi}\int_{0}^{\pi} F_p \sin\theta \, d\theta \, d\phi + \int_{-\pi}^{-\pi/2}\int_{0}^{\pi} F_p \sin\theta \, d\theta \, d\phi}{\int_{-\pi/2}^{\pi/2}\int_{0}^{\pi} F_p \sin\theta \, d\theta \, d\phi}. \tag{2.6}$$

Figure 2.9 shows the heat redistribution (ε) of KELT-9b plotted along with other hot-Jupiters. In previous papers (Wallack et al., 2021, Komacek & Showman, 2016), it has been shown that for hot Jupiters, the incident stellar flux is the primary decider of the level of ε. However in Bell & Cowan (2018), they predict a rising heat redistribution for UHJ due to the H_2 dissociation and recombination increasing the heat transport around the planet. Our work agrees with this theory and in Figure 2.9, it appears that ε does indeed fall with planet equilibrium temperatures up to around 2500 K, however after that the ε rises again with temperature and KELT-9b's ε calculated in this paper supports this trend.

Table 2.6 | Bond albedo and heat redistribution in the three bandpasses.

Bandpass	A_B	ε
CHEOPS	$-0.168^{+0.096}_{-0.092}$	$0.314^{+0.051}_{-0.058}$
TESS	-0.025 ± 0.032	$0.342^{+0.016}_{-0.017}$
Spitzer	-0.109 ± 0.068	0.257 ± 0.013

2.4.5 Comparison with *Spitzer*/TESS literature

2.4.5.1 TESS

We find that for the phase curve parameters, our TESS hotspot offset of $-12.32 \pm 0.97°$ is inconsistent with the offset reported in Wong et al. (2020b) (hereafter W20) ($5.2 \pm 0.9°$) by over 5σ (N.B. this error is a combination of the uncertainty in this paper's value and W20). However we obtain larger values for the offset in all passbands, and the *Spitzer* result is consistent with previous analyses. This lends credibility to our TESS measurement. For the other orbital parameters our planetary radius ($R_p = 0.079142 \pm 0.000099\,R_\star$) in the TESS bandpass is consistent with W20.

For some of the global parameters, our best-fit impact parameter ($b = 0.195^{+0.016}_{-0.015}$) differs from the W20 value by 1.4σ. Our best-fit semi-major axis ($a = 3.0914^{+0.0090}_{-0.0100}\,R_\star$) is different from the W20 value by around 4σ and our best-fit period ($P = 1.48111949 \pm 0.00000034$ days) is different to W20's value by 3.5σ. Finally, our best-fit orbital inclination ($i = 86.38^{+0.29°}_{-0.30}$) is just over 1.5σ away from the inclination reported in W20 and 1.6σ away from Ahlers et al. (2020).

We find that for the TESS phase curves, the eclipse depth reported in this paper from the phase curve fit (645 ± 15 ppm) is consistent with the eclipse depth found in W20 (650^{+14}_{-15} ppm). As discussed in Section 2.4.2, from our fitted eclipse depth and nightside flux we derived a TESS dayside brightness temperature of 4643 ± 26 K which is also consistent with W20 (4600 ± 100 K). Our TESS nightside brightness temperature of 3177^{+60}_{-61} K is consistent within 1.2σ of W20's nightside temperature (3040 ± 100 K). Following from this, in this work we have used the method in (Morris et al., 2022) to derive the Bond albedo and heat redistribution efficiency. Our values differ with the Bond albedo in W20 by 2.3σ and the heat redistribution parameter is consistent within 1σ. The gravity-darkening parameters will be discussed in Section 2.4.5.3.

2.4.5.2 *Spitzer*

For the orbital and system parameters, the planetary radius and transit duration differ with the same parameters reported in Mansfield et al. (2020) (hereafter M20) by 2.1σ and 6σ respectively, indicative of the different reduction methods influencing the derived parameters.

For the phase curve parameters, the *Spitzer* hotspot offset reported in this paper ($-18.2^{+1.7}_{-1.6}{}^{\circ}$ eastwards) is consistent the offset reported in M20 ($-18.7^{+2.1}_{-2.3}{}^{\circ}$). However as mentioned in Section 2.4.2, our nightside brightness temperature is inconsistent with the nightside brightness temperature reported in M20 by 3.5σ. The dayside brightness temperature reported in this paper is consistent with M20's value by just under 2σ.

2.4.5.3 Gravity-darkened transits

We find a sky-projected spin orbit angle of $-85.67^{+0.46}_{-0.45}$ degrees which is consistent with the spin orbit angle reported in Ahlers et al. (2020) (hereafter A20), and Gaudi et al. (2017). Our value of the gravity-darkening coefficient, β, ($0.2270^{+0.0077}_{-0.0080}$) is not consistent with A20, but is consistent with the Claret (2016) theoretical value. Our best-fit stellar inclination, $i^* = 47.1 \pm 1.1^{\circ}$ (related to the stellar obliquity ϕ, specified in A20, by $i^* = 90^{\circ} - \phi$), and stellar rotation period ($P_{\rm rot} = 18.96 \pm 0.34$ hours) are consistent with the value reported in A20.

Using the fitted values for i^*, i and λ we used Equation 2.1 to calculate a value for the true spin orbit angle of $84.36^{+0.37}_{-0.38}{}^{\circ}$. This is within 1σ of the value A20 reported.

2.5 Discussion

2.5.1 Challenges of simulating UHJs

Tidally locked, highly irradiated exoplanets, including UHJs, are complex, 3D objects. General circulation models (GCMs), which are numerical solvers of the 3D fluid equations, have been adapted to study hot Jupiters (see, e.g.: Showman et al., 2009, Rauscher & Menou, 2010, Heng et al., 2011, Kataria et al., 2013, Mayne et al., 2014). Recently, GCMs have been used to study UHJs (e.g.: Tan & Komacek, 2019).

The higher temperatures of UHJs present additional technical challenges for GCMs.

As we have shown in Figure 2.4, the atmosphere of KELT-9b transitions from temperatures where it is dominated by atomic hydrogen on its dayside to being dominated by molecular hydrogen on its nightside, verifying the prediction of Bell & Cowan (2018). Since the specific heat capacity at constant pressure, c_P, varies as the reciprocal of the mean molecular mass m, i.e., $c_P \propto 1/m$, it implies that c_P changes by a factor of 2 within the atmosphere of an UHJ, unlike for a regular hot Jupiter where it is roughly constant. The transformation from atomic to molecular hydrogen (and back) means that an additional cooling/heating term needs to be inserted into the governing equations (Bell & Cowan, 2018, Tan & Komacek, 2019). KELT-9b is an extreme example of these processes occurring in UHJs and correctly reproducing the observed dayside-to-nightside flux redistribution will require them to be simulated correctly. The CHEOPS, TESS, and *Spitzer* phase curves presented in the current study, as well as their associated temperature maps, will provide valuable constraints for future GCM studies of KELT-9b.

Another important constraint provided by the current work is that the climate of KELT-9b is somewhat stable: over around 270 orbital periods, the globally averaged dayside temperature varies by less than 50 K (see Section 2.4.3 on results of occultation analysis). These results are consistent with theoretical expectations produced from GCM analysis in works such as Showman et al. (2009) and Komacek & Showman (2020). Simulating variability accurately using GCMs is challenging, as it depends on the choice of governing equations (e.g.: Cho et al., 2008), numerical dissipation (e.g.: Heng et al., 2011, Thrastarson & Cho, 2011) and choice of bottom boundary condition (e.g.: Liu & Showman, 2013). In particular, our inability to specify numerical dissipation, which is often required to numerically stabilise GCM runs, from first principles (Heng et al., 2011) implies that energy and momentum conservation, and therefore our ability to accurately predict wind speeds and variability, is limited (Goodman, 2009).

In these ways, observations of UHJs lead our current ability to simulate them, with KELT-9b presenting the most extreme case study. The empirical constraints derived here therefore provide important checks on future GCMs of UHJs.

2.5.2 Anticipating JWST multi-wavelength phase curves

Formally, the spherical and Bond albedos are monochromatic and bolometric quantities, respectively. The spherical albedo is the monochromatic version of the Bond albedo

(monochromatic version of equation 2.5). One of the key limitations of the current study is that the measured CHEOPS, TESS, and *Spitzer* phase curves are neither monochromatic nor bolometric. Essentially, our ability to extract temperatures and Bond albedos is based on an extrapolation: the assumption that the spectral energy distribution (SED) of KELT-9b follows a perfect blackbody. Generally, a non-blackbody SED sampled in the CHEOPS versus *Spitzer* bandpasses will return different brightness temperatures. These differences translate into differences in the inferred Bond albedos that we report in Table 2.6.

In the era of the James Webb Space Telescope (JWST), multi-wavelength phase curves, which will be monochromatic to a good approximation, will become the norm. Two questions concerning the data analysis and interpretation of JWST thermal phase curves arise.

2.5.2.1 May we still use box models to extract Bond albedos from JWST thermal phase curves?

Generally, the heating of an atmosphere by starlight occurs in the near-ultraviolet to optical range of wavelengths, which is processed and re-emitted in the infrared range of wavelengths as thermal emission. (As already mentioned in the introduction, KELT-9b is a special case where its dayside thermal emission radiates in the optical.) While it is possible to quantify the wavelength-dependent flux of starlight incident upon the *top* of the atmosphere, it is much more challenging to describe how much starlight penetrates to each atmospheric layer as a function of wavelength. Any such attempt will be model-dependent and probabilistic (in a Bayesian sense).

If one integrates over all wavelengths, the bolometric flux of starlight is simply given by the Stefan-Boltzmann law. If the set of JWST thermal phase curves covers the entire wavelength range of the SED, then one may empirically derive the bolometric thermal flux emitted by the atmosphere. The Bond albedo may then be inferred without any assumption on the nature of the SED of the exoplanetary atmosphere, i.e., it is not necessary to assume a blackbody SED. Essentially, one bypasses the need for a 0D box model.

Alternatively, one could still perform an analysis like we have done in this paper and obtain different Bond albedos for every JWST thermal phase curve, assuming a blackbody SED for each surface element of the planet. However, as previously explained, this assumption will not be perfect for a planet with non-blackbody behaviour. Therefore the

former approach, assuming the JWST phase curves cover the entire planetary SED, would be much more accurate to determine the total bolometric flux of the planet, and therefore a more accurate (single value) of the Bond albedo.

2.5.2.2 Is it possible to extract spherical albedos from JWST thermal phase curves?

As mentioned, the spherical albedo is the monochromatic version of the Bond albedo. At first thought, if JWST can produce monochromatic phase curves, it is easy to suggest this could translate into a set of spherical albedos for the planet. However this would be incorrect. In principle, if one knew exactly how much starlight was deposited in a specific atmospheric layer, then one could compare that to the thermal emission from that layer and derive the spherical albedo. However, as previously described this would be a model-dependent exercise that involves some assumption on the model atmosphere in order to perform radiative transfer from the top of the atmosphere to the layer in question.

Specifically, equation (2.5) describes our approach for deriving the Bond albedo from a 2D temperature map. Despite the CHEOPS, TESS, and *Spitzer* thermal phase curves being neither monochromatic nor bolometric, this equation allows one to work with temperatures because of the assumption of a blackbody SED. When JWST multi-wavelength thermal phase curves are available, the numerator of equation (2.5) may be generalised such that F_p is empirically derived from the data with no need to assume a blackbody SED. However, the denominator cannot be generalised in a straightforward way as $\sigma T_\star^4$ needs to be replaced by the flux of starlight deposited in the same atmospheric layer. In principle, it is possible to solve for these wavelength-dependent fluxes within a holistic framework that simultaneously interprets phase-dependent emission spectra and wavelength-dependent phase curves. Such a framework would have to account for scattered starlight versus thermal emission as functions of wavelength. However, as explained in the previous subsection, calculating the Bond albedo would still be possible from the JWST thermal phase curves alone, provided they sufficiently spanned the planetary SED. As the Bond albedo describes the planet's input and output energy bolometrically, it removes the need to undertake the difficult task of probing the individual atmospheric layers.

2.6 Conclusion

In this work we have simultaneously analysed CHEOPS phase curves as well as public phase curves from TESS and *Spitzer* to infer joint constraints on the phase curve variation, gravity-darkened transits and occultation depth in the three bandpasses (Figure 2.2). From this analysis we find the following results:

- We derive 2D temperature maps of the atmosphere at three different depths, and calculate dayside and nightside brightness temperatures of the planet in each bandpass (Figure 2.4, Table 2.5 and Sections 2.4.1 and 2.4.2).
- The day-night heat redistribution of ~ 0.3 confirms theoretical expectations of enhanced energy transfer to the planetary nightside due to dissociation and recombination of molecular hydrogen in ultra-hot Jupiters (Figure 2.9, Table 2.6 and Section 2.4.4).
- We also find a Bond albedo consistent with zero (Table 2.6 and Section 2.4.4).
- We also analyse 9 CHEOPS occultations of KELT-9 and find no evidence of variability of the brightness temperature of the planet, excluding variability greater than 1% (1σ) (Figure 2.8 and Section 2.4.3).

Appendix

2.A Transit best-fits

Figure 2.10 shows the transit models and photometry.

2.B Posterior distributions

Figure 2.11 shows the posterior distributions for the phase curve parameters.

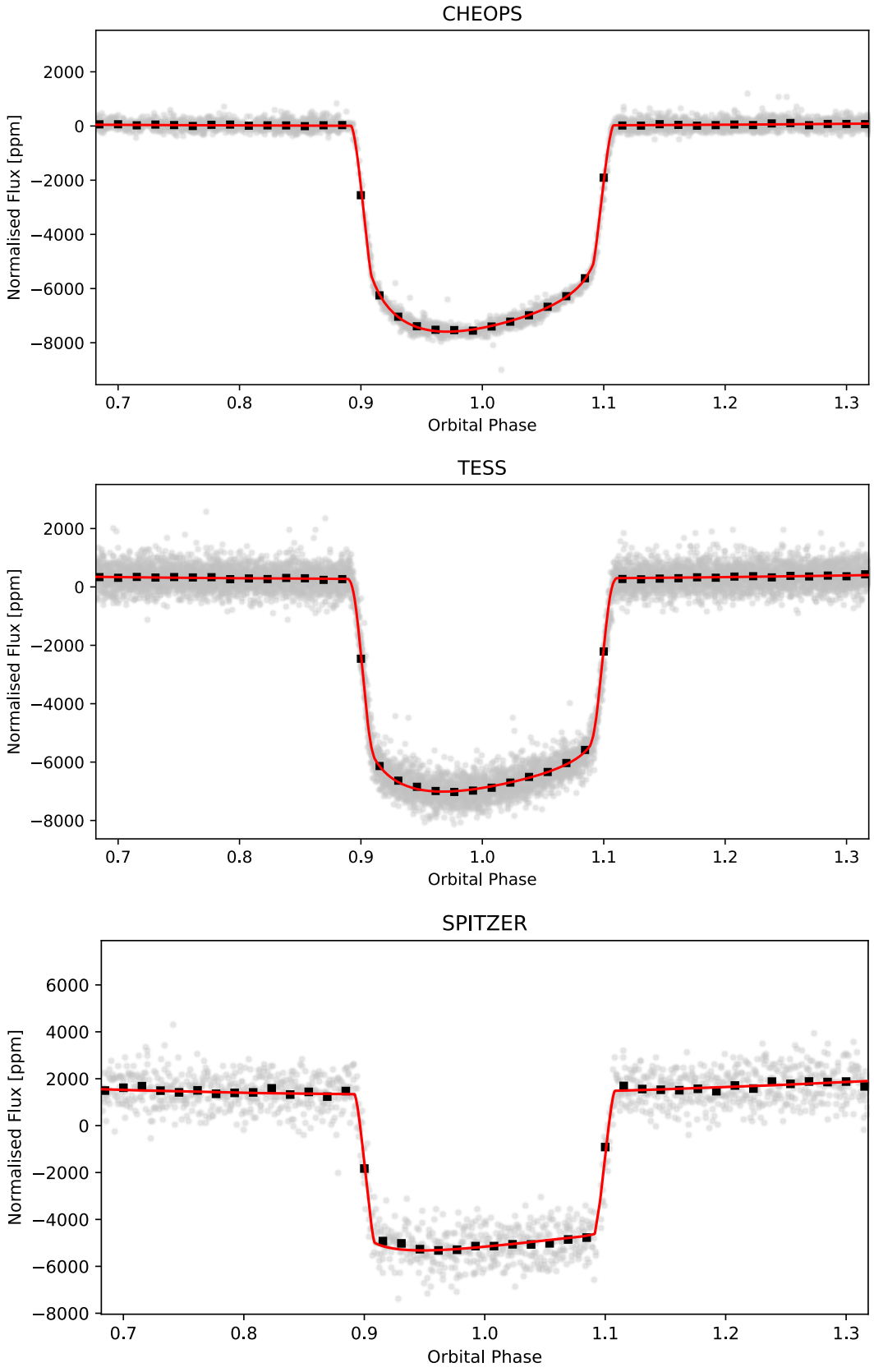

Figure 2.10 | CHEOPS, TESS, and *Spitzer* phase-folded and detrended transits overplotted with the best-fit transit model (in red), with all other models and systematics removed. In black are the binned grey datapoints, with error bars that are smaller than the point size in all panels so they are not visible.

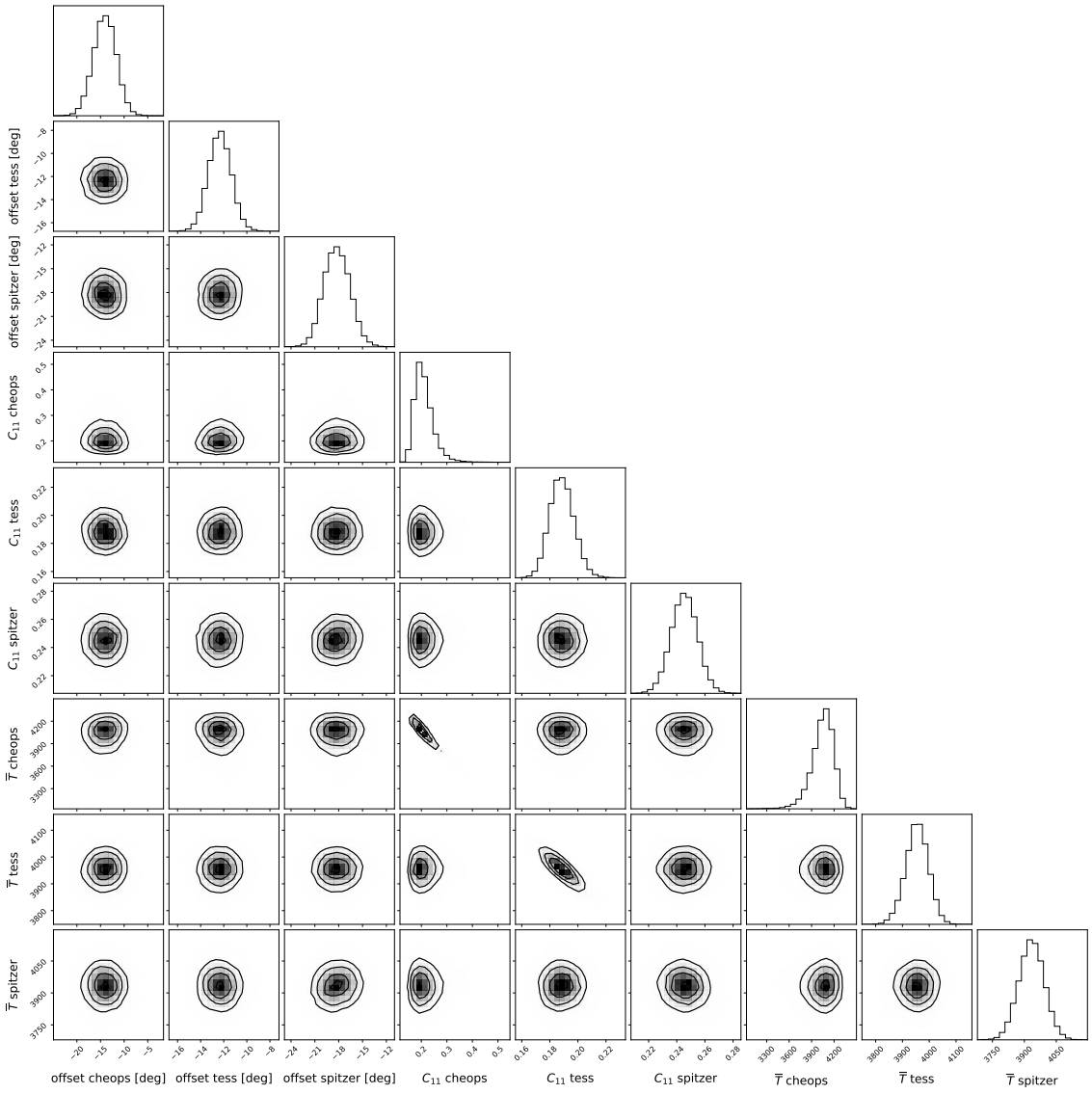

Figure 2.11 | Corner plot showing posteriors of the phase curve parameters in the joint fit. The three contour lines in each subplot refer to the 1-, 2- and 3-sigma contour levels.

Chapter 3

Using `catwoman` to constrain morning and evenings on exoplanets: a new semi-analytical approach and prospects with transmission spectroscopy

This chapter has been published in two papers:

- **Jones, K.** and Espinoza, N. 2022, Journal of Open Source Software, 7(72):2382, doi: 10.21105/joss.02382, *catwoman: A transit modelling python package for asymmetric light curves*
- Espinoza, N. and **Jones K.** 2021, AJ, 162(4):165, doi: 10.3847/1538-3881/ac134d (edited into British English), *Constraining Mornings and Evenings on Distant Worlds: A new Semianalytical Approach and Prospects with Transmission Spectroscopy*

Exoplanet transits have been studied by astrophysicists since Charbonneau et al. (2000) observed the first transit of HD 209458b. At the simplest level, they can be used to measure the planet-to-star radius and other orbital parameters such as the impact parameter and orbital inclination (the two of course being related). However, following on from looking at complex phase curve models with KELT-9b (Section 2), there is much more we can potentially extract from a transit, if we have the suitable tools. The simple transit model from Mandel & Agol (2002) assumes the planet is a uniform sphere and that the atmosphere is also uniform around the whole globe. However, especially for tidally-

locked hot Jupiters, this is not expected to be the case (see, e.g. Powell et al., 2019, Parmentier et al., 2018). In the early days of transit photometry, the data was not precise enough to warrant searching for these more complex signals, however with TESS, CHEOPS and JWST (and others) now operating, the time has come. In this chapter, we detail `catwoman`, a Python package developed by myself and my collaborators designed to model asymmetric exoplanet transits. We then go further to show the impact of this new model in the age of JWST observations.

Code Summary

When exoplanets pass in front of their stars from our point of view on Earth, they imprint a transit signature on the stellar light curve which, to date, has been assumed to be symmetric in time, owing to the planet being modelled as a circular area occulting the stellar surface (Kreidberg, 2015, Luger et al., 2019, Mandel & Agol, 2002). However, this signature might be asymmetric due to several possible effects, one of which is the different temperature/pressure and/or chemical compositions the different terminator regions a transiting planet could have (see, e.g. Powell et al., 2019). Being able to model these asymmetric signatures directly from transit light curves could give us an unprecedented glimpse into planetary 3-dimensional structure, helping constrain models of atmospheric evolution, structure, and composition.

`catwoman` is a Python package that models these asymmetric transit light curves, calculating light curves for any radially symmetric stellar limb darkening law where planets are modelled as two semi-circles of different radii, using the integration algorithm developed in Kreidberg (2015) and implemented in the `batman` library, from which `catwoman` builds upon. It is fast, efficient, and open-source with full documentation available to view at `https://catwoman.readthedocs.io`.

The light curves are modelled as follows: The decrease in flux, δ, as a planet transits its star can be approximated by the sum

$$\delta = \sum_{i=1}^{N} I(x_m)\Delta A(x_m, R_{p,1}, R_{p,2}, \phi, d), \tag{3.1}$$

where the semi-circles are split into iso-intensity bands centreed on the star. For each intersectional segment (see Figure 3.1), its area, ΔA, is multiplied by the intensity of the star, and these strips are summed to generate the full δ for a specific separation between the centre of the star and planet, d. The code then increments d by a small pre-determined amount (based on the time array given by the user) and recalculates δ.

The width of the iso-intensity bands determines the truncation error of the model. The model is first initialized with parameters including a maximum truncation error either set by the user or taken as the pre-set value of 1 ppm. As in `batman`, `catwoman` first calculates many models with varying widths and geometrically searches for a width that produces an error less than 1% away (and always less than) the specified level. The model

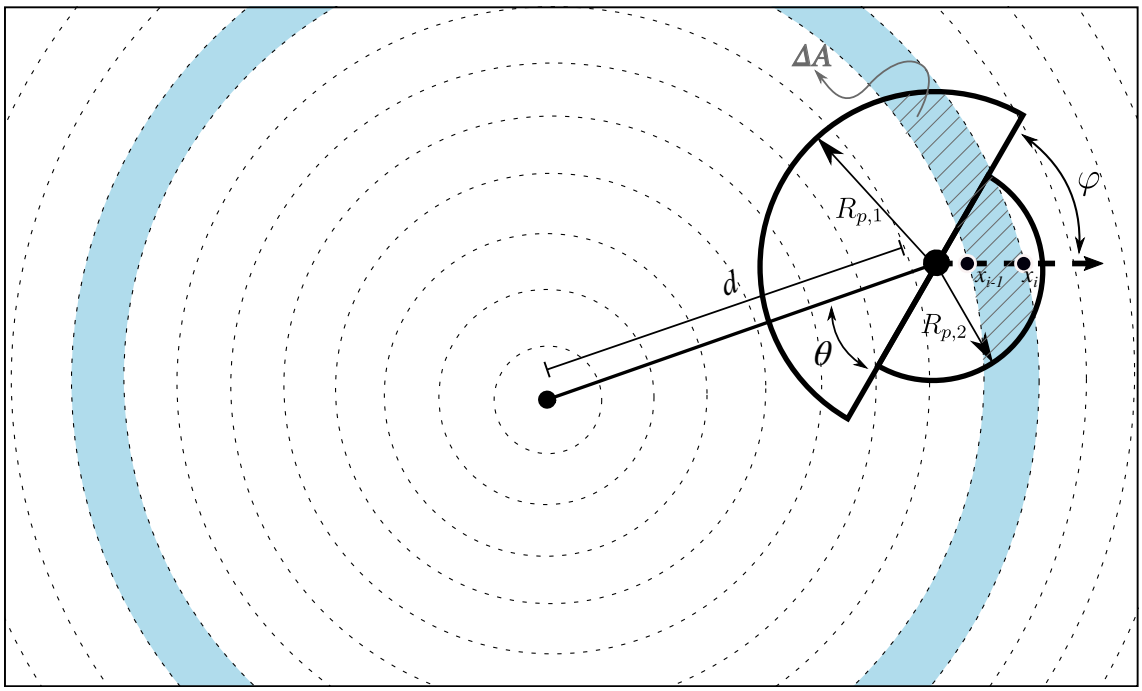

Figure 3.1 | Diagram of the geometric configuration during transit of two stacked semi-circles (one of radius $R_{p,1}$; indicated by the arrow going up, and another of radius $R_{p,2}$; indicated by the arrow going down) that model the (possible) different limbs of an exoplanet transiting in front of a star. The area of the star has been divided into different sections of radius x_i (dashed circles) — between each subsequent section, the star is assumed to have a radially symmetric intensity profile (e.g., blue band between x_{i-1} and x_i above). In order to obtain the lightcurve such an object would produce, the challenge is to calculate the intersectional area between a given iso-intensity band and the stacked semi-circles, ΔA (blue band with dashed grey lines). Note the stacked semi-circles are inclined by an angle φ with respect to the planetary orbital motion (illustrated by the dashed arrow moving to the right), which accounts for the possibility of having planetary spin-orbit misalignments ($\varphi = \pi/2$ implies no spin-orbit misalignment). θ is the angle between the base of the semi-circles and the line that joins the centres, d.

then uses this width value to calculate the desired light curves. A lower specified error, and therefore thinner iso-intensity bands, produces more accurate light curves; however, more steps are needed to calculate δ, which takes more time.

`catwoman` also allows for ϕ, the angle of rotation of the semi-circles, to vary as a free parameter, which is something no other model has tried to implement, accounting for the possibility of spin-orbit misalignments of the planet. The two semi-circle radii, $R_{p,1}$ and $R_{p,2}$, and other orbital variables are also completely free parameters.

`catwoman` was designed to be used by astronomical researchers. For a realistic light curve with 100 in-transit data points, `catwoman` takes around 340 seconds to produce 1 million quadratic-limb-darkened light curves on a single 1.3 GHz Intel Core i5 processor. It is used in Espinoza & Jones (2021).

Abstract

The technique of transmission spectroscopy — the variation of the planetary radius with wavelength due to opacity sources in the planet's terminator region — has been to date one of the most successful in the characterisation of exoplanet atmospheres, providing key insights into the composition and structure of these distant worlds. A common assumption made when using this technique, however, is that the variations are the same in the entire terminator region. In reality, the morning and evening terminators might have distinct temperature, pressure and thus compositional profiles due to the inherent 3-D nature of the planet which would, in turn, give rise to different spectra on each side of it. Constraining those might be fundamental for our understanding of not only the weather patterns in these distant worlds, but also of planetary formation signatures which might only be possible to extract once these features are well understood. Motivated by this physical picture, in this work we perform a detailed study on the observational prospects of detecting this effect. We present an open-source semi-analytical framework with which this information can be extracted directly from transit lightcurves, and perform a detailed study on the prospects of detecting the effect with current missions such as *TESS* and upcoming ones such as *JWST*. Our results show that these missions show great promise for the detection of this effect. Transmission spectroscopy studies with *JWST*, in particular, could provide spectra of each of the limbs allowing us to convey 3-D information previously accessible only via phase-curves.

3.1 Introduction

The technique of transmission spectroscopy — the wavelength dependence of the planetary radius during transit (Seager & Sasselov, 2000, Hubbard et al., 2001, Burrows et al., 2003, Fortney, 2005), has been one of the most successful ones in the past decade to explore the composition and structure of exoplanet atmospheres, providing key insights into their interior structures and compositions (see, e.g., Kreidberg et al., 2018, for a review). From an observational perspective, to obtain a transit spectrum researchers typically fit a transit model to precise wavelength-dependent lightcurves in order to retrieve the transit depths, $(R_p/R_*)^2$, as a function of wavelength. Typically, the fitting procedure relies on one simple, but key assumption: the terminator region we observe during transit is ho-

mogeneous. There is already growing evidence that this assumption might actually be unrealistic in relatively hot ($T_{\rm eq} > 1000$ K) exoplanet atmospheres, where the day-to-night differences might in turn imply different structures and overall compositions in their morning and evening[1] terminators (see, e.g., Fortney et al., 2010, Dobbs-Dixon et al., 2012, Kempton et al., 2017, Powell et al., 2019, MacDonald et al., 2020, Helling et al., 2020, and references therein). Constraining them might give precious insights into circulation patterns and compositional stratification which might probe to be fundamental for our understanding of the weather patterns in distant worlds. For example, hazes are expected to be photochemically produced and thus they would most likely be able to form in the dayside (Kempton et al., 2017, Powell et al., 2019). These could, in turn, be transported to the trailing limb, while clouds could be transported from the nightside (where they are expected to form due to the lower temperatures) into the leading limb, thus resulting in a drastically different transmission spectrum between them, and thus effective sizes of the radii of each limb (Kempton et al., 2017, Powell et al., 2019). Directly detecting this effect would not only serve to put theories like the ones proposed by Kempton et al. (2017) and Powell et al. (2019) to the test, but would directly impact on the fundamental assumptions of transmission spectroscopy studies to date, implying there is not *one* set of properties (e.g., abundances) to extract from transmission spectra. This is, in turn, critical to perform inferences on e.g., formation scenarios based on extracted molecular abundances with this technique (see, e.g., Öberg et al., 2011, Mordasini et al., 2016, Espinoza et al., 2017, and references therein).

Previous works (e.g., Dobbs-Dixon et al., 2012, Line & Parmentier, 2016, Kempton et al., 2017, Powell et al., 2019, MacDonald et al., 2020) have already studied the prospects and impact of limb inhomogeneities on transit spectra. Overall, the consensus seems to be that there is already both observational and theoretical evidence that this is an effect that is important to consider and that might even be impacting current transit spectra. Line & Parmentier (2016), Kempton et al. (2017) and Powell et al. (2019) have already laid out the foundation of the theoretical aspects of detecting this effect, while MacDonald et al. (2020) has in fact studied publicly available transmission spectra in order to show that they can actually be explained as arising from two distinct temper-

[1] In this work, the morning and evening limbs are also referred to as the leading and trailing limbs, respectively.

ature/pressure profiles. In this work, we explore these prospects from an observational perspective which aims at detecting the effect of limb asymmetries *directly in transit lightcurves*, such that interpretations can be made at a later stage on each of the limbs.

Detecting limb-asymmetries at the lightcurve level could have important impacts on how researchers typically approach transit spectroscopy for several reasons. First, it could imply that performing inference about the limbs on transit depths obtained through lightcurve fits using the classic Mandel & Agol (2002) symmetric transit model is subject to be biased, as the lightcurves would be essentially fit with the wrong model. If the limbs have different properties, their transit spectrum -and thus their "transit depths"- would be different, injecting lightcurve asymmetries that these models cannot properly account for. Second, performing inference on the transit depths obtained through these symmetric transit models also necessitates a handful of assumptions in order to overcome the degeneracies that fitting a single transmission spectrum with two different temperature, pressure and abundance profiles imply. This, in turn, diminishes the discovery space to the assumptions made by our models, which might be quite a restrictive imposition, especially in the era of ultra-high spectrophotometric precision such as the ones the upcoming *James Webb Space Telescope* (*JWST*) will be opening up. Here, we propose instead that if indeed limb asymmetries can be detected in the transit lightcurves themselves, this would open up a whole new and direct framework for obtaining information about them. In this framework, we would be able to extract *two* "limb spectra" from a given transit lightcurve: one spectrum for each limb, which we could interpret individually at a later stage through, e.g., atmospheric retrievals and/or forward models. It is important to note that the essence of this proposition is not particularly new (it has already been suggested by the work of von Paris et al. 2016). Our contribution in this work is to perform a deep dive into (a) *how* we might actually perform this characterisation in a fast and reliable way, (b) *what is the level of detectability* of this effect with current and near-future instrumentation and (c) to show how, in some cases, this might even be *the most efficient way of extracting this information* from transit lightcurves. Some of these points have already been touched upon by Powell et al. (2019) at different degrees of depth; here we expand and homogenise the discussion from an observational perspective, which we believe complements these previous works on this topic.

Our work is organised as follows. In Section 3.2 we present a new semi-analytical

method to extract the transit depths from each of the limbs of an exoplanet. The core idea of this method was actually already put forward by von Paris et al. (2016), where each of the limbs of the exoplanet are modelled as stacked semi-circles. However, we expand on this modelling framework in that our calculation is made in a semi-analytical fashion, making use of geometrical arguments and the algorithm used by `batman` (Kreidberg, 2015). This makes the lightcurve computation much faster than the numerical scheme described in von Paris et al. (2016), and allows us to expand it to account for sky-projected *planetary* spin-orbit misalignments. We present a python library to generate lightcurves with this new algorithm, `catwoman` (Jones & Espinoza, 2020), in Section 3.2.1, provide an overview of the model and validate it against a numerical implementation in Section 3.2.2. In Section 3.3 we present simulations in which we explore the feasibility of detecting this effect with current precise photometry such as that of the *Transiting Exoplanet Survey Satellite* mission (*TESS*; Ricker et al., 2015) and near-future instrumentation such as spectrophotometry to be obtained by the upcoming *JWST*. In Section 4.5 we present a discussion and implications of our results, along with a case-study on the exoplanet HAT-P-41b, which we use to demonstrate how extracting the spectrum of the limbs of this exoplanet might give insights into possible models that give rise to the observed transit spectrum by the *Hubble Space Telescope* (*HST*). We summarise our main conclusions in Section 3.5.

3.2 Modelling limb asymmetries in transit lightcurves

The idea proposed by von Paris et al. (2016) to model the signatures of asymmetric limbs in transit lightcurves involves a very simple concept: approximate the terminator regions of the leading and trailing limbs as two stacked semi-circles with different radii. In essence, the idea is that each limb produces an independent transit spectrum that we ought to recover by modelling the lightcurve imprinted by them. In that work, the authors used a numerical framework to compute the resulting lightcurve, which is relatively computationally expensive. Here we use the same idea but tackle the problem from a different angle: instead of using a numerical approach, we employ a semi-analytical framework, which in turn allows for faster lightcurve computations. In this new framework, the stacked semi-circles are also allowed to be *rotated* with respect to the orbital

motion, expanding thus the proposed framework by von Paris et al. (2016).

The basic problem we are trying to tackle is that of producing a transit lightcurve of two stacked semi-circles of (normalised, with respect to the stellar) radii $R_{p,1}$ and $R_{p,1}$ in front of their host star, where the semi-circles may be inclined with respect to the orbital motion by an angle φ. The geometrical configuration of the problem is depicted in Figure 3.1. We follow Kreidberg (2015) and assume a radially symmetric intensity profile $I(x)$, where $0 < x < 1$ is the normalised radial coordinate measured from the centre of the star. With this, we can express the fraction of stellar light blocked by the object, δ, as (see Figure 3.1)

$$\delta = \sum_{i=1}^{N} I\left(x_m\right) \Delta A(x_m, R_{p,1}, R_{p,2}, \varphi, d), \tag{3.2}$$

where $x_m = (x_i + x_{i-1})/2$ is the middle point between x_i and x_{i-1}, and $\Delta A(x_m, R_{p,1}, R_{p,2}, \varphi, d)$ (for which we shall refer to in what follows simply as ΔA) is the inter-sectional area between the stacked semi-circles and the iso-intensity band depicted in Figure 3.1, where $R_{p,1}$ and $R_{p,2}$ are the radii of the semi-circles, φ is the rotation of the base of the semi-circles with respect to the orbital motion of the planet and d is the distance between the centre of the star and the semi-circles. Because the form of $I\left(x_m\right)$ is usually known/parametrised via so-called limb-darkening laws, the challenge of finding the lightcurve of this configuration of stacked, rotated semi-circles is to find ΔA. The full derivation of this is presented in Appendix 3.A; we present an overview of our implementation and validation of our approach below.

3.2.1 Implementation and model overview

Our semi-analytic approach to the problem has been implemented in the `catwoman` library (Jones & Espinoza, 2020), which is fully documented[2] and available on Github[3]. In practice, `catwoman`'s code-base is that of `batman` Kreidberg (2015), and as such the library inherits most of the high-level functionalities of this latter library. A `catwoman` lightcurve, thus, receives as inputs the time-of-transit centre t_0, the period P of the orbit, the scaled semi-major axis a/R_*, the inclination i of the orbit with respect of the plane of the sky, the eccentricity e and argument of periastron ω of the orbit, and a set of limb-darkening coefficients for any of the laws already available in `batman`. On top of these,

[2] http://catwoman.readthedocs.io

[3] https://github.com/KathrynJones1/catwoman

catwoman takes as input the radii of each of the stacked semi-circles, $R_{p,1}$ and $R_{p,2}$, and the angle φ between the axis that connects them and the vector that follows the direction of motion in the orbit (see Figure 3.1).

The motivation behind allowing to define the angle φ in the lightcurve generation comes from the possibility of being able to detect the sky-projected spin-orbit misalignment of the *planet*, which is something the eclipse mapping technique for both lightcurves (Rauscher et al., 2007, Williams et al., 2006) and radial-velocities (Nikolov & Sainsbury-Martinez, 2015) are able to do in principle. As will be shown in Section 3.3.3, detecting the effect of asymmetric lightcurves due to morning/evening terminator structural and/or compositional inhomogeneities almost guarantees the possibility of putting constraints on this angle, and ignorance on its value does not have a great impact on the detectability of the effect. One important point to consider on this parameter is that this defines the *instantaneous* angle between the axis that joins the semi-circles and the direction of the orbital motion (see Figure 3.1; orbital motion indicated with a dashed-line arrow). Because orbits as projected in the plane of the sky are curved in general, this means the axis that joins the semi-circles *rotates* when compared against a straight line projected in this plane. This effect has been implemented within catwoman as well (see Appendix 3.A); we validate this implementation against a numerical implementation in the next sub-section.

3.2.2 Validation of the semi-analytical approach

In order to validate the semi-analytical approach presented here and implemented in the catwoman library, we built a numerical model that is also able to generate asymmetric lightcurves due to terminator inhomogeneities but through a completely independent and straightforward (albeit "brute-force") approach. While by construction catwoman is able to reach any desired precision level (as that is a parameter that can be modified and is tested for convergence before running lightcurve model evaluations), our objective with this alternative approach is to validate and illustrate that catwoman is indeed able to generate asymmetric lightcurves with accuracies of at least 10 ppm, which are the noise limits ultra-precise spectrophotometers like the upcoming *JWST* will be able to reach (Greene et al., 2016). Our implementation of this numerical scheme is also available in Github[4], and is detailed below.

[4] https://github.com/nespinoza/numerical_catwoman

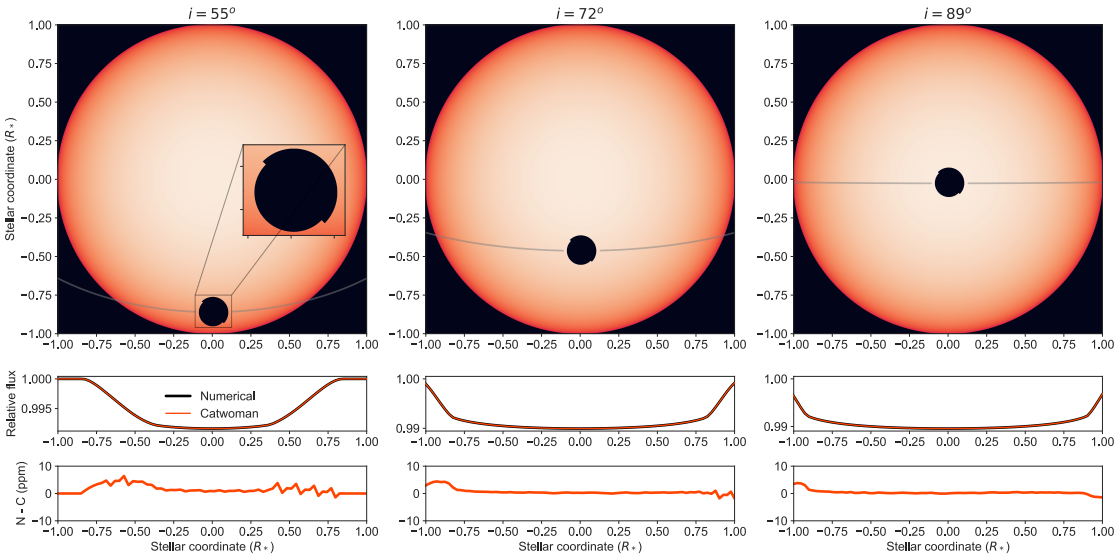

Figure 3.2 | Comparison between a numerical implementation of the lightcurve generation of asymmetrical transits and the semi-analytical formalism presented in our work, implemented in the `catwoman` library. Examples are shown for orbital inclinations of 55^o (left), 72^o (middle) and 89^o (right) — all of them assume a period of 3 days, a quadratic limb-darkening law ($u_1 = 0.3$, $u_2 = 0.2$), $a/R_* = 1.5$ and zero eccentricity. The top images are snapshots of our numerical model which include a limb-darkened star (orange) and a planet with asymmetric terminator regions ($R_{p,1} = 0.1$, $R_{p,2} = 0.09$ and $\varphi = -45^o$) transiting in front of it; middle panels show the retrieved lightcurves from both methods, and the bottom panels show the difference between the two. Most of the residuals observed in this latter panel are due to errors on our numerical model scheme (see text); by construction, our `catwoman` models in these computations had a 1 ppm error limit.

Our approach of this numerical version of the lightcurve generation of asymmetrical transits is very similar to that of von Paris et al. (2016), and consists of simply discretizing the plane of the sky into $n_p \times n_p$ "pixels" centred around the target star. Pixels within the star are filled with values between 0 and 1 according to a given intensity profile $I(\mu)/I(1)$, while positions that include either the planet or the sky are filled with zeroes. The precision on the lightcurves generated by this scheme, thus, can be optimised by simply increasing n_p. In practice, this is implemented by populating a matrix of dimensions (n_p, n_p), on which we first fill all pixels within a distance of $n_p/2$ from the centre of this matrix (i.e., $(n_p/2, n_p/2)$) with intensities given by the defined intensity profile (a quadratic law in the case of our implementation) — all other pixels are filled with zeroes. With this, we sum all the pixel values to compute our out-of-transit flux. Our algorithm then, using as inputs the coordinates of the centre of the planet with respect to a reference frame centred on the star (X, Y) at each time-step and the input angle φ, computes the slope of the orbital motion $s = dY/dX$ by simple differences at each time-step i, i.e., $s_i = (Y_{i+1} - Y_i)/(X_{i+1} - X_i)$. This is then used to compute the instantaneous rotation of the axis that joins the stacked semi-circles with respect to the orthogonal system that defines the (X, Y) positions as $\arctan(s_i) + \varphi$. This axis is then used to separate the areas covered by both semi-circles, pixels inside of which are set to zero.

We use this simple numerical scheme to validate the semi-analytical framework developed in this work by computing a set of cases including a challenging one in which the planetary orbit is significantly curved. This latter case allows us, in turn, to verify that our method outlined in Appendix 3.A is correctly accounting for the rotation of the axis that joins the semi-circles with respect to the orthogonal system that defines the (X, Y) positions of the planet. To generate this, we simulate an exoplanet with a period of 3 days, time-of-transit centre $t_0 = 0$, scaled semi-major axis $a/R_* = 1.5$ and zero eccentricity for three inclinations: $i = 55$, 72 and 89 degrees. For the star, we define a quadratic limb-darkening profile with $u_1 = 0.3$ and $u_2 = 0.2$. As for the physical properties of the planet, we assume it to have asymmetric terminator regions with $R_{p,1} = 0.1$, $R_{p,2} = 0.09$ and $\varphi = -45^o$. Planetary positions (X, Y) were obtained using `catwoman` (which uses the exact same method as `batman` to calculate them) for 100 equally spaced timestamps between -0.5 and 0.5 days. We performed numerical simulations with $n_p = 2500$, 5000, 10000, 20000 and 40000 (i.e., doubling the number of pixels

on each side of our matrix), and found that the maximum flux changes roughly halved as well between each of those runs. These changes reached 4 ppm between $n_p = 20,000$ and $n_p = 40,000$, which we consider as our maximum error on the fluxes of our numerical scheme when selecting this latter number for n_p. Simulations using both our numerical (with $n_p = 40,000$) and semi-analytical (through the `catwoman` library, with a maximum error set to 1 ppm[5]) schemes are presented in Figure 3.2. As can be observed, the differences between both are *very* small; they reach peak differences of less than 7 ppm — most of which are explained by the errors defined by our numerical scheme.

For all practical purposes, these limits give us confidence that our semi-analytical framework works as expected for precisions which are better than current and near-future instruments such as *JWST*, which is expected to reach about 10 ppm lightcurve precisions (Greene et al., 2016). We note that the speed increase of the `catwoman` library in comparison to the numerical implementation is huge: `catwoman` takes a couple hundreds of milliseconds to generate a lightcurve in a 2.9 GHz Intel Core i9 processor. The numerical implementation takes tens of seconds to generate the same model, although this latter one is a pure-Python code, whereas the `catwoman` library is a mixture of Python and C. In general, in experiments made with this processor, `catwoman` takes about twice the time `batman` takes to generate a lightcurve. This is consistent with the fact that the `catwoman` code-base is inherited from the `batman` one, and goes to show that the analytical part of `catwoman` is as fast as `batman`'s — only that we perform it twice, one for each of the stacked semi-circles.

3.3 Detectability of the effect

Although the pioneering study of von Paris et al. (2016) already tried to detect the effect of asymmetric transit lightcurves produced by non-uniform cloud cover on precise data of three exoplanets obtained by the *Kepler* mission and *HST*, a systematic study of the detectability of the effect has not been done either on real or simulated transit lightcurves. Such a study is very timely as the *TESS* satellite (Ricker et al., 2015) has just started its extended mission re-observing some of the most promising targets to detect this effect

[5] In `catwoman`, we inherit the maximum allowable truncation error for numerical integration from `batman`; see Section 3.4 in Kreidberg (2015).

and as *JWST* prepares for launch. These missions have a key advantage over *Kepler*: they allow us to target objects with large scale-heights, for which this effect should be more prominent in the data even if they are observed over shorter time-scales.

The question of the detectability of the effect in a given dataset is, however, a complex one. It is not only related to the precision of the lighcurves themselves in order to be able to detect the effect (which is evident will depend on the difference between the effective size of the terminator region on the leading and trailing limb of the exoplanet), but also to the correlation between the parameters that could impact on a transit lightcurve. It could be that the lightcurve indeed is asymmetric but a given transit parameter is able to correct for this if a symmetric model is used. Indeed, von Paris et al. (2016) identified that the evidence for asymmetric lightcurves is heavily impacted by the knowledge of the ephemerides: a small shift in the time-of-transit centre on a symmetric transit model could lead to an equally good fit to one with an asymmetric model, even for intrinsically asymmetric lightcurves. As such, in order to *claim* the detection of this effect, one needs to perform proper model comparison. In this work, we choose to use Bayesian model evidences to this end. In particular, we assume both the symmetric and asymmetric lightcurve models are equiprobable a-priori, which implies the difference between the log-evidence of an asymmetric lightcurve, $\ln Z_A$ to the one obtained from a symmetric one, $\ln Z_S$, $\Delta \ln Z = \ln Z_A - \ln Z_S$, is equal to

$$\Delta \ln Z = \ln \frac{Z_A}{Z_S} = \ln \frac{\mathcal{P}(A|\text{Data})}{\mathcal{P}(S|\text{Data})},$$

where $\mathcal{P}(A|\text{Data})$ is the probability of the asymmetric model given the data and $\mathcal{P}(S|\text{Data})$ is the probability of the symmetric model given the data.

In what follows, we simulate asymmetric lightcurves using the `catwoman` library with *JWST*-like and *TESS*-like cadences, in order to study how the detectability of the effect changes with our knowledge of different parameters of the model and the lightcurve precision using bayesian evidences as the metric for detectability. We decide not to generate simulations for *HST*, as the gaps between orbits of the observatory imply a special, case-by-case analysis on the detectability of the effect — we leave such a study for future work. For each of the cases described below we generate asymmetric lightcurves with a range of radius differences between the leading ("morning") and trailing ("evening") limbs. We parametrise this in our simulations in terms of the corresponding "transit depth" each side of the planet implies. To this end, we fix $R_{p,1}/R_*$ to 0.1 in order to emulate a typical hot

Jupiter planet-to-star radius ratio, and then define

$$R_{p,2}/R_* = \sqrt{\left(R_{p,1}/R_*\right)^2 + 2\Delta\delta}, \tag{3.3}$$

where $\Delta\delta$ is the morning-to-evening transit depth difference. The factor of 2 in front of this term stems from the fact that here we define $\Delta\delta$ as the transit depth difference *between the transit depth imprinted in the lightcurve by each of the stacked semi-circles.* In other words, $\Delta\delta = \delta_2 - \delta_1$, where $\delta_i = (1/2)(R_{p,i}^2/R_*^2)$. While there is no consensus in the literature as to how small or large morning-to-evening transit depth differences should be (e.g., Kempton et al. (2017) predict between 100-400 ppm differences for WASP-121b; Powell et al. (2019) predict values as large as 1000 ppm) we choose here to take a conservative upper limit on the effect of 500 ppm; in our simulations, thus, $\Delta\delta$ ranges from 5 to 500 ppm in 30 log-spaced bins. For each of those combinations, we simulate 5 datasets of noisy transit lightcurves with noise levels σ_w ranging from 10 to 1000 ppm in 30 log-spaced bins as well. We calculate the average of the log-evidences for symmetric and asymmetric models fitted to that data in each $(\Delta\delta, \sigma_w)$ pair, which is then used to compute the difference between the log-evidences. In all of our simulations the period is set to 1 day, the semi-major axis to stellar radius ratio to $a/R_* = 10$, inclination to 90 degrees, and a circular orbit is assumed. We note this set of parameters define a worst-case scenario for the detection of the effect. The reason is that most of the information used to infer the limb asymmetries comes from ingress and egress, as has already been shown by previous works (see, e.g., von Paris et al., 2016, Kempton et al., 2017, Powell et al., 2019). The ingress/egress duration in a circular orbit is given by

$$\tau = \left(\frac{P}{\pi}\right)\left(\frac{1}{\sqrt{1-b^2}}\right)\left(\frac{R_p}{R_*}\right)\left(\frac{R_*}{a}\right).$$

In the case of these simulations, this gives an ingress/egress duration of only $\tau = 4.6$ minutes. As a comparison, the archetypal hot Jupiter HD 209458b (Charbonneau et al., 2000, Henry et al., 2000) has $\tau = 25.7$ minutes. Our simulations in this Section, thus, can be seen as *lower limits and/or very conservative estimates* on the detectability of the effect. We explore the variation of the precision on the limb asymmetries with ingress/egress duration along with a case-study of a real hot Jupiter in Section 4.5.

To perform the fits to our simulated data, we implemented `catwoman` (Jones & Espinoza, 2020) in the `juliet` (Espinoza et al., 2019) package, which already implements `batman` (Kreidberg, 2015) for symmetric lightcurve models, and allows us to compute

Bayesian evidences for our model comparison using MultiNest (Feroz et al., 2009) via the PyMultiNest wrapper (Buchner et al., 2014). Table 3.1 lists the prior distributions used in our experiments — we explain and detail each of those below.

3.3.1 Detecting asymmetric lightcurves with *JWST*

In order to perform the simulations for *JWST*-like observations, we needed to calculate a typical cadence for observations to be taken by the observatory for time-series exposures. In this work, we focus on observations aiming to constrain the effect using NIRISS/SOSS, as this instrument allows us to obtain spectra all the way down to 0.6 μm through the combination of data from Order 1 ($1 - 3$ μm) and 2 ($0.6 - 1$ μm). Given that the largest limb asymmetries seem to be in the transition between optical and NIR wavelengths (see, e.g., Kempton et al., 2017, Powell et al., 2019), we believe this will usually be the instrument of choice to characterise the effect for bright targets (with the alternative being, of course, NIRSpec/PRISM for fainter targets). Considering the reset time for this instrument is relatively short (couple of seconds), it sufficed for our work to know the typical integration time of a *JWST* observation with SOSS. For a solar-type, $V = 11$ star, according to the *JWST* Exposure Time Calculator[6] (ETC; Pontoppidan et al., 2016), "saturation" is attained at about 20-60 groups per integration for NIRISS/SOSS, which implies maximum integration times between 40-80 seconds per datapoint in the time-series. We arbitrarily decided to use 20 seconds for the cadence of our simulations in order to simulate observations trying to target half-saturation values, which has been a typical strategy for *HST* observations[7].

In this case we tried three different simulations, in order to illustrate the impact of different assumptions in this one-transit, 20-second cadence case: (a) one in which everything but the radii of both sides of the exoplanet $R_{p,1}$ and $R_{p,2}$ are known, (b) one in which everything but the radii and the the limb-darkening coefficients of the star are known, and finally (c) one in which everything but the radii, the limb-darkening coefficients of the star and the time-of-transit centre are known. The limb-darkening law that was assumed to generate and fit the lightcurves was a quadratic law with $(u_1, u_2) = (0.3, 0.2)$, which

[6] https://jwst.etc.stsci.edu/

[7] But see https://jwst-docs.stsci.edu/methods-and-roadmaps/jwst-time-series-observations/tso-saturation.

Table 3.1 | Priors and parameters used for our experiments in Section 3 for the `catwoman` model fits. The `batman` fits used similar priors, with the caveat that this model assigns a uniform radius for the entire planet R_p/R_* for which we use the same prior as for $R_{p,1}/R_*$ below, and doesn't fit for φ. $U(a,b)$ below stands for a uniform distribution between a and b.

Parameter	Prior	Comment
P (days)	—	Fixed to 1
T_0 (days)	$U(-0.1, 0.1)$	Fixed to 0 when assumed known.
$R_{p,1}/R_*$	$U(0,1)$	
$R_{p,2}/R_*$	$U(0,1)$	
φ (deg)	$U(-90, 90)$	Only used in Section 3.3.3. Fixed to 90 otherwise.
q_1[a]	$U(0,1)$	Fixed to 0.25 when assumed known.
q_2[a]	$U(0,1)$	Fixed to 0.3 when assumed known.
e	—	Fixed to 0
ω	—	Fixed to 90
a/R_*	—	Fixed to 10
b	—	Fixed to 0

[a] These parameters correspond to the parametrization presented in Kipping (2013) for sampling physically plausible combinations of the quadratic limb-darkening coefficients.

are representative values for solar-type stars. In our `juliet` fits, we assumed the uninformative priors for two-parameter limb-darkening laws proposed by (Kipping, 2013) for the cases in which limb-darkening was assumed to be unknown; for the time-of-transit centre, a uniform prior with a width of 4.8 hours around the real predicted time of transit centre was imposed. The results for these simulations are presented in Figure 3.3.

As can be observed from the simulations, the asymmetric transit lightcurves should be detectable (i.e., $\Delta \ln Z \gtrsim 2$) for morning-to-evening depth differences above around 25 ppm for a wide range of precisions at least in white-light (i.e., adding all the flux over the entire wavelength range of a given instrument), where *JWST* observations should achieve tens of ppm precision per point in the transit lightcurves, and as long as the ephemerides are well known and constrained. If they are not, however, as can be observed in the rightmost panel of Figure 3.3a, the actual detection of the effect becomes extremely challenging because, as it has been already noted by von Paris et al. (2016), changes in the time-of-transit centre in a symmetric model can account for the asymmetry in the lightcurve. The changes in this timing are very small — only a couple of seconds of shifts in the time-of-transit centre suffice to mimic the asymmetry in the transit lightcurves (see Section 3.4.3 for details). This implies that to detect this effect in white-light, very precise timings are needed in order to claim a detection.

It is important to note that although from the above results the detection of the effect *directly* in the white-light lightcurves even with *JWST*-like precisions seems relatively challenging to do with only one transit in the absence of precise timing constraints, the observatory has the advantage that it can perform spectro-photometry and, thus, the effect can be detected through the wavelength dependence of the radii at each side of the terminator region, as has already been highlighted by Powell et al. (2019) — see also Section 4.5. In particular, NIRISS/SOSS can produce extremely precise (tens of ppm) white-light transit lightcurves in Orders 1 and 2, which can be used to claim a detection of the effect using these white-light transit lightcurves alone at much higher significance levels (and thus be sensitive to much lower morning-to-evening depth differences) than the ones shown here. Lightcurves like these, in addition, should provide very precise morning and evening depths. Figure 3.3b and 3.3c show an example lightcurve fit on a 50 ppm-precision lightcurve, where the injected morning-to-evening depth difference was of 270 ppm. As can be seen in Figure 3.3b, both evening and morning depths are highly

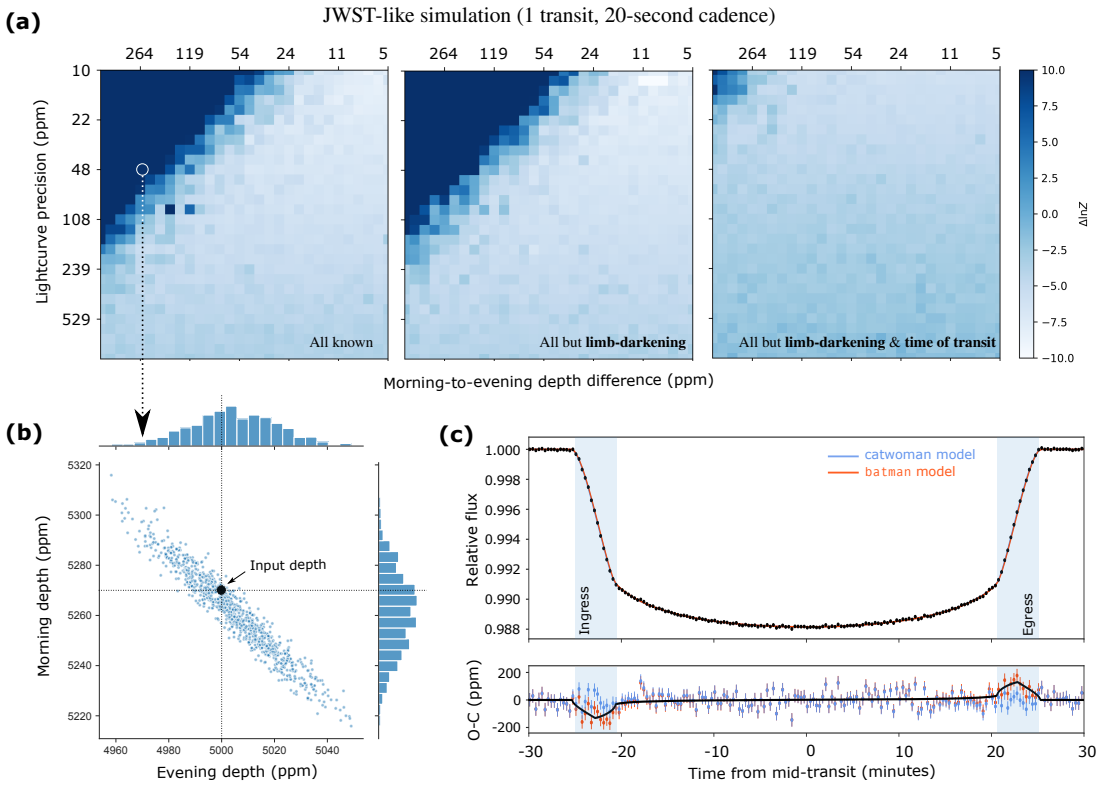

Figure 3.3 | **Injection and recovery simulations of asymmetric lightcurves due to differences in the morning and evening terminator for *JWST*-like cadence (1 transit, 20-second cadence, 1-day period, 4.6-minute ingress/egress duration).** **(a)** Detection map in the morning-to-evening depth difference versus lightcurve precision (both in ppm) map; darker regions show the detectability region of the effect when all the parameters other than the planetary radius is known (left), other than the planetary radius and limb-darkening (centre) and other than the planetary radius, limb-darkening and time-of-transit centre (right). Colours indicate the difference between the log evidences, $\Delta \ln Z$, of asymmetric (`catwoman`) models and symmetric (`batman`) models. Note how if the time-of-transit centre is unknown, detecting the effect gets very challenging. **(b)** Posterior samples of the morning and evening limb depths on an example lightcurve with 50 ppm precision and a morning-to-evening depth difference of 270 ppm; note the high correlation (but good recovery) of the limb depths; true input value is marked with dashed lines. **(c)** Simulated transit lightcurve corresponding to the posterior shown in (b); models (`batman` in orangered; `catwoman` in blue) are indistinguishable in the top panel; the residual panel, however, clearly shows the differences: the residuals using the `batman` model (orangered) show bumps at ingress and egress; the `catwoman` model residuals (blue) correctly model those bumps. The black line in the bottom panel shows the difference between the best-fit `batman` and `catwoman` models.

correlated, but nonetheless provide precise constraints in this case on each of about 16 ppm, giving in this case a retrieved morning-to-evening depth difference of $\Delta\delta = 257 \pm 32$ ppm — fully consistent with the input value[8]. Most of the information to constrain those depths come from ingress and egress, as is evident in the residuals (blue for `catwoman`, red for `batman`) of Figure 3.3c. We provide a deeper understanding on the relation between lightcurve precision and morning and evening depth precisions in Section 4.5.

3.3.2 Detecting asymmetric lightcurves with *TESS*

Although the *TESS* mission has a significantly smaller aperture than *JWST*, the cadence and types of observations the mission does are excellent for the detection of asymmetries in transit lightcurves. The mission not only attains an exquisite precision, but it is also able to observe several transits of the same exoplanet, mitigating the problem we observed with only one transit in *JWST*-like observations like the ones simulated in the previous subsection. We performed the same simulations that we did for *JWST* but with a *TESS*-like cadence of 2-minutes, where we only consider observations on a 27-day period (i.e., one *TESS* sector). Interestingly, the three cases that we tried in the previous sub-section (all known, all but limb-darkening known and all but limb-darkening and the time-of-transit centre known) all resulted in practically identical results — we show the one corresponding to the case in which all the parameters are assumed to be known but the radius, the limb-darkening coefficients and the time-of-transit centre in Figure 3.4.

As can be observed, the results are very similar to the ones of *JWST*. This is a combination of the fact that there is about a 27-fold increase in the number of transits, which helps with the 6-fold increase on the cadence of the observations as compared to the *JWST* ones. The fact that there are more transits, in addition, helps with the problem *JWST* will face related to the ephemerides where in our analysis, of course, there is an implicit assumption regarding no possible deviations from strict periodicity in the transit times. We reiterate, however, that our simple simulations in Section 3.3.1 did not consider the huge advantage that *JWST* has over *TESS* regarding the ability to measure wavelength-dependent transits, which should in turn break the degeneracy with the ephemerides as already suggested by Powell et al. (2019). We delve deeper into the benefits of wavelength-dependent *JWST*

[8]Note the precisions of each limb do not add in quadrature to the constraint on the limb-difference. This is expected, again, due to the correlation between each of the limb depths.

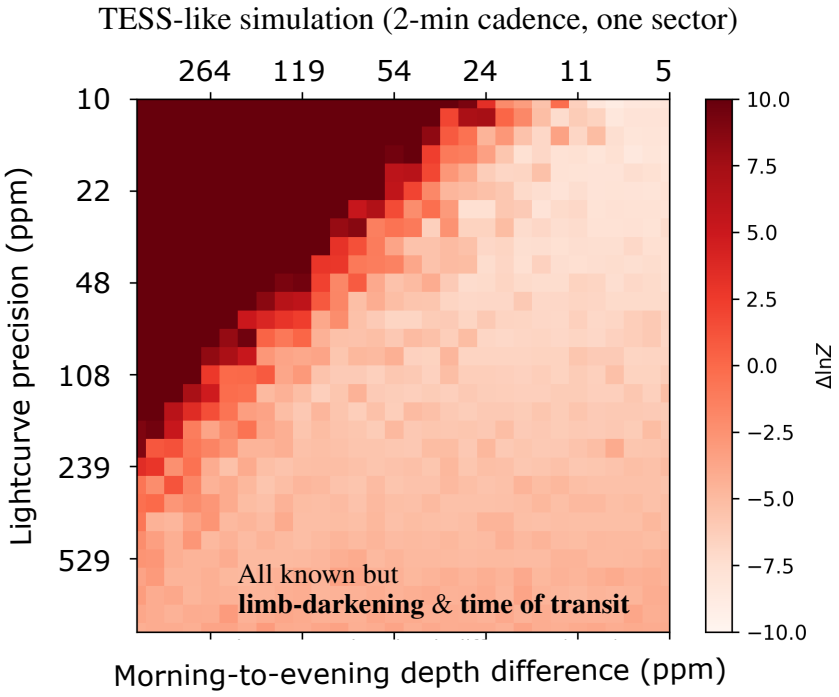

Figure 3.4 | Simulations of asymmetric lightcurves due to differences in the morning and evening terminator transmission spectra for *TESS*-like cadence (2-minute cadence, one sector, 1-day period, 4.6-minute ingress/egress duration) when all the parameters other than the planetary radius, limb-darkening and time-of-transit centre are known. Colours indicate the difference between the log evidences of asymmetric models and symmetric models (positive meaning odds ratios in favour of asymmetric lightcurve models).

transit observations for detecting the limbs of exoplanets in Section 4.5.

Although few targets attain the precisions at which one might statistically distinguish between an asymmetric and a symmetric model directly from the transit lightcurves with *TESS* in one sector, the fact that many targets are observed by more than one sector makes this effect within reach of what *TESS* is currently able to detect. Targets in the *JWST* Continuous Viewing Zone (CVZ) are particularly appealing to try to detect this effect. For example, WASP-62b (V = 10.3), for which the median per point precision was 880 ppm during the prime mission in 2-minute cadence, has been observed to date in more than 20 sectors, providing a combined per-point precision per transit of about at least $880/\sqrt{20} \approx 200$ ppm — a promising precision level to constrain the effect of asymmetric limbs if we assume a simulation like the one in Figure 3.4 also applies to an exoplanet like WASP-62b. The recent *HST* study by Alam et al. (2021) makes this target also particularly appealing to detect this effect, as the atmospheric retrievals performed on its spectrum point it to have a colder temperature ($\approx$ 800 K) than what is expected from its equilibrium temperature ($\approx$ 1400 K). This is one of the key hints that there might indeed be differences between the limbs of this exoplanet, as suggested by the work of MacDonald et al. (2020).

3.3.3 Detectability assuming φ is not known

As a final test on the detectability of the effect, we explore whether our ignorance on the angle φ can impact it; we take our *JWST*-like simulation as a proxy for studying this, given the similarity in the shape of the detectability maps presented between *JWST* and *TESS* in Figures 3.3 and 3.4. To explore this, we use a transit lightcurve whose parameters are defined by the same ones as in the previous experiments, but in this case we set $\varphi = 45$ degrees as the ground-truth, and set a uniform prior between -90 and 90 degrees for the parameter in our fits. Our results for a *JWST*-like simulation (using the same cadence as in Section 3.3.1) are shown in Figure 3.5 where in addition to the detectability map, we also show a portion of the posterior distribution of a simulation with the same properties as the one shown in Figure 3.3 for the case in which φ was fixed — i.e., a lightcurve precision of 50 ppm, and a morning-to-evening depth difference of 270 ppm.

As can be seen, the detectability region (i.e., the medium blue and dark-blue region) of the plot has shifted by a small amount with respect to the one presented in Figure 3.3

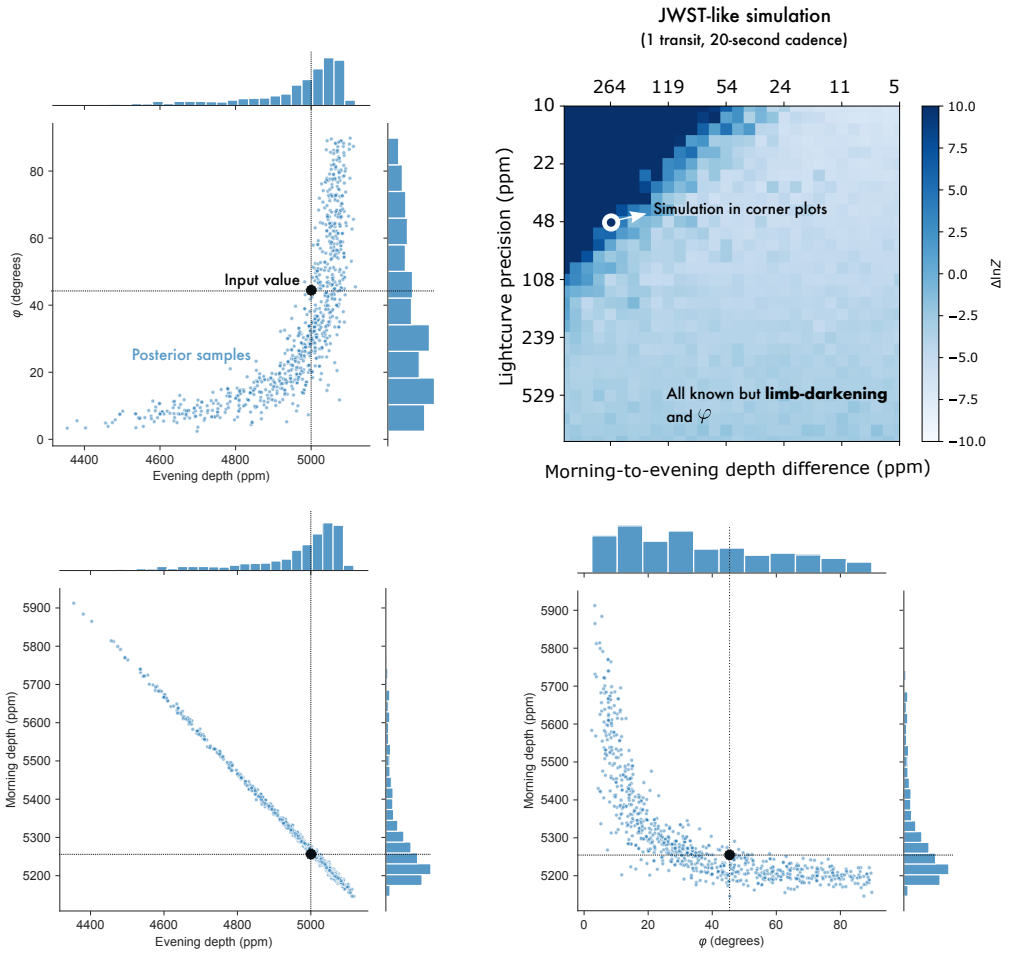

Figure 3.5 | **Simulations allowing for an unknown projected planetary spin angle, φ.** The simulations presented above are similar to those shown on the centre panel of Figure 3.3a, but this time also allowing for φ to be a free parameter. In addition to the detectability map, shown in the top right corner, we present a portion of the posterior distribution (which has two modes, allowing for both positive and negative values of φ; see text) of the limb depths and angle φ as corner plots for the very same limb difference (270 ppm) and lightcurve precision (50 ppm) as that shown in Figure 3.3 (indicated here as a white circle in the top right detectability plot. Black dot on the corner plots indicates the true input value.)

implying that a slightly better lightcurve precision is needed in order to detect the effect if the angle φ is not known a-priori. In addition, given our large prior on φ, we actually detect two posterior modes (of which we show only one in Figure 3.5): one allowing for positive and one allowing for negative values of φ, each swapping the posterior distributions between the evening and morning limb. This was expected by construction: a model with φ and a given value of $R_{p,1} = a$ and $R_{p,2} = b$ is the same as a model with $-\varphi$ with $R_{p,1} = b$ and $R_{p,2} = a$. If we take the mode with positive values for φ, we note that in this case the evening and morning depths themselves are much more uncertain. This gives rise to a retrieved morning-to-evening depth difference of 250^{+374}_{-113} ppm — again consistent, but much less precise than the constraint assuming a known value of φ presented in Section 3.3.1. The constraint on φ itself is also not very precise; for this particular simulation, we obtain $\varphi = 32^{+33}_{-20}$ degrees; fully consistent with the input value, but not very constraining to understand the underlying, true projected planetary spin-angle.

Before moving into the next Section, it is important to reiterate that the precisions and detectability limits shown here were obtained for a very conservative —worst-case scenario— system with a very small ingress/egress duration. As will be shown in Section 3.4.1, the odds of detecting the effect on systems which have better prospects for it (i.e., systems with longer ingress/egress durations) are in reality much higher. The lower limits we set here, thus, seem promising for the detection of the effect with current and near-future instrumentation.

3.4 Discussion

In previous sections, we have presented both the details of our semi-analytic framework for generating asymmetric transit lightcurves due to morning/evening terminator heterogeneities — including its validation against simpler (but more computationally expensive) models — and a study of the detectability of the effect with current missions like *TESS* and future observatories like *JWST*. Although our results are encouraging for the detection of the effect, there are many aspects to pay attention to when performing lightcurve analyses and/or when planning observations to detect the effect, including complementary methodologies, which we discuss below.

3.4.1 Asymmetric terminator depths precision

While in Section 3.3 we presented lower limits on the statistical detection of the effect on transit lightcurves based on bayesian evidences, an important aspect of interpreting transit lightcurve fits with the semi-analytic model presented in this work will involve constraining the actual measured transit depths of each side of the planet. This will be useful not only to extract transit spectra of the different limbs when using wavelength-dependent lightcurves such as the ones to be obtained by *JWST*, but also to compute the maximum possible transit depth differences allowed by the data when analysing broadband data such as the one from missions like *TESS*.

An important detail to consider when extracting transit depths from asymmetric limbs is the fact that the observable quantities that are directly constrained by the data are the areas of each of the semi-circles through the transit depths each of them produce. In symmetric models, where the limbs are assumed to be equal, the transit depth is simply $\delta = (R_p^2/R_*^2)$ — the projected area of the planet over the projected area of the star. In the asymmetric case, however, the projected area of the *semi-circles* are the quantities of interest, — the transit depth of each limb being given by $\delta_i = (1/2)(R_{p,i}^2/R_*^2)$. This is what effectively defines the transit spectrum of each limb and is, in turn, what should be used to compare against theoretical transmission spectroscopy models.

Figure 3.6 shows how the precision of the transit depths of each limb depend on the lightcurve precision, as well as the precision of the entire area of the planet, defined by the depth $\delta_1 + \delta_2$, for the case of the exoplanet simulated in Section 3.3 with an ingress/egress duration of $\tau = 4.6$ minutes (solid lines). As can be seen, the precision on the transit depth of the entire planet is always much smaller than the corresponding for both semi-circles, but the relationship between the two is not simple, as the transit depths of the semi-circles are highly correlated with each other. Indeed, the transit depth of the entire planet is constrained by *the entire lightcurve*, whereas the transit depths of each side of the planet (sampled by the semi-circles in our model) are mostly constrained by ingress and egress. This implies, in turn, that this latter precision would of course increase on systems with larger ingress/egress durations, which in many cases might be the optimal ones to target in order to maximise the chances to unveil this effect.

The simulations presented in Section 3.3 for $\tau = 4.6$ min. ingress/egress durations were performed to show lower-limits on the detection of the effect, and even in those

cases the odds were very favourable given current (e.g., *TESS*) and future (e.g. *JWST*) lightcurve precisions and cadences. Hot Jupiters typically have longer ingress/egress durations, and some of the already characterised ones by missions like, e.g., *HST*, show good prospects for the detection of the effect as well. As an example, we repeat the *JWST* simulations in Section 3.3 for HAT-P-41b, which we select as is one of the most thoroughly characterised ultra-hot Jupiters in transmission — all the way from near-UV, optical and up to near-infrared wavelengths (Wakeford et al., 2020, Lewis et al., 2020, Sheppard et al., 2021). We tune the physical and orbital parameters of the system to the ones used in Wakeford et al. (2020), which imply a 23.9 minutes ingress/egress duration. The cadence (53 seconds) and number of datapoints (500) for our simulations are set to the ones optimised by PandExo[9] (Batalha et al., 2017) using NIRISS/SOSS as the instrument of choice such that SUBSTRIP256 does not saturate (which would be the setup of choice in order to obtain simultaneous spectroscopy in the near-infrared and the optical through Orders 1 and 2 for this target[10]). For consistency, we set the limb-darkening coefficients to the average ones on Order 1 of NIRISS/SOSS (but we note these do not impact on the overall precision and detectability, as was already shown in Section 3.3). The resulting precisions of this experiment are presented in Figure 3.6 as dashed lines. As can be observed, the precision change on the transit depths of each of the limbs is significant, and ranges from a 60% to 70% improvement in it. The precision change in the transit depth of the entire planet, however, is much smaller (and driven mainly by the difference in the absolute transit depths and transit durations), which acts as a baseline in showing quantitatively how the prospects of detecting asymmetric limb-differences are very sensitive to the ingress/egress duration.

One might argue that in Figure 3.6, one could observe two transits of the exoplanet with 4.6 min. ingress/egress duration in order to match the signal-to-noise of the exoplanet with the 23.9 min. ingress/egress duration. Although this would be true if the observatory only targeted the transit event, in practice there are observational overheads (like, e.g., pre-post transit baselines, and overall observatory overheads beyond clock time on-target) that have to be included in that reasoning. For instance, the time recommended in the

[9] https://exoctk.stsci.edu/pandexo/

[10] We note HAT-P-41b saturates below about 2 microns with NIRSpec/PRISM, which is the reason why we don't discuss this instrument in the context of this exoplanet.

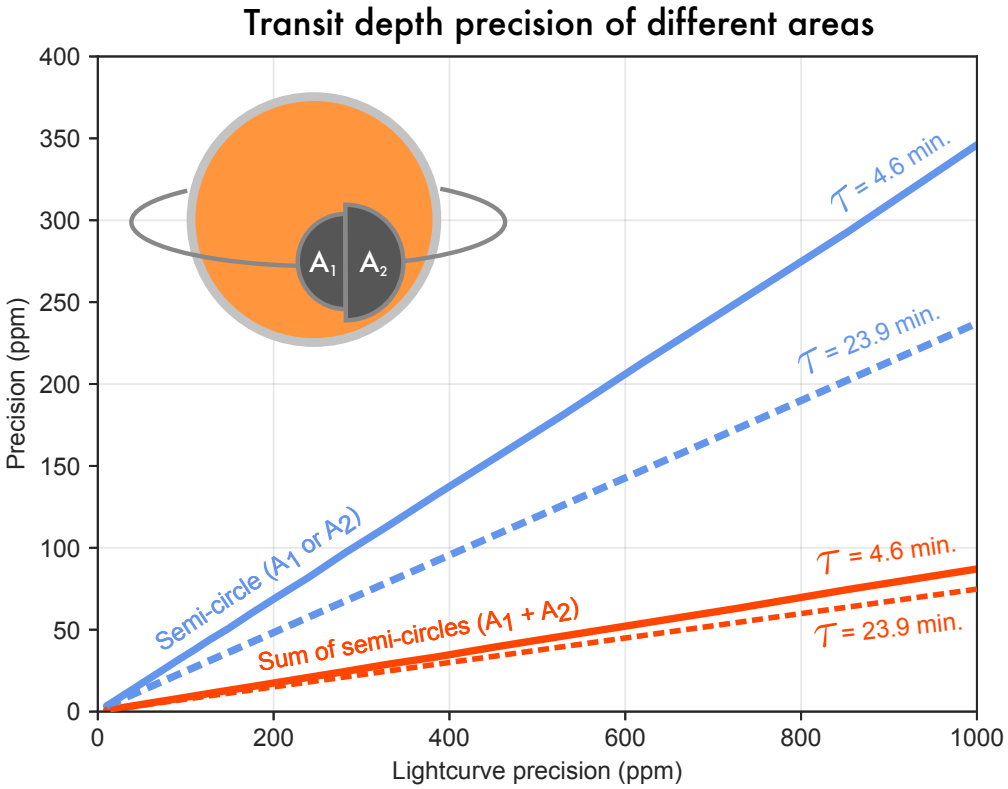

Figure 3.6 | Transit depth precision on the semi-circles (transit depth defined as $\delta_i = (1/2)(R_{p,i}/R_*)^2$, with $R_{p,i}$ being the area of semi-circle i; blue lines) and their sum (whose transit depth is $\delta_1 + \delta_2$; red lines) as a function of lightcurve precision. Precisions for systems with short (4.6 min., solid lines) and long (23.9 min., typical for hot Jupiters) transit ingress/egress durations, τ, are presented. **Main point:** Transit depth precisions of the limb of exoplanets are much less precise and much more dependant on transit ingress/egress duration than the transit depth produced by the entire area of the planet (i.e., the classically defined "transit depth").

JWST documentation[11] one should spend in a target during a transit is given by the dwell equation, which reads

$$T_{\rm dwell} = 0.75 + {\rm MAX}(2, T_{14}) + T_{14} + 1 \text{ hr}, \tag{3.4}$$

where T_{14} is the transit duration in hours. The exoplanet with an 4.6 min ingress/egress duration has a 1-hour total transit duration, which gives $T_{\rm dwell} = 4.75$. The exoplanet with a 23.9 min ingress/egress duration has a 3.6-hour transit duration, $T_{\rm dwell} = 8.95$. Two transits of the 1-hour transit duration target would imply a requested time of 9.5 hours, which is at least half an hour more expensive than the 3.6-hour transit duration target — all this without considering extra observatory overheads. The conclusion, thus, is that the efficiency of the time and targets to be requested to detect the effect have to be studied on a case-by-case basis.

In addition to the above, it is also important to note that the posterior distributions of the limbs show typically non-negligible correlations (see, e.g., Figures 3.3 and 3.5). This is important to consider because this covariance carries extra information that could become important when performing inference on the limbs (through, e.g., atmospheric retrievals). In our experiments, we observed the shape of the posterior distribution (measured through the correlation — i.e., the covariance divided by the standard deviations of the marginal posterior distribution of each limb) remained fairly constant across the parameter space covered in our work; it simply shrinks as better precisions are achieved. We also found the posterior distribution of the limbs is very well approximated in the case of a known angle ϕ by a two-dimensional gaussian distribution, which is characterised not only by the mean and standard deviation of the marginal posterior distributions, but also by the covariance between the limbs. We provide a practical example of how to use this information in a retrieval framework in the next sub-section.

3.4.2 The importance of constraining limb spectra

In order to showcase the importance of directly using transit lightcurves to constrain the limbs of exoplanets, and demonstrate that this indeed might be *the most efficient avenue to constrain the transit spectrum of the limbs*, we use HAT-P-41b as a case-study, using both real *HST* data and simulated *JWST* observations.

[11] https://jwst-docs.stsci.edu/

We first analyse the *HST* data presented in Wakeford et al. (2020), Lewis et al. (2020) and Sheppard et al. (2021). In particular, we take the HST/WFC3 (1.1-1.6 μm), STIS G430L (0.3-0.5 μm) and G750L (0.5-0.9 μm) data from Sheppard et al. (2021), and the WFC3 UVIS G280 (0.2-0.8 μm) data from Wakeford et al. (2020). In order to perform the atmospheric retrievals, we use the framework developed in MacDonald et al. (2020), namely, one in which the *transmission spectrum* is fit with a model using *two* different atmospheric structures, each of which represents one of the limbs. To this end, we use and slightly modify the "chemically consistent" `CHIMERA`[12] atmospheric retrieval framework of Line et al. (2013), such that two transmission spectra are modelled at each iteration of the algorithm. Each of those has a different temperature and cloud structure, as well as different C/O ratios; the temperature at the top of the atmosphere is forced to be always colder for one limb than for the other in order to simulate energy redistribution processes that might be happening between the limbs. Chemical equilibrium is assumed for each limb. Once those are computed, each model transit depth is multiplied by $1/2$ in order to compute the spectra of each of the limbs, δ_i. These are then added together to form the "combined" transit depth that we compare against the *HST* transit spectrum. We decide to leave the metallicity, the 10 bar radius, and the overall temperature-pressure profile shape (other than the temperature at the top at the atmosphere) as common parameters between the limbs, as we assume the *HST* data would not be sensitive to those parameters. We also only use the data at wavelengths longer than 0.35 μm, as the publicly available opacities within `CHIMERA` only go down to this particular wavelength range. The retrieval is performed using nested sampling with the the `pymultinest` library (Buchner et al., 2014) which makes use of the MultiNest (Feroz et al., 2009) algorithm. The full set of priors used for our `CHIMERA` atmospheric retrievals in what follows are presented in Table 3.2.

The best-fit retrieval to the *HST* data using this two-limb retrieval framework is presented on the top panel of Figure 3.7; the corresponding retrieved temperature-pressure profile is also presented in the left panel of Figure 3.8. Posterior credibility intervals for each parameter fit in the retrieval are presented in the second column of Table 3.3. As can be seen in Figure 3.7, while the retrieved transit spectrum follows the data fairly well, the individual retrieved limb spectra shows a wide range of possible solutions, suggest-

[12] https://github.com/mrline/chimera

Table 3.2 | Priors and parameters used for our Section 3.4.2 CHIMERA atmospheric retrievals. These are composed by two limbs, one forced to be colder than the other. $U(a, b)$ below stands for a uniform distribution between a and b. For detailed discussions on each parameter, see Line et al. (2013) for the general framework and Mai & Line (2019) for the implementation of the cloud model used in this work, which is that of Ackerman & Marley (2001).

Parameter	Prior	Comment
Parameters individual to each limb		
$T_{\rm irr}$ (K)	$U(1000, 2500)$	Stellar input at top of atmosphere.
$\log_{10} C/O$	$U(-2, 0.3)$	Log C/O ratio.
$\log_{10} K_{zz}$ (cm^2/s)	$U(5, 11)$	Log-eddy diffusion coefficient.
$f_{\rm sed}$	$U(0.5, 5)$	Sedimentation efficiency.
$\log_{10} P_{\rm base}$ (bar)	$U(-6, 1.5)$	Cloud base pressure.
$\log_{10} f_{\rm cond}$	$U(-15, -2)$	Cloud condensate mixing ratio at cloud base.
Parameters common to both limbs		
[M/H]	$U(-2, 3)$	Atmospheric metallicity.
f_R	$U(0.5, 1.5)$	Multiplicative factor to 10 bar "fiducial" radius.
$\log_{10} \kappa_{IR}$ (cm^2/g)	$U(-3, 0)$	T/P profile IR opacity.
$\log_{10} \gamma_1$	$U(-3, 0)$	Log visual-to-IR opacity.

ing that they are fairly unconstrained by the data. Indeed, the overall posterior values for all parameters are largely indistinguishable between the limbs. For example, the temperatures at the top of the atmosphere are 1210^{+227}_{-132} K and 1522^{+519}_{-241} K for the "cold" and "hot" limbs, respectively, which are completely consistent with each other. The rest of the parameters, while fairly unconstrained by the data, all point towards a cloudy nature in HAT-P-41b's atmosphere; our solution suggest a relatively high-altitude cloud-deck solution, whose base is at about 10 mbar — a picture in good agreement with the forward modelling performed in Lewis et al. (2020). While the retrievals in that work preferred a near-UV opacity source shaping the spectrum instead of clouds, most of these retrievals were done fitting the atomic and molecular abundances directly — without chemical constraints between them. The only chemical equilibrium retrieval performed in it needed a large temperature (> 2500 K) to be able to build up the necessary H^- opacity to explain the data better. The chemical equilibrium retrieval performed here, while including H^- opacity, is much more constrained in temperature as we didn't allow the possibility for the temperature at the limbs to exceed 2500 K. Nonetheless, while we see a possible second mode in the temperature posterior in Figure 3.7 where the hot limb can reach temperatures of about 2300 K, we see no buildup of posterior density above this range. While our retrieval could thus be interpreted as an alternative solution to the observed *HST* data, we don't discuss this in length here as the objective of this experiment was to only obtain *a* possible solution for a two-limb model given the *HST* data, in order to showcase the importance of constraining limb spectra with upcoming high-precision facilities, as we will illustrate and quantify below.

The next experiment we ran consisted of taking the median of all the parameters found from our two-limb retrieval of the HAT-P-41b *HST* data — i.e., the medians presented in the second column of Table 3.3 — and use the corresponding limb models implied by them to simulate a single *JWST* NIRISS/SOSS transit observation using the `catwoman` transit model introduced in this work. As in the last sub-section, we used PandExo to estimate the per-integration lightcurve precision for this transit observation, with which we simulated 608, 53-second integrations — i.e., a 8.95-hour exposure, the recommended time-on-target for *JWST* observations, obtained using equation 3.4. To generate the transit models at each wavelength, we used the same transit parameters used by Wakeford et al. (2020) with the exception of the radius for each limb, for which we use the model

described above. As for limb-darkening, we used the ExoCTK (Bourque et al., 2021) limb-darkening tool[13] to compute the limb-darkening coefficients of the quadratic law for orders 1 and 2 of NIRISS/SOSS.

We tackled the analysis of these simulated lightcurves in two different ways, in order to showcase why performing inference on the limb spectra is the best way to optimally extract information about the limbs of exoplanets. The first consisted of extracting *transit* spectra from them by simply fitting these lightcurves with `batman` lightcurve models, with the same procedure explained in Section 3.3.1. Then, we performed two-limb retrievals on this transit spectrum using the same modified `CHIMERA` atmospheric retrievals described above and performed on the *HST* data. The results of that experiment are presented in the middle panel of Figure 3.7, the retrieved pressure-temperature profiles are also shown in the middle column of Figure 3.8; posterior credibility intervals for each fitted parameter fit in the retrieval are presented in the third column of Table 3.3. As can be seen, these two-limb retrievals constrain much better the different limbs than the *HST* data, but still have a fairly large uncertainty, such that the retrieved limb spectra overlaps between the limbs at certain wavelengths. While the posteriors for most parameters are fairly wide (mainly due to the cloudy nature of this particular exoplanet), the temperature posterior distribution is much better constrained than the corresponding one for the *HST* data: they have uncertainties that are about 1 to 2-fold smaller for the cold limb and about 2 to 5-fold smaller for the hot limb.

Next, we performed the transit fitting using our `catwoman` model, again, using the same procedures as the ones outlined in Section 3.3.1; this allowed us to extract *limb spectra directly from the transit lightcurves*. In order to perform retrievals on these limb spectra, however, we had to slightly modify the log-likelihood of our retrievals because, as explained in the previous sub-section, for each wavelength bin the two limb depths are strongly correlated. We characterise the posterior distributions of the limb depths at each wavelength bin in our simulations as multivariate gaussians, which are described by covariance matrices Σ_w and mean vectors $\vec{\mu}_w = [\delta_{1,w}, \delta_{2,w}]$ for each wavelength w. The covariance matrices were estimated in the case of our fits by computing the sample covariance matrix of the posterior samples of the limb depths at each wavelength bin.

[13] https://exoctk.stsci.edu/limb_darkening

With this, the log-likelihood we use in our retrievals is given by:

$$\ln \mathcal{L} = -\frac{1}{2} \sum_{w} 2 \ln 2\pi + \ln |\Sigma_w| + \vec{r}_w^T \Sigma_w^{-1} \vec{r}_w$$

with $\vec{r}_w = \vec{\mu}_w - \vec{m}_w$ being the vector of residuals, with $\vec{m}_w$ being the vector containing the model limb spectra at the given wavelength bin w.

The results of performing the retrieval on the limb spectra directly using the framework described above are presented in the bottom panel of Figure 3.7, with the corresponding retrieved pressure-temperature profiles shown in the right column of Figure 3.8; posterior credibility intervals for each fitted parameter fit in the retrieval are presented in the fourth column of Table 3.3. As can be observed, the constraints on the limb spectra are much better than the ones obtained from fitting the transit spectra. The corresponding limb spectral models are much better differentiated by our retrievals, allowing us to tightly constrain any features that might arise in them. The temperature posteriors for the limbs are also much better constrained; in particular, there is a 2 to 4-fold precision increase on the temperature of the cold limb, and 3 to 8-fold precision increase in the hot limb when compared against the *HST* data. In addition, the correlation between the retrieved limb temperatures is much smaller for this limb retrieval, as can be observed on the posterior distribution presented in Figure 3.7. This tighter constraint on the temperature can also be visually observed in Figure 3.8, where the much tighter constraint in the temperature-pressure profile of each limb is illustrated as well. These results showcase that extracting and analysing limb spectra directly allows us to constrain much more tightly the properties of the limbs than methods that rely on extracting this information from "classic" transit spectra [14].

Aside from impacting directly on inferences made with atmospheric retrievals, as has been shown above, we would like to highlight that extracting limb spectra directly from transit lightcurves has an additional, unique benefit: it opens up the discovery space for atmospheric features that might be individual to each of the limbs. This, in turn, has the benefit of allowing a direct comparison against Global Circulation Models (GCM). GCM modelling assumptions and implementation details have been actively driven by observations in the past few years. For instance, until recently clouds and hazes were typically

[14]The full set of posterior samples for all parameters along with the data used to perform the retrievals can be found in the following Github repository: https://github.com/nespinoza/hat-p-41b-retrieval-posteriors

Table 3.3 | Posterior credibility intervals (C.I.) of the two-limb retrieval made on real *HST* data and simulated *JWST/NIRISS* data of HAT-P-41b. C.I. below correspond to medians and 68% credibility bands around it. For details on the definition for each parameter and priors, see Table 3.2.

Parameter	Posterior C.I. (transit spectrum, *HST*)	Posterior C.I. (transit spectrum, *JWST*[a])	Posterior C.I. (limb spectra, *JWST*[a])
Parameters for the "cold" limb			
$T_{\rm irr}$ (K)	1210^{+227}_{-132}	1197^{+130}_{-115}	1237^{+59}_{-70}
$\log_{10} C/O$	$-0.85^{+0.56}_{-0.65}$	$-0.98^{+0.42}_{-0.57}$	$-0.99^{+0.42}_{-0.56}$
$\log_{10} K_{zz}$ (cm^2/s)	$7.9^{+1.7}_{-1.6}$	$8.0^{+1.9}_{-1.9}$	$7.7^{+1.9}_{-1.7}$
$f_{\rm sed}$	$3.4^{+1.6}_{-1.7}$	$3.4^{+1.6}_{-1.7}$	$3.3^{+1.8}_{-1.7}$
$\log_{10} P_{\rm base}$ (bar)	$-2.1^{+1.9}_{-1.9}$	$-1.9^{+2.1}_{-2.5}$	$-1.8^{+2.1}_{-2.6}$
$\log_{10} f_{\rm cond}$	$-7.0^{+3.1}_{-4.5}$	$-9.3^{+3.6}_{-3.5}$	$-9.2^{+3.9}_{-3.5}$
Parameters for the "hot" limb			
$T_{\rm irr}$ (K)	1522^{+519}_{-241}	1592^{+94}_{-108}	1567^{+66}_{-76}
$\log_{10} C/O$	$-0.68^{+0.50}_{-0.78}$	$-1.16^{+0.49}_{-0.52}$	$-1.23^{+0.51}_{-0.48}$
$\log_{10} K_{zz}$ (cm^2/s)	$8.0^{+1.7}_{-1.7}$	$7.8^{+2.0}_{-1.8}$	$7.8^{+2.1}_{-1.8}$
$f_{\rm sed}$	$3.1^{+1.6}_{-1.5}$	$3.3^{+1.7}_{-1.6}$	$3.3^{+1.7}_{-1.7}$
$\log_{10} P_{\rm base}$ (bar)	$-2.5^{+2.0}_{-1.9}$	$-1.9^{+2.1}_{-2.5}$	$-1.9^{+2.1}_{-2.5}$
$\log_{10} f_{\rm cond}$	$-8.0^{+3.8}_{-4.0}$	$-9.1^{+3.7}_{-3.6}$	$-9^{+3.8}_{-3.7}$
Parameters common to both limbs			
[M/H]	$2.06^{+0.24}_{-0.37}$	$2.02^{+0.036}_{-0.041}$	$2.022^{+0.037}_{-0.039}$
f_R	$1.0276^{+0.0072}_{-0.0087}$	$1.0273^{+0.0017}_{-0.0027}$	$1.0276^{+0.0014}_{-0.0022}$
$\log_{10} \kappa_{IR}$ (cm^2/g)	$-2.23^{+0.51}_{-0.50}$	$-1.92^{+0.75}_{-0.61}$	$-2.32^{+0.57}_{-0.43}$
$\log_{10} \gamma_1$	$-1.57^{+0.72}_{-0.81}$	$-1.74^{+0.77}_{-0.75}$	$-1.76^{+0.95}_{-0.80}$

[a] The *JWST* simulations had as underlying true values the medians from our *HST* retrievals.

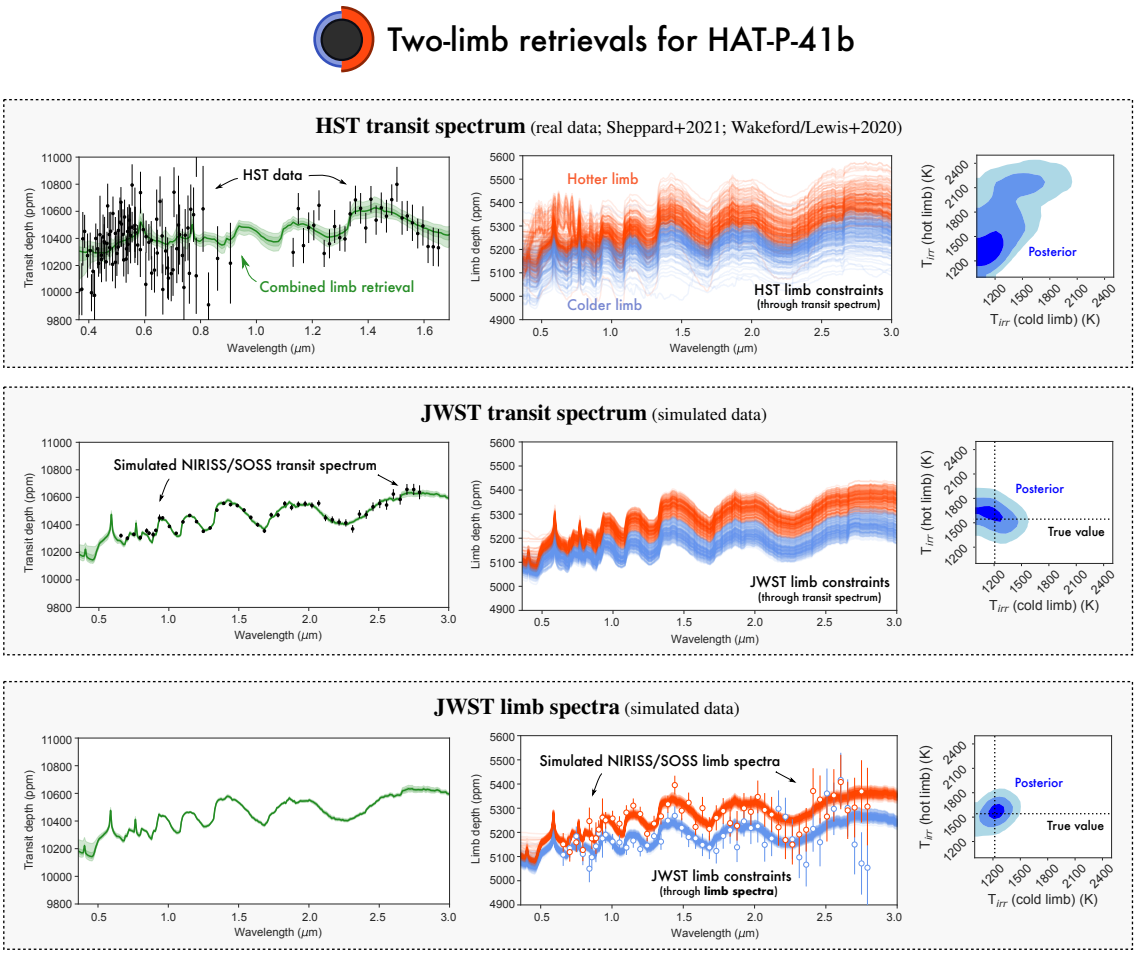

Figure 3.7 | **Two-limb retrievals made on real *HST* and simulated *JWST* data.** (*Top*) Observed transit spectrum by *HST* STIS (< 1.0 μm) and *HST* WFC3/IR (> 1.0 μm; black points with errorbars) of HAT-P-41b presented in Wakeford et al. (2020), Lewis et al. (2020) and Sheppard et al. (2021), along with the retrieved transit spectrum (left; green bands representing the 68% and 95% credibility intervals), 200 random draws from the posterior retrieved limb models (middle) and posterior distribution of the temperatures of those limbs (right). (*Middle*) Same, but for two-limb retrievals made on a simulated *JWST* NIRISS/SOSS transit spectrum. (*Bottom*) Same, but for a retrieval made on the *limb spectra*, extracted directly from simulated transit lightcurves. See text for details. **Main point:** Retrievals made directly on limb spectra (bottom panel) constrain much better the limb models than retrievals made on "classic" transit spectra (top and middle panels).

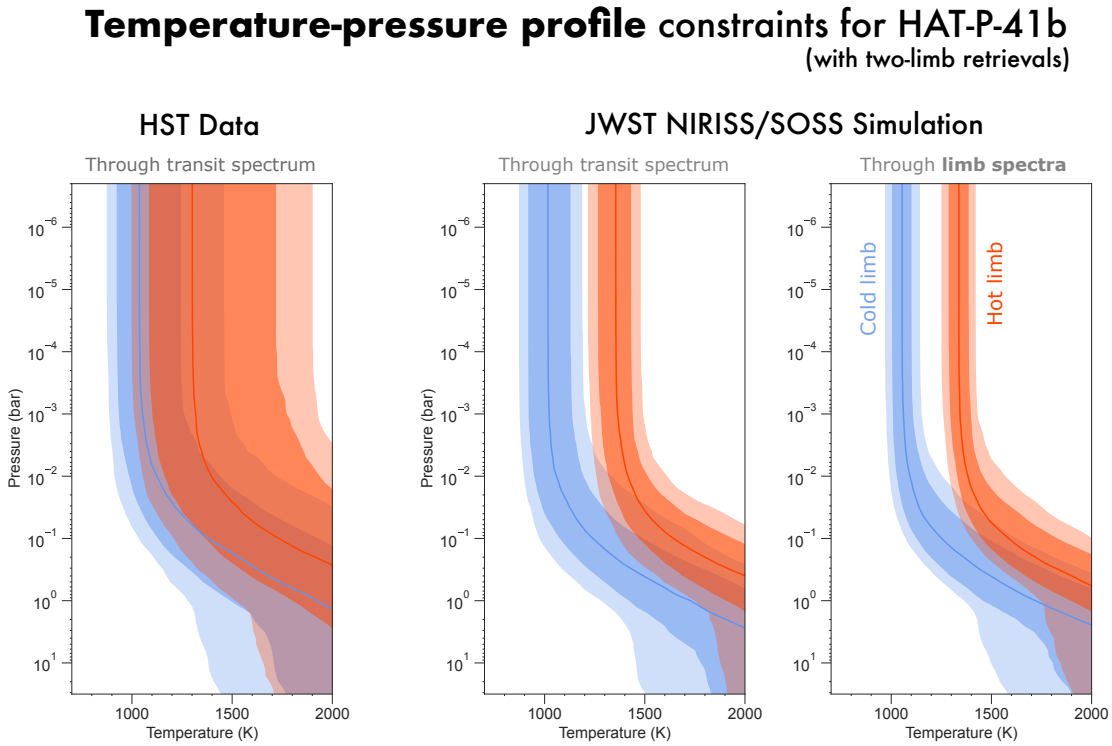

Figure 3.8 | **Retrieved HAT-P-41b temperature-pressure profiles from two-limb retrievals**. (*Left*) Profiles for the cold (blue) and hot (red) limbs for the two-limb retrievals performed on *HST*'s transit spectrum, show in Figure 7 (top panel). (*Middle*) Profiles for the same limbs and retrieval performed on the simulated *JWST*'s transit spectrum, shown in Figure 7 (middle panel). (*Right*) Profiles for the same limbs as for the middle panels, but performed on *JWST*'s ***limb*** spectra, shown in Figure 7 (lower panel). **Main point:** limb retrievals extracted through limb spectra provide much more precise temperature-pressure profiles for each limb at the pressures probed by transit spectroscopy ($\sim$ 1 mbar).

added in a post-processing stage, not including feedback from these components in the modelling. Recent works such as those of Roman & Rauscher (2019) and Parmentier et al. (2021) have managed to implement clouds in their GCMs directly, showing in turn that this is critical to understand the overall cloud structure itself and heat redistribution in the planets under study, which has provided a much better match to observed phase-curve observations. We believe the study of limb spectra can open up a similar set of insights providing key advancements in the overall modelling of exoplanetary atmospheres.

From an observational perspective, it is interesting to consider that observations aiming to extract these limb spectra can be much cheaper than, e.g., phase-curves. Whereas a single NIRISS/SOSS transit for HAT-P-41b, for instance, would amount to a total science time to a *JWST* proposal of about 8.95 hours (using Equation 3.4), a full phase-curve for this particular exoplanet requires over 65 hours. In this sense, extraction of limb spectra could serve as a good diagnostic as to what to expect in a phase-curve observation *before* performing these expensive observations. Since for a fixed planetary and stellar radii the ingress/egress duration increases with the square-root of the semi-major axis (i.e., $\tau \propto \sqrt{a}$), this technique for detecting limb asymmetries might in turn be an excellent alternative avenue to studying morning and evenings of longer period planets where phase-curve signals are too small to be detectable in a reasonable amount of time.

3.4.3 Timing variation biases due to asymmetric terminator depths

In Section 3.3 we discussed how, as predicted by von Paris et al. (2016), small changes in the time-of-transit centre can give rise to equally good fits on symmetric models (such as the ones assumed by the `batman` package, for instance), even if the data is truly arising from an asymmetric transit model (although this limitation can be bypassed if the aim is to retrieve limb spectra by simultaneously fitting transit lightcurves at different wavelengths; see, e.g., Powell et al., 2019). It is important to note that this in turn can give rise to biases in transit times if a symmetric model is used when the data in fact comes from an asymmetric model such as the one modelled by the `catwoman` library. In our simulations, these can give rise to timing offsets of up to 5 seconds, which is in turn within the timing precision that the *TESS* mission is able to reach, and will be for sure within reach of the *JWST* mission. Care must be taken, thus, when searching for small (second-level) timing offsets in these precise transit lightcurves in the search of, e.g., transit timing variations.

3.4.4 Limitations of this study

It is important to note that throughout this work, we have assumed that the only alternative model to that of limb asymmetries is that of a symmetric limb in order to explain transit lightcurves asymmetries. However, there are other competing effects that might give rise to asymmetric lightcurves as well. For instance, known stellar effects such as gravity darkening (see, e.g., Ahlers et al., 2020, and references therein) and yet-to-be uncovered effects/properties such as exoplanetary rings (see, e.g., Rein & Ofir, 2019, and references therein) can also give rise to asymmetric lightcurves. Performing a detailed model comparison study between these effects and the one studied here is out the scope of this work, but we warn researchers that proper care must be taken when aiming to claim the detection of asymmetric limbs in light of these possibilities. While effects like, e.g., gravity darkening are most likely known at good enough precisions in order to understand when a given transit lightcurve might be asymmetric due to this effect or at the very least to put limits on asymmetries generated by it, known unknowns such as exoplanetary rings might be more complicated to rule out. Perhaps the easiest way to constrain this would be through the wavelength-dependence of these asymmetries, which we hypothesise should be markedly different in the case of exoplanetary rings and those produced by opacity sources in an exoplanetary atmosphere. Still, it is important to be mindful of these alternative hypotheses when analysing data on the search of these lightcurve asymmetries.

In addition to the above, the very validity of the framework developed here — i.e., fitting transit lightcurves with a model of two "stacked", rotated semi-circles — remains to be put to the test with real data, and has plenty of room for improvement as we increase the precision of our measurements. For instance, our model assumes a sharp discontinuity at the poles, whereas some GCMs actually predict smooth transitions at them (see, e.g., Pluriel et al., 2020, and references therein), even suggesting morning and evening terminators might be *themselves* asymmetric. While a path in the right direction, our model is just an approximation to reality by construction, as those simplifications were the ones that allowed us to create a modelling scheme that is fast and efficient to apply to real transit lightcurve data. We expect that the detection of the signatures of mornings and evenings on actual, precise transit lightcurves from *TESS* or *JWST* could indeed motivate more flexible and accurate models for their shapes guided by GCM modelling (or the data themselves) that could expand on the simple modelling scheme discussed in this work.

While these shapes might be complex enough that simple geometrical arguments like the ones made in this work would most likely not be easy to make, making the problems hard to parametrize, we are hopeful that good ideas might flourish in the exoplanet community to make this happen. There currently exists a continuum of lightcurve analysis methods ranging from few-number-of-parameter but constrained models like ours to very flexible but large-number-parameter models like the shadow imaging technique presented in Sandford & Kipping (2019). We believe expanding our model in the direction discussed above lies in between those methodologies, and is thus bounded — and therefore approachable. Developing this idea further, however, is outside the scope of this work.

3.5 Conclusions

In this work, we have presented a detailed study on the observational prospects of directly detecting transit lightcurve asymmetries due to inhomogeneous exoplanetary limbs with current and near-future instrumentation. A semi-analytical framework was introduced in Section 3.2 to fit transit lightcurves in order to extract the transit depths of the different limbs, a problem which is approximated as a pair of stacked semi-circles of different radii transiting a limb-darkened star following von Paris et al. (2016). Implemented in the `catwoman` python library (Jones & Espinoza, 2020), this framework allows for the fast computation of these lightcurves, which are even able to model the rotation of the axis that joins the semi-circles, being thus able to characterise sky-projected planetary spin-orbit misalignmements in a complementary fashion to that allowed by the eclipse mapping technique for both lightcurves (Rauscher et al., 2007, Williams et al., 2006) and radial-velocities (Nikolov & Sainsbury-Martinez, 2015).

A detailed feasibility study was presented in Section 3.3 for detecting the effect with current existing facilities such as *TESS* and near-future observatories such as *JWST*. Even in a worst-case scenario of a planetary transit with a very small ingress/egress duration (which is the portion of the lightcurve that mainly constrains the limbs), the prospects for detecting the effect are very promising, even considering our ignorance on the angle that defines the sky-projected planetary spin-orbit misalignment. If aiming at detecting the effect with only one transit, however, care must be taken as the time of transit centre is highly degenerate with the limb asymmetries (i.e., a small shift in the time-of-transit can

give rise to a similarly good fit to that of an asymmetric lightcurve due to inhomogeneous limbs).

Finally, we showed in Section 4.5 how important the transit ingress/egress duration is for the detection of the effect. We used HAT-P-41b as a case-study to showcase the prospects for extracting the spectra of each of its limbs, and concluded that analysing the lightcurves directly with the methods presented in this work might be one of the most efficient ways to obtain a global picture of each of the limbs, with *JWST*-like precisions enabling the extraction of their spectra given the exquisite spectrophotometric precision the observatory will be able to achieve.

We believe the promise of being able to characterise the limbs of exoplanets could play a pivotal role in our understanding of the 3-dimensional structure of exoplanets, and could provide observations that can inform current (e.g., GCM, transmission spectroscopy models) and future (e.g., phase-curves) models and observations aimed at the characterisation of exoplanet atmospheres. The technique might, in turn, be a much less time-demanding technique to probe the 3D structure of longer period exoplanets, where phase-curves can be prohibitively expensive. Overall, we believe exploring the detectability of the effect in real transit lightcurves is critical to understand the limitations of the technique of transit spectroscopy when it comes to interpreting structural profiles such as temperature/pressure profiles and abundances in a 1-dimensional fashion (MacDonald et al., 2020). This, in turn, will be fundamental to make claims regarding formation mechanisms of these exoplanets based on the latter (Öberg et al., 2011, Espinoza et al., 2017, Mordasini et al., 2016), and their overall dependence with planetary properties (see, e.g., Sing et al., 2016, Welbanks et al., 2019, and references therein).

Appendix

3.A Deriving ΔA

In order to derive the decrement of flux due to the transit of a pair of stacked semi-circles given by equation 3.2, we must find ΔA, the inter-sectional area between the stacked semi-circles and the iso-intensity band depicted in Figure 3.1. As already noted by Kreidberg (2015) in the case of a circle, this area is simply the inter-sectional area of the stacked semi-circles with the circle of radius x_i, $A(x_i, R_{p,1}, R_{p,2}, d, \varphi)$, minus the same inter-sectional area but with the circle of radius x_{i-1}, $A(x_{i-1}, R_{p,1}, R_{p,2}, d, \varphi)$, i.e.,

$$\Delta A = A(x_i, R_{p,1}, R_{p,2}, d, \varphi) - A(x_{i-1}, R_{p,1}, R_{p,2}, d, \varphi).$$

This implies that to find ΔA one has to first find a general form for the inter-sectional area between the stacked semi-circles and a circle. These stacked semi-circles, in turn, are composed of two semi-circles, and thus the problem reduces to calculating the area of the intersection between a circle and two (rotated) *semi-circles* with a common centre: one of radius $R_{p,1}$ and another of radius $R_{p,2}$, but rotated by 180 degrees. Given a general formula for such intersection, $A_S(R, R_S, d, \theta)$, where R is the radius of the circle, R_S the radius of the semi-circle, d the distance between the centre of the circle and the semi-circle and θ the rotation angle of the semi-circle with respect to d, then

$$A(x, R_{p,1}, R_{p,2}, d, \varphi) = A_S(x, R_{p,1}, d, \varphi) + A_S(x, R_{p,2}, d, \varphi + \pi).$$

If we find a general form for $A_S(\cdot)$, then we solve the problem. We tackle this problem in the next sub-section.

3.A.1 Intersection area between a circle and a semi-circle

Although the case of calculating the intersection area between two circles can be obtained via elemental trigonometry, the problem of calculating the intersection area between a

circle and a (rotated) *semi*-circle is not, in general, as straightforward.

We first note that the problem of finding the intersection area of a circle of radius R and a semi-circle of radius R_S rotated by an angle θ with respect to the line that joins the centres of length d is the same problem as the intersection area of a semi-circle and a *circle rotated by an angle θ with respect to the line that joins the centres*. This symmetry argument allows us to put the horizontal axis of this problem in the base of the semi-circle, simplifying the notation of the problem. Without loss of generality, we put the origin in the centre of the base of the semi-circle. This transformed geometry of the problem is shown in Figure 3.9; here the white dashed area inside the semi-circle is the area of interest (i.e., the one that leads to $A_S(R, R_S, d, \theta)$).

As is evident in Figure 3.9, there are three different cases (a, b and c) we have to take care of in order to find a general formula for $A_S(R, R_S, d, \theta)$:

- Case (a), divided into sub-cases (a-1), (a-2) and (a-3), deals with the problem in which the circle is rotated such that it lies above the semi-circle. If we identify the coordinates of the centre of the circle as $(x_0, y_0) = (-d\cos\theta, d\sin\theta)$, case a) deals with the problem in which $\theta > 0$ and, thus, $d\sin\theta > 0$. Here, the intersection points between the circle and the semi-circle have coordinates (a_1, b_1) and (a_2, b_2). The geometry depicted in Figure 3.9 for this case implies that $b_1 = 0$. This is because for $b_1 > 0$, the problem is the same as the intersection of two circles (one of radius R and another of radius R_S), which has a known analytical solution (see, e.g., Kreidberg, 2015). Here the area of interest, A_S, is given by the area of the semi-circle ($\pi R_S^2/2$) minus $A_1 + A_2$ for case (a-1) and by $A_1 + A_2 + A_3$ for cases (a-2) and (a-3). The different sub-cases depend, in turn, on the location of the intersection points and the position of (a_3, b_3), the position of the maximum extension of the circle in the x-axis.

- Case (b) deals with the problem in which the circle is rotated such that it lies *below* the semi-circle, i.e., where $\theta < 0$ and, thus, $d\sin\theta < 0$. In addition, this case handles only problems in which one intersection of the circle with the semi-circle is in its base and the other is with the upper part of the semi-circle. Once again, the intersection points between the circle and the semi-circle have coordinates (a_1, b_1) and (a_2, b_2). In this case, however, $b_2 = 0$; the cases in which $b_2 \neq 0$ (i.e., when the right-most intersection is on the upper part of the semi-circle) and in which $b_2 = 0$

and $b_1 = 0$ (i.e., in which the left-most intersection is also on the base of the semi-circle) is taken care of by case c). The area of interest for case (b) is $A_S = A_1 + A_2$.

- Finally, case (c), divided into sub-cases (c-1), (c-2) and (c-3), deals with the problem in which the circle is either rotated above or below the semi-circle, but where there are two intersections with both either in the base (c-1) or in the upper part of the semi-circle (c-2) or four intersection points (c-3) between the circle and the semi-circle. In this case, the area of interest, A_S can be calculated directly via basic trigonometry and thus we don't identify here the intersection points by coordinates but by the red points in order to guide the reader.

Cases (a), (b) and (c) defined above will all be calculated assuming that the centre of the circle is to the left of the semi-circle. The reason for doing this is that the problem has reflective symmetry with respect to the line that goes through the centre of the semi-circle and that is perpendicular to its base. As such, for $0 < \theta < \pi/2$ we have that $A_S(R, R_S, d, \theta) = A_S(R, R_S, d, \pi - \theta)$, whereas for $-\pi/2 < \theta < 0$, $A_S(R, R_S, d, \theta) = A_S(R, R_S, d, \theta - \pi)$. In what follows, we solve each of the cases separately.

3.A.1.1 Case (a)

Before looking at the integrals that lead to the intersection area between the circle and the semi-circle in this case, let us obtain the expressions for the intersection points (a_1, b_1) and (a_2, b_2). To do this, we first note that the point where the circle intersects with the line $y = 0$ (which is the line that passes through the base of the semi-circle) is given by

$$x_{\rm int} = -d\cos\theta \pm \sqrt{R^2 - d^2\sin^2\theta}. \tag{3.5}$$

If the discriminant of this expression is negative (or zero), which in this case implies that $|d\sin\theta| \geq R$, then there is no (or one) intersection of the circle with the x-axis. In this case, the intersectional area can either be zero if $d \geq R + R_S$ or equal to solving the problem of the intersection between two circles of radius R and R_S in the case in which $d < R + R_S$. If the latter case is true, in turn, the intersectional area reduces to πR^2 when $d + R < R_S$ (i.e., when the circle is inside the semi-circle).

If $|d\sin\theta| < R$, then we have two solutions for the intersection points of the circle and the x-axis, $x_{\rm int}$. The cases in which both solutions are inside the semi-circle, i.e., when $|x_{\rm int}| \leq R_S$, will be handled in case (c), as depicted in Figure 3.9. If both solutions are

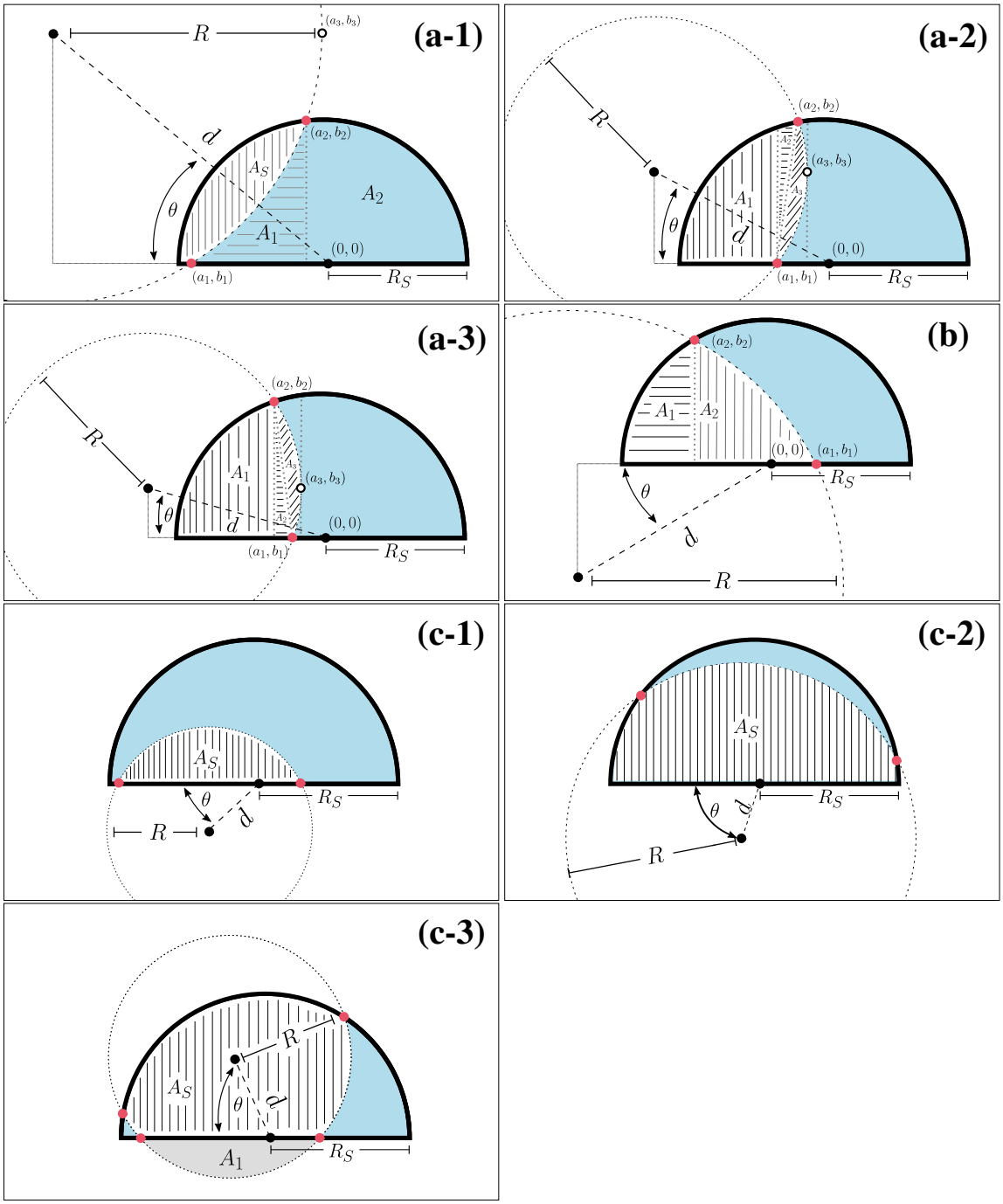

Figure 3.9 | Transformed geometry of the problem — we chose to rotate the circle of radius R around the semi-circle of radius R_S by an angle θ. This problem is the same as having the semi-circle rotated with respect to the line that joins the centres (of length d) by an angle θ. The general problem can, in turn, be divided in three cases: (a) when the centre of the circle is above the base of the semi-circle (divided, in turn in sub-cases a-1, a-2 and a-3), (b) when the centre of the circle is below the base of the semi-circle and the intersection points are not both touching the base or the edge of the semi-circle and (c) when there are two (c-1) or more (c-2) simultaneous intersection points with either at the edge or at the base of the semi-circle; this latter case can be solved using basic trigonometry. In all cases, the intersection points between the semi-circle and the circle are indicated by red dots. In all cases, the area of interest is the white dashed one inside the semi-circles.

outside the semi-circle, i.e., when $|x_{\rm int}| > R_S$, there are two possibilities. If $d \geq R + R_S$, the intersection area is zero — in this case, the circle is always to the left of the semi-circle. If, on the other hand, $d < R + R_S$, then because the intersections with the x-axis happen outside the semi-circle, there are two options: either the circle intersects twice with the upper part of the semi-circle (a case that will be solved in case (c-2)) or the circle covers all of the semi-circle, in which case the intersectional area is $\pi R_S^2/2$. If $\theta > 0$, then this leaves us, finally, with the problem we will solve for case (a) (is this is not true then case (b) will apply), in which $x_{\rm int}$ has both one solution outside and another one inside the semi-circle. Because here we are dealing with the cases in which the centre of the circle is always to the left of the centre of the semi-circle, this implies that the intersection point inside the semi-circle will always be the right-most intersection point, i.e., the solution of $x_{\rm int}$ with the positive sign. In the notation of Figure 3.9, this gives the intersection points

$$\begin{aligned} a_1 &= -d\cos\theta + \sqrt{R^2 - d^2\sin^2\theta}, \\ b_1 &= 0. \end{aligned}$$

The intersection point between the upper part of the semi-circle and the circle, (a_2, b_2), is obtained by simply equating the equation of the circle $((x + d\cos\theta)^2 + (y - d\sin\theta)^2 = R^2)$ with the equation of the semi-circle, taking it as a full circle $(x^2 + y^2 = R_S^2)$ to begin with. This yields

$$b_2 = -A\sin\theta + \cos\theta\sqrt{R_S^2 - A^2}, \tag{3.6}$$

$$a_2 = b_2\tan\theta + \frac{A}{\cos\theta}, \tag{3.7}$$

where

$$A = \frac{R^2 - R_S^2 - d^2}{2d}.$$

As we are not dealing with two intersecting circles, but an intersecting circle and semi-circle, we have chosen the largest b_2 which will give rise to the a_2, and therefore the point of intersection, that is on the semi-circle.

Finally, an important set of coordinates to define are the ones for (a_3, b_3). As illustrated in Figure 3.9, these are the coordinates of the maximum value attained in the x-axis by the circle. The coordinates for this point are, evidently,

$$\begin{aligned} a_3 &= -d\cos\theta + R, \\ b_3 &= d\sin\theta. \end{aligned}$$

First, we take on **case (a-1)**. This case occurs when the conditions for case (a) are met and when the point (a_3, b_3) is *outside* the semi-circle, which in turn implies in this case that $b_3 \geq b_2$. To solve it, the strategy to obtain A_S is to compute analytic solutions to the areas A_1 and A_2 depicted in Figure 3.9, and then subtract these to $\pi R_S^2/2$. First, A_1 is simply the area under the curve of the circle from $x = a_1$ to $x = a_2$. Because in this case $a_1 < a_2 < a_3$, we are going to integrate the lower part of the circle; this implies the equation of the (in this case semi) circle is simply

$$y = -\sqrt{R^2 - (x + d\cos\theta)^2} + d\sin|\theta|.$$

Integrating this from $x = a_1$ to $x = a_2$ yields

$$A_1 = \frac{R^2}{2}\Delta f + d\sin|\theta|(a_2 - a_1), \tag{3.8}$$

where $\Delta f = f(a_1) - f(a_2)$, with

$$f(x) = \left(\frac{x + d\cos\theta}{R^2}\right)\sqrt{R^2 - (x + d\cos\theta)^2} + \arcsin\left(\frac{x + d\cos\theta}{R}\right).$$

Next, we work on obtaining area A_2. This is simply the area under the curve of the semi-circle, whose equation is $y = \sqrt{R_S^2 - x^2}$. Integrating this from $x = a_2$ to $x = R_S$ yields

$$A_2 = \frac{R_S^2}{2}\left[\frac{\pi}{2} - h(a_2)\right], \tag{3.9}$$

where

$$h(x) = \arcsin\left(\frac{x}{R_S}\right) + \frac{x}{R_S}\sqrt{1 - \frac{x^2}{R_S^2}}.$$

Thus using the definitions for A_1 given in equation (3.8) and for A_2 given in equation (3.9), area A_S is given in this case by

$$\boxed{A_S = \frac{\pi R_S^2}{2} - \frac{R^2}{2}\Delta f - d\sin|\theta|(a_2 - a_1) - \frac{R_S^2}{2}\left[\frac{\pi}{2} - h(a_2)\right]}.$$

Now, we take on **case (a-2)**. In this case $b_3 < b_2$, however, $a_2 > a_1$. In this case, the area of interest is $A_S = A_1 + A_2 + A_3$, as depicted in Figure 3.9. First, area A_1 in this case is the area of the semi-circle from $x = -R_S$ to $x = a_1$. Integrating once again the equation of the semi-circle ($y = \sqrt{R_S^2 - x^2}$) in this range one obtains

$$A_1 = \frac{R_S^2}{2}\left[h(a_1) + \frac{\pi}{2}\right]. \tag{3.10}$$

Area A_2 in this case can be calculated as the area under the same semi-circle between $x = a_1$ and $x = a_2$ *minus* $b_2(a_2 - a_1)/2$, which is the area of the triangle formed between the points (a_1, b_1), (a_2, b_2) and $(a_2, 0)$. Integrating the semi-circle between $x = a_1$ and $x = a_2$ and subtracting $b_2(a_2 - a_1)/2$, we obtain

$$A_2 = \frac{R_S^2}{2}\left[h(a_2) - h(a_1)\right] - \frac{b_2(a_2 - a_1)}{2}. \tag{3.11}$$

Finally, area A_3 reduces to obtaining the segment of a circle generated by drawing a chord between points (a_1, b_1) and (a_2, b_2). To this end, we ought to know the angle α (in radians) these points make with respect to the centre of the circle. This can be easily obtained by the Law of Cosines to give

$$\alpha = \arccos\left(1 - \frac{(a_2 - a_1)^2 + b_2^2}{2R^2}\right).$$

With this, the area of the segment A_3 is thus, simply

$$A_3 = \frac{R^2}{2}\left(\alpha - \sin\alpha\right). \tag{3.12}$$

Finally, then, using the definition for A_1 in equation (3.10), for A_2 in equation (3.11) and for A_3 in equation (3.12), we get in this case

$$\boxed{A_S = \frac{R_S^2}{2}\left[h(a_2) + \frac{\pi}{2}\right] - \frac{b_2(a_2 - a_1)}{2} + \frac{R^2}{2}\left(\alpha - \sin\alpha\right)}.$$

Finally, we solve **case (a-3)**. In this case again $b_3 < b_2$, however, $a_1 > a_2$. Here, equation (3.10) also applies for A_1, but the upper limit of the integral is in this case a_2 instead of a_1. This implies that in this case

$$A_1 = \frac{R_S^2}{2}\left[h(a_2) + \frac{\pi}{2}\right]. \tag{3.13}$$

To obtain area A_2 in this case, we note that here this is simply the area of the triangle formed by the points with coordinates (a_1, b_1), (a_2, b_2) and $(a_2, 0)$. In this case, thus,

$$A_2 = \frac{b_2(a_1 - a_2)}{2}. \tag{3.14}$$

Finally, to obtain A_3 we use equation (3.12) which also applies for this case. Using then the definition for A_1 in equation (3.13), for A_2 in equation (3.14) and for A_3 in equation (3.12), we get in this case

$$\boxed{A_S = \frac{R_S^2}{2}\left[h(a_2) + \frac{\pi}{2}\right] + \frac{b_2(a_1 - a_2)}{2} + \frac{R^2}{2}\left(\alpha - \sin\alpha\right)}.$$

3.A.1.2 Case (b)

Case (b) is similar in many ways to case (a), with the only difference that now the coordinates of the centre of the circle change to $(-d\cos\theta, -d\sin|\theta|)$, and thus some functions and integration ranges change signs. In this case, the intersection points of the circle with the x-axis are the same as the ones given in equation (3.5), and thus all of the discussion given at the beginning of the past sub-section also applies for case (b). In particular, the intersection points (a_1, b_1) and (a_2, b_2) derived for case (a) are the same for this case.

In this case, the area of interest is the sum of area A_1 and A_2. The former is the integral of the semi-circle circle from $x = -R_S$ to $x = a_2$, which is an integral which was already found in equation (3.13). As for area A_2, this is the integral of the upper part of the circle of radius R, i.e., of the function

$$y = \sqrt{R^2 - (x + d\cos\theta)^2} - d\sin|\theta|.$$

However, the integral of this from $x = a_2$ to $x = a_1$ is exactly the same integral calculated in case (a-1), whose result is on equation (3.8), because the integrand there was the same integrand that we have here but multiplied by -1, and the limits of integration there were reversed with respect to the ones we have here (i.e., they went from a_1 to a_2) — because inverting the limits of integration is the same as calculating the integral multiplied by -1, both effects cancel out. Thus, area A_2 in our case is area A_1 in case (a-1). Thus, for case (b), we have that $A_S = A_1 + A_2$, i.e.,

$$\boxed{A_S = \frac{R_S^2}{2}\left[h(a_2) + \frac{\pi}{2}\right] + \frac{R^2}{2}\Delta f + d\sin|\theta|(a_2 - a_1)}.$$

3.A.1.3 Case (c)

Case (c) focuses on when $|d\sin\theta| < R$, i.e. there are two solutions for the intersection points of the circle with the line $y = 0$.

More specifically, **case (c-1)** occurs also when $|x_{\text{int}}| \leq R_S$, i.e. when the two solutions for the intersection points are inside the semi-circle and when the part of the circle above the intersection points is completely enclosed within the semi-circle (see Figure 3.9). This can be quantitatively described by theoretically 'extending' the semi-circle into a full circle of radius R_S. The coordinates of intersection of these two circles (setting the centre of the circle of radius R_S at the origin) can be found by substituting $x^2 + y^2 = R_S^2$

into $(x + d\cos\theta)^2 + (y + d\sin\theta)^2 = R^2$ to give the y coordinates:

$$y = -A\sin\theta \pm \cos\theta\sqrt{R_S^2 - A^2},$$

where

$$A = \frac{R^2 - R_S^2 - d^2}{2d}.$$

This is similar to equations 3.6 and 3.7 except the position of the circles relative to the origin have been changed slightly.

Therefore case (c-1) applies when $|x_{\rm int}| \leq R_S$ *and either*:

- There is no solution for the intersection of the two circles. This will occur when $A^2 > R_S^2$.
- Both of the y-coordinate solutions are real and negative, i.e. when $-A\sin\theta \pm \cos\theta\sqrt{R_S^2 - A^2} < 0$.

Case (c-2) occurs when $|x_{\rm int}| > R_S$ and when there are two intersection points on the curved edge of the semi-circle. For this case, the y-coordinates of intersection between the circle R and the full circle of radius R_S must be positive. Using the same equations as above, this is when $-A\sin\theta \pm \cos\theta\sqrt{R_S^2 - A^2} \geq 0$, where A is defined as in case (c-1).

Case (c-3) occurs when $|x_{\rm int}| \leq R_S$ and when there are two further intersection points on the curved edge of the semi-circle, making a total of four intersections points. Therefore case (c-3) is when $|x_{\rm int}| \leq R_S$ and $-A\sin\theta \pm \cos\theta\sqrt{R_S^2 - A^2} \geq 0$.

To solve case (c-1), the points of intersection in the base of the semi-circle can be obtained via equation 3.5:

$$x_{\rm int}^{\pm} = -d\cos\theta \pm \sqrt{R^2 - d^2\sin^2\theta}.$$

The problem is then just calculating the area of the segment A_S which is a well-known geometric problem with the solution

$$\boxed{A_S = R^2\arccos\left(\frac{y}{R}\right) - xy,}$$

where

$$\begin{aligned} x &= (1/2)(x_{\text{int}}^{+} + |x_{\text{int}}^{-}|), \\ &= \sqrt{R^2 - d^2 \sin^2\theta}, \\ y &= -d \sin\theta. \end{aligned}$$

To solve case (c-2), the problem can be set up by first theoretically 'extending' the semi-circle into a full circle of radius R_S and calculating the area of intersection of the two circles using the equations described in Kreidberg (2015):

$$A_{\text{int}} = R^2 \arccos u + R_S^2 \arccos v - (1/2)\sqrt{w}, \tag{3.15}$$

where

$$\begin{aligned} u &= (d^2 + R^2 - R_S^2)/(2dR), \\ v &= (d^2 + R_S^2 - R^2)/(2dR_S), \\ w &= (-d + R + R_S)(d + R - R_S)(d - R + R_S)(d + R + R_S). \end{aligned}$$

Using A_{int}, one can find A_S by subtracting half the area of the 'extended' circle of radius R_S to yield

$$\boxed{A_S = A_{\text{int}} - \pi R_S^2/2.}$$

To solve case (c-3), the problem needs to be split up into two parts. The first part involves finding the area of intersection, A_{int}, of the circle and the semi-circle 'extended' into a full circle of radius R using the same method from part (c-2) and the second involves finding area A_1. As can be seen from the Figure 3.9, once these two areas are found, it is simply a matter of subtracting A_1 from A_{int} to find A_S.

To find A_1 is a very similar problem to case (c-1), the points of intersection along the base of the semi-circle can be found using equation 3.5 and then the problem reduces to that of finding the area of a segment, which is A_1 in this case. Following a similar method for case (c-1),

$$A_1 = R^2 \arccos\left(\frac{-y}{R}\right) + xy,$$

where x and y are defined the same as for case (c-1), however note change in sign of y, due to the change of orientation of the shapes. As mentioned, A_{int} is the same as in case (c-2) and is described in equation 3.15.

Therefore the total intersection area A_S, is given by

$$\boxed{A_S = A_{\text{int}} - A_1}$$

3.A.2 Deriving θ

In this paper we have defined θ as the angle between the base of the semi-circle and the line that extends from the base of the semi-circle to the centre of the circle (of length d). Importantly, θ is defined as *positive* when extending clockwise, assuming the centre of the circle is to the left of the semi-circle which, as explained in section 3.A.1, due to the symmetry of the problem, can always be achieved by flipping the frame of reference.

θ is calculated from parameters that correspond to how the system physically appears in the sky. To explain, we place the centre of the star at the origin of a 2-dimensional Cartesian coordinate system. Due to the symmetry of the star, the planet is assumed to move from left to right (horizontally) across it so that the dY/dX gradient of the direction of motion of the planet at t_0 (inferior conjunction) is 0 (planet moves along the X-direction only). This coordinate system is *different* from the frame of reference used in section 3.A.1 when the frame is rotated so that the centre of the base of the semi-circle is at the origin and the base lies along the y=0 axis.

θ therefore depends on the angle the semi-circle is rotated through with respect to the X-direction in the 2D system defined above, ϕ, the impact parameter, b and whether the semi-circle is originally to the left or the right of the centre of the circle. The latter is characterised by the time, t and the time of inferior conjunction, t_0 and by assuming the planet moves from left to right. It is important to note that ϕ will be static if the planet moves in an almost straight line across the star (along the X-direction only). However due to orbital mechanics, the orbital path may appear curved and as such the planet will rotate slightly as it crosses the star. This rotation will perturb ϕ in such a way as discussed in 3.A.3.

ϕ is defined in this paper between the range $-\pi/2$ to $\pi/2$, from the X-axis to the base of the *top* semi-circle, where a positive angle is defined going in the anticlockwise direction. Once this is used to find the θ for $R_{p,1}$, to obtain the θ for $R_{p,2}$, one simply has to multiply θ by -1, due to the change in direction.

Table 3.4 shows how θ is calculated for the different values of ϕ, b and t for $R_{p,1}$.

Table 3.4 | θ calculation procedure, given different values of ϕ, b and t for $R_{p,1}$

t	b	ϕ	θ
$\leq t_0$	positive	$< \arccos b/d$	$-\phi - \arcsin b/d$
		$\geq \arccos b/d$	$-\pi + \phi + \arcsin b/d$
$\leq t_0$	negative	$\leq -\arccos \lvert b\rvert/d$	$\pi + \phi - \arcsin \lvert b\rvert/d$
		$> -\arccos \lvert b\rvert/d$	$-\phi + \arcsin \lvert b\rvert/d$
$> t_0$	positive	$< -\arccos b/d$	$-\pi - \phi + \arcsin b/d$
		$\geq -\arccos b/d$	$\phi - \arcsin b/d$
$> t_0$	negative	$\leq \arccos \lvert b\rvert/d$	$\phi + \arcsin \lvert b\rvert/d$
		$> \arccos \lvert b\rvert/d$	$\pi - \phi - \arcsin \lvert b\rvert/d$

3.A.3 Change in ϕ and the impact parameter of the semi-circle as a function of phase due to orbital mechanics

Using the same coordinate system as described in 3.A.2, if the planet were to move in a straight line across the star, then the planet's impact parameter, b, would stay constant at the value of the impact parameter defined at t_0 (the time of inferior conjunction). From Seager (2010) this is defined as

$$b = \frac{a\cos i}{R_{star}}\left(\frac{1-e^2}{1-e\sin\varpi}\right), \tag{3.16}$$

where a is the semi-major axis, i is the inclination of the orbit, e is the eccentricity, ϖ is the longitude of periastron and $R_{\rm star}$ is the radius of the star. However due to the orbital motion of the planet around the star, from the perspective of our X-Y system, the orbital path of the planet is curved across the sky, and so the impact parameter becomes a function of time. For the most accurate model, b used in the equations in 3.4 should be adjusted to

$$b = -r\sin(\omega + f)\cos i, \tag{3.17}$$

where

$$r = \frac{a(1-e^2)}{1+e\cos f}, \tag{3.18}$$

$$\cos f = \frac{\cos E - e}{1 - e\cos E}, \tag{3.19}$$

$$E - e\sin E = \frac{2\pi}{T}(t - t_0). \tag{3.20}$$

T is the orbital period of the planet, t is the current time of interest and t_0 is the time of periastron passage. The last equation can be solved numerically using a Newton-Raphson method.

Furthermore, due to the change in gradient of the planet's orbit with respect to this coordinate system, the angle between the base of the semi-circle and the X-axis will change slightly as it passes across the star. Because of how the method of deriving θ from ϕ is configured, we need this changing angle at every time-step instead of using the original 'static' ϕ. The change in angle caused by this movement will be labelled ψ and should be added to the original ϕ to create an 'updated' ϕ_{new}. To derive ψ and make it clearer, b has been re-labelled to y, where x and y are the coordinates of this 2D system with the centre of the star at (0,0). By differentiating,

$$\mathrm{d}y = -r\cos(\varpi + f)\cos i\,\mathrm{d}f. \tag{3.21}$$

Also explained in Seager (2010), the x-coordinate of the centre of the semi-circle will move as

$$x = -r\cos(\varpi + f), \tag{3.22}$$

and so

$$\mathrm{d}x = -r\sin(\varpi + f)\,\mathrm{d}f. \tag{3.23}$$

Therefore ψ can be calculated from

$$\tan\psi = \frac{\mathrm{d}y}{\mathrm{d}x}, \tag{3.24}$$

$$\psi = \arctan[\cot(\varpi + f)\cos i]. \tag{3.25}$$

Then, ϕ should be adjusted so that

$$\phi_{new} = \phi_{old} + \psi \tag{3.26}$$

Software used: `NumPy` (Harris et al., 2020), `Scipy` (Virtanen et al., 2020), `Matplotlib` (Hunter, 2007), `batman` (Kreidberg, 2015), `juliet` (Espinoza et al., 2019), `catwoman` (Jones & Espinoza, 2020).

Chapter 4

Enceladus and Jupiter as exoplanets: the opposition surge effect

This chapter has been submitted to A&A as **Jones, K. D.**, Morris, B. M. and Heng, K. (in review), *Enceladus and Jupiter as exoplanets: the opposition surge effect*.

The light that we receive from an exoplanet can be a mixture of the thermal emission from the planet and reflected light from the star. In Chapter 2, we investigated the thermal emission and temperature maps of the atmosphere of an ultra-hot Jupiter, and in Chapter 3, we looked at how transmitted light through a planet's atmosphere can give us amazing insights in to the 3D atmospheric structure and composition of a planet. However, this is only half the story. As we have discussed, modelling all aspects of the phase curve is essential to maximising our knowledge of exoplanet climates.

Assuming an atmosphere is present, the stellar light reflected by the planet back into space is dependent on many properties of the planetary atmosphere, including, but not limited to, composition, opacity, temperature and pressure. It also unlocks information about the probability a molecule will scatter light, as opposed to absorb it, at a specific wavelength (single-scattering albedo) as well as the directionality of the scatter (scattering asymmetry parameter, see Section 1.4.2). If there is no atmosphere, then the reflection depends on the type and terrain of the surface. To build up a 'grand-unified scattering model', we need to understand all the physics that goes into reflection mechanisms, for different types of planets. For a logical first step (which is often overlooked), we can turn to the Solar System objects for insights. It is reasonable to assume we will never achieve the precision of the observations of Solar System objects, especially for those

like the Moon where we have taken real samples of the lunar soil. However, we *can* artificially remove dimensions from our Solar System observations and images to mimic those that we take of exoplanets and use this data as a 'ideal-case' test for our exoplanet models. There are caveats to this, however. Mainly, the type of exoplanets we are able to study and observe are much closer to their host stars and have much higher equilibrium temperatures than the Solar System planets. However, with new infrared instruments, we are beginning to probe planets with smaller radii. Therefore, this work is important to understand the different physical sources to our observed planetary signals before we turn to the more difficult task of analysing Earth-like planets.

Abstract

Planets and moons in our Solar System have strongly peaked reflected light phase curves at opposition. In this work, we produce a modified reflected light phase curve model and use it to fit the Cassini phase curves of Jupiter and Enceladus. This "opposition effect" is caused by shadow hiding (particles/rough terrain cast shadows which are not seen at zero phase) and coherent backscattering (incoming light constructively interferes with outgoing light). We find tentative evidence for coherent backscattering preference in Jupiter compared to shadow hiding, and no evidence of preference in Enceladus. We show that the full-width half-maximum (FWHM) of Jupiter's opposition peak is an order of magnitude larger than that of Enceladus and conclude that this could be used as a solid-surface indicator for exoplanets. We investigate this and show that modelling the opposition peak FWHM in solid-surface exoplanets would be unfeasible with JWST or the Future Habitable Worlds Observatory due to the very large signal-to-noise required over a small phase range.

4.1 Introduction

For over a century, observations have shown that phase curves of many Solar System bodies have sharp peaks in reflectance at opposition. It has also been shown that the moons and rocky planets produce narrower peaks than the gas giants (see, e.g. Sudarsky et al., 2005, Dyudina et al., 2016).

Two underlying mechanisms driving the "opposition effect" are: shadow hiding (SH) and coherent backscattering (CB). Shadow hiding, first theorised in von Seeliger (1887), occurs on rough surfaces, for example, a rocky planet or moon. When illuminated near quadrature, the roughness casts shadows, reducing the illuminated area and the total reflected light. Close to zero phase, the particles/rough terrain hide their own shadow and the body gets much brighter when viewed face-on. As this involves the shadows cast by the incoming light, this effect only works with singly-scattered light. The second mechanism is coherent backscattering. This is an effect that works with both singly and multiply-scattered light. As described thoroughly in Hapke (2002), CB occurs when the light is scattered in such a way that it coherently interferes with the incoming light and therefore the observer views an increase in brightness near zero phase. This effect can

only occur in an inhomogeneous particulate medium where the particles have very high single-scattering albedos (ratio of scattering to absorption) and the particles have radii similar to the wavelength of the incoming light (Helfenstein et al., 1997).

For exoplanets, observing a phase curve is a crucial tool in characterising a planetary atmosphere. With new space and ground-based telescopes coming online, we can begin to probe smaller, more Earth-like planets. These cooler planets require us to observe in the optical to obtain a reflected-light phase curve. Due to all the possible signals which contribute to the overall phase curve, modelling these observations can be difficult and significant inhomogeneities can be detected (see, e.g. Morris et al., 2024). Therefore understanding the signals within phase curves and being able to model them correctly is crucial for the investigations of planetary atmospheres and origins.

If it were possible to detect the opposition effect in exoplanet phase curves, could this reveal surface and/or atmospheric information? In this paper we develop our own opposition effect phase curve model (Section 4.2.2) and test it with multi-wavelength phase curves of Jupiter and Enceladus (see Section 4.3). In Section 4.3.3, we investigate the differences between the full-width half-maximum of the opposition peak in Jupiter and Enceladus. In Section 4.4.1 we look at whether this feature could be used as a solid-surface exoplanet detector. We detail the caveats and further interpretations in Section 4.5.

4.2 Methods

4.2.1 Jupiter and Enceladus Cassini Data

We use multi-wavelength phase curves of both Jupiter and Enceladus previously published by Li et al. (2018) and Li et al. (2023), which reported images and combined reflectance phase curves taken with Cassini/ISS, Cassini/VIMS, and the Hubble Space Telescope (HST). Figure 4.1 shows these Jupiter phase curves as a function of wavelength. Due to the limited number of images taken by the Cassini flyby, the phase coverage is not homogeneous. We limit the dataset to Jupiter phase curves with sufficient phase coverage by removing phase curves with fewer than 40 datapoints. Figure 4.2 shows the Enceladus phase curves. By eye it is possible to detect, particularly for Enceladus, the sharp increase in the reflected light flux near zero phase.

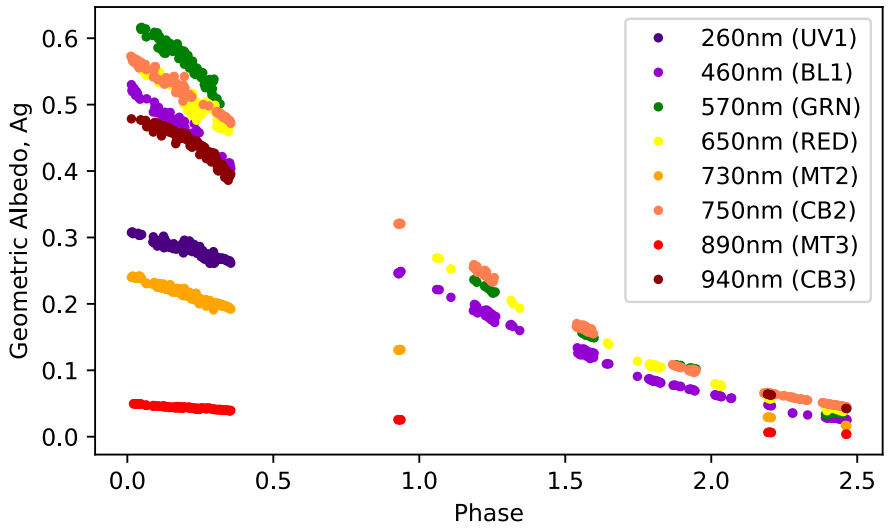

Figure 4.1 | Jupiter Cassini phase curves from Li et al. (2018), with their corresponding colour filter used in this analysis. The datapoint colours are a crude guide for the different wavelengths of the filters. The raw error bars from the original dataset are plotted but not visible. In our fitting routine we include a scaling factor to adjust these uncertainties.

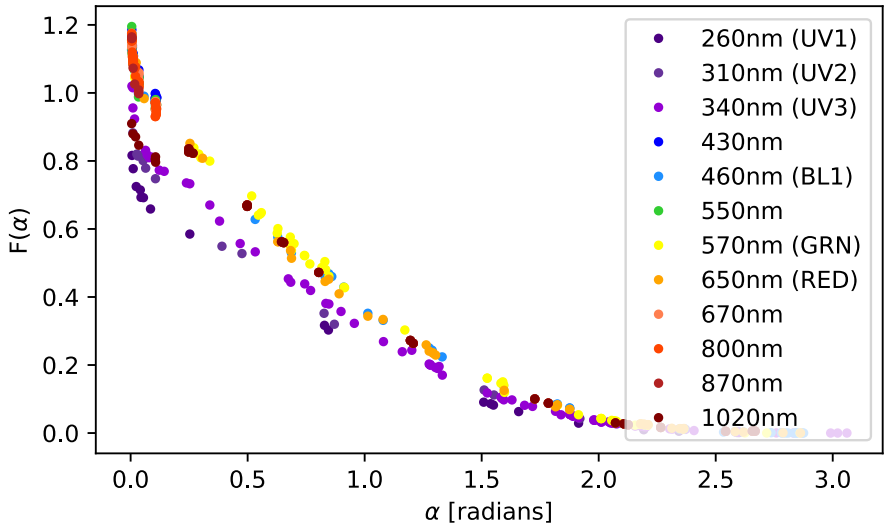

Figure 4.2 | Enceladus Cassini phase curves from Li et al. (2023), with their corresponding colour filter used in this analysis. The datapoint colours are a crude guide for the different wavelengths of the filters. Some of the filters do not have alternative names. The raw error bars from the original dataset are plotted but not visible. In our fitting routine we include a scaling factor to adjust these uncertainties.

4.2.2 Reflected light phase curve model

To fit these phase curves, we use the reflected light phase curve model developed in Heng et al. (2021), and recently applied to more planets in Morris et al. (2024). This is a unique model that can produce closed-form phase curve solutions for any scattering phase function specified by the user, making it flexible enough for both exoplanets and Solar System objects. The model is analytic and has few free parameters, allowing for fast computing time during model-fitting within a Bayesian inference framework.

Following Heng & Li (2021), we model reflected light phase curves with a single Henyey-Greenstein scattering phase function:

$$P(\alpha) = \frac{1 - g^2}{(1 + g^2 + 2g\cos\alpha)^{3/2}}, \tag{4.1}$$

where g is the scattering asymmetry parameter, and α is the orbital phase angle. This phase function allows for both forward and backward scattering in variable amounts and limits the number of free parameters in the model.

The reflected light phase curve model describes the reflected flux as a function of phase $F(\alpha)$. We introduce an opposition peak following Hapke (2002) by multiplying an additional term $(1 + \delta_{\rm opp})$ so the reflected flux is:

$$F = F_\star A_g \Psi(\alpha)\left(1 + \delta_{\rm opp}(\alpha)\right), \tag{4.2}$$

where $F_\star$ is the stellar flux, A_g is the geometric albedo, Ψ is the integral phase function and $\delta_{\rm opp}(\alpha)$ depends on the mechanism for the opposition surge.

There are two possible origins for the opposition peak: shadow hiding (SH) and coherent backscattering (CB). Hapke (2002) notes that the correction term associated with SH should act only on singly scattered light, whereas CB acts on both singly and multiply scattering light. However, Hapke (2002) also notes the similarity of the SH and CB formulae and recommends that the entire opposition effect be modelled by the SH formula alone. For this reason, we apply the correction term to both singly and multiply scattered light for both SH and CB. We aim to investigate the differences between these two models at an appropriate level of accuracy as set by the precision of the data themselves.

From the empirical descriptions of Hapke (1986) and Hapke et al. (1993) we take the SH functional form to be

$$\delta_{\rm SH}(\alpha) = \frac{B_0}{1 + (1/h_{\rm SH})\tan(\alpha/2)}, \tag{4.3}$$

where α is the phase angle, B_0 is a constant describing the amplitude of the SH peak and $h_{\rm SH}$ is a dimensionless constant describing the width of the SH peak. It follows that the full-width half-maximum (FWHM) of the shadow hiding peak is

$$\mathrm{FWHM}_{\rm SH} = 2h_{\rm SH}. \tag{4.4}$$

The form for CB is similar to and derives from Akkermans et al. (1988) with a random walk of photons in a scattering medium, and Hapke (2002):

$$\delta_{\rm CB}(\alpha) = \frac{B_0}{2}\frac{1 + \frac{1-e^{-x}}{x}}{(1+x)^2}, \tag{4.5}$$

where

$$x = \frac{\tan(\alpha/2)}{h_{\rm CB}}. \tag{4.6}$$

We expect that SH and CB act on the phase curve together, but it is still uncertain how both effects act simultaneously. For decades, the underlying mechanism of the opposition effect on the Moon was thought to be solely shadow-hiding (see, e.g. Hapke, 1963, Gehrels et al., 1964). However, by measuring the polarisation of light reflected off lunar soil samples, Hapke et al. (1993) showed that CB was also a major contributor to this effect (with later support in Helfenstein et al., 1997, Hapke et al., 1998). Therefore, whilst there is evidence for both mechanisms causing the peak in rocky bodies, it is still not understood which dominates or whether they are also both present to cause the opposition peaks seen in Jupiter and Saturn.

In this paper, we perform a comprehensive model comparison between the SH model, CB model and a model without the inclusion of any opposition model, for both Jupiter and Enceladus. We compare all these approaches using the leave-one-out (LOO) cross-validation statistic (Vehtari et al., 2015) and interpret our results in Section 4.3.1. To perform the model fitting for the phase curves, we use `numpyro` (Phan et al., 2019, Bingham et al., 2019) with an MCMC sampler running with 8 chains, 2000 burn-in steps and 3000 steps. We confirmed the chains had converged after the fitting procedure by inspecting the Gelman-Rubin statistic $\hat{r} < 1.01$ for each free parameter (Gelman & Rubin, 1992). Tables 4.3 and 4.4 shows the priors used for the free parameters within the SH model, which is the same as the priors we used for the CB model. We then measure and compare the FWHM of the opposition peaks in the Jupiter and Enceladus phase curves (see Section 4.3.3).

4.3 Solar System Results

4.3.1 Cross-validation favours models with opposition peaks

We fit the Jupiter phase curves with an SH model, a CB model and a model without the inclusion of any opposition model, and compare all these approaches using cross-validation. The non-opposition effect model was immediately ruled out by a negligible LOO model weight compared to the models with the opposition effect included. Therefore Jupiter likely has an opposition peak, in agreement with previous works including Heng & Li (2021), Dyudina et al. (2016) and Mayorga et al. (2016). Figure 4.3 shows an example of the models fitted to the 463 nm phase curve. Even by visual inspection, it is clear that the model without an opposition peak does not accurately capture the phase curve flux less than around 20 degrees.

Fitting separate CB and SH models to Jupiter's phase curves, we found that seven out of eight phase curves prefer the CB model. If this is implying that CB dominates the opposition peak of Jupiter, this could be due to the lack of a surface on Jupiter, preventing dark shadows from forming (and consequently disappearing at opposition). The presence of CB implies multiple-scattering is occurring in Jupiter's atmosphere and that the scattering particles have an inhomogeneous size distribution (Hapke, 2002, Hapke et al., 1998).

We show the values of the model weights as a function of wavelength in Figure 4.4 and in Table 4.1. We do not find a trend in wavelength.

Figure 4.5 shows one of the Enceladus phase curves (observed with the 798 nm filter), along with the best fits for the CB, SH, and no opposition peak models. We find that the models with an opposition peak were a much better fit for all phase curves.

Seven out of 12 Enceladus phase curves prefer CB, and the other five prefer SH (see Figure 4.6). Examining the top panel of Figure 4.6, we see no correlation with model selection and wavelength. The non-preference of either model here could suggest that the data does not have sufficient precision to distinguish between them. It also does not rule out the possibility that both effects are present on Enceladus and the opposition peak that we observe is a complex combination of the two. For example, Dlugach & Mishchenko (2013) showed that CB can take place in closely packed mediums and planetary surfaces and, as mentioned previously, we also have evidence for both SH and CB on the Moon.

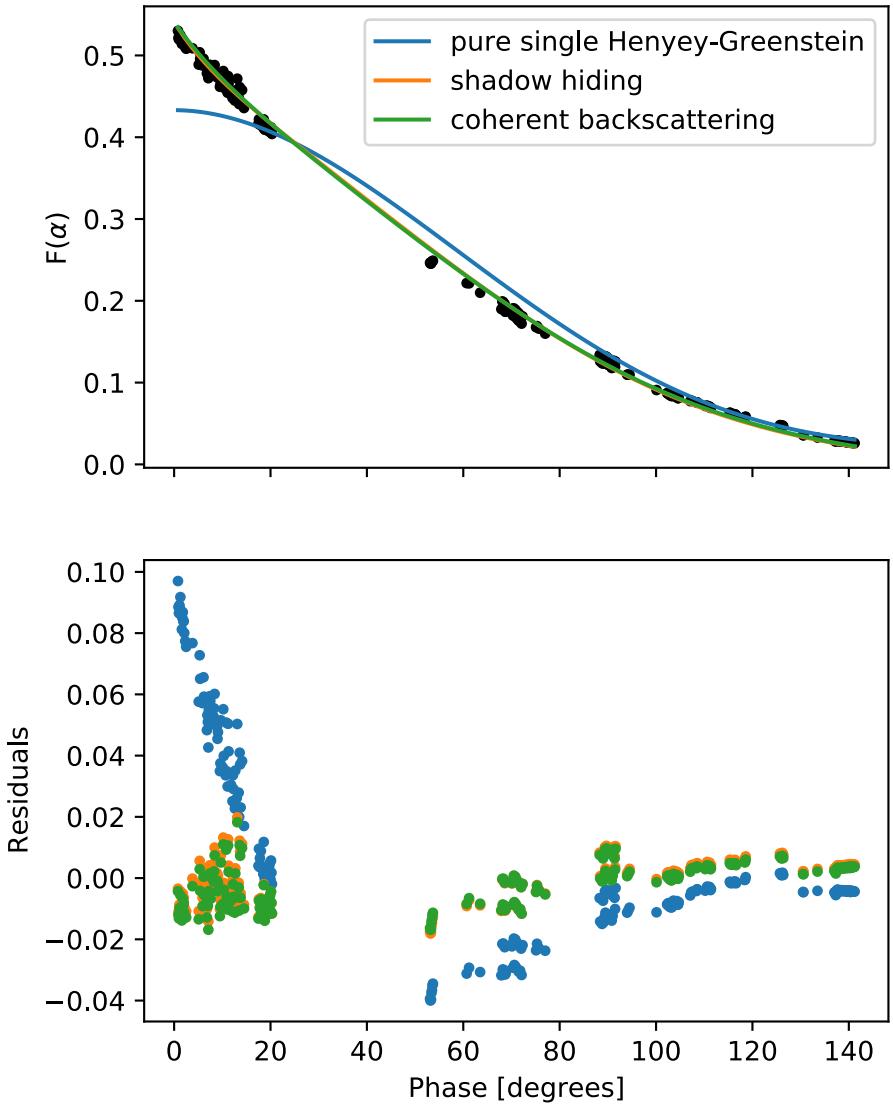

Figure 4.3 | Top panel shows the best fit models to one of Jupiter's phase curves (filter BL1, 463 nm) for three different models: a pure single Henyey Greenstein model with no additional opposition peak, shadow hiding model, and coherent backscattering model. The second panel is showing the residuals of these best fits. It is clear that the model with no opposition peak is the worst fit to the data. The other two models produce, by eye, almost identical fits, which is expected since the functional forms are similar. We choose not to show the uncertainties here as they change slightly depending on the model fit. However the residuals still show subtle differences. Using the LOO model selection statistic, we conclude that the coherent backscattering model is the best fitting model for this phase curve, along with all-but-one of the other Jupiter Cassini phase curves. The corner plot showing the posteriors for the shadow hiding model in this plot are in Appendix 4.A, Figure 4.11.

Wavelength [nm]	Filter	Preferred Model	Weight
260	UV1	CB	1.00
460	BL1	CB	0.99
570	GRN	CB	1.00
650	RED	CB	1.00
730	MT2	CB	1.00
750	CB2	CB	1.00
890	MT3	SH	1.00
940	CB3	CB	1.00

Table 4.1 | For each of Jupiter's Cassini phase curves we report here the preferred model from our fitting procedure. 7/8 phase curves prefer the coherent backscattering model (CB) over the shadow hiding model (SH). The wavelength column refers to the effective wavelength of the filter used. The 'Weight' is the LOO model weight of the preferred model.

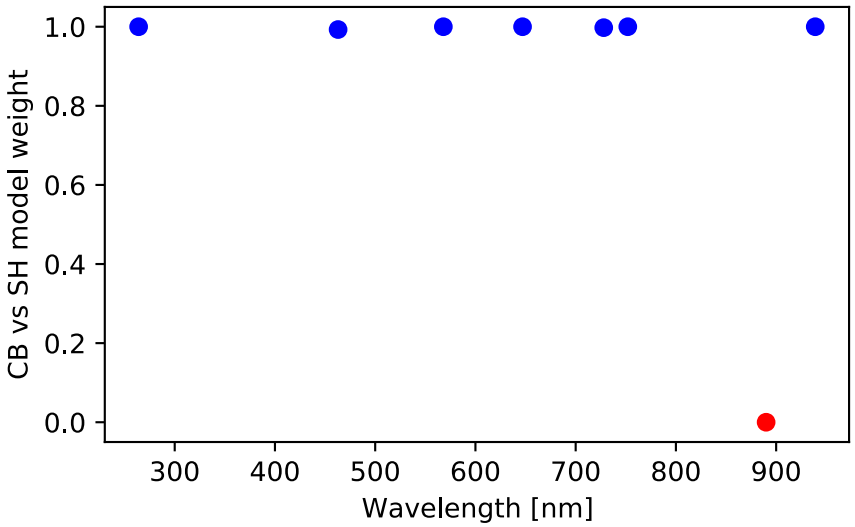

Figure 4.4 | The LOO model weight of the CB model vs the SH model for the Jupiter phase curves plotted against wavelength. When the model weight is close to 1, then the CB model is preferred (blue points), however close to 0 indicates that SH is preferred (red points). The red point shows the only phase curve where the SH model is preferred.

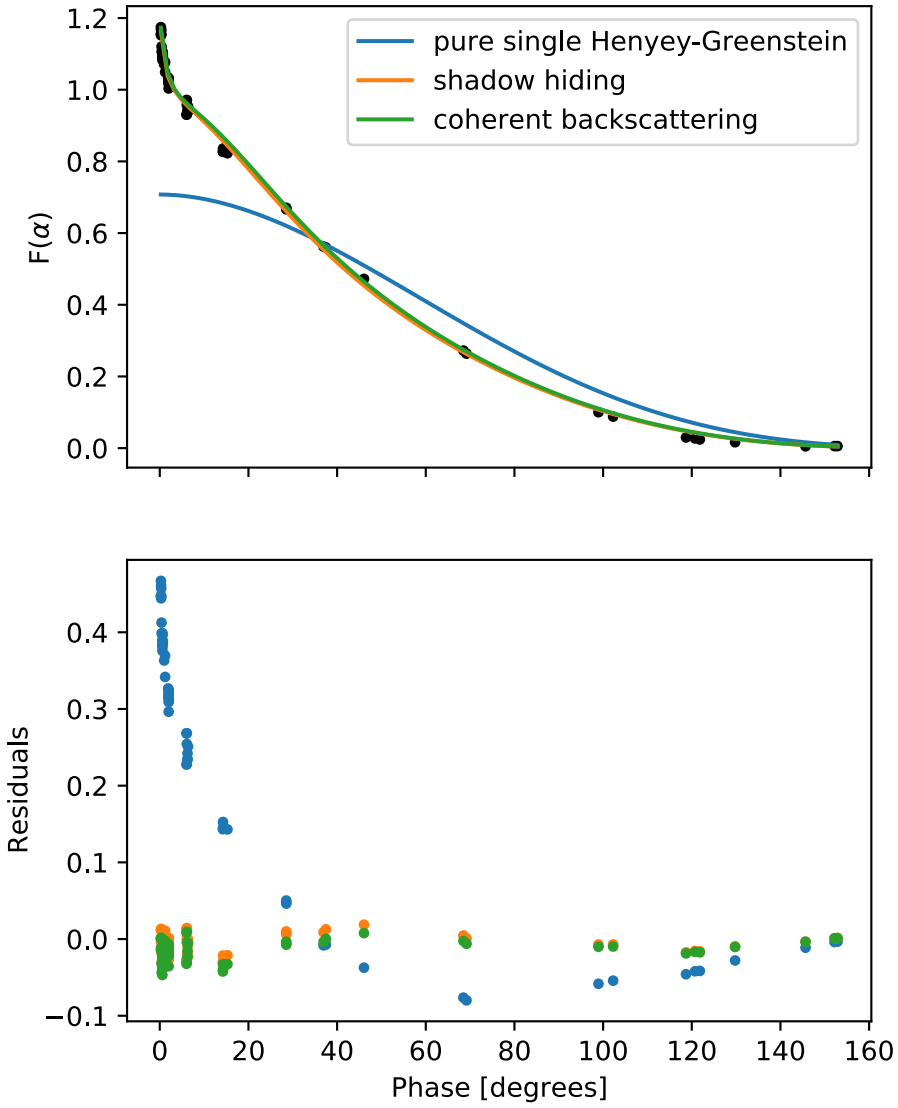

Figure 4.5 | Top panel shows the best fit models to one of Enceladus' phase curves (filter 798 nm) for three different models: a pure single Henyey-Greenstein model with no additional opposition peak, shadow hiding model, and coherent backscattering model. The second panel is showing the residuals of these best fits. It is clear that the model with no opposition peak is the worst fit to the data. The other two models produce, by eye, almost identical fits, which is expected since the functional forms are similar. However the residuals still show subtle differences. Using the LOO model selection statistic allows us to conclude that the coherent backscattering model is preferred by 7/12 of the phase curves, however not significantly. The corner plot showing the posteriors for the shadow hiding model are in Appendix 4.A, Figure 4.12.

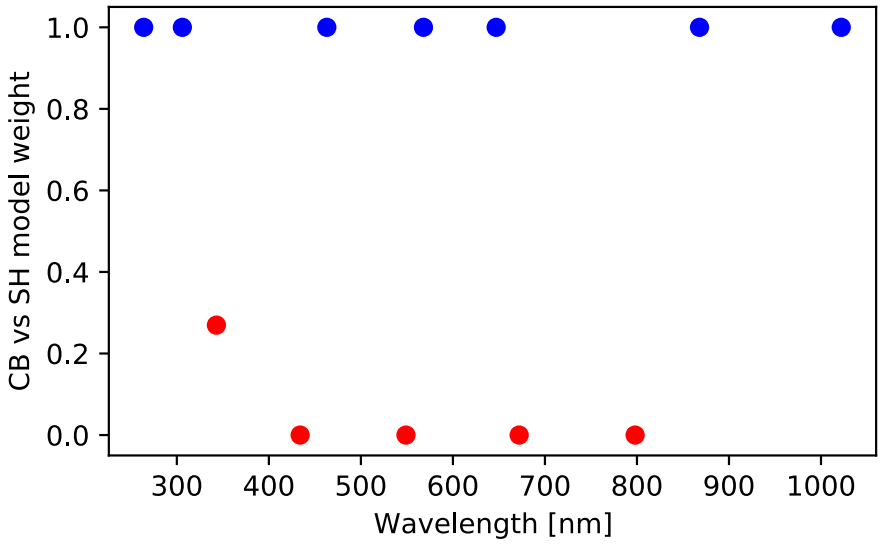

Figure 4.6 | Top panel shows the LOO model weight of the CB model vs the SH model for the Enceladus phase curves. I.e. when the model weight is close to 1, then the CB model is preferred (blue points), however close to 0 indicates that SH is preferred (red points). The red points show the phase curves where the SH model is confirmed. Bottom panel shows the LOO model weight plotted against the number of datapoints in each phase curve. There is a tentative negative correlation here, indicating that the more datapoints in a phase curve, the stronger the SH model is preferred.

Wavelength [nm]	Filter	Preferred Model	Weight
260	UV1	CB	1.00
310	UV2	CB	1.00
340	UV3	SH	1.00
430	-	SH	0.73
460	BL1	CB	1.00
550	-	SH	1.00
570	GRN	CB	1.00
650	RED	CB	1.00
670	-	SH	1.00
800	-	SH	1.00
870	-	CB	1.00
1020	-	CB	1.00

Table 4.2 | For each of Enceladus' Cassini phase curves we report here the preferred model from our fitting procedure. 7/12 phase curves prefer the coherent backscattering model (CB) and the others prefer the shadow hiding model (SH). The wavelength column refers to the effective wavelength of the filter used. The 'Weight' is the LOO model weight of the preferred model.

4.3.2 Information from the fitted parameters

The best-fit results of the fitted parameters for Jupiter and Enceladus (with the shadow-hiding model) are shown in Tables 4.3 and 4.4. The single-scattering albedo ω describes the fraction of light reflected in a single scattering event. When ω is close to unity, the majority of the light is scattered, and absorption dominates as $\omega \to 0$. In the top panel of Figure 4.7, we find $\omega \sim 1$ for Enceladus across the full range of wavelengths. This is consistent with Enceladus having no atmosphere to absorb the incoming light and an icy solid surface which has a high optical albedo. Jupiter also has $\omega \sim 1$ for most of the wavelength range, apart from methane absorption bands near 750 nm and 900 nm.

The scattering asymmetry parameter, g, parameterizes a bias towards forward- or backscattering (see Equation 4.1). Forward scattering dominates for positive g, and backward scattering dominates for negative g. The fit results for Jupiter show $g > 0$, indicating

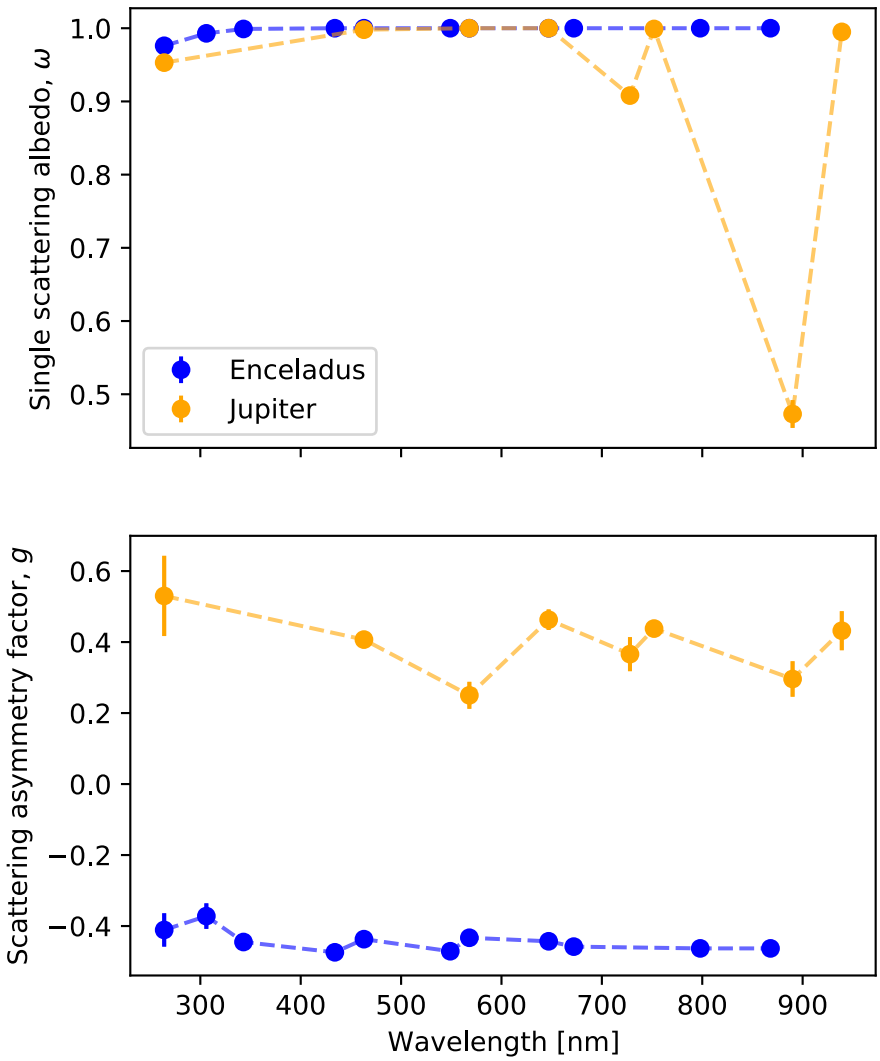

Figure 4.7 | Fitted values of the scattering asymmetry factor, g, and the single-scattering cross section, ω, across wavelength for Jupiter (orange) and Enceladus (blue). In the first panel, we see the single scattering albedo decrease (i.e. more absorption) around 750 nm and 900 nm for Jupiter, which is attributed to the methane absorption bands. We do not see this feature in Enceladus, since it has no considerable atmosphere. Both Jupiter and Enceladus show no trends in the asymmetry factors (second panel) across the wavelength range. This implies that the size of the scattering particles are always equivalent to the wavelengths, and therefore inhomogenous in these cases. For Enceladus, g is significantly lower, and negative, indicating that most of the light that hits the scattering particles/surface is reflected backwards. This follows our intuition since Enceladus has an icy surface and no atmosphere, compared to Jupiter's thick atmosphere and no solid surface.

Table 4.3 | Best-fit parameter results of the SH model fitting to Jupiter phase curves. Shown also are the priors used for the fitted parameters in the model, along with the results of the derived parameter (FWHM).

Wavelength	**g**	ω	$h_{\mathbf{SH}}$ **[radians]**	B_0	**FWHM [radians]**
260nm(UV1)	0.5 ± 0.1	0.954 ± 0.004	0.3 ± 0.2	0.4 ± 0.2	0.7 ± 0.4
460nm(BL1)	0.41 ± 0.02	0.9977 ± 0.0002	0.18 ± 0.01	0.56 ± 0.02	0.35 ± 0.02
570nm(GRN)	0.25 ± 0.04	0.99998 ± 0.00003	0.22 ± 0.03	0.46 ± 0.04	0.44 ± 0.07
650nm(RED)	0.46 ± 0.03	0.9997 ± 0.0001	0.10 ± 0.02	0.26 ± 0.02	0.20 ± 0.04
730nm(MT2)	0.37 ± 0.05	0.908 ± 0.004	0.19 ± 0.02	0.51 ± 0.03	0.39 ± 0.03
750nm(CB2)	0.44 ± 0.02	0.9995 ± 0.0001	0.06 ± 0.01	0.155 ± 0.009	0.17 ± 0.02
890nm(MT3)	0.30 ± 0.05	0.47 ± 0.02	0.66 ± 0.09	3.1 ± 1.2	1.3 ± 0.2
940nm(CB3)	0.43 ± 0.06	0.995 ± 0.001	0.21 ± 0.05	0.37 ± 0.06	0.4 ± 0.1
Prior	U(-1,1)	U(0,1)	U(0,10)	U(0,10)	-

Table 4.4 | Best-fit parameter results of the SH model fitting to Enceladus phase curves. Shown also are the priors used for the fitted parameters in the model, along with the results of the derived parameter (FWHM).

Wavelength	**g**	ω	$h_{\mathbf{SH}}$ **[radians]**	B_0	**FWHM [radians]**
260nm (UV1)	−0.41 ± 0.05	0.98 ± 0.01	0.2 ± 0.8	$0.7^{+1.4}_{-0.6}$	$0.4^{+1.7}_{-0.3}$
310nm (UV2)	0.37 ± 0.04	0.993 ± 0.05	0.07 ± 0.05	0.5 ± 0.2	0.1 ± 0.1
340nm (UV3)	−0.445 ± 0.008	0.999 ± 0.001	0.007 ± 0.002	0.46 ± 0.03	0.014 ± 0.004
430nm	−0.474 ± 0.009	1.000 ± 0.000	0.0090 ± 0.004	0.26 ± 0.02	0.018 ± 0.008
460nm (BL1)	−0.437 ± 0.006	1.000 ± 0.000	0.017 ± 0.006	0.24 ± 0.01	0.03 ± 0.01
550nm	−0.471 ± 0.007	1.000 ± 0.000	0.007 ± 0.002	0.28 ± 0.01	0.014 ± 0.004
570nm (GRN)	−0.433 ± 0.007	1.000 ± 0.000	0.016 ± 0.008	0.21 ± 0.01	0.03 ± 0.02
650nm (RED)	−0.443 ± 0.01	1.000 ± 0.000	0.03 ± 0.02	0.27 ± 0.02	0.06 ± 0.04
670nm	−0.458 ± 0.007	1.000 ± 0.000	0.013 ± 0.003	0.027 ± 0.01	0.026 ± 0.006
800nm	−0.463 ± 0.005	1.000 ± 0.000	0.009 ± 0.002	0.298 ± 0.009	0.018 ± 0.004
870nm	−0.463 ± 0.008	1.000 ± 0.000	0.008 ± 0.003	0.29 ± 0.02	0.016 ± 0.006
Prior	U(-1,1)	U(0,1)	U(0,10)	U(0,10)	-

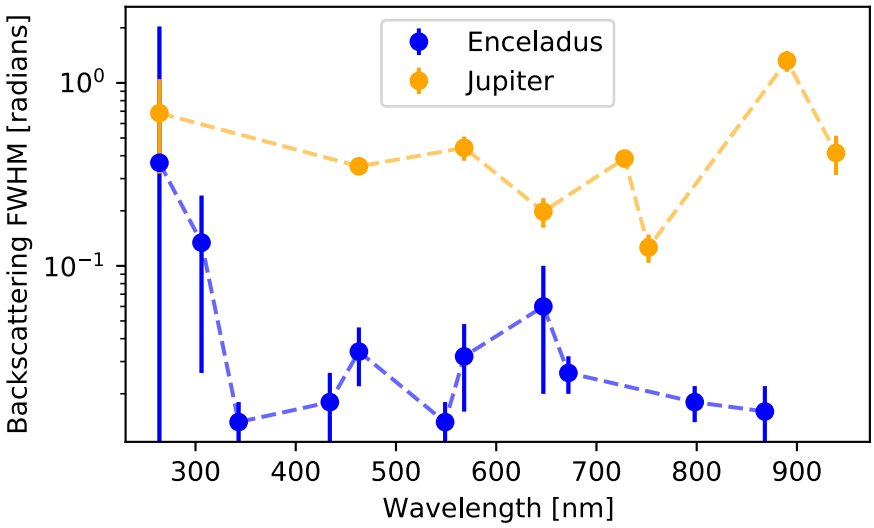

Figure 4.8 | The measured backscattering FWHM in the Jupiter (orange points) and Enceladus (blue points) phase curves. We find that there is generally an order of magnitude difference between the Enceladus and Jupiter measurements across the wavelength range.

that the scattering surface is composed of particles larger than the observing wavelengths (Heng & Li, 2021). That g remains relatively constant across the wavelength range implies the presence of a size distribution of particles (Heng & Li, 2021). For Enceladus, the inferred values for g are negative implying that reverse scattering dominates. This follows our intuition since Enceladus has an icy surface and no atmosphere, compared to Jupiter's thick atmosphere and no solid surface. However, due to the single Henyey-Greenstein scattering phase function being developed to describe scattering off a particle, and not reflection off a surface, it is less clear how to interpret g in the context of a solid surface.

From the inferred values of $h_{\rm CB}$ (not shown), the transport mean free path associated with coherent backscattering is $\sim$ 0.1–1 times the wavelength probed.

4.3.3 FWHM as a solid surface detector

From previous studies (e.g. Dyudina et al., 2016), we see that one of the distinguishing features between the opposition effect from our Solar System objects is the 'peaky-ness' of the opposition maximum near zero phase. To quantify this, we used the best fit SH model to measure the FWHM (Equation 4.4) of the different Jupiter and Enceladus phase curves and plotted them as a function of wavelength (see Figure 4.8).

We find the FWHM of Enceladus' opposition peak to be an order of magnitude larger

than Jupiter across the wavelength range. This helps quantify what we have seen in the rest of the Solar System, which is that the solid planets seem to have much smaller opposition FWHM peaks than the gaseous planet (Dyudina et al., 2016). This could be due to the difference in how light is scattered on a surface compared to within a gas. It could also be due to the dominant backscattering source or even the average distance between the scattering particles themselves.

4.4 Application to exoplanet phase curves

4.4.1 Rocky exoplanets

Characterising the climates of exoplanets is now, in my opinion, one of the most important topics of research in the exoplanet field. Finding more methods to do this is therefore extremely valuable. We have so far proposed the possibility that measuring an opposition peak in the phase curve of a planet and then measuring the FWHM of this peak would be an indicator of whether the planet has a significant atmosphere or not.

In order to test whether this would be possible with an exoplanet, we ran a series of injection-recovery tests. Using a simulated phase curve of K2-141b, one of the most observable super-Earths (see, e.g. Barragán et al., 2018, Malavolta et al., 2018), we injected an Enceladus-like opposition peak using the best-fit parameters from our model fitting in Section 4.3.3. We took the SH model results since they were not ruled out by the data and as we only want to measure the FWHM of the peak, both the CB and SH fit should give the same result. Additionally, the formula for calculating the FWHM from the SH is easily obtained from Equation 4.4. We then adjusted the noise floor to simulate observations from both JWST and a future Habitable Worlds Observatory-like telescope. We took performance specifications from The LUVOIR Team (2019) as a starting point for the Habitable Worlds Observatory, and in-flight spectrophotometric precision measurements for JWST/NIRSpec from Mikal-Evans et al. (2023). We investigated how many observations are necessary to measure the injected (true) FWHM. Figure 4.9 shows the simulated phase curve (without the eclipse) with noise levels consistent with 10^3 and 10^5 JWST observations. From these fits we obtain the h_{SH} posterior distribution, allowing us to calculate the FWHM as shown in Figure 4.10.

Our results are shown in Figure 4.10. We ran the test with two different simulated

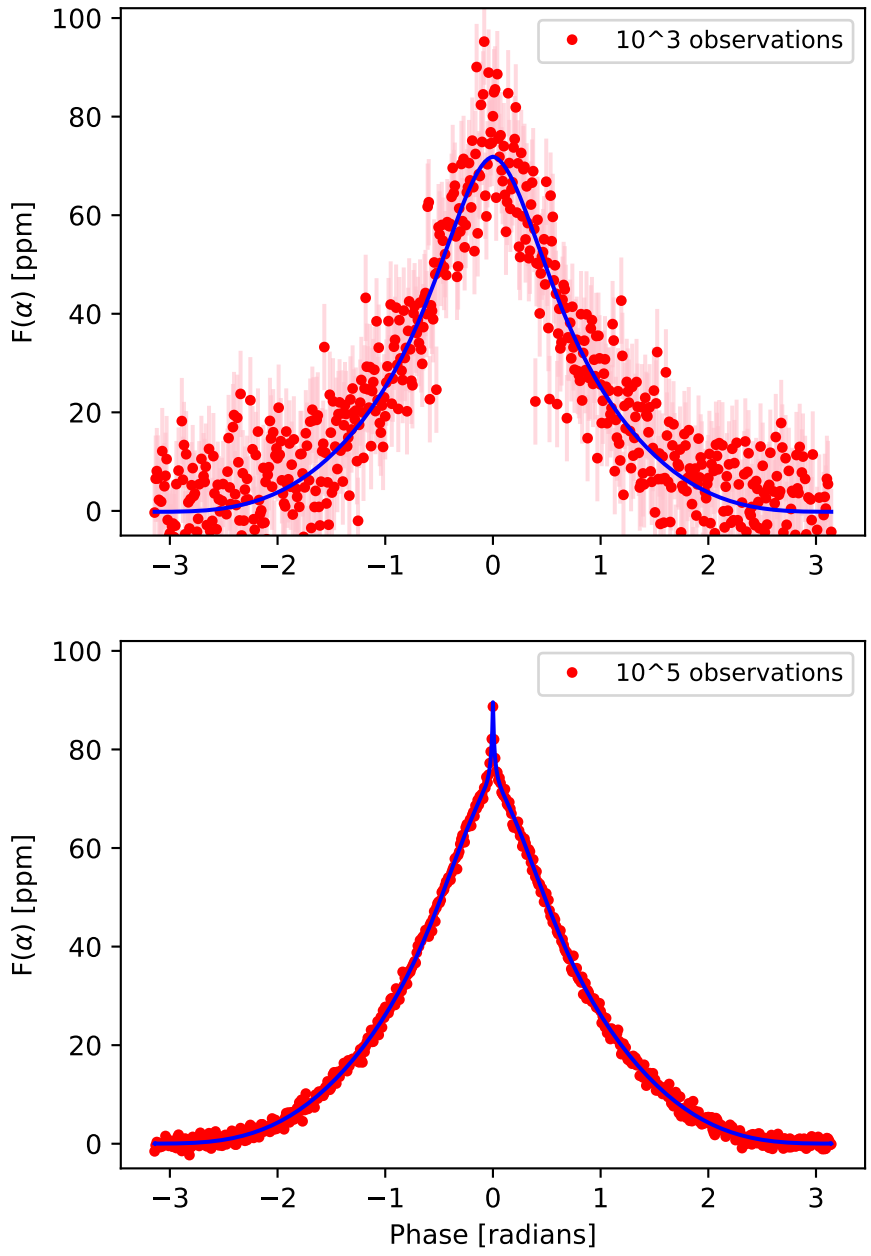

Figure 4.9 | Top and bottom panel show the same simulated phase curve model of K2-141b, a super-Earth (red points, with green errorbars). The blue line shows the best fit of our opposition effect model. The noise here is at a level consistent with 10^3 JWST observations (top panel) and 10^5 observations (bottom panel).

phase curves: one with and one without an eclipse present. This was important for us to test since an eclipse blocks the light from the planet near zero phase, exactly when the opposition peak signal is the strongest. Therefore we expect a present eclipse to make the fits less accurate than when we have all the data near zero phase. A phase curve with no eclipse could be produced by a non-transiting planet.

From our results we see that with JWST and a phase curve with an eclipse, it would take upwards of $\sim 10^6$ phase curves in order to reach the precision necessary to reach FWHM measurements consistent with the true value. Using the lower predicted noise floor of Habitable Worlds, this decreases to $\sim 10^5$ phase curves. Comparing these to the results when we use a phase curve with no eclipse present, the number of required observations significantly decreases. JWST requires $\sim 10^4$ phase curves, whilst Habitable Worlds requires $\sim 10^3$. Clearly both of these results show that this technique is not feasible with both current and planned future individual exoplanet observations. Perhaps it could still be used in the future for non-transiting exoplanets if a global population phase curve stacking technique was applied (e.g. Sheets & Deming, 2017).

4.4.2 Jupiter-like exoplanets

We repeated the above injection and recovery test using simulated phase curves of HAT-P-7b and injecting them with an opposition-effect signal using the best fit parameters from the previous analysis on the Jupiter phase curves. We then used an MCMC fitting method to recover the h_{SH} parameter (and therefore the FWHM) and compared this to the true value of the injected FWHM.

We find that both with and without an eclipse present in the phase curve, the number of observations required to contrain the FWHM is $\sim 10^2$ lower than our previous investigation with a rocky exoplanet.

Since the FWHM we injected is much wider than the one we injected to mimic a rocky exoplanet, it has an effect over a larger range of phases, so more data contributes to constraining the opposition effect parameters, and fewer observations are needed. The second is that the orbital period is longer, so at a fixed exposure cadence, there are more observations per phase. Furthermore, the R_p/a for this type of planet is much larger than for the Enceladus-like planet (mostly due to the larger radius), increasing the amplitude of the phase curve and therefore our SNR. In Section 4.5.4, we investigated the parameter

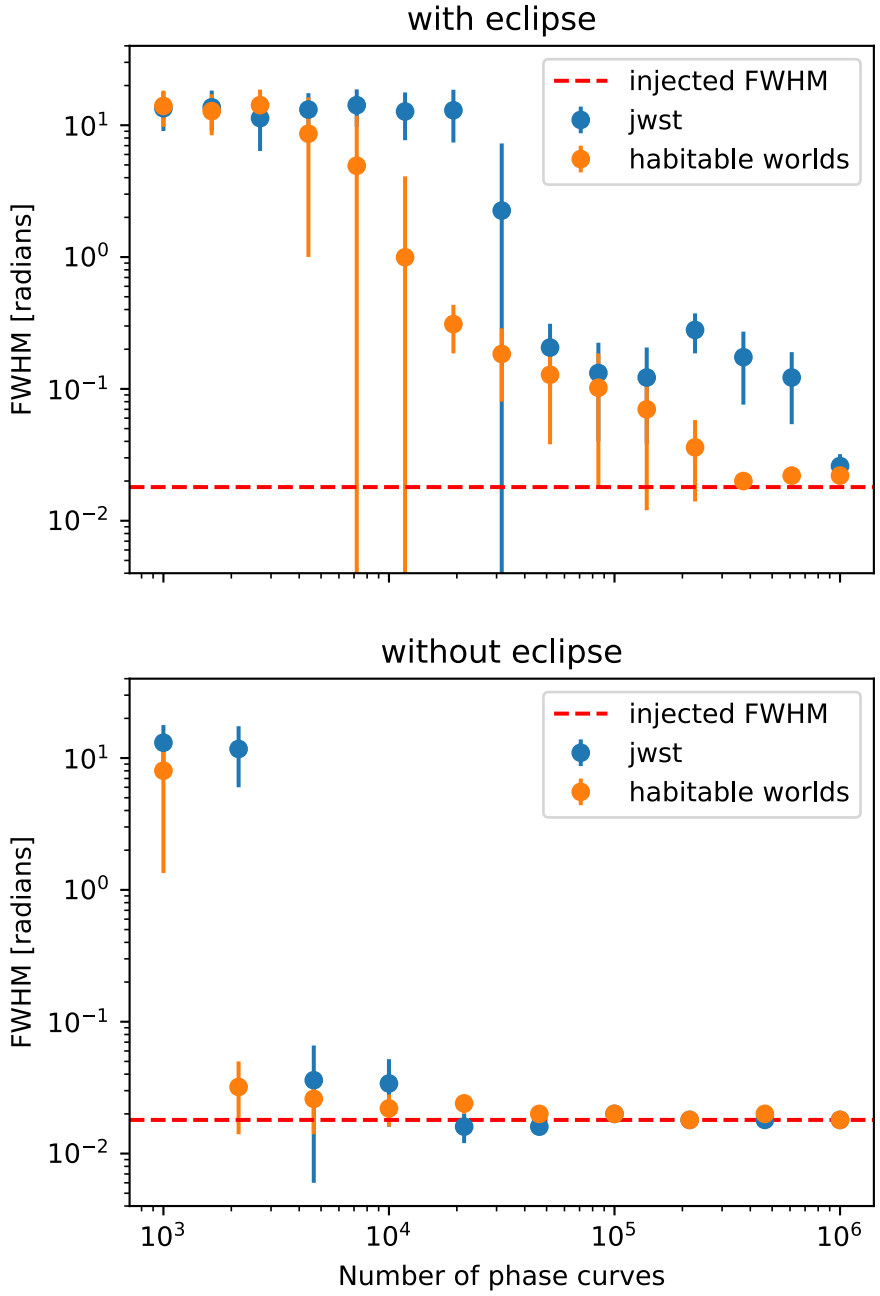

Figure 4.10 | An overview of the feasibility of detecting an Enceladus-like opposition effect signal in an exoplanet phase curve using both JWST and the future Habitable Worlds Observatory. The first panel shows the results when we use phase curves with an eclipse present and the second panel shows results without an eclipse present. The red line shows the FWHM value of the injected signal and the blue and orange points show the retrieved value, with 1σ errorbars. We find that, as expected, this signal is easier to detect in phase curves without an eclipse present, however this is still way beyond feasibility for both JWST and Habitable Worlds.

space of planetary orbital period and semi-major axis to see where the opposition signal would have the highest signal-to-noise.

4.5 Discussion

4.5.1 The effect of neglected surface properties on reflectance

The reflected light phase curve model in Section 4.2.2 describes a spherical planet built on formalism established in Hapke (1981) and extended in Heng et al. (2021). We adopted a parameterization for shadow hiding from Hapke (2002), which implied that shadows are cast by topographical features that could be any optically thick obstruction to light, including mountains or clouds. The scale and shape of the shadow-casters was not parameterized in the model.

The full diversity of planetary surfaces in the Solar System cannot be described with shadow hiding or coherent backscattering, alone or in combination. Hapke (1984) established a parametrization for reflected light phase curves with macroscopic roughness. Model lunar phase curves with surface roughness agreed well with observations after taking into account the distribution of surface slopes measured from lunar orbiters (Helfenstein, 1988). Later work also established the effect of regolith porosity on phase curves (Hapke, 2008).

A primary motivation for this study was to evaluate whether or not opposition surges are useful solid surface detectors for exoplanets. In Section 4.4.1, we showed that Enceladus-like opposition surges are unlikely to be measured in exoplanet phase curve observations in the foreseeable future. As such, we have not added further complexity to the models fit to the phase curves of Enceladus or Jupiter, since it is unlikely to affect the likelihood of opposition surge detections in exoplanets. Much higher precision phase curves are available elsewhere, and their precision requires the inclusion of these higher order effects in model fits. For example, Enceladus observations from Voyager and from the ground by Verbiscer & Veverka (1994) required macroscopic roughness to model the phase curve. Since the phase curve model here is parametrised through the single scattering albedo and scattering asymmetry parameter, the inferences for both parameters on Enceladus must be interpreted with these model limitations in mind.

Despite our highly simplified model and wider phase angle coverage, the results pre-

sented in this work agree well with Verbiscer & Veverka (1994). Verbiscer & Veverka (1994) found $\omega = 0.999 \pm 0.002$ and $g = -0.39 \pm 0.02$, with opposition surge factor $B_0 = 0.21 \pm 0.07$. The Voyager instrument response with the clear filter has most transmittance between 400-600 nm, so the Cassini filter at 550 nm is likely the closest analogue in Table 4.4. We find smaller g and greater B_0 in the Cassini 550 nm filter than the Voyager clear filter observations. The difference between solutions may be attributable to the difference in filter transmittance or the inclusion of regolith compaction in the analysis by Verbiscer & Veverka (1994). The small disagreement between parameters inferred in the two analyses is insufficient to change the outcome of the likelihood of opposition surge detection in exoplanets in Section 4.4.1.

4.5.2 Selecting an appropriate model

We fitted a set of reflected light phase curve models to Solar System observations. The scattering phase functions of these models are semi-empirical and constructed to fit observations of Solar System objects, but it is not clear from the theory which models should be applied to a given planet. Given the similarity of the model shapes, we have seen that trying to distinguish the preferred model (CB or SH) from current observations is very difficult. We could only tentatively conclude there was evidence for CB model being preferred for Jupiter. This of course does not rule out the possibility of both effects being present with one more dominant than the other or that the true solution is a different model entirely. Even for the Moon, where studies have been made on the Moon rock samples themselves, there are still many outstanding questions in regards to the contributions of CB and SH to the lunar opposition peak. There have been studies (see, e.g. Helfenstein et al., 1997) showing evidence that CB contributes to the peak at very small phase angles, and SH continues out to larger phase angles - however this is not conclusive. There is also very little investigation into the cause of the observed opposition effect on gaseous planets.

Furthermore, due to the known wavelength-dependence of some scattering properties, we expected some colour-dependence in the best-fit parameters however this was not detected in the results.

However, due to SH and CB being direct outcomes of the scattering properties of the surface/atmosphere, unravelling these dependencies would provide information about the

composition and particles on these planets.

4.5.3 Interpreting the best-fit parameters

For fitting our reflected light curves, we used, like other previous studies (see, e.g. Helfenstein et al., 1997, Heng & Li, 2021), a single Henyey-Greenstein scattering phase function to describe the preferred scattering direction of an incoming ray to a scattering particle. This function includes the scattering asymmetry parameter, g, which controls the amount of forward vs backward backscattering. When g is close to 1 there is only forward scattering, whilst if g is close to -1 then there is only backscattering present. Fitting for Enceladus, we derived a negative g. This is more difficult to interpret since the scattering medium of Enceladus is a surface and not atmospheric gas. Therefore g is harder to interpret in this scenario, which is not the medium the phase function was designed to model. Also, the scattering properties that can be derived from g are probably not reliable for describing Enceladus' suface. For Jupiter, since it has a large extended atmosphere, we believe this model is appropriate. Future works should take care in choosing the scattering phase function and be aware of its limitations in regards to solid bodies without atmospheres.

4.5.4 Optimal planet parameters for detecting the opposition effect

For a fixed planet radius R_p and opposition scattering parameters, two parameters dominate the signal-to-noise of the opposition peak: planetary orbital period and stellar mass. As the period increases, the number of datapoints per phase increases by the same amount. Therefore the signal-to-noise (SNR) due to the number of datapoints goes as

$$\mathrm{SNR} \propto \mathrm{N}_{\mathrm{exp}}^{1/2} \propto \mathrm{P}^{1/2}, \tag{4.7}$$

where N_{exp} is the number of exposures and P is the planetary orbital period. As the mass of the host star increases, by Kepler's Third Law, the semi-major axis (a) also increases, for a fixed period. The amplitude of the reflected light phase curve of a planet is equal to $A_g(R_p/a)^2$. Therefore the SNR goes as

$$\mathrm{SNR} \propto \mathrm{amplitude} \propto \mathrm{a}^{-2} \propto \mathrm{P}^{-4/3}. \tag{4.8}$$

These show that the amplitude of the phase curve dominates how the SNR of the opposition peak changes with period, i.e. as the period of the planet decreases, the SNR increases.

4.6 Conclusion

- Reflected light phase curves of Solar System objects contain opposition peaks, which contain information about the surfaces where scattering occurs.
- We fit Jupiter and Enceladus phase curves with a semi-empirical reflected light phase curve model and found that models with an opposition peak model are significantly preferred over simpler models, in agreement with previous Solar System work.
- We showed that the FWHM of Jupiter's opposition peak is an order of magnitude larger than that of Enceladus, uncovering the opportunity to differentiate solid from gaseous exoplanets using the FWHM of phase curve opposition peaks.
- Cross-validation suggests a tentative preference for CB in Jupiter's phase curve over SH, and a preference for SH in the phase curve of Enceladus.
- We show that observations are unlikely to accurately measure the FWHM of a phase curve opposition peak in the next few decades, with either JWST or HWO.

Appendix

4.A Best fit results

We show here in Figure 4.11 and 4.12 the resulting posterior distributions of our fitted parameters during our analysis in Section 4.3.1.

4.B Comparison to Heng & Li (2021)

This current analysis follows on from the work in Heng & Li (2021), where they tested different single scattering laws on a similar dataset from Li et al. (2018) of Jupiter phase curves. These phase curves not only consisted of observed data, but were interpolated so that they had homogeneous phase and wavelength coverage. We initially repeated our analysis in Section 4.3.1 with these interpolated phase curves. However we found this often led to bimodal solutions, which we speculated was an artifact of the interpolation procedure. Therefore we decided to use the original uninterpolated data in this analysis.

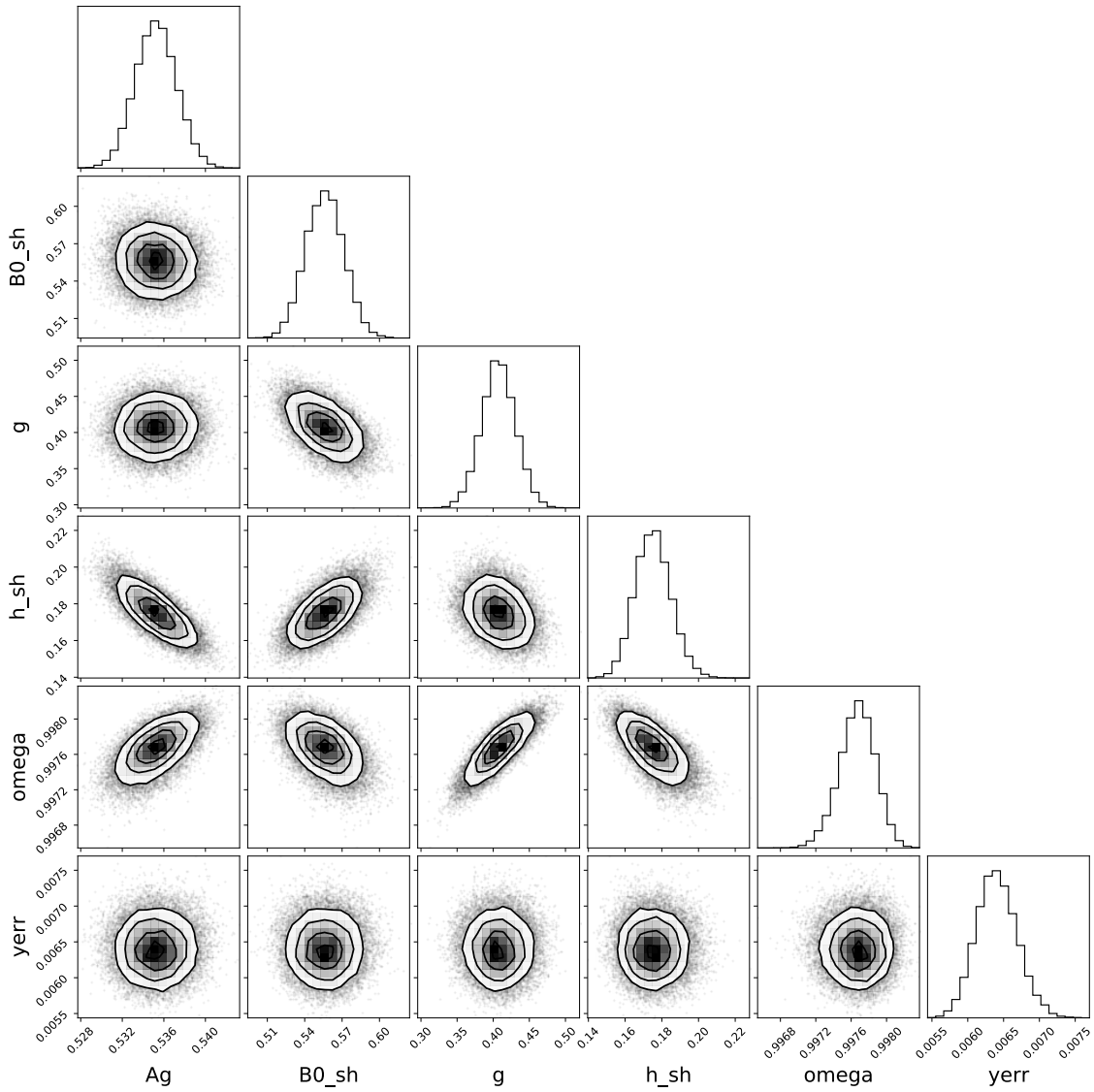

Figure 4.11 | Corner plot showing the shadow hiding model best fit posteriors to the BL1 (463 nm) Jupiter phase curve, as shown in Figure 4.3.

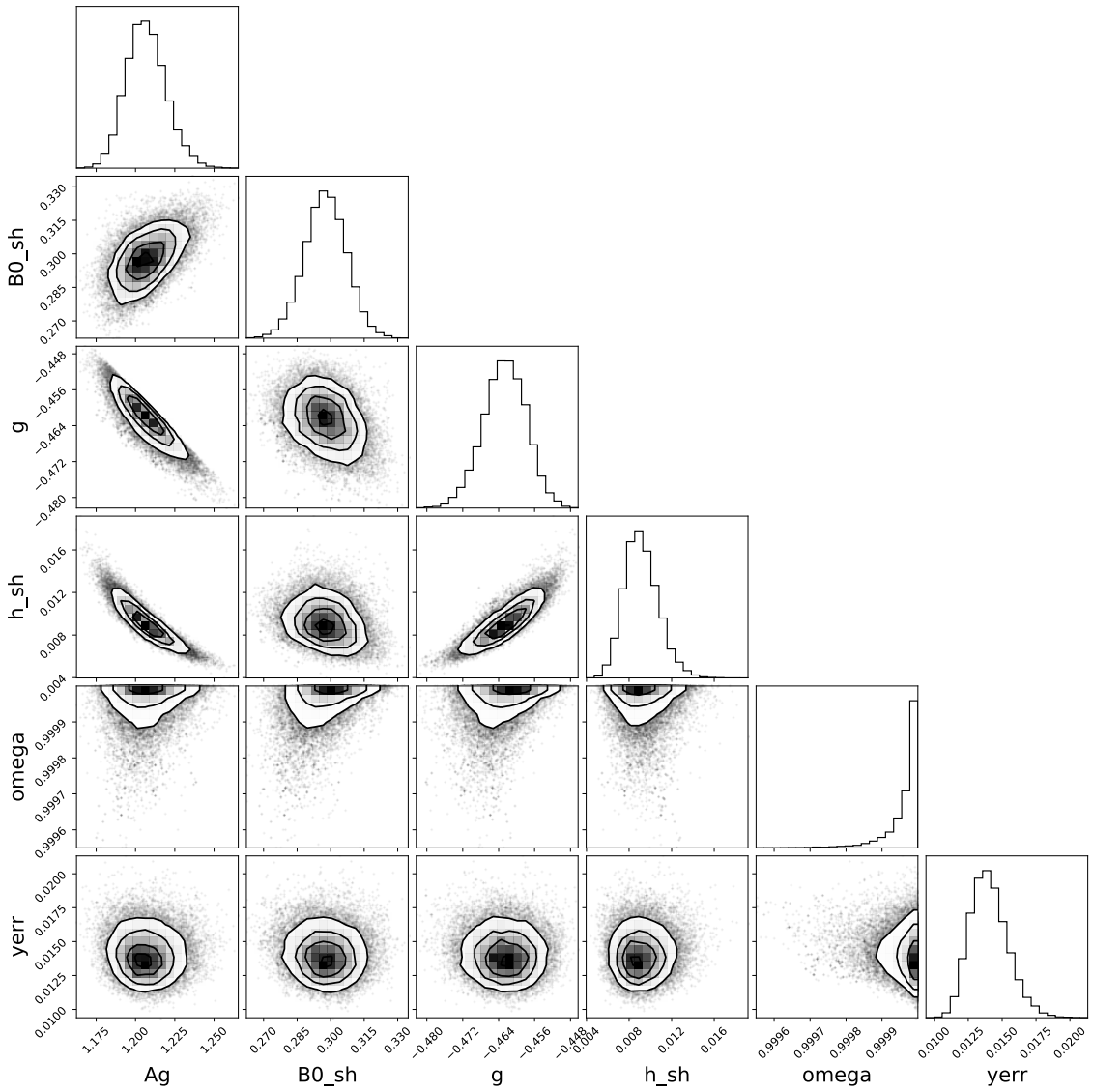

Figure 4.12 | Corner plot showing the shadow hiding model best fit posteriors to the 798nm Enceladus phase curve, as shown in Figure 4.5.

Chapter 5

The Effect of Atmospheric Chemistry on the Optical Geometric Albedos of Hot Jupiters

This chapter has been submitted to A&A as **Jones, K. D.**, Morris, B. M. and Heng, K. (in review), *The Effect of Atmospheric Chemistry on the Optical Geometric Albedos of Hot Jupiters*.

Following on from Chapter 4, where we explored how a specific physical phenomenon affects the reflected light of a planet and whether this would be detectable from an exoplanet phase curve, we zoom out now to look at a set of hot Jupiters and their geometric albedo distributions. The geometric albedo is defined as the proportion of light reflected by the planet when it is fully illuminated by its host star (i.e. at zero phase) with respect to the observer. Therefore, measuring this flux as a function of wavelength can provide a wealth of information about the atmospheric structure, composition and scattering properties of the exoplanet. It is also relatively 'simple' to observe, by measuring the eclipse depth as the planet moves behind its star, we can calculate the total flux coming from the fully-illuminated hemisphere of the planet and the geometric albedo (see Section 1.4.5). In the first half of this chapter, we collate and investigate the current geometric albedo measurements of 35 hot Jupiters, including 3 new measurements using CHEOPS. As the geometric albedo is a wavelength-dependent quantity, we also compare these measurements across wavelength filters.

In previous work by Heng et al. (2021), they derived a formula for the geometric

albedo given a single-scattering albedo (assuming that single-scattering can be described by any reflection law and multiple scattering is isotropic) as a function of wavelength. We use this model to investigate the theoretical dependence of A_g on other variables, such as metallicity, temperature and pressure. The unique part of this work is that we integrate the A_g over the TESS and CHEOPS bandpasses, and compare the posterior distributions of the theoretical values to the observation sample, taking into the uncertainties of the observations. Hence, this work is a step in the direction of linking theoretical albedo models with the observations to gain information about the scattering properties of hot Jupiter atmospheres.

Abstract

We investigate the geometric albedos of hot Jupiters by comparing observational data from space telescopes TESS, Kepler, CoRoT, and CHEOPS against theoretical models. The study aims to understand the distribution of observed geometric albedos across different bandpasses and how these observations align with or deviate from model predictions. We have curated a comprehensive sample of observed geometric albedos, using either existing Spitzer secondary eclipse measurements or a scaling law between the equilibrium and dayside temperature to remove any contaminating thermal planetary emission. We then utilised hierarchical Bayesian modelling to identify trends with planetary properties such as equilibrium temperature, gravity, and stellar metallicity. On a population level, we found no statistical difference in the distributions of geometric albedos measured by TESS compared to those by Kepler, CoRoT and CHEOPS. We confront the geometric albedo sample with a simple, but first principles, model that includes Rayleigh scattering by molecular hydrogen and absorption by sodium, water and titanium oxide and vanadium oxide. We find that the abundance of sodium and water are the key absorbers that influence the geometric albedos of hot Jupiters, whilst the addition of titanium oxide and vanadium oxide results in vanishing geometric albedos that are inconsistent with the observed distributions.

5.1 Introduction

The geometric albedo of a planet, moon or exoplanet is the fraction of light reflected at full illumination with respect to the observer (at superior conjunction). Geometric albedo is a wavelength-dependent quantity and may be larger than unity if the incoming light is preferentially reflected back in the direction of the observer. In the Solar System, there is a long and rich history of measuring the geometric albedos of moons and planets using data from Voyager (see, e.g. Hanel et al., 1981) and Cassini (see, e.g. Pitman et al., 2010, Buratti et al., 2022). For Jupiter, geometric albedo *spectra* have been measured (e.g. Li et al., 2018).

For exoplanets, the geometric albedo may be inferred from measurements of the

eclipse depth (D), planetary radius (R_p) and semi-major axis (a) (Seager, 2010),

$$D = A_g \left(\frac{R_p}{a} \right)^2 , \tag{5.1}$$

where it is assumed that the light is being measured at a wavelength where thermal emission from the exoplanet is negligible and only reflected starlight is present (Heng & Demory, 2013).

In practice, the geometric albedos of exoplanets are measured over broad photometric bandpasses, rather than at specific wavelengths, for example, those obtained by the CoRoT (e.g. Auvergne et al., 2009, Dang et al., 2018), Kepler (e.g. Borucki et al., 2010, Morris et al., 2024, Heng & Demory, 2013, Heng et al., 2021), CHEOPS (e.g. Benz et al., 2021, Brandeker et al., 2022, Krenn et al., 2023) and TESS (e.g. Ricker et al., 2015, Wong et al., 2021) space telescopes. Almost all of these measurements are of hot Jupiters, due to their large eclipse depths and short periods leading to more significant eclipse depth measurements. Many hot Jupiters have been found to have low albedos, such as HD 189733b (0.076 ± 0.016, CHEOPS, Krenn et al., 2023) and HD 209458b (0.096 ± 0.016, CHEOPS, Brandeker et al., 2022), while some show higher albedos, most likely due to reflective clouds, like Kepler-7 b ($0.25^{+0.01}_{-0.02}$, Kepler, Demory et al., 2011b, Heng et al., 2021, Morris et al., 2024).

Atmospheric processes affect the reflectivity of exoplanet atmospheres. Sudarsky et al. (2000) predicted that hot Jupiters would have small geometric albedos because their high atmospheric temperatures may activate strong absorption of visible light by lines of sodium and potassium. Burrows et al. (2008) calculated albedo models for HD 209458b and HD 189733b and found a model without scattering clouds was able to reproduce the MOST (Microvariability and Oscillations of Stars satellite, Walker et al., 2003) observations (Rowe et al., 2008). Cahoy et al. (2010) modelled the albedos of Jupiter and Neptune analogues and found that clouds influenced the albedo spectra and temperature drove the effects of clouds more than metallicity. Madhusudhan et al. (2012) developed an analytic geometric albedo model framework including three different types of scattering phase functions to investigate the dependence of polarisation of Rayleigh scattering in the atmosphere on the planetary orbital inclination. In Mallonn et al. (2019), they obtained geometric albedo limits for a number of ultra-hot Jupiters and found values consistent with low reflectivity in the optical to near-infrared. Heng et al. (2021) derived a general analytic formula for the geometric albedo, which Brandeker et al. (2022) used to demon-

strate that the $\sim$ 10% geometric albedo of HD 209458b may be explained by scattering from molecular hydrogen and absorption from water and sodium.

The trends between different hot Jupiter properties and their geometric albedos have been a topic of study since the first occultation measurement of TrES-1b in 2005 (Charbonneau et al., 2005). Previous studies have included the set of hot Jupiters observed with Kepler (see, e.g. Heng & Demory, 2013, Angerhausen et al., 2015, Esteves et al., 2015), and with TESS (Wong et al., 2021). They found a tentative positive correlation between dayside temperature and geometric albedo for the planets with $1500 < T_{\rm day} < 3000\,{\rm K}$.

The growing, but heterogeneous, body of albedo measurements constrains the atmospheric physics of these planets. In this work, we investigate the distribution of observed geometric albedos from the TESS, CHEOPS, Kepler and CoRoT missions. We divide the four missions into two groups since CHEOPS, Kepler, and CoRoT (hereafter, CKC) have bandpasses with similar transmittance-weighted mean wavelengths ($\bar{\lambda}$ = 674, 664, 695 nm, respectively), and the TESS bandpass has more transmittance in the red ($\bar{\lambda}$ = 797 nm). We compare the observed albedos with the results from a simplified geometric albedo model (derived from Heng et al., 2021) to answer the following questions:

- Should we expect geometric albedo measurements in different filter bandpasses to have the same underlying distribution?
- Do geometric albedos correlate with equilibrium temperature, planetary surface gravity, stellar metallicity, or effective stellar temperature?
- Do correlations between albedo and planet properties dependent on the photometric bandpass of the measurements (e.g. Kepler, TESS)?
- Does the scatter in albedo observations set constraints on the atmospheric properties of hot Jupiters?

In Section 5.2.1 we describe our data curation methods and the procedure we followed to thermally decontaminate the albedos of targets where that had not been done previously. The curated albedo measurements are shown in Table 5.1. Section 5.2.2 details our theoretical geometric albedo model and the prior assumptions used to produce the albedo distributions we investigate in Section 5.4. In Section 5.3 we investigate whether the observational data is correlated with other system or atmospheric parameters, and to

what significance. We also explore the variations between the TESS and CKC datasets. In Section 5.5.2 we synthesise our findings from both the observations and the modelling and present a flowchart to show what information can be determined from measuring the geometric albedo of a planet.

5.2 Methods

5.2.1 Data curation and thermal decontamination

We divide geometric albedo measurements into two categories: those from the CoRoT, Kepler or CHEOPS missions, which have similar optical filters; and TESS measurements at slightly longer optical wavelengths.

The observed flux coming from the planet can be a combination of reflected starlight and thermal emission from the planet itself. The process of removing thermal emission to compute the albedo is called thermal decontamination (see, e.g. Heng & Demory, 2013). Thermal decontamination was already performed by Wong et al. (2021) for the TESS observations. There were a few objects where only an upper limit was reported. For these planets, we reapplied the thermal decontamination with the same method as in Wong et al. 2021, and kept the full error bars, even if they went below zero, to reduce the statistical bias towards $A_g > 0$. We exclude KELT-1b from consideration, as it is a brown dwarf. We also exclude Kepler-13Ab, as Wong et al. (2021) have shown that the inferred TESS geometric albedo depends heavily on the assumed infrared absorbers.

Many of the CoRoT and Kepler albedos in the literature have not been thermally decontaminated. For these albedos, we decontaminate with:

$$A_g = D\left(\frac{a}{R_p}\right)^2 - \frac{\int F_\lambda \mathcal{T}\, d\lambda}{\int F_{\star,\lambda} \mathcal{T}\, d\lambda}\left(\frac{a}{R_\star}\right)^2, \tag{5.2}$$

where F_λ is the planetary thermal dayside flux as a function of wavelength, $F_{\star,\lambda}$ is the stellar flux as a function of wavelength, and $\mathcal{T}$ is the telescope transmission function. Since these albedos are measured in wide bandpasses, we assume a blackbody for the thermal emission of the planet ($F_\lambda = \pi B_\lambda(T_{\rm day})$), with an integrated dayside hemisphere temperature. Where available, we use dayside temperatures derived from previous Spitzer observations. Many of the CoRoT and Kepler objects have no Spitzer measurements, so we estimate the dayside temperatures with the scaling relationship between $T_{\rm day}$ and the

equilibrium temperature ($T_{\rm eq}$) calibrated by Beatty et al. (2019). We account only for uncertainties on the measured eclipse depths, $T_\star$, $a/R_\star$, $R_p/R_\star$ and $T_{\rm day}$. The list of decontaminated geometric albedo values are reported in Table 5.1.

5.2.2 Modelling the bandpass-integrated geometric albedo

The geometric albedo may be calculated from first principles, if the single-scattering albedo (ω) is known, using the analytical formula derived by Heng et al. (2021),

$$A_g = \frac{\omega}{8}(P_0 - 1) + \frac{\epsilon}{2} + \frac{\epsilon^2}{6} + \frac{\epsilon^3}{24}, \tag{5.3}$$

where $\epsilon = (1-\gamma)/(1+\gamma)$ and $\gamma = \sqrt{1-\omega}$. P_0 is a constant which describes the amount of single-scattering. This formula was derived for a semi-infinite atmosphere (Chandrasekhar, 1960), where the optical depth (but not the spatial distance) transitions from zero to infinity. We construct the single-scattering albedo ω with

$$\omega = \frac{0.9\sigma_{H_2}}{0.9\sigma_{H_2} + \sum X_M \sigma_M}, \tag{5.4}$$

where X_M is the volume mixing ratio (relative abundance by number) of a chemical species M (e.g. water, sodium), and σ_M is the opacity of M. We assume a cloud-free hydrogen-dominated atmosphere consistent with the cosmic abundance of hydrogen and helium, but ignore the scattering and absorption by helium. We assume that the other species have a total mixing ratio well below 1%. We compute mixing ratios X_M with `FastChem` (Stock et al., 2018; 2022, Kitzmann et al., 2024) for several hundred species in chemical equilibrium given the temperature, pressure and metallicity. We retrieve atomic and molecular opacities σ_M from `DACE`[1], which were computed with HELIOS-K (Grimm & Heng, 2015, Grimm et al., 2021). We access opacities and mixing ratios from `DACE` and `FastChem` using the radiative transfer package `shone` (Morris et al., in prep.)[2].

To compute the bandpass-integrated geometric albedo, one needs to integrate the geometric albedo over the bandpass filter, weighted by the stellar spectral flux,

$$\bar{A_g} = \frac{\int A_g(\lambda) F_{\star,\lambda} \mathcal{T}\, d\lambda}{\int F_{\star,\lambda} \mathcal{T}\, d\lambda}. \tag{5.5}$$

We note here that this equation is correct using the TESS transmission filter due to it being an energy counter, however for CoRoT, Kepler and CHEOPS, an additional factor

[1] https://dace.unige.ch

[2] https://github.com/bmorris3/shone

of λ must be applied to both the numerator and denominator as they are photon counters (Rodrigo & Solano, 2020). In our model, for a given stellar effective temperature, we use a PHOENIX spectrum to model the stellar spectral flux $F_{\star,\lambda}$ (Husser et al., 2013).

We begin with a range of metallicities, temperatures and pressures given the measured properties of the planets in Table 5.1, and assume chemical equilibrium to calculate the volume mixing ratios of each species. Planets at high temperatures are more likely to be near chemical equilibrium, but the threshold effective temperature at which this approximation breaks down is not easily specified. We parameterise the gas-phase chemistry by a metallicity, which assumes that the ratios of elemental abundances are locked to their solar values. In practice, chemical equilibrium results in ratios of water to sodium that depend only on the assumed temperature and pressure. We also run a second model with water and sodium abundances that are allowed to deviate from chemical equilibrium.

In this investigation we include species that are: (a) expected to be present in hot Jupiters within the range of equilibrium temperatures in Table 5.1; and (b) have significant absorption bands in the optical. We include H_2O and Na, along with Rayleigh scattering from H_2, and test the effects of adding TiO and VO.

The range of stellar effective temperatures $T_\star$ is guided by the minimum and maximum values corresponding to the objects of our sample: 4550 to 8000 K. We need both the stellar temperature, and also the temperature of the planet at optical depth $\tau \sim 1$ in the atmosphere. The relationship between these temperatures is complex and not known in general, so we sample these two temperatures independently. We use a range of values of the temperatures equal to the range of equilibrium temperatures in our sample (between 1300 and 2700 K), where equilibrium temperature is defined as

$$T_{\rm eq} = T_\star \sqrt{\frac{R_*}{2a}}, \tag{5.6}$$

where R_* is the stellar radius and and a is the semi-major axis. Equilibrium temperature is not the same as the dayside temperature of the planet, however in our simple model, it is enough to guide our chosen temperature range.

We set a prior on metallicity $\log \mathcal{U}(-1, 1)$ based off an empirical scaling relation between metallicity and planetary mass (Swain et al., 2024, Wakeford et al., 2017). The range of pressures used follows the estimated photospheric pressures of hot Jupiters.

5.3 Geometric Albedo Observations

5.3.1 Observed geometric albedo trends

The set of observed geometric albedos are reported in Table 5.1. In total there are 17 targets in the CKC band and 19 in the TESS band. We divide the objects into two section: those in the top section have their albedos taken directly from previous analyses (where thermal decontamination has been carried out); and in the bottom half, we used eclipse depths and dayside temperatures from the enumerated references to decontaminate the geometric albedos (see method in Section 5.2.1). All of the targets are within the warm to hot Jupiter regime with equilibrium temperatures ranging from 1179±11 K to 2764±37 K.

Caption for Table 5.1: Collection of hot Jupiter exoplanets with their reported geometric albedo (A_g) and other stellar and planetary parameters. Objects in the top half of the table have their albedos taken directly from previous analyses (where thermal decontamination has been carried out). For objects in the lower half, using measured eclipse depths and dayside temperatures from the references specified, we have calculated the thermally decontaminated geometric albedos (see method in Section 5.2.1). The 'Band' column details which bandpass the planet's eclipse depth was measured in, and therefore which bandpass the geometric albedo corresponds to. $T_{\rm eq}$ refers to the equilibrium temperature of the planet, calculated from the other values in this table using equation 5.6.[(a)]Bonomo et al. (2017), [(b)]Barge et al. (2008), [(c)]Deming et al. (2011), [(d)]Alonso et al. (2009), [(e)]Alonso et al. (2008), [(f)]Dang et al. (2018), [(g)]Esteves et al. (2015), [(h)]Morris et al. (2024), [(i)]Wong et al. (2021), [(j)]Patel & Espinoza (2022), [(k)]Collins et al. (2017), [(l)]Désert et al. (2011), [(m)]Heng et al. (2021), [(n)]Beatty et al. (2019), [(o)]Fortney et al. (2011), [(p)]Lillo-Box et al. (2014), [(q)]Wong et al. (2020a), [(r)]Collier Cameron et al. (2010), [(s)]von Essen et al. (2020), [(t)]Turner et al. (2016), [(u)]Sousa et al. (2018), [(v)]Delrez et al. (2016), [(w)]Bourrier et al. (2020), [(x)]Lendl et al. (2020), [(y)]Deline et al. (2022), [(z)]Brandeker et al. (2022), [(α)]Sousa et al. (2021), [(β)]Krenn et al. (2023)

Table 5.1 | See caption above

Object	T_* [K]	Fe/H	$T_{\rm eq}$ [K]	log(g) [cgs]	a/R_*	Band	A_g
CoRotT-2b	$5625 \pm 120^{(a)}$	$0.0 \pm 0.1^{(a)}$	1556 ± 27	$3.58 \pm 0.03^{(e)}$	$6.70 \pm 0.03^{(e)}$	Corot	$0.08^{+0.08(f)}_{-0.04}$
HAT-P-7b	$6350 \pm 80^{(a)}$	$0.26 \pm 0.08^{(a)}$	2264 ± 21	$3.30 \pm 0.09^{(g)}$	$4.1545^{+0.0029(g)}_{-0.0025}$	Kepler	$0.09 \pm 0.02^{(h)}$
Kepler-7b	$5933 \pm 50^{(a)}$	$0.11 \pm 0.05^{(a)}$	1670 ± 17	$2.612 \pm 0.052^{(a)}$	$6.637 \pm 0.021^{(g)}$	Kepler	$0.25^{+0.01(m)}_{-0.02}$
Kepler-41b	$5750 \pm 100^{(a)}$	$0.38 \pm 0.11^{(a)}$	1808 ± 32	$2.926 \pm 0.057^{(a)}$	$5.053 \pm 0.021^{(g)}$	Kepler	$0.13^{+0.01(h)}_{-0.02}$
Qatar-1b	$5013^{+93(k)}_{-88}$	$0.171 \pm 0.096^{(k)}$	1400 ± 28	$3.39 \pm 0.03^{(k)}$	$6.41^{+0.11(i)}_{-0.10}$	TESS	$0.14 \pm 0.11^{(i)}$
TrES-2b	$5850 \pm 50^{(a)}$	$-0.15 \pm 0.1^{(a)}$	1458 ± 18	$3.30 \pm 0.03^{(a)}$	$7.903^{+0.019(g)}_{-0.016}$	Kepler	$0.01^{+0.00(h)}_{-0.01}$
TrES-3b	$5650 \pm 75^{(a)}$	$-0.19 \pm 0.08^{(a)}$	1613 ± 50	$3.40 \pm 0.03^{(a)}$	$5.82^{+0.12(j)}_{-0.13}$	TESS	$0.14 \pm 0.13^{(i)}$
WASP-4b	$5436 \pm 34^{(a)}$	$-0.05 \pm 0.04^{(a)}$	1648 ± 13	$3.213 \pm 0.098^{(a)}$	$5.438^{+0.044(q)}_{-0.057}$	TESS	$0.09 \pm 0.09^{(q)}$
WASP-5b	$5770 \pm 65^{(a)}$	$0.09 \pm 0.04^{(a)}$	1762 ± 41	$3.455 \pm 0.043^{(a)}$	$5.36 \pm 0.22^{(q)}$	TESS	$0.0002^{+0.166(q)}_{-0.174}$
WASP-12b	$6250 \pm 100^{(a)}$	$0.32 \pm 0.12^{(a)}$	2526 ± 48	$3.015 \pm 0.059^{(a)}$	$3.062^{+0.063(i)}_{-0.066}$	TESS	$0.13 \pm 0.06^{(i)}$
WASP-19b	$5500 \pm 100^{(a)}$	$0.02 \pm 0.09^{(a)}$	2055 ± 42	$3.222 \pm 0.048^{(a)}$	$3.582^{+0.074(q)}_{-0.067}$	TESS	$0.17 \pm 0.07^{(q)}$
WASP-33b	$7430 \pm 100^{(r)}$	$0.1 \pm 0.2^{(r)}$	2764 ± 37	$3.459 \pm 0.098^{(t)}$	$3.614 \pm 0.009^{(s)}$	TESS	$-0.04 \pm 0.04^{(s)}$
WASP-36b	$5900 \pm 150^{(a)}$	$-0.26 \pm 0.1^{(a)}$	1738 ± 59	$3.540 \pm 0.023^{(a)}$	$5.76^{+0.26(q)}_{-0.27}$	TESS	$0.16 \pm 0.15^{(q)}$
WASP-43b	$4798 \pm 216^{(u)}$	$-0.13 \pm 0.08^{(u)}$	1559 ± 71	$3.675 \pm 0.019^{(a)}$	$4.734^{+0.054(q)}_{-0.053}$	TESS	$0.13 \pm 0.06^{(q)}$
WASP-46b	$5725 \pm 39^{(u)}$	$-0.18 \pm 0.03^{(u)}$	1630 ± 36	$3.533 \pm 0.036^{(a)}$	$6.17^{+0.28(q)}_{-0.24}$	TESS	$0.38 \pm 0.27^{(q)}$
WASP-64b	$5550 \pm 150^{(a)}$	$-0.08 \pm 0.11^{(a)}$	1669 ± 54	$3.272 \pm 0.038^{(a)}$	$5.53^{+0.14(q)}_{-0.25}$	TESS	$0.38 \pm 0.26^{(q)}$
WASP-77Ab	$5500 \pm 80^{(a)}$	$0.00 \pm 0.11^{(a)}$	1712 ± 30	$3.475 \pm 0.020^{(a)}$	$5.162^{+0.120(q)}_{-0.080}$	TESS	$0.06 \pm 0.05^{(q)}$
WASP-100b	$6900 \pm 120^{(a)}$	$-0.03 \pm 0.1^{(a)}$	2102 ± 39	$3.24 \pm 0.14^{(a)}$	$5.389 \pm 0.064^{(q)}$	TESS	$0.22 \pm 0.08^{(q)}$
WASP-121b	$6460 \pm 140^{(v)}$	$0.13 \pm 0.09^{(v)}$	2339 ± 51	$2.970 \pm 0.017^{(w)}$	$3.815^{+0.018(q)}_{-0.032}$	TESS	$0.26 \pm 0.06^{(q)}$
HD209458b	$6065 \pm 50^{(a)}$	$0.00 \pm 0.05^{(a)}$	1445 ± 13	$2.958 \pm 0.013^{(a)}$	$8.807 \pm 0.051^{(z)}$	CHEOPS	$0.096 \pm 0.016^{(z)}$
HD189733b	$4969 \pm 48^{(\alpha)}$	$-0.08 \pm 0.03^{(\alpha)}$	1179 ± 11	$3.332 \pm 0.026^{(a)}$	$8.8843 \pm 0.0175^{(\beta)}$	CHEOPS	$0.076 \pm 0.016^{(\beta)}$
CoRoT-1b	$6298 \pm 66^{(a)}$	$0.06 \pm 0.07^{(a)}$	2039 ± 24	$3.06 \pm 0.07^{(b)}$	$4.92 \pm 0.08^{(b)}$	Corot	$0.064^{+0.110(c,d)}_{-0.139}$
HAT-P-7b	$6350 \pm 80^{(a)}$	$0.26 \pm 0.08^{(a)}$	2264 ± 21	$3.30 \pm 0.09^{(g)}$	$4.1545^{+0.0029(g)}_{-0.0025}$	TESS	$0.078^{+0.102(i)}_{-0.103}$
Kepler-5b	$6297 \pm 60^{(a)}$	$0.04 \pm 0.06^{(a)}$	1763 ± 17	$3.410 \pm 0.034^{(a)}$	$6.450^{+0.021(g)}_{-0.025}$	Kepler	$0.097 \pm 0.037^{(g,l)}$
Kepler-6b	$5647 \pm 44^{(a)}$	$0.34 \pm 0.04^{(a)}$	1461 ± 16	$3.062 \pm 0.018^{(a)}$	$7.503 \pm 0.022^{(g)}$	Kepler	$0.059 \pm 0.035^{(g,l)}$
Kepler-8b	$6210 \pm 150^{(a)}$	$-0.055 \pm 0.03^{(a)}$	1669 ± 16	$2.84 \pm 0.12^{(a)}$	$6.854^{+0.018(g)}_{-0.017}$	Kepler	$0.109^{+0.050(g,n)}_{-0.052}$
Kepler-12b	$5950 \pm 100^{(a)}$	$0.07 \pm 0.04^{(a)}$	1480 ± 15	$2.572 \pm 0.045^{(a)}$	$8.019^{+0.014(g)}_{-0.013}$	Kepler	$0.084 \pm 0.040^{(g,o)}$
Kepler-43b	$6050 \pm 100^{(a)}$	$0.4 \pm 0.1^{(a)}$	1620 ± 27	$3.766 \pm 0.028^{(a)}$	$6.975^{+0.041(g)}_{-0.047}$	Kepler	$0.036 \pm 0.250^{(g,n)}$
Kepler-76b	$6409 \pm 95^{(a)}$	$-0.1 \pm 0.2^{(a)}$	2145 ± 33	$3.499 \pm 0.082^{(a)}$	$4.464^{+0.041(g)}_{-0.049}$	Kepler	$0.148^{+0.028(g,n)}_{-0.025}$
Kepler-91b	$4550 \pm 75^{(p)}$	$0.11 \pm 0.07^{(p)}$	2036 ± 38	$3.0 \pm 0.1^{(g)}$	$2.496^{+0.043(g)}_{-0.050}$	Kepler	$0.362^{+0.250(g,n)}_{-0.234}$
Kepler-412b	$5750 \pm 90^{(a)}$	$0.27 \pm 0.12^{(a)}$	1848 ± 29	$3.117 \pm 0.043^{(a)}$	$4.841^{+0.023(g)}_{-0.024}$	Kepler	$0.066^{+0.047(g,n)}_{-0.042}$
WASP-3b	$6400 \pm 100^{(a)}$	$0.0 \pm 0.2^{(a)}$	1947 ± 46	$3.368 \pm 0.039^{(a)}$	$5.40 \pm 0.19^{(i)}$	TESS	$0.181^{+0.190(i)}_{-0.197}$
WASP-5b	$5770 \pm 65^{(a)}$	$0.09 \pm 0.04^{(a)}$	1762 ± 41	$3.455 \pm 0.043^{(a)}$	$5.36 \pm 0.22^{(q)}$	TESS	$0.0002^{+0.166(q)}_{-0.174}$
WASP-18b	$6400 \pm 100^{(a)}$	$0.00 \pm 0.09^{(a)}$	2406 ± 40	$4.323 \pm 0.058^{(a)}$	$3.539^{+0.039(q)}_{-0.035}$	TESS	$-0.038^{+0.076(q)}_{-0.070}$
WASP-78b	$6100 \pm 150^{(a)}$	$-0.35 \pm 0.14^{(a)}$	2219 ± 59	$2.903 \pm 0.064^{(a)}$	$3.778^{+0.060(q)}_{-0.098}$	TESS	$0.189^{+0.207(q)}_{-0.211}$
WASP-189b	$8000 \pm 80^{(x)}$	$0.29 \pm 0.13^{(x)}$	2641 ± 28	$3.27 \pm 0.05^{(x)}$	$4.587^{+0.037(y)}_{-0.034}$	CHEOPS	$0.202^{+0.046(n,y)}_{-0.048}$

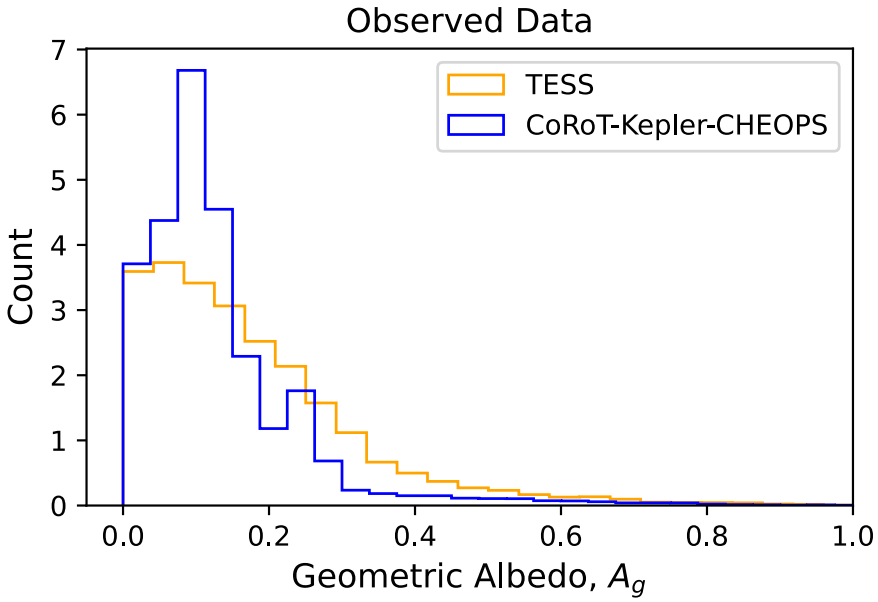

Figure 5.1 | The distribution of observed geometric albedos for both bandpasses (CoRoT-Kepler-CHEOPS (CKC) in blue and TESS in orange), where each observation (from Table 5.1) is treated as a Gaussian distribution with a width given by the 1-sigma uncertainty reported. This histogram plot is made from 10,000 samples of each observation and then normalised. The CKC sample peaks around $A_g = 0.1$ whereas the TESS sample has a wider peak and has a maximum at $A_g = 0$. However, this could be a result of the much wider errorbars in the TESS data, smoothing out any peaks.

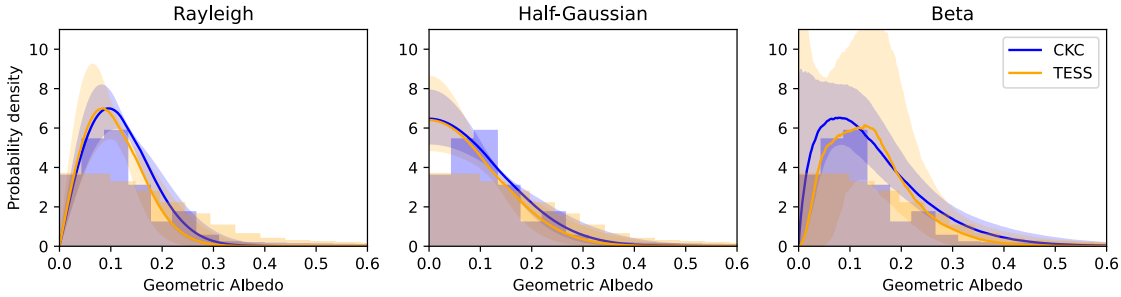

Figure 5.2 | Three panels show the best-fit models (Rayleigh, half-Gaussian and Beta distributions) plotted over the observed geometric albedos, with the shading showing the 1σ uncertainties in the fits. In orange is the TESS band and in the blue, the CKC band. We find that the best-fit models from the two bandpasses are consistent. We also find that, by calculating the BIC of each fit, that the Rayleigh distribution is the best-fitting model for this data (although not very significantly) and the Beta distribution the worst.

The set of geometric albedos in each bandpass group is shown in Figure 5.1. We draw 10,000 samples from the geometric albedo posterior distribution, assuming a Gaussian distribution with means and standard deviations defined by the observation and its uncertainty. Since the observations have large uncertainties that may extend to negative albedos (so that we didn't bias our fitting procedures), we take the absolute value before comparing to the model posteriors. The TESS albedo posterior samples peak at zero and the CKC samples peak around $A_g = 0.1$. The CKC samples also have a narrower peak than the TESS samples, however this width will be very dependent on the uncertainties of the observations. This more positive peak of the bluer bandpasses is, however, in line with expectations, because scattering affects the blue end of the spectrum.

Following a similar approach to Sagear & Ballard (2023), we compare these observed albedo distributions with three empirical albedo distribution models within a hierarchical Bayesian framework. The hypothetical, empirical albedo distributions are Rayleigh, half-Gaussian and Beta distributions, chosen for their simplicity, and to test whether the albedo distributions go to zero counts at zero albedo or not. The Rayleigh and half-Gaussian functions have only one free parameter, σ, and the Beta function has two parameters, a and b. The likelihood functions for each distribution can be found in Appendix 5.A. The best-fit models are shown in Figure 5.2 and Table 5.2 details the best-fit parameter values for the CKC and TESS dataset.

We compare the Bayesian Information Criterion (BIC) between each albedo distribu-

Table 5.2 | Results of fitting different distributions to the observed geometric albedo data (see Figure 5.2). We fit independent distributions to the CKC and TESS datasets. Both Rayleigh and the half-Gaussian distribution have only 1 free parameter (σ) whereas the Beta distribution has two (a, b), which we fit for in log space to improve the efficiency of our sampling. The best-fit values show that all parameters are consistent across bandpass, indicating the distributions (CKC and TESS) are not significantly different. The BIC results show the three models fit the data similarly well, as the values are all within 10 points of each other. However we still do see, and one can confirm this by eye by looking at Figure 5.2, that the Rayleigh distribution performs the best for both bandpass datasets, as it has the lowest BIC value.

Distribution	Parameter	Best-fit value	BIC
Rayleigh	$\sigma_{\rm CH}$	0.088 ± 0.013	-336.2
	$\sigma_{\rm T}$	0.089 ± 0.021	-349.3
Half-Gaussian	$\sigma_{\rm CH}$	0.128 ± 0.027	-335.4
	$\sigma_{\rm T}$	0.129 ± 0.037	-348.7
Beta	($\log(a_{\rm CH})$, $\log(b_{\rm CH})$)	(0.264 ± 0.209, 1.221 ± 0.216)	-333.3
	($\log(a_{\rm T})$, $\log(b_{\rm T})$)	(0.509 ± 0.528 1.488 ± 0.496)	-346.3

tion model, and find that no model is strongly preferred. The Rayleigh function has the smallest BIC, for both CKC and TESS data, and the Beta function has the highest. From the difference between the CKC and TESS distributions, we see that the best-fit parameters are consistent with each other. Again following Sagear & Ballard (2023), we use the probability ratio:

$$R = \frac{P(D_1 D_2|H_1)}{P(D_1|H_0)P(D_2|H_0)}, \tag{5.7}$$

to evaluate whether a joint fit to the CKC and TESS datasets is preferred over individual fits. Here D_1 and D_2 represent the CKC and TESS geometric albedos and hypothesis H_1 states that a joint fit is best to fit these datasets, whilst H_0 states that individual fits to

the datasets is best. $P(D_1|H_0)$ and $P(D_2|H_0)$ are the likelihoods of the best-fit models to the individual datasets and $P(D_1D_2|H_1)$ is the likelihood of the best-fit joint model. If a joint fit is preferred, this gives us evidence that the samples are from the same underlying distribution. For the Rayleigh model we obtain $\ln(R) = 9.27$, for half-Gaussian $\ln(R) = 9.41$ and for Beta $\ln(R) = -19.1$. The two best-fitting models have positive values for $\ln(R)$, which implies that the joint fit likelihood is higher than the combined individual fits. We conclude there is no evidence for a difference in the underlying distributions of the TESS vs CKC-measured geometric albedos.

Next, we take the set of thermally decontaminated albedos and investigate whether they show any correlation with other system parameters. We show the albedos plotted against these parameters in Figure 5.3. We fit both a constant and a linear model to the geometric albedos as a function of a range of parameters, taking into account the uncertainties in both the system parameters and the albedos, with `emcee` (Hogg et al., 2010, Foreman-Mackey et al., 2013). The albedo uncertainties are likely underestimated in this decontamination process, so we include an error bar scaling factor as a free parameter. These fits are intended for finding first-order trends – we note that the linear fits allow non-physical, negative albedos. We show the BIC (Bayesian Information Criterion) results of these model comparisons in Table 5.3.

The uncertainties of the geometric albedos are large compared to the range of possible values (between 0 and 1). In general, the uncertainties for the TESS measurements have larger error bars than the CKC measurements. This is partially due to the error on the reported eclipse depth. Most of the Kepler objects have very tight constraints on their eclipse depths, due to the high number of eclipses per object. The slopes of these linear fits are sensitive to the measurements at the extremes. Typically ΔBIC is less than 10 between constant and linear models, suggesting no preference for correlations. There is a weak preference for the linear model with $\log(g)$ and [Fe/H] in the CKC band (where ΔBIC=12.1).

Whilst the albedo measurements show little or no correlations with system parameters, the geometric albedo measurements are very uncertain. Another reason for this uncertainty comes from the thermal decontamination procedure, which often involves multiple assumptions (e.g. blackbody planets) and very uncertain dayside temperature measurements due to limited infrared observations. Emitted flux scales with T^4, so these

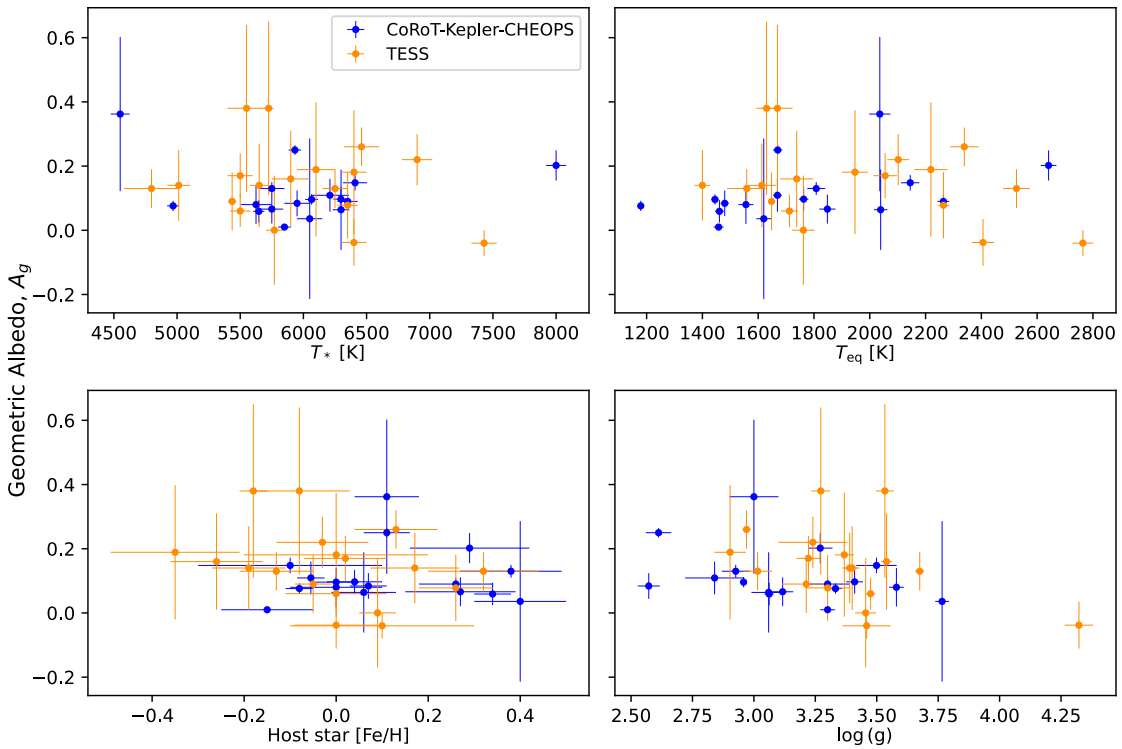

Figure 5.3 | Geometric albedos and physical parameters for targets observed with CoRoT-Kepler-CHEOPS (blue points) and TESS (orange points). The trend results can be found in Table 5.3. Note here we are using the stellar metallicity as a proxy for planetary metallicity.

Table 5.3 | Result of the trend analysis of the observed geometric albedos versus various stellar/planetary parameters ('Independent Variable' in this table). As explained in Section 5.3, we fit two different trends to the geometric albedo data: a constant and a linear trend, considering uncertainties in both the albedo and free parameter. We calculated the BIC difference between these two models for each free parameters and for each bandpass dataset. Typically, a ΔBIC < 10 is considered not significant. Overall, we find no significant trends. There is a slight preference for a linear model across the different variables, however since the ΔBIC is mostly below 10, this is not significant. If the model can't choose between a constant or a linear trend, then we conclude there is little evidence to suggest the data shows a correlation. The only combination where there is a $\Delta BIC > 10$ is the CKC albedos as a function of log(g). Physically, this could be interesting, however, looking at the data, it is clear that the trend is mostly driven by the few outer points at the low and high end of the log(g) space. At this point, more precise data across the full range of the free parameter is needed to confirm this correlation.

Independent Variable	Band	Linear model BIC	Constant model BIC	Δ BIC
$T_\star$	TESS	-49.0	-48.4	0.6
	CHEOPS-Kepler-CoRoT	-38.0	-40.2	-2.2
$T_{\rm eq}$	TESS	-48.9	-48.4	0.50
	CHEOPS-Kepler-CoRoT	-41.8	-40.2	1.6
Log(g)	TESS	-54.4	-48.4	6.0
	CHEOPS-Kepler-CoRoT	-52.3	-40.2	12.1
[Fe/H]	TESS	-46.7	-48.5	-1.8
	CHEOPS-Kepler-CoRoT	-49.3	-40.2	9.1

uncertainties propagate through to the geometric albedo. A more correct thermal decontamination approach would use the full planetary emission spectrum, but almost none of these planets, to date, have full SED measurements from, e.g., JWST.

5.4 Theoretical model results

5.4.1 Geometric albedos in chemical equilibrium

We began our modelling efforts by assuming chemical equilibrium in the planet's atmosphere (see Section 5.2.2 for model details). Table 5.4 details the priors used for the sampling distributions. We sampled over $T_\star$, $T_{\rm planet}$, pressure and metallicity (i.e. the

observed atmospheric metallicity).

Table 5.4 | Priors distributions for the input to our geometric albedo model assuming chemical equilibrium. This model includes H_2O and Na.

Parameter	Assumed distribution
$T_\star$	$\mathcal{U}(4550, 8000)$ K
$T_{\rm planet}$	$\mathcal{U}(1300, 2700)$ K
pressure	$\log \mathcal{U}(-3, -1)$ bar
$[M/H]$	$\log \mathcal{U}(-1, 1)$

Figure 5.4 shows the results in the CHEOPS and TESS bandpass. Abundances of the species are not free parameters themselves, but are calculated from the M/H ratio, pressure and temperature. As we have already mentioned, the use of a single number (the metallicity) to describe the gas-phase chemical abundances is a simple assumption. The metallicity is correlated with the geometric albedo due to larger abundances of absorbing molecules increasing the opacity in the atmosphere. From our results it is clear that water and sodium have strong and similar effects on suppressing the albedo. For the same chemical abundances, we generally measure a lower A_g in the TESS bandpass than the CHEOPS bandpass. Interestingly, the albedo distributions from the different bandpasses have little overlap. The most reflective planet in the TESS bandpass almost always has a lower albedo than the least reflective planet in CHEOPS bandpass. This is not borne out by the observations. We do not show the albedos as a function of T_*, $T_{\rm planet}$ and pressure, as these show no discernible correlation.

5.4.2 Geometric albedos out of equilibrium

Next, we relax the assumption that the planet's atmosphere is in chemical equilibrium, using the priors in Table 5.5. To parameterise the disequilibrium, we use a scaling factor to perturb the mixing ratios of each species relative to the equilibrium value. We independently sample over a distribution of 'scaling factors' which has the form of $\log \mathcal{U}[-1, 1]$ in log space for both sodium and water. Our results are shown in Figure 5.5. We find similar trends as in Section 5.4.1, however with a larger scatter of A_g for a fixed chemical abundance.

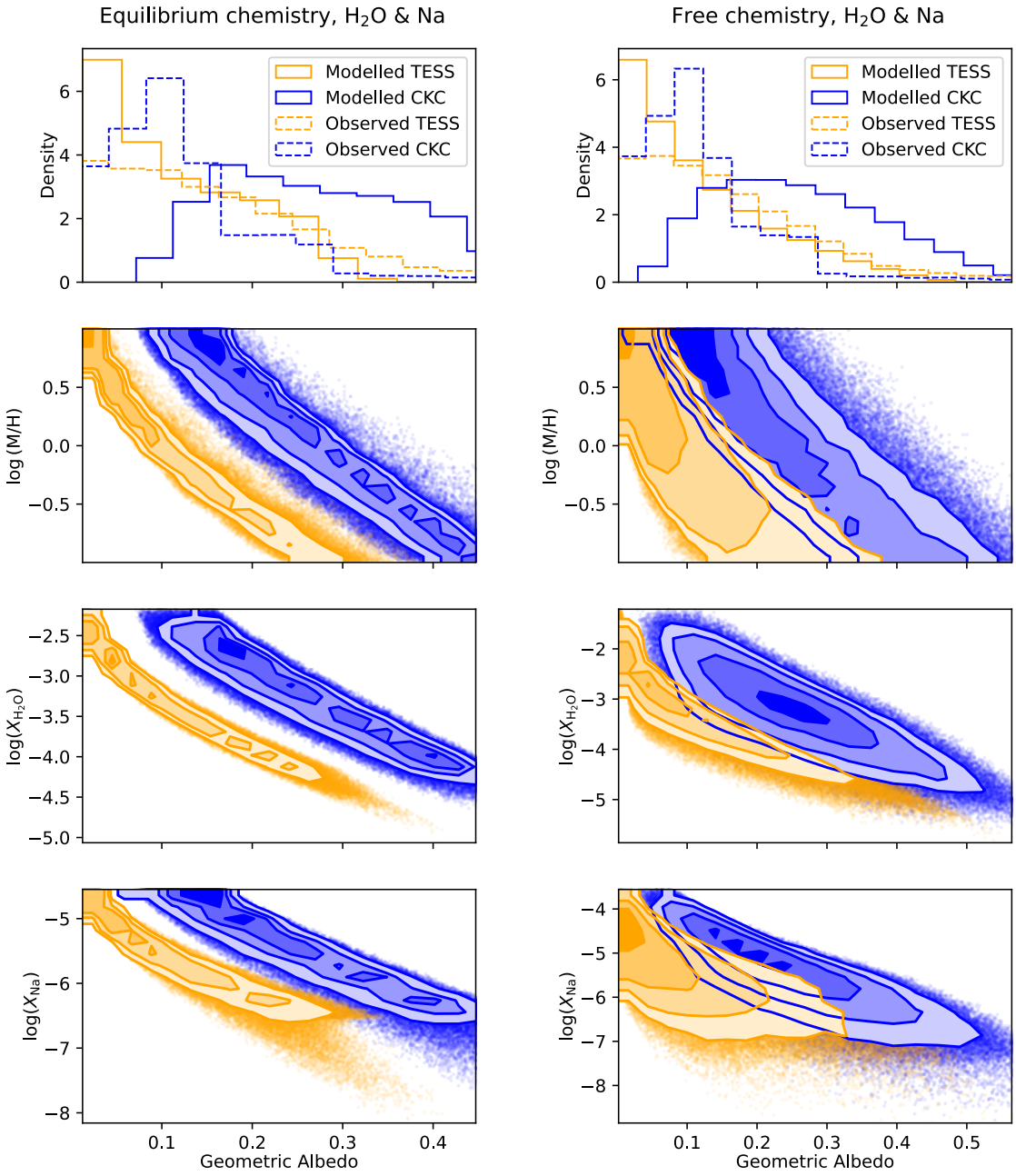

Figure 5.4 | Geometric albedo model results, produced by sampling over the input parameter prior distributions (see Table 5.4) and assuming chemical equilibrium. The wavelength-dependent albedos were then bandpass-integrated to produce the expected albedos in the TESS (orange) and CKC (blue) band. Not shown are the albedos as a function of T_*, $T_{\rm planet}$ and pressure, as these show no discernible correlation. We find that the metallicity (log [M/H]) has the largest impact on the geometric albedo and that from this, water abundance produces slightly tighter constraints on A_g than sodium. We also see very distinct differences between the CHEOPS and TESS bandpasses.

Figure 5.5 | Geometric albedo model results, produced by sampling over the input parameter prior distributions (see Table 5.5) and using a scaling factor distribution to move the model away from chemical equilibrium. The wavelength-dependent albedos were then bandpass-integrated to produce the expected albedos in the TESS (orange) and CKC (blue) band. We find similar results to the chemical equilibrium model: temperature and pressure had no effect on the geometric albedo (so they are not shown here), and metallicity is the main driver. Due to increased parameter space from the relaxation of the chemical equilibrium constraint, the posteriors of TESS and CKC albedos are now wider and begin to overlap slightly. It is clear that the higher the metallicity, the lower the geometric albedo.

Table 5.5 | Priors distributions for the input to our geometric albedo model with chemical abundances scaling factors to shift the model away from chemical equilibrium. This model includes H_2O and Na.

Parameter	Assumed distribution
$T_\star$	$\mathcal{U}(4550, 8000)$ K
$T_{\rm planet}$	$\mathcal{U}(1300, 2700)$ K
pressure	$\log \mathcal{U}(-3, -1)$ bar
$[M/H]$	$\log \mathcal{U}(-1, 1)$
scale X_{H_2O}	$\log \mathcal{U}(-1, 1)$
scale $X_{\rm Na}$	$\log \mathcal{U}(-1, 1)$

Due to the increased scatter, the values of A_g in the TESS and CHEOPS bandpass are permitted to overlap. However it is still clear that, on average, the albedos from CHEOPS are higher than from TESS. From the width of the posterior distributions, we observe that water has a stronger influence than sodium in the TESS bandpass and they both have similar-strength correlations in the CHEOPS band. It is perhaps expected that water would have a stronger influence, due to having a larger number of absorption lines in the optical than sodium.

5.4.3 Does the theoretical model match the observations?

We reproduce the range of albedos observed with TESS and CKC using a model with only H_2, water and sodium. In our model simulations, the very low metallicity planets produce low albedos, in both the CHEOPS and TESS band, because there are too few absorbers to stop the Rayleigh scattering from dominating. This strong correlation between albedo and metallicity is not mirrored in the observations, if we assume the stellar metallicity is equal or correlated to the planet's metallicity. However there are huge uncertainties on the stellar metallicity measurements, making it very difficult to detect any trends. From planet formation, stellar metallicity and planetary metallicity share no simple linear relation, especially if there is condensation involved which acts to remove metals from the gas phase. We also find no significant correlation with the stellar temperature, planetary temperature or pressure. Over the range considered, these parameters only have a very

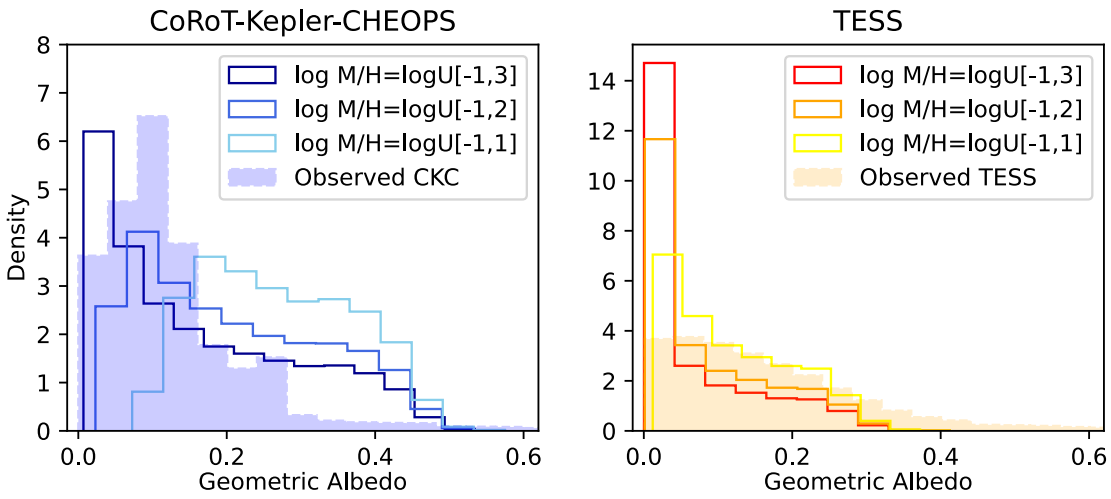

Figure 5.6 | The assumed priors for the underlying abundances of water and sodium have a large influence on the modelled geometric albedo. On the left panel we show the distributions in the CHEOPS bandpass, and on the right we show the distributions in the TESS bandpass. We overlay the observed distribution to suggest perhaps the underlying effective metallicity distribution is within these ranges, however we are also very aware that the uncertainties of the observations highly influence this shape (due to the low number of observations).

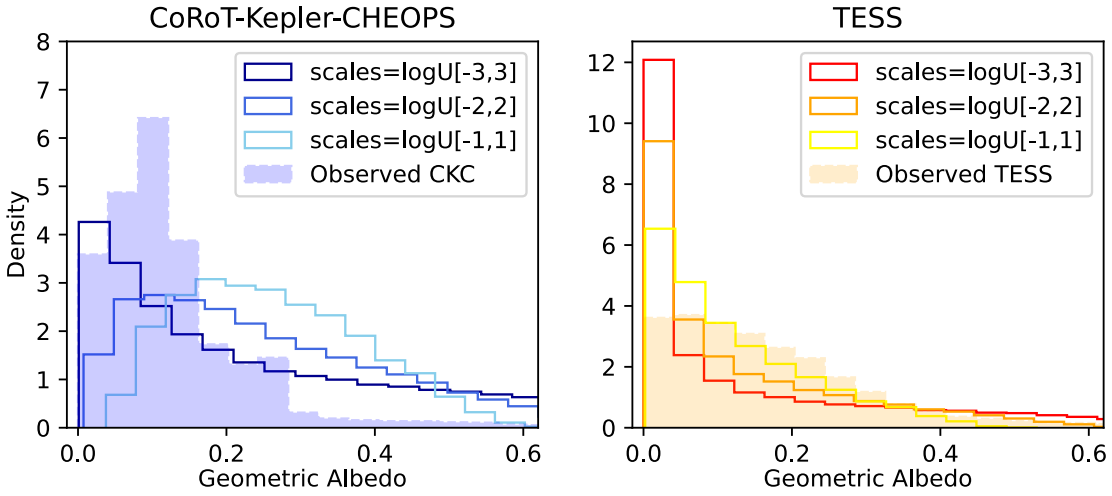

Figure 5.7 | How far away from equilibrium the abundances of water and sodium are permitted to go have a large influence on the modelled geometric albedo. This is mostly due to the fact larger metallicities can be explored with a larger scaling prior. On the left panel we show the distributions in the CHEOPS bandpass, and on the right we show the distributions in the TESS bandpass. Here we keep the metallicity distribution fixed to $\log \mathcal{U}[-1, 1]$. We overlay the observed distribution.

small effect on the cross-section of the chemical species and so it is expected that they should not have a significant influence on A_g.

The comparison between the theoretical and observed distributions is very informative. We find both similarities and differences between the shapes of the distributions, for example, the peak of the modelled CKC results is at a higher albedo than the TESS distribution. A physical explanation for this could be due the TESS bandpass having more optical absorption lines than the CKC band, reducing the overall albedo of the targets. Although this matches what we find in the data, we believe the observed sample size is too small to trust this as a result. More observations would be needed to confirm this hypothesis. We also find that, due to the metallicity constraints, the CKC modelled distribution does not reach zero. In Figure 5.6, we show how the distributions depend on the assumed metallicity prior. The higher the metallicities probed, the greater a pile-up of albedos at zero. In Figure 5.7, we show how increasing the distance the model can probe away from chemical equilibrium changes the shape of the modelled distributions. This is mostly due to the fact that larger metallicities can be explored with a larger scaling prior.

5.4.4 Theoretical models with more absorbers

Based on the analogy to brown dwarfs, Fortney et al. (2008) predicted the existence of two classes of hot Jupiters based on the absence or presence of TiO and VO. Whilst there has been a handful of confirmed detections of TiO or VO in hot Jupiters to date (see, e.g. Nugroho et al., 2017, Chen et al., 2021), the prediction of Fortney et al. (2008) is not widely supported. One possible reason is the sequestration of titanium and vanadium into condensates by a "cold trap" on the nightside of hot Jupiters (see, e.g. Parmentier et al., 2013). If they are condensed, then they would not contribute to the stellar absorption in the atmosphere, in the way our model works. Therefore, even if the initial abundances of TiO and VO are correctly predicted by gas-phase equilibrium chemistry, their final abundances are controlled by atmospheric dynamics and condensation. Nevertheless, we test the effects of TiO and VO by allowing their abundances to be scaled by a factor relative to chemical equilibrium. We assume that condensation is a key process, so we do not let the scaling factors of TiO or VO be greater than 1 (or 0 in log-space). For the other species and parameters, we use similar priors to the other models (see Table 5.6). Our results are shown in Figure 5.8. We see that including these strong-optical absorbers, even at small abundances, drastically reduces the observed geometric albedo. We find that these distributions are very different from the observed distribution, in both the CHEOPS and TESS bandpass. This is evidence to support the absence of TiO and VO in hot Jupiter atmospheres.

5.5 Discussion

5.5.1 Geometric albedos are primarily determined by the abundance of absorbers

Using our geometric albedo model (Section 5.2.2), we have shown evidence that the abundances of absorbing chemical species in the atmosphere (or 'effective' metallicity) is one of the main drivers for determining the geometric albedo of a planet. From Figure 5.8, we see that when (optical) absorbers are abundant in the atmosphere, the (optical) geometric albedo is low. The exact correlation depends on which absorbers are present and whether the atmosphere is near chemical equilibrium or not.

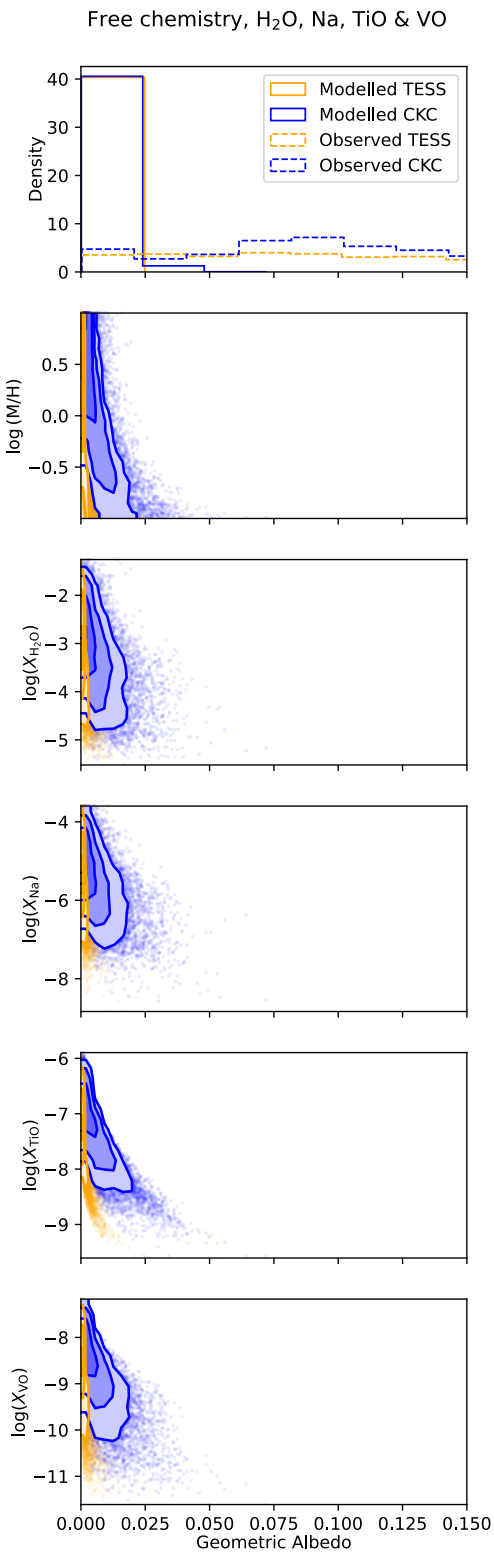

Figure 5.8 | Geometric albedo model results, produced by sampling over the input parameter prior distributions (see Table 5.6) and using a scaling factor distribution to move the model away from chemical equilibrium. The wavelength-dependent albedos were then bandpass-integrated to produce the expected albedos in the TESS (orange) and CKC (blue) band. We find that the presence of additional optical absorbers forces the albedo to stay near zero, even when the metallicity is low.

Table 5.6 | Priors distributions for the input to our geometric albedo model with chemical abundance scaling factors to shift the model away from chemical equilibrium. This model includes H_2O, Na, TiO and VO.

Parameter	Assumed distribution
$T_\star$	$\mathcal{U}(4550, 8000)$ K
$T_{\rm planet}$	$\mathcal{U}(1300, 2700)$ K
pressure	$\log \mathcal{U}(-3, -1)$ bar
$[M/H]$	$\log \mathcal{U}(-1, 1)$
scale X_{H_2O}	$\log \mathcal{U}(-1, 1)$
scale $X_{\rm Na}$	$\log \mathcal{U}(-1, 1)$
scale $X_{\rm TiO}$	$\log \mathcal{U}(-1, 0)$
scale $X_{\rm VO}$	$\log \mathcal{U}(-1, 0)$

The other potential correlates that we considered were atmospheric temperature, pressure and stellar temperature. We found no significant correlation between these parameters and the geometric albedo, within the ranges set by our observations. This is because the opacities of the atmospheric species do not vary significantly within this temperature and pressure range. Temperature has more of an impact on the volume-mixing ratio, however, but the change is insufficient to affect the bandpass-integrated albedo. One caveat here is that the model does not assume a correlation between stellar temperature and planet temperature, as this is beyond the scope of the model. Another caveat is that our model does not feature clouds, which, if present, may be more dependent on temperature and pressure and therefore influence the geometric albedo more significantly (see Section below).

5.5.2 What this means for atmospheric characterisation

We have summarised our model results in Figure 5.9. The steps are outlined as follows:

- First, measure the optical geometric albedo of the planet.
- If the albedo is high ($A_g \gtrsim 0.2$), then the planetary atmosphere likely produces significant scattering (to scatter the starlight back into space), or it has few absorbers (allowing Rayleigh scattering to dominate).

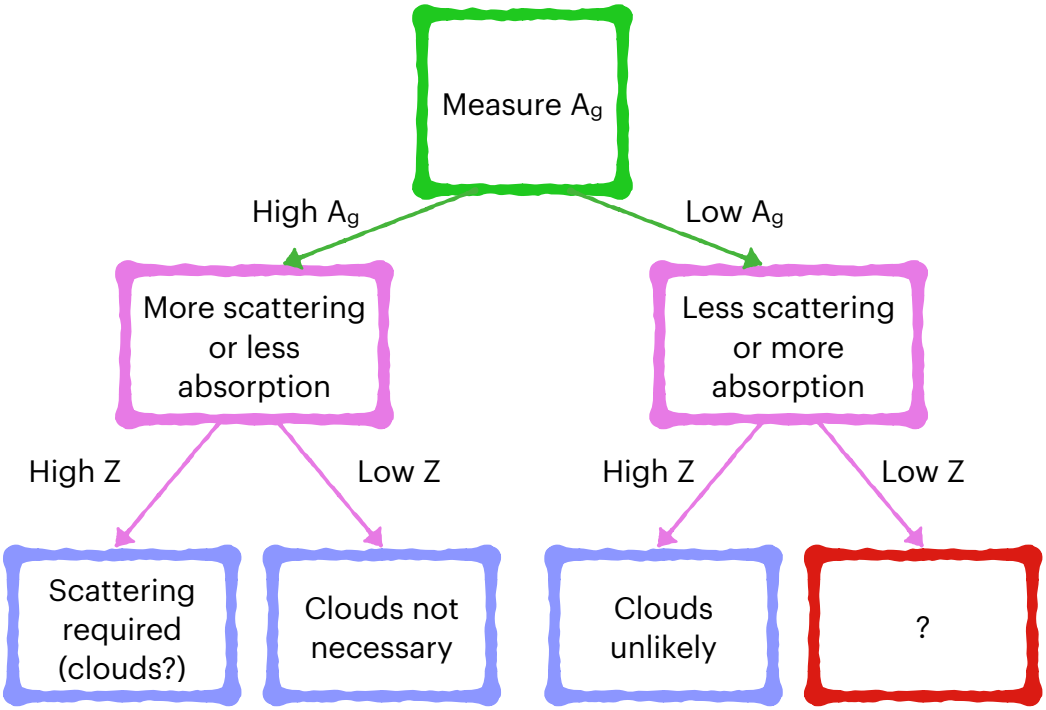

Figure 5.9 | From our model results we show here a diagram demonstrating how the geometric albedo and metallicity of an exoplanet can inform us about the atmospheric conditions. With a high albedo and high metallicity, we predict that more scattering mechanism are present, for example clouds. If the albedo is high and the metallicity is low, we have shown that this is possible without the addition of clouds. If the albedo is low and the metallicity is high, we predict that present clouds are unlikely, depending on the chemical composition in the atmosphere. We have also shown that if there is a low albedo and also a very low metallicity, the this is perhaps a very difficult scenario to occur physically and potentially could not be possible.

- If the albedo is low ($A_g \lesssim 0.05$), then this could imply the atmosphere has little scattering, or it is abundant in absorbers.

- If the albedo is high and the metallicity is high, significant additional scattering in the atmosphere is required to produce the observed albedo. None of our models (with different absorbers or abundance combinations) have been able to produce high geometric albedos when the metallicity is high. Reflective clouds would be an obvious solution to produce the additional scattering required.

- High albedos can be produced by planets with low metallicity if they have only only water and sodium present. Adding more absorbers such as TiO and VO causes the albedo to decline rapidly without the addition of clouds. This scenario is sensitive to the absorbers in the atmosphere.

- Alternatively, if the albedo is low and the metallicity is high, abundant absorbers must dominate over the Rayleigh scattering in the atmosphere. **This scenario may also imply that clouds are not present in this atmosphere**, since clouds tend to boost the geometric albedo.

- The final combination is a low geometric albedo and low metallicity, which, we have shown in our water and sodium models, is impossible unless the chemistry strays far from equilibrium.

5.5.3 Which parameters control the spread in A_g?

Figure 5.4 shows that the model albedo distributions with equilibrium chemistry have higher probability density near $A_g = 0$ than the CKC observations, which peak $A_g = 0.2$. The observed TESS albedos may lack this peak because the albedo uncertainties are much larger.

The model geometric albedo distributions increase towards $A_g \rightarrow 0$ mostly due to high metallicities. Perhaps the highest metallicities in this prior are excluded by the observations, and may not occur in nature. Looking at the stellar metallicities associated with the observations, they are all below [Fe/H] ~ 0.4. At present, devising any further parametrisation to relate stellar metallicity and planet metallicity might be premature.

We note that the spread in geometric albedos is larger with disequilibrium chemistry. In equilibrium, the geometric albedos observed in the two bandpasses do not overlap. This is not something that is seen in the observations.

5.5.4 Albedo differences between bandpasses

For the model in chemical equilibrium with only water and sodium, we see large discrepancies between the TESS and the CHEOPS bandpass, despite significant wavelength overlap between the bandpasses. Even with our generous priors allowing mixing ratios to range from 0.1-10 times the equilibrium abundance (and more, see Figure 5.7), the posteriors are clearly still distinct.

However, we found that observed albedos from TESS and CKC are very similar. In Section 5.3, we curated geometric albedos in the literature and concluded the CKC and TESS observed albedo datasets come from the same underlying distribution. There are two likely reasons why the observed albedo distributions are mutually consistent, but the model albedo distributions are inconsistent. The first is that the observational uncertainties are too large to identify small differences. The second is that the model is quite simplified. At planetary temperatures near 2000 K, we expect condensation of clouds to play an important role in the observed albedos, which may obscure any differences between the albedo distributions from CKC and TESS.

5.5.5 Future work

With the help of CHEOPS and Kepler, we have very precise eclipse depth measurements, giving us the total planetary flux in a specific bandpass. The problem is how to decouple the reflected light from the thermal emission of the planet. From measurements of the solar spectrum (e.g. Fraunhofer, 1918), we know that approximating stars and planets as black bodies is a bad approximation. The step-up from this is to fit a planetary model spectrum to both Spitzer infrared eclipse depths and then extrapolate this model into the optical. Of course, two data points is not ideal for fitting a full atmospheric spectrum. The most 'correct' method would be to take a full emission spectrum of the planet and jointly fit a reflected light component and a thermal emission component to obtain the true A_g. With the James Webb Space Telescope (JWST) optical-to-IR modes such as NIRSpec prism, we can begin to effectively decontaminate secondary eclipses. The Nancy Grace

Roman Space Telescope is set for launch in 2027, which may increase the number of known planets by over an order of magnitude (Wilson et al., 2023, Tamburo et al., 2023), and enable direct imaging in reflected light (see, e.g. Carrión-González et al., 2021), giving us a more direct method to separate the thermal and reflected light.

Furthermore, the community has been working for over a decade to understand cloud formation in these planets, and this work will be crucial for creating more accurate atmospheric models. As we see on Earth, clouds reflect significant amounts of solar light and so it is reasonable to assume they would have an impact on the scattering in a hot Jupiter's atmosphere. In Section 5.5.2, we discussed cases where clouds were and were not necessary to explain the derived geometric albedo, given a certain metallicity. Future work should now include trying to integrate a cloud model within a normal atmospheric model to estimate geometric albedos of planets. Other types of increased-scattering phenomenon, such as hazes, should also be investigate as these enhance the amount of rayleigh scattering. However this also depends on knowing the chemical compositions of a planet's atmosphere, something that is now becoming possible for these larger planets with JWST.

5.6 Conclusion

In this chapter, we have conducted an investigation into the geometric albedos of hot Jupiters, comparing observational data from several space telescopes—TESS, Kepler, CoRoT, and CHEOPS—with theoretical models. Our findings demonstrate that the geometric albedo of these exoplanets is primarily influenced by the abundance of atmospheric absorbers, with metallicity playing a crucial role. The observed albedo distributions across different bandpasses do not exhibit significant differences. This differs from the models, where, if chemical equilibrium is assumed, there is a clear separation between the geometric albedos in the TESS bandpass compared to the CHEOPS bandpass. However, there are large uncertainties on the observed datapoints which could be masking real structure in the distributions.

Our modelling efforts highlight the challenges in accurately predicting geometric albedos, especially when deviating from chemical equilibrium. The inclusion of additional absorbers like TiO and VO in our models consistently results in lower albedos, emphasis-

ing the complexity of these atmospheres and how much the specific absorbers influence the reflectivity of the planet.

Looking forward, the introduction of more precise instruments, particularly JWST and the Nancy Grace Roman Space Telescope, will be influential in refining our understanding of these albedo measurements by providing more accurate spectral data. This will allow for better separation of reflected and thermal emission components and precision atmospheric composition measurements of hot Jupiter atmospheres. Our work lays the groundwork for future studies to further explore the connection between atmospheric composition and reflectivity in exoplanet atmospheres.

Appendix

5.A Likelihood distributions

Here we detail the likelihood distributions used to fit the Rayleigh, half-Guassian and Beta distribution to the distribution of the observed geometric albedo data. K is the total number of A_g observations and N is the number of samples of each observation distribution.

$$\log \mathcal{L}_{\text{Rayleigh}} = -\log(N) + \sum_{k=1}^{K} \log \left[\sum_{n=1}^{N} \frac{{A_{g_k}}^n}{\sigma^2} \exp\left(\frac{-{A_{g_k}}^{n2}}{2\sigma^2} \right) \right] \tag{5.8}$$

$$\log \mathcal{L}_{\text{half-Gauss}} = -\log(N) + \sum_{k=1}^{K} \log \left[\sum_{n=1}^{N} \exp\left(\frac{-{A_{g_k}}^{n}}{2\sigma} \right)^2 \frac{\sqrt{2}}{\sigma\sqrt{\pi}} \right] \tag{5.9}$$

$$\log \mathcal{L}_{\text{Beta}} = -\log(N) + \sum_{k=1}^{K} \log \left[\sum_{n=1}^{N} \frac{\Gamma(a+b)({A_{g_k}}^n)^{a-1}(1-{A_{g_k}}^n)^{b-1}}{\Gamma(a)\Gamma(b)} \right] \tag{5.10}$$

Chapter 6

Conclusion

6.1 Thesis summary

In the introduction of this thesis (Section 1.4), we defined two important questions: *'Are there habitable exoplanets?'* and *'What causes the variation we observe in exoplanet climates?'*. These questions are, of course, deeply related, since life (as we know it) demands to exist within a certain climate (see, e.g. McKay, 2014, Cockell et al., 2016, Lingam & Loeb, 2018). Therefore, understanding the physics and chemistry of exoplanet atmospheres is the first step towards answering these questions.

In this thesis, I have used space-based phase curve observations of exoplanets to explore their atmospheric climates. This has included investigating their temperature structure, atmospheric composition, opacity and scattering properties using newly developed models. It has also involved reducing and preparing observational data from space-based instruments such as CHEOPS, to extract the most precise astrophysical data and separate it from erroneous noise sources. In the following subsections, we summarise our main results by chapter.

6.1.1 Chapter 2: The Stable Climate of KELT-9b

In this chapter, we investigated the ultra-hot Jupiter KELT-9b using observations from the CHEOPS, TESS, and *Spitzer* space telescopes to analyse its phase curve and occultations. Four full orbits and nine occultations of this planet were observed with CHEOPS over a period of two years. From the data obtained, we derived 2D temperature maps of KELT-9b's atmosphere at different atmospheric depths, revealing dayside brightness

temperatures of 4796 ± 46 K (CHEOPS), 4643 ± 26 K (TESS), and 4870 ± 67 K (*Spitzer*). Nightside temperatures, whilst lower, remain above 2900 K, indicating effective heat redistribution from the dayside to the nightside, with a calculated heat redistribution efficiency of around 0.3.

Our analysis confirmed a Bond albedo close to zero, implying that almost no stellar light is reflected by the planet. Therefore, the planet's flux is almost completely dominated by thermal emission. No significant variability in the planet's brightness temperature was detected, ruling out brightness temperature fluctuations greater than 1% (at 1σ confidence), suggesting that the planet's atmosphere remains stable over time. These findings contribute to a better understanding of the thermal dynamics of ultra-hot Jupiters, particularly the dissociation and recombination of molecular hydrogen, which helps drive energy transport around these planets.

6.1.2 Chapter 3: Using `catwoman` to constrain morning and evenings on exoplanets

We next explored the detection of asymmetric limbs of exoplanets during transit. We developed and introduced a new semi-analytical framework and Python package, `catwoman`, designed to model these asymmetries more quickly and efficiently than previous numerical methods. By modelling the planet's limbs as two semi-circles with distinct radii, the model provides a way to extract the transit depths of each limb separately, offering valuable insights into the planet's 3D atmospheric structure.

The study conducts simulations using simulated and real data from space missions JWST and TESS, demonstrating that, even in difficult observational scenarios with short ingress and egress durations, the detection of asymmetric limbs is possible. The results show that precise measurements of ingress and egress timings are critical for detecting such asymmetries, particularly when using high-precision instruments like JWST, which can provide data across different wavelengths.

Furthermore, the findings suggest that the detection of these asymmetries could have a profound impact on our understanding of exoplanetary weather patterns, atmospheric composition, and heat redistribution. The ability to extract spectra for both the morning and evening limbs separately allows for more precise modelling of atmospheric dynamics, providing insights into the physical processes occurring in these distant worlds. We

conclude that the use of this semi-analytical approach in combination with upcoming high-precision missions will significantly enhance the study of exoplanets, opening new opportunities for understanding their atmospheres and overall structure.

Since the publication of `catwoman`, it has been used extensively by the community to study hot Jupiter atmospheres with the new JWST telescope. For example, very recently Espinoza et al. (2024) published the first direct morning and evening transmission spectra in a wide wavelength range for hot Jupiter WASP-39b. They detected significant differences between the limbs, with the evening limb transit depth being on average 405 ± 88 ppm deeper than the morning limb, equating to 177^{+65}_{-57} K difference in temperature. Using GCM models and the observed spectra, they found evidence for a cloudy morning terminator and clear evening terminator. Furthermore, in Murphy et al. (2024), they observed a spectroscopic transit (2.5 - 4.0 μm) of hot Jupiter WASP-107b and, using `catwoman`, found evidence for limb asymmetry, with a hotter evening limb and colder morning limb.

6.1.3 Chapter 4: Enceladus and Jupiter as Exoplanets

In this chapter, we investigated the opposition surge effect in the reflected light phase curves of Jupiter and Enceladus, using data from the Cassini mission. The opposition effect, observed as a sharp increase in brightness near zero phase (i.e. when the object is fully illuminated with respect to the observer), arises from two primary mechanisms: shadow hiding (SH) and coherent backscattering (CB). We developed a framework using previous opposition effect models and embedded them within a geometric albedo model. We then mapped that new model to the observed phase curves of Jupiter and Enceladus, and found that Jupiter's phase curves are largely dominated by CB, which was expected due to its thick gaseous atmosphere. In contrast, Enceladus exhibits a combination of SH and CB effects, consistent with its icy surface lacking an atmosphere. The full-width half-maximum (FWHM) of Jupiter's opposition peak is significantly broader than that of Enceladus, reinforcing the idea that gaseous bodies exhibit different scattering behaviours compared to rocky or icy bodies.

We further investigated whether this opposition surge effect could be used to distinguish between gaseous and rocky exoplanets. Our results suggest that the FWHM of the opposition peak could serve as an indicator of a planet's surface type, with a narrower peak

implying a solid surface. However, current observational tools like JWST lack the precision to reliably detect these subtle features in exoplanet phase curves due to the very high signal-to-noise ratios required. Despite this limitation, we proposed that future telescopes, such as the Habitable Worlds Observatory, might be able to apply this technique, especially for non-transiting exoplanets or through stacked phase curve observations, opening new future opportunities for characterising exoplanet surfaces.

6.1.4 Chapter 5: Geometric albedo of hot Jupiters

In this chapter we performed an in-depth analysis of the geometric albedos of hot Jupiters using data from the TESS, CHEOPS, Kepler, and CoRoT space telescopes. Our aim was to detect trends in albedo measurements and understand their underlying distributions by comparing observations across different photometric bandpasses. After carefully curating the current known geometric albedo measurements, our results showed that with the current set of measured geometric albedos, there were no significant trends and no differences across various bandpasses. The Rayleigh distribution was found to best fit the observed data, though the differences in Bayesian Information Criterion (BIC) between different models were small, preventing any strong conclusions about the exact nature of the distribution. In addition, we explored potential correlations between geometric albedo and planetary parameters like equilibrium temperature, stellar surface gravity, and metallicity, but, again, found no significant trends.

We further explored how atmospheric composition influences the geometric albedos of hot Jupiters. We used a theoretical geometric albedo model and found that certain atmospheric absorbers, such as titanium oxide (TiO) and vanadium oxide (VO), can significantly reduce the albedo by absorbing more of the host star's light. This adds complexity to predicting albedo values, particularly in atmospheres where chemical equilibrium might be disrupted. We highlight the need for more precise spectral data from both existing and upcoming missions, like JWST and the Roman Space Telescope, to better distinguish between reflected light and thermal emission from exoplanet atmospheres, as this adds significant uncertainty to the albedo measurement. These future observations are expected to refine our understanding of how atmospheric composition and dynamics impact planetary albedos, leading to more accurate models of exoplanet reflectivity.

6.2 What is next?

In only 30 years, the field of exoplanetary science has evolved from the first detection of an exoplanet, to determining atmospheric compositions using high-resolution spectra. This rapid advancement has been made possible by the constant development of space and ground-based telescopes. Observational data fuels innovation in both the theoretical and modelling techniques, as the more precise and abundant the observations are, the more they unlock information about the physical and chemical processes occurring within these distant worlds.

Due to their large radii, small orbital separations and high temperatures, hot Jupiters have been the first targets of the community. With space telescopes including CHEOPS, TESS and *Spitzer*, we have the precision to investigate their atmospheric climates, heat transport processes, reflectivity, and more. The work we detailed in Chapter 2, showed how we selected one of the most favourable targets, KELT-9b, and analysed phase curve observations across three wavelength bands in order to explore the atmospheric heat re-distribution efficiency, 2D temperature maps and Bond albedo of the planet. Observations unlock science, however they also set limits on how much complexity can be extracted due to the inherent noise floor of the instrument used. With JWST's high precision spectroscopic instruments, we can now go even further with hot Jupiter targets.

Multi-wavelength phase curves of hot Jupiters contain an abundance of atmospheric information about the whole surface of the planet. Very recently, JWST has started to take these types of observations (see, e.g. Mikal-Evans et al., 2023, Bell et al., 2023). Due to the spectroscopic longitudinal information from these phase curves, studies are able to investigate and model the 2D temperature maps of the planets and produce both day and nightside emission spectra. In Mikal-Evans et al. (2023), these spectra were able to reveal insights about the possible presence of clouds on the nightside of the ultra-hot Jupiter WASP-121b, where it is cool enough for them to form. They also noted that this could be why GCM models overpredict the observed nightside temperature of this planet (Parmentier et al., 2018), as they do not take into account possible cloud coverage.

Clouds are often left out of atmospheric models or added very simply as generic 'grey-cloud decks', which affect the observed atmospheric spectrum by distorting the features (see, e.g. Inglis et al., 2024). We know they are abundant in forming from looking at the Solar System: 100% of the objects in our Solar System with an atmosphere have

some level of cloud formation. This is where our work in Chapter 3 will improve our understanding of cloud formation in hot Jupiter exoplanets. By comparing the evening and morning limbs of an exoplanet, particularly those which are tidally-locked, the goal is that one can distinguish between the cloudy morning limb and the clear evening limb. As mentioned in Section 6.1.2, there are studies already using `catwoman` to do just this. However, in order to gain an understanding of cloud properties in types of exoplanets as a population, many more studies need to be conducted. Currently, I am a collaborator on the JWST program running as part of JWST Proposal 2113, 'Exploring the morning and evening limbs of a transiting exoplanet' (PI: Espinoza), which will perform analysis on six different targets, drastically increasing the sample size of this population.

Clouds can also have significant effects on the albedo (i.e. reflectivity) of a planet. When looking at the Earth from space, our clouds appear white because they reflect a significant amount of the Sun's visible light. Understanding the connection between albedo and cloud coverage/composition is something we must investigate and take advantage of. That is where our work in Chapter 5 is important. We developed a self-consistent model that can take atmospheric composition and other parameters as inputs and calculate the theoretical geometric albedo. In future work, this can be taken further to include cloud models, possibly derived from GCM models, in order to calculate a more reliable albedo value. Deriving the geometric albedo as a function of wavelength also requires careful modelling and decontamination of the planetary thermal emission, which is easier if you have full phase curve observations (see, e.g. Morris et al., 2024). Alongside other studies, more observations of exoplanets should be taken in order to increase our geometric albedo sample. If we are able to characterise which planets have clouds and which do not, this could lead to very insightful conclusions about the distribution of geometric albedo measurements.

The synergy between observational data and models is crucial in order to extract information about a planet. However, as more and more exoplanets are discovered and characterised, we are beginning to run into a new problem - computing time. Atmospheric models span a large complexity range, with the most complex needing the most computational power. If the data is precise enough, we of course would like to fit it with our most complex and physically-motivated model. Therefore, as we move into a new age of exoplanet science, it is very important that these models are *scalable*. We still require

these models to work quickly and accurately when we have 10s, 100s or 1000s of targets, and so it is the responsibility of the modeller to build their code with this in mind. As computational architecture is evolving, it is now possible to adapt codes to run on GPUs or mixed CPU/GPUs with shared memories, enabling much faster parallel computations. Soon, we will have brand new observations from missions such as PLATO, ARIEL and Roman, of hot Jupiters all the way to rocky Earth-like planets and we require the tools to analyse this volume of data within a reasonable time-frame. Looking further into the future, the Habitable Worlds Observatory comes into view. A large space telescope with UV, optical and infrared capabilities would completely revolutionise atmospheric characterisation of even rocky planets and search for at least 25 habitable worlds[1].

As our instruments get more sensitive, we can begin to probe planets smaller than hot Jupiters. Sub-Neptunes are a class of planets with radii between the Earth and Neptune that are assumed to have hydrogen-dominated atmospheres. These planets are becoming key targets of the community as it has been predicted these could hold large amounts of water, perhaps even in a liquid form (see, e.g. Madhusudhan et al., 2021). Recently in Kempton et al. (2023), they observed a spectroscopic phase curve of the sub-Neptune GJ1214b (Charbonneau et al., 2009) with JWST (MIRI LRS). From the dayside spectra, they derived a 3σ detection of water absorption and, with GCM simulations, predict a high metallicity atmosphere with a thick layer of clouds or haze. This layer explains the high reflectivity the planet exhibits ($A_B = 0.51 \pm 0.06$) and is further evidence that understanding the reflectivity and scattering properties within a planet's atmosphere gives us insights into its climate.

As we look to characterise smaller planets, our signals get smaller and our inferences become more uncertain. The next frontier to bring us closer to answering the question of habitable worlds is characterising super-Earths. As introduced in Section 1.3.2, these are assumed-rocky planets with a secondary atmosphere. However, we currently do not have conclusive evidence for this type of atmosphere on these planets. Due to their smaller scale-heights and radii, their transmission and emission spectral signatures are very difficult to detect confidently. However, understanding the origin and composition of different secondary atmospheres is a very important goal for the community focussed on habitability. Future missions such as PLATO and Roman will look to significantly increase the

[1] https://science.nasa.gov/astrophysics/programs/habitable-worlds-observatory/

sample and precision of super-Earth observations. With JWST, there have been a few of these observations. Namely 55 Cnc e occulatations (Hu et al., 2024, Patel et al., 2024), GJ1132b transits (May et al., 2023) and TOI-836b transits (Alderson et al., 2024). As is evidenced in the observations of GJ1132b and TOI-836b, super-Earth transmission and emission spectra are pushing up against the limit of JWST's noise floor. Only 55 Cnc e has so far shown distinct features in its emission spectrum, however, due to the extreme variability between visits, its atmospheric composition is far from being understood.

In order to achieve everything we have discussed above, we require our exoplanet observations to be reliable. With ground-based telescopes, we have the luxury of accessing them during operation to fix any unexpected problems. However, the noise, due to the Earth's atmosphere, is much higher and must be mitigated using a 'control' star which adds further uncertainty into the data. For space telescopes, every effort is made to ensure their stability and precision on the ground before they are launched into space. However, there are always unforeseen sources of noise in the data at the beginning of operation. For example with *Spitzer*, it took years to understand and mitigate the effect of intra-pixel sensitivity which caused large measured flux variations on the order of 10% (see, e.g. Ingalls et al., 2016, Stevenson et al., 2012). CHEOPS also had erroneous signals at the start of the mission. In the first set of observations we noticed a ramp-like feature at the beginning of each observation. This was found to be due to changes in the temperature of the telescope tube as it moved between pointings. Luckily, there is a thermistor on-board which scales linearly with this ramp and so this is now used to remove this unwanted feature (Morris et al., 2021). With JWST, we are also finding unexpected systematics. Due to the number of different instruments, each one seems to come with a unique set of challenges. Systematics have so far included 1/f noise in NIRSS SOSS, 10 Hz and 390 Hz heater noise in MIRI and both positive and negative ramps at the beginning of observations from a range of instruments.

The future of exoplanet science is very exciting as we continue to push the boundaries of both observational capabilities and theoretical modelling. With missions like JWST and CHEOPS already providing unprecedented insights, and upcoming missions such as PLATO and Roman set to rapidly expand our sample of potentially-habitable exoplanets, the field is on the verge of transformative discoveries. As we move to characterising smaller planets, such as sub-Neptunes and super-Earths, the need for scalable, efficient

models becomes even more pressing. The challenge will be to extract meaningful science from increasingly complex and numerous datasets, whilst overcoming instrumental noise limits. By combining high-precision, multi-wavelength data with advanced models, we will not only deepen our understanding of planetary climates but also move closer to answering the profound questions of habitability in our Universe.

Acknowledgements

I would firstly like to thank my supervisor, Brett Morris. You taught me (almost) everything I know and I truly don't know how I would have made it to the end of my PhD without you. Amongst so many other things that are too long to list, you stuck by me, encouraged me, fought in my corner and took me to some amazing places (with some amazing food). I can't thank you enough for the time and energy you spent supervising me, even when you didn't have to. Thank you also for the free counselling and life-advice, not to mention the history and linguistic lessons and the fun-facts about bees. I appreciate it all and I hope I can visit you in Baltimore soon.

I would also like to thank my other supervisors Brice-Olivier Demory and Kevin Heng. Thank you Brice for helping me grow as an observer, for pushing me to go further in my work and always reminding me to keep the science questions at the forefront. Thank you also for taking on the pastoral role as my supervisor and allowing me to have a flexible work schedule when I most needed it.

Thank you also to my ghost-supervisor and friend Daniel Kitzmann (or the Kitzking as he is colloquially known). For answering all of my really stupid questions and listening to my many rants, you helped give me confidence in my own work and knowledge. You also bought me lots of beer which helped too.

I would also like to thank Susanne Wampfler for all your help and support when I was going through difficult times. You made me feel listened to and gave me the options I needed to get back on track. Thank you also for being on my PhD defence committee and for helping me with the final hurdles of submitting my PhD thesis.

Thank you to Nathan Mayne for being my external examiner and for your thoughtful and insightful comments that helped improve my thesis.

Thank you also to Susanne Reffert for chairing my defence.

Thank you to my other work colleagues for their collaboration and for helping me

grow as a scientist, especially Néstor Espinoza, Matthew Hooton, Bibi Prinoth, Hannah Diamond-Lowe, Natalie Allan, Jens Hoeijmakers and Monika Lendl.

Thank you to all my friends that stuck with me and gave me your help and support on this journey.

To Chloe, for being an amazing friend and always being there for me, especially in the really rough times. Thank you also for inviting me on that first Triple-T hike.

To Erik, my PhD brother, thank you for all the Thursday beers and the support you have given me over the years. I hope we can have more Thursday beers in Oxford.

To Anna, for always being there for me and showing me true resilience.

To Anika, for all your support and for all the fun times in Basel - let's go to karaoke soon.

To Nick, for being there when I've needed help and support, and for your masterful baking.

To Andrin, for your friendship and all the fun times, and for occasionally letting me see your cat.

To the G6 crew (past and present): Marit, Marko, Clémence, Beatrice, Niall, Jesse (Dutch), Jo Ann, Beni, Jesse (Swiss), Jeanne, Romane, Hugh, Leander, thank you for the all the laughs and the fun times - and the legendary G6 pop-up bar.

To my amazing friends back home, Kirstie, Ned, Nigel, Joe and Sam, thank you for your constant support and for always being there for me.

To Tobias, also known as Triple-T, I'm so grateful this journey has led me to you. I liebe di.

To my family, Mum and Dad, Iwan, Grandma and Grandad, none of this would be possible without you.

Bibliography

Ackerman, A. S. & Marley, M. S. 2001, The Astrophysical Journal, 556, 872

Agol, E., Cowan, N. B., Knutson, H. A., et al. 2010, The Astrophysical Journal, 721, 1861

Ahlers, J. P., Johnson, M. C., Stassun, K. G., et al. 2020, The Astronomical Journal, 160, 4

Ahrer, E.-M., Stevenson, K. B., Mansfield, M., et al. 2023, Nature, 614, 653

Akkermans, E., Wolf, P., Maynard, R., & Maret, G. 1988, Journal de Physique, 49, 77

Alam, M. K., López-Morales, M., MacDonald, R. J., et al. 2021, The Astrophysical Journal, 906, L10

Alderson, L., Batalha, N. E., Wakeford, H. R., et al. 2024, The Astronomical Journal, 167, 216

Alderson, L., Wakeford, H. R., Alam, M. K., et al. 2023, Nature, 614, 664

Alonso, R., Alapini, A., Aigrain, S., et al. 2009, Astronomy and Astrophysics, 506, 353

Alonso, R., Auvergne, M., Baglin, A., et al. 2008, Astronomy and Astrophysics, 482, L21

Amundsen, D. S., Mayne, N. J., Baraffe, I., et al. 2016, Astronomy and Astrophysics, 595, A36

Angerhausen, D., DeLarme, E., & Morse, J. A. 2015, Publications of the Astronomical Society of the Pacific, 127, 1113

Arcangeli, J., Désert, J.-M., Line, M. R., et al. 2018, The Astrophysical Journal, 855, L30

Arcangeli, J., Désert, J.-M., Parmentier, V., et al. 2019, Astronomy and Astrophysics, 625, A136

Armstrong, D. J., de Mooij, E., Barstow, J., et al. 2016, Nature Astronomy, 1, 0004

Auvergne, M., Bodin, P., Boisnard, L., et al. 2009, Astronomy and Astrophysics, 506, 411

Barge, P., Baglin, A., Auvergne, M., et al. 2008, Astronomy and Astrophysics, 482, L17

Barnes, J. W. 2009, The Astrophysical Journal, 705, 683

Barragán, O., Gandolfi, D., Dai, F., et al. 2018, Astronomy and Astrophysics, 612, A95

Barros, S. C. C., Akinsanmi, B., Boué, G., et al. 2022, Astronomy and Astrophysics, 657, A52

Batalha, N. E., Mandell, A., Pontoppidan, K., et al. 2017, Publications of the Astronomical Society of the Pacific, 129, 064501

Batalha, N. M. 2014, Proceedings of the National Academy of Science, 111, 12647

Baxter, C., Désert, J.-M., Parmentier, V., et al. 2020, Astronomy and Astrophysics, 639, A36

Beatty, T. G., Marley, M. S., Gaudi, B. S., et al. 2019, The Astronomical Journal, 158, 166

Beaulieu, J. P., Bennett, D. P., Fouqué, P., et al. 2006, Nature, 439, 437

Bell, T., Ahrer, E.-M., Brande, J., et al. 2022, The Journal of Open Source Software, 7, 4503

Bell, T. J. & Cowan, N. B. 2018, The Astrophysical Journal, 857, L20

Bell, T. J., Kreidberg, L., Kendrew, S., et al. 2023, arXiv e-prints, arXiv:2301.06350

Bello-Arufe, A., Buchhave, L. A., Mendonça, J. M., et al. 2022, Astronomy and Astrophysics, 662, A51

Benz, W., Broeg, C., Fortier, A., et al. 2021, Experimental Astronomy, 51, 109

Bingham, E., Chen, J. P., Jankowiak, M., et al. 2019, J. Mach. Learn. Res., 20, 28:1

Blackwell, D. E. & Shallis, M. J. 1977, Monthly Notices of the Royal Astronomical Society, 180, 177

Bohren, C. F. & Huffman, D. R. 1983, Absorption and scattering of light by small particles, Research supported by the University of Arizona and Institute of Occupational and Environmental Health. New York, Wiley-Interscience, 1983, 541 p.

Bonfanti, A., Delrez, L., Hooton, M. J., et al. 2021, Astronomy and Astrophysics, 646, A157

Bonfanti, A., Ortolani, S., & Nascimbeni, V. 2016, Astronomy and Astrophysics, 585, A5

Bonfanti, A., Ortolani, S., Piotto, G., & Nascimbeni, V. 2015, Astronomy and Astrophysics, 575, A18

Bonomo, A. S., Desidera, S., Benatti, S., et al. 2017, Astronomy and Astrophysics, 602, A107

Borsa, F., Rainer, M., Bonomo, A. S., et al. 2019, Astronomy and Astrophysics, 631, A34

Borucki, W. J., Koch, D., Basri, G., et al. 2010, Science, 327, 977

Bourque, M., Espinoza, N., Filippazzo, J., et al. 2021, The Exoplanet Characterization Toolkit (ExoCTK)

Bourrier, V., Kitzmann, D., Kuntzer, T., et al. 2020, Astronomy and Astrophysics, 637, A36

Brandeker, A., Heng, K., Lendl, M., et al. 2022, Astronomy and Astrophysics, 659, L4

Brown, T. M. 2001, The Astrophysical Journal, 553, 1006

Buchner, J., Georgakakis, A., Nandra, K., et al. 2014, Astronomy and Astrophysics, 564, A125

Buratti, B. J., Hillier, J. H., Dalba, P. A., et al. 2022, The Planetary Science Journal, 3, 200

Burke, C. J., Christiansen, J. L., Mullally, F., et al. 2015, The Astrophysical Journal, 809, 8

Burrows, A., Ibgui, L., & Hubeny, I. 2008, The Astrophysical Journal, 682, 1277

Burrows, A., Sudarsky, D., & Hubbard, W. B. 2003, The Astrophysical Journal, 594, 545

Cahoy, K. L., Marley, M. S., & Fortney, J. J. 2010, The Astrophysical Journal, 724, 189

Carrión-González, Ó., García Muñoz, A., Santos, N. C., et al. 2021, Astronomy and Astrophysics, 651, A7

Cassan, A., Kubas, D., Beaulieu, J. P., et al. 2012, Nature, 481, 167

Castelli, F. & Kurucz, R. L. 2003, in IAU Symposium, Vol. 210, Modelling of Stellar Atmospheres, ed. N. Piskunov, W. W. Weiss, & D. F. Gray, A20

Chandrasekhar, S. 1960, Radiative transfer

Changeat, Q. & Al-Refaie, A. 2020, The Astrophysical Journal, 898, 155

Chao, K.-H., deGraffenried, R., Lach, M., et al. 2021, Chemie der Erde / Geochemistry, 81, 125735

Charbonneau, D., Allen, L. E., Megeath, S. T., et al. 2005, The Astrophysical Journal, 626, 523

Charbonneau, D., Berta, Z. K., Irwin, J., et al. 2009, Nature, 462, 891

Charbonneau, D., Brown, T. M., Latham, D. W., & Mayor, M. 2000, The Astrophysical Journal, 529, L45

Chauvin, G., Lagrange, A. M., Dumas, C., et al. 2004, Astronomy and Astrophysics, 425, L29

Chen, G., Pallé, E., Parviainen, H., Murgas, F., & Yan, F. 2021, The Astrophysical Journal, 913, L16

Cho, J. Y. K., Menou, K., Hansen, B. M. S., & Seager, S. 2008, The Astrophysical Journal, 675, 817

Claret, A. 2016, Astronomy and Astrophysics, 588, A15

Claret, A. 2017, Astronomy and Astrophysics, 600, A30

Claret, A. 2021, VizieR Online Data Catalog (other), 0690, J/other/RNAAS/5

Claret, A. & Bloemen, S. 2011, Astronomy and Astrophysics, 529, A75

Cockell, C. S., Bush, T., Bryce, C., et al. 2016, Astrobiology, 16, 89

Collier Cameron, A., Guenther, E., Smalley, B., et al. 2010, Monthly Notices of the Royal Astronomical Society, 407, 507

Collins, J. M., Jones, H. R. A., & Barnes, J. R. 2017, Astronomy and Astrophysics, 602, A48

Cowan, N. B. & Agol, E. 2011, The Astrophysical Journal, 729, 54

Csizmadia, S., Pasternacki, T., Dreyer, C., et al. 2013, Astronomy and Astrophysics, 549, A9

Cumming, A., Butler, R. P., Marcy, G. W., et al. 2008, Publications of the Astronomical Society of the Pacific, 120, 531

Dang, L., Cowan, N. B., Schwartz, J. C., et al. 2018, Nature Astronomy, 2, 220

Dawson, R. I. & Johnson, J. A. 2018, Annual Review of Astronomy and Astrophysics, 56, 175

Deline, A., Hooton, M. J., Lendl, M., et al. 2022, Astronomy and Astrophysics, 659, A74

Delrez, L., Ehrenreich, D., Alibert, Y., et al. 2021, Nature Astronomy, 5, 775

Delrez, L., Santerne, A., Almenara, J. M., et al. 2016, Monthly Notices of the Royal Astronomical Society, 458, 4025

Deming, D., Sada, P. V., Jackson, B., et al. 2011, The Astrophysical Journal, 740, 33

Demory, B.-O., Gillon, M., de Wit, J., et al. 2016a, Nature, 532, 207

Demory, B. O., Gillon, M., Deming, D., et al. 2011a, Astronomy and Astrophysics, 533, A114

Demory, B.-O., Gillon, M., Madhusudhan, N., & Queloz, D. 2016b, Monthly Notices of the Royal Astronomical Society, 455, 2018

Demory, B.-O., Seager, S., Madhusudhan, N., et al. 2011b, The Astrophysical Journal, 735, L12

Désert, J.-M., Charbonneau, D., Demory, B.-O., et al. 2011, The Astrophysical Journal Supplement Series, 197, 14

Dlugach, Z. M. & Mishchenko, M. I. 2013, Solar System Research, 47, 454

Dobbs-Dixon, I., Agol, E., & Burrows, A. 2012, The Astrophysical Journal, 751, 87

Doppler, C. 1842, Über das farbige Licht der Doppelsterne und einiger anderer Gestirne des Himmels, Vol. 2 (Abhandlungen der Königlichen Böhmischen Gesellschaft der Wissenschaften), 465–482

Dressing, C., Ansdell, M., Crooke, J., et al. 2024, in American Astronomical Society Meeting Abstracts, Vol. 244, American Astronomical Society Meeting Abstracts, 210.04

Dyudina, U. A., Zhang, X., Li, L., et al. 2016, in AAS/Division for Planetary Sciences Meeting Abstracts, Vol. 48, AAS/Division for Planetary Sciences Meeting Abstracts #48, 202.08

Ehrenreich, D., Delrez, L., Akinsanmi, B., et al. 2023, Astronomy and Astrophysics, 671, A154

Ertel, S., Defrère, D., Hinz, P., et al. 2020, The Astronomical Journal, 159, 177

Espinoza, N., Fortney, J. J., Miguel, Y., Thorngren, D., & Murray-Clay, R. 2017, The Astrophysical Journal, 838, L9

Espinoza, N. & Jones, K. 2021, The Astronomical Journal, 162, 165

Espinoza, N. & Jordán, A. 2015, Monthly Notices of the Royal Astronomical Society, 450, 1879

Espinoza, N., Kossakowski, D., & Brahm, R. 2019, Monthly Notices of the Royal Astronomical Society, 490, 2262

Espinoza, N., Steinrueck, M. E., Kirk, J., et al. 2024, Nature, 632, 1017

Esteves, L. J., De Mooij, E. J. W., & Jayawardhana, R. 2015, The Astrophysical Journal, 804, 150

Euler, L. 1767, Novi Commentarii academiae scientiarum Petropolitanae, 11, 144

Feinstein, A. D., Radica, M., Welbanks, L., et al. 2023, Nature, 614, 670

Feroz, F., Hobson, M. P., & Bridges, M. 2009, Monthly Notices of the Royal Astronomical Society, 398, 1601

Foreman-Mackey, D. 2018, Research Notes of the American Astronomical Society, 2, 31

Foreman-Mackey, D., Agol, E., Ambikasaran, S., & Angus, R. 2017, The Astronomical Journal, 154, 220

Foreman-Mackey, D., Hogg, D. W., Lang, D., & Goodman, J. 2013, Publications of the Astronomical Society of the Pacific, 125, 306

Fortney, J. J. 2005, Monthly Notices of the Royal Astronomical Society, 364, 649

Fortney, J. J., Demory, B.-O., Désert, J.-M., et al. 2011, The Astrophysical Journal Supplement Series, 197, 9

Fortney, J. J., Lodders, K., Marley, M. S., & Freedman, R. S. 2008, The Astrophysical Journal, 678, 1419

Fortney, J. J., Shabram, M., Showman, A. P., et al. 2010, The Astrophysical Journal, 709, 1396

Fraunhofer, J. 1814, in Denkschriften der Königlichen Akademie der Wissenschaften zu München (Memoirs of the Royal Academy of Sciences in Munich) (Bayerische Akademie der Wissenschaften)

Fraunhofer, J. 1918, in Denkschriften der Königlichen Akademie der Wissenschaften zu München (Memoirs of the Royal Academy of Sciences in Munich) (Bayerische Akademie der Wissenschaften)

Gai, A. D. & Knuth, K. H. 2018, The Astrophysical Journal, 853, 49

Gaia Collaboration, Brown, A. G. A., Vallenari, A., et al. 2021, Astronomy and Astrophysics, 649, A1

Gardner, J. P., Mather, J. C., Abbott, R., et al. 2023, Publications of the Astronomical Society of the Pacific, 135, 068001

Gardner, J. P., Mather, J. C., Clampin, M., et al. 2006, Space Science Reviews, 123, 485

Gaudi, B. S., Stassun, K. G., Collins, K. A., et al. 2017, Nature, 546, 514

Gehrels, T., Coffeen, T., & Owings, D. 1964, The Astronomical Journal, 69, 826

Gelman, A. & Rubin, D. B. 1992, Statistical Science, 7, 457

Gillon, M., Demory, B. O., Benneke, B., et al. 2012, Astronomy and Astrophysics, 539, A28

Gillon, M., Triaud, A. H. M. J., Demory, B.-O., et al. 2017, Nature, 542, 456

Goodman, J. 2009, The Astrophysical Journal, 693, 1645

Greene, T. P., Line, M. R., Montero, C., et al. 2016, The Astrophysical Journal, 817, 17

Grimm, S. L. & Heng, K. 2015, The Astrophysical Journal, 808, 182

Grimm, S. L., Malik, M., Kitzmann, D., et al. 2021, The Astrophysical Journals, 253, 30

Hanel, R., Conrath, B., Herath, L., Kunde, V., & Pirraglia, J. 1981, Journal of Geophysical Research, 86, 8705

Hapke, B. 1981, Journal of Geophysical Research, 86, 4571

Hapke, B. 1984, Icarus, 59, 41

Hapke, B. 1986, Icarus, 67, 264

Hapke, B. 2002, Icarus, 157, 523

Hapke, B. 2008, Icarus, 195, 918

Hapke, B., Nelson, R., & Smythe, W. 1998, Icarus, 133, 89

Hapke, B. W. 1963, Journal of Geophysical Research, 68, 4571

Hapke, B. W., Nelson, R. M., & Smythe, W. D. 1993, Science, 260, 509

Harris, C. R., Millman, K. J., van der Walt, S. J., et al. 2020, Nature, 585, 357

Helfenstein, P. 1988, Icarus, 73, 462

Helfenstein, P., Veverka, J., & Hillier, J. 1997, Icarus, 128, 2

Helling, C., Kawashima, Y., Graham, V., et al. 2020, Astronomy and Astrophysics, 641, A178

Heng, K. & Demory, B.-O. 2013, The Astrophysical Journal, 777, 100

Heng, K. & Li, L. 2021, The Astrophysical Journal, 909, L20

Heng, K., Lyons, J. R., & Tsai, S.-M. 2016, The Astrophysical Journal, 816, 96

Heng, K., Menou, K., & Phillipps, P. J. 2011, Monthly Notices of the Royal Astronomical Society, 413, 2380

Heng, K., Morris, B. M., & Kitzmann, D. 2021, Nature Astronomy, 5, 1001

Heng, K. & Showman, A. P. 2015, Annual Review of Earth and Planetary Sciences, 43, 509

Heng, K. & Workman, J. 2014, The Astrophysical Journal Supplement Series, 213, 27

Henry, G. W., Baliunas, S. L., Donahue, R. A., Fekel, F. C., & Soon, W. 2000, The Astrophysical Journal, 531, 415

Hoeijmakers, H. J., Ehrenreich, D., Kitzmann, D., et al. 2019, Astronomy and Astrophysics, 627, A165

Hoeijmakers, H. J., Snellen, I. A. G., & van Terwisga, S. E. 2018, Astronomy and Astrophysics, 610, A47

Hogg, D. W., Bovy, J., & Lang, D. 2010, arXiv e-prints, arXiv:1008.4686

Hooton, M. J., Hoyer, S., Kitzmann, D., et al. 2022, Astronomy and Astrophysics, 658, A75

Hooton, M. J., Watson, C. A., de Mooij, E. J. W., Gibson, N. P., & Kitzmann, D. 2018, The Astrophysical Journal, 869, L25

Howard, A. W., Marcy, G. W., Bryson, S. T., et al. 2012, The Astrophysical Journals, 201, 15

Hoyer, S., Guterman, P., Demangeon, O., et al. 2020, Astronomy and Astrophysics, 635, A24

Hu, R., Bello-Arufe, A., Zhang, M., et al. 2024, Nature, 630, 609

Hu, R., Demory, B.-O., Seager, S., Lewis, N., & Showman, A. P. 2015, The Astrophysical Journal, 802, 51

Hubbard, W. B., Fortney, J. J., Lunine, J. I., et al. 2001, The Astrophysical Journal, 560, 413

Hunter, J. D. 2007, Computing in Science and Engineering, 9, 90

Husser, T.-O., Wende-von Berg, S., Dreizler, S., et al. 2013, Astronomy and Astrophysics, 553, A6

Ingalls, J. G., Krick, J. E., Carey, S. J., et al. 2016, The Astronomical Journal, 152, 44

Inglis, J., Batalha, N. E., Lewis, N. K., et al. 2024, The Astrophysical Journal, 973, L41

Jenkins, J. M., Twicken, J. D., McCauliff, S., et al. 2016, in Society of Photo-Optical Instrumentation Engineers (SPIE) Conference Series, Vol. 9913, Software and Cyberinfrastructure for Astronomy IV, ed. G. Chiozzi & J. C. Guzman, 99133E

Jones, K. & Espinoza, N. 2020, The Journal of Open Source Software, 5, 2382

Kataria, T., Showman, A. P., Lewis, N. K., et al. 2013, The Astrophysical Journal, 767, 76

Keating, D., Cowan, N. B., & Dang, L. 2019, Nature Astronomy, 3, 1092

Kempton, E. M. R., Bean, J. L., & Parmentier, V. 2017, The Astrophysical Journal, 845, L20

Kempton, E. M. R., Zhang, M., Bean, J. L., et al. 2023, Nature, 620, 67

Kepler, J. 1619, Ioannis Keppleri Harmonices mundi libri V (The Five Books of Johannes Kepler's The Harmony of the World) (Linz, Austria: Lincii Austriae)

Kilpatrick, B. M., Kataria, T., Lewis, N. K., et al. 2020, The Astronomical Journal, 159, 51

Kipping, D. M. 2013, Monthly Notices of the Royal Astronomical Society, 435, 2152

Kitzmann, D., Heng, K., Rimmer, P. B., et al. 2018, The Astrophysical Journal, 863, 183

Kitzmann, D., Stock, J. W., & Patzer, A. B. C. 2024, Monthly Notices of the Royal Astronomical Society, 527, 7263

Komacek, T. D. & Showman, A. P. 2016, The Astrophysical Journal, 821, 16

Komacek, T. D. & Showman, A. P. 2020, The Astrophysical Journal, 888, 2

Kopparapu, R. K., Ramirez, R., Kasting, J. F., et al. 2013, The Astrophysical Journal, 765, 131

Kreidberg, L. 2015, Publications of the Astronomical Society of the Pacific, 127, 1161

Kreidberg, L., Line, M. R., Parmentier, V., et al. 2018, The Astronomical Journal, 156, 17

Krenn, A. F., Lendl, M., Patel, J. A., et al. 2023, Astronomy and Astrophysics, 672, A24

Lally, M. & Vanderburg, A. 2022, The Astronomical Journal, 163, 181

Lambert, J. H. 1892, Photometria, sive De mensura et gradibus luminis, colorum et umbrae (Leipzig, W. Engelmann)

Lanotte, A. A., Gillon, M., Demory, B. O., et al. 2014, Astronomy and Astrophysics, 572, A73

Leleu, A., Alibert, Y., Hara, N. C., et al. 2021, Astronomy and Astrophysics, 649, A26

Lendl, M., Csizmadia, S., Deline, A., et al. 2020, Astronomy and Astrophysics, 643, A94

Lewis, N. K., Wakeford, H. R., MacDonald, R. J., et al. 2020, The Astrophysical Journal, 902, L19

Li, L., Guan, L., Li, S., et al. 2023, Icarus, 394, 115429

Li, L., Jiang, X., West, R. A., et al. 2018, Nature Communications, 9, 3709

Lightkurve Collaboration, Cardoso, J. V. d. M. a., Hedges, C., et al. 2018, Lightkurve: Kepler and TESS time series analysis in Python

Lillo-Box, J., Barrado, D., & Bouy, H. 2014, Astronomy and Astrophysics, 566, A103

Lindegren, L., Bastian, U., Biermann, M., et al. 2021, Astronomy and Astrophysics, 649, A4

Line, M. R. & Parmentier, V. 2016, The Astrophysical Journal, 820, 78

Line, M. R., Wolf, A. S., Zhang, X., et al. 2013, The Astrophysical Journal, 775, 137

Lingam, M. & Loeb, A. 2018, International Journal of Astrobiology, 17, 116

Liu, B. & Showman, A. P. 2013, The Astrophysical Journal, 770, 42

Lodge, M. G., Wakeford, H. R., & Leinhardt, Z. M. 2024, Monthly Notices of the Royal Astronomical Society, 527, 11113

Lothringer, J. D., Barman, T., & Koskinen, T. 2018, The Astrophysical Journal, 866, 27

Luger, R., Agol, E., Foreman-Mackey, D., et al. 2019, The Astronomical Journal, 157, 64

Luhman, K. L., Tremblin, P., Birkmann, S. M., et al. 2023, The Astrophysical Journal, 949, L36

Luque, R., Osborn, H. P., Leleu, A., et al. 2023, Nature, 623, 932

MacDonald, R. J., Goyal, J. M., & Lewis, N. K. 2020, The Astrophysical Journal, 893, L43

Madhusudhan, N., Lee, K. K. M., & Mousis, O. 2012, The Astrophysical Journal, 759, L40

Madhusudhan, N., Piette, A. A. A., & Constantinou, S. 2021, The Astrophysical Journal, 918, 1

Madhusudhan, N., Sarkar, S., Constantinou, S., et al. 2023, The Astrophysical Journal, 956, L13

Mai, C. & Line, M. R. 2019, The Astrophysical Journal, 883, 144

Malavolta, L., Mayo, A. W., Louden, T., et al. 2018, The Astronomical Journal, 155, 107

Mallonn, M., Köhler, J., Alexoudi, X., et al. 2019, Astronomy and Astrophysics, 624, A62

Mandel, K. & Agol, E. 2002, The Astrophysical Journal, 580, L171

Mansfield, M., Bean, J. L., Stevenson, K. B., et al. 2020, The Astrophysical Journal, 888, L15

Marigo, P., Girardi, L., Bressan, A., et al. 2017, The Astrophysical Journal, 835, 77

May, E. M., MacDonald, R. J., Bennett, K. A., et al. 2023, The Astrophysical Journal, 959, L9

Mayne, N. J., Baraffe, I., Acreman, D. M., et al. 2014, Astronomy and Astrophysics, 561, A1

Mayor, M. & Queloz, D. 1995, Nature, 378, 355

Mayorga, L., Jackiewicz, J., Rages, K., et al. 2016, in AAS/Division for Planetary Sciences Meeting Abstracts, Vol. 48, AAS/Division for Planetary Sciences Meeting Abstracts #48, 202.07

McArthur, B. E., Endl, M., Cochran, W. D., et al. 2004, The Astrophysical Journal, 614, L81

McKay, C. P. 2014, Proceedings of the National Academy of Science, 111, 12628

Meier, T. G., Bower, D. J., Lichtenberg, T., Tackley, P. J., & Demory, B.-O. 2021, The Astrophysical Journal, 908, L48

Meier Valdés, E. A., Morris, B. M., Demory, B. O., et al. 2023, Astronomy and Astrophysics, 677, A112

Mendonça, J. M., Malik, M., Demory, B.-O., & Heng, K. 2018, The Astronomical Journal, 155, 150

Mikal-Evans, T., Sing, D. K., Dong, J., et al. 2023, The Astrophysical Journal, 943, L17

Mordasini, C. 2018, in Handbook of Exoplanets, ed. H. J. Deeg & J. A. Belmonte, 143

Mordasini, C., van Boekel, R., Mollière, P., Henning, T., & Benneke, B. 2016, The Astrophysical Journal, 832, 41

Morris, B. M., Delrez, L., Brandeker, A., et al. 2021, Astronomy and Astrophysics, 653, A173

Morris, B. M., Heng, K., Jones, K., et al. 2022, Astronomy and Astrophysics, 660, A123

Morris, B. M., Heng, K., & Kitzmann, D. 2024, Astronomy and Astrophysics, 685, A104

Murphy, M. M., Beatty, T. G., Schlawin, E., et al. 2024, arXiv e-prints, arXiv:2406.09863

Nikolov, N. & Sainsbury-Martinez, F. 2015, The Astrophysical Journal, 808, 57

Nugroho, S. K., Kawahara, H., Masuda, K., et al. 2017, The Astronomical Journal, 154, 221

Öberg, K. I., Murray-Clay, R., & Bergin, E. A. 2011, The Astrophysical Journal, 743, L16

O'Malley-James, J. T. & Kaltenegger, L. 2017, Monthly Notices of the Royal Astronomical Society, 469, L26

Owens, N., de Mooij, E. J. W., Watson, C. A., & Hooton, M. J. 2021, Monthly Notices of the Royal Astronomical Society, 503, L38

Parmentier, V., Fortney, J. J., Showman, A. P., Morley, C., & Marley, M. S. 2016, The Astrophysical Journal, 828, 22

Parmentier, V., Line, M. R., Bean, J. L., et al. 2018, Astronomy and Astrophysics, 617, A110

Parmentier, V., Showman, A. P., & Fortney, J. J. 2021, Monthly Notices of the Royal Astronomical Society, 501, 78

Parmentier, V., Showman, A. P., & Lian, Y. 2013, Astronomy and Astrophysics, 558, A91

Parviainen, H. 2015, Monthly Notices of the Royal Astronomical Society, 450, 3233

Patel, J. A., Brandeker, A., Kitzmann, D., et al. 2024, arXiv e-prints, arXiv:2407.12898

Patel, J. A. & Espinoza, N. 2022, The Astronomical Journal, 163, 228

Peixóto, J. P. & Oort, A. H. 1984, Rev. Mod. Phys., 56, 365

Phan, D., Pradhan, N., & Jankowiak, M. 2019, arXiv e-prints, arXiv:1912.11554

Pino, L., Désert, J.-M., Brogi, M., et al. 2020, The Astrophysical Journal, 894, L27

Pitman, K. M., Buratti, B. J., & Mosher, J. A. 2010, Icarus, 206, 537

Pluriel, W., Zingales, T., Leconte, J., & Parmentier, V. 2020, Astronomy and Astrophysics, 636, A66

Pontoppidan, K. M., Pickering, T. E., Laidler, V. G., et al. 2016, in Society of Photo-Optical Instrumentation Engineers (SPIE) Conference Series, Vol. 9910, Observatory Operations: Strategies, Processes, and Systems VI, ed. A. B. Peck, R. L. Seaman, & C. R. Benn, 991016

Powell, D., Feinstein, A. D., Lee, E. K. H., et al. 2024, Nature, 626, 979

Powell, D., Louden, T., Kreidberg, L., et al. 2019, The Astrophysical Journal, 887, 170

Powell, D., Zhang, X., Gao, P., & Parmentier, V. 2018, The Astrophysical Journal, 860, 18

Quanz, S. P., Ottiger, M., Fontanet, E., et al. 2022, Astronomy and Astrophysics, 664, A21

Rauer, H., Aerts, C., Cabrera, J., et al. 2024, arXiv e-prints, arXiv:2406.05447

Rauscher, E. & Menou, K. 2010, The Astrophysical Journal, 714, 1334

Rauscher, E. & Menou, K. 2013, The Astrophysical Journal, 764, 103

Rauscher, E., Menou, K., Seager, S., et al. 2007, The Astrophysical Journal, 664, 1199

Rein, E. & Ofir, A. 2019, Monthly Notices of the Royal Astronomical Society, 490, 1111

Ricci, L., Cazzoletti, P., Czekala, I., et al. 2017, The Astronomical Journal, 154, 24

Ricker, G. R., Winn, J. N., Vanderspek, R., et al. 2015, Journal of Astronomical Telescopes, Instruments, and Systems, 1, 014003

Rodrigo, C. & Solano, E. 2020, in Contributions to the XIV.0 Scientific Meeting (virtual) of the Spanish Astronomical Society, 182

Roman, M. & Rauscher, E. 2019, The Astrophysical Journal, 872, 1

Roth, A., Parmentier, V., & Hammond, M. 2024, Monthly Notices of the Royal Astronomical Society, 531, 1056

Rowe, J. F., Matthews, J. M., Seager, S., et al. 2008, The Astrophysical Journal, 689, 1345

Rustamkulov, Z., Sing, D. K., Mukherjee, S., et al. 2023, Nature, 614, 659

Sagear, S. & Ballard, S. 2023, arXiv e-prints, arXiv:2305.17157

Salmon, S. J. A. J., Van Grootel, V., Buldgen, G., Dupret, M. A., & Eggenberger, P. 2021, Astronomy and Astrophysics, 646, A7

Salvatier, J., Wieckiâ, T. V., & Fonnesbeck, C. 2016, PyMC3: Python probabilistic programming framework

Sandford, E. & Kipping, D. 2019, The Astronomical Journal, 157, 42

Schanche, N., Hébrard, G., Collier Cameron, A., et al. 2020, Monthly Notices of the Royal Astronomical Society, 499, 428

Schwartz, J. C., Kashner, Z., Jovmir, D., & Cowan, N. B. 2017, The Astrophysical Journal, 850, 154

Scuflaire, R., Théado, S., Montalbán, J., et al. 2008, Astrophysics and Space Science, 316, 83

Seager, S. 2010, Exoplanets

Seager, S. & Sasselov, D. D. 2000, The Astrophysical Journal, 537, 916

Sheets, H. A. & Deming, D. 2017, The Astronomical Journal, 154, 160

Sheppard, K. B., Welbanks, L., Mandell, A. M., et al. 2021, The Astronomical Journal, 161, 51

Showman, A. P., Fortney, J. J., Lian, Y., et al. 2009, The Astrophysical Journal, 699, 564

Sing, D. K., Fortney, J. J., Nikolov, N., et al. 2016, Nature, 529, 59

Skrutskie, M. F., Cutri, R. M., Stiening, R., et al. 2006, The Astronomical Journal, 131, 1163

Smith, R. W. 1987, The British Journal for the History of Science, 20, 482–483

Sousa, S. G., Adibekyan, V., Delgado-Mena, E., et al. 2018, Astronomy and Astrophysics, 620, A58

Sousa, S. G., Adibekyan, V., Delgado-Mena, E., et al. 2021, Astronomy and Astrophysics, 656, A53

Spergel, D., Gehrels, N., Breckinridge, J., et al. 2013, arXiv e-prints, arXiv:1305.5422

Stevenson, K. B., Harrington, J., Fortney, J. J., et al. 2012, The Astrophysical Journal, 754, 136

Stock, J. W., Kitzmann, D., & Patzer, A. B. C. 2022, Monthly Notices of the Royal Astronomical Society, 517, 4070

Stock, J. W., Kitzmann, D., Patzer, A. B. C., & Sedlmayr, E. 2018, Monthly Notices of the Royal Astronomical Society, 479, 865

Sudarsky, D., Burrows, A., Hubeny, I., & Li, A. 2005, The Astrophysical Journal, 627, 520

Sudarsky, D., Burrows, A., & Pinto, P. 2000, The Astrophysical Journal, 538, 885

Swain, M. R., Hasegawa, Y., Thorngren, D. P., & Roudier, G. M. 2024, Space Science Reviews, 220, 61

Tamburo, P., Muirhead, P. S., & Dressing, C. D. 2023, The Astronomical Journal, 165, 251

Tan, X. & Komacek, T. D. 2019, The Astrophysical Journal, 886, 26

The LUVOIR Team. 2019, arXiv e-prints, arXiv:1912.06219

Thrastarson, H. T. & Cho, J. Y.-K. 2011, The Astrophysical Journal, 729, 117

Tinetti, G., Eccleston, P., Haswell, C., et al. 2021, arXiv e-prints, arXiv:2104.04824

Torres, G., Konacki, M., Sasselov, D. D., & Jha, S. 2003, in American Astronomical Society Meeting Abstracts, Vol. 203, American Astronomical Society Meeting Abstracts, 17.09

Tsai, S.-M., Lee, E. K. H., Powell, D., et al. 2023, Nature, 617, 483

Turner, J. D., Pearson, K. A., Biddle, L. I., et al. 2016, Monthly Notices of the Royal Astronomical Society, 459, 789

van de Hulst, H. C. 1957, Light Scattering by Small Particles

Vehtari, A., Gelman, A., & Gabry, J. 2015, arXiv e-prints, arXiv:1507.04544

Verbiscer, A. J. & Veverka, J. 1994, Icarus, 110, 155

Virtanen, P., Gommers, R., Oliphant, T. E., et al. 2020, Nature Methods, 17, 261

von Essen, C., Mallonn, M., Borre, C. C., et al. 2020, Astronomy and Astrophysics, 639, A34

von Paris, P., Gratier, P., Bordé, P., Leconte, J., & Selsis, F. 2016, Astronomy and Astrophysics, 589, A52

von Seeliger, H. 1887, Abhandlungen der Bayerischen Akademie der Wissenschaften, Mathematisch-Naturwissenschaftliche Klasse, 16, 405

von Zeipel, H. 1924, Monthly Notices of the Royal Astronomical Society, 84, 665

Wakeford, H. R., Sing, D. K., Kataria, T., et al. 2017, Science, 356, 628

Wakeford, H. R., Sing, D. K., Stevenson, K. B., et al. 2020, The Astronomical Journal, 159, 204

Walker, G., Matthews, J., Kuschnig, R., et al. 2003, The Publications of the Astronomical Society of the Pacific, 115, 1023

Wallack, N. L., Knutson, H. A., & Deming, D. 2021, The Astronomical Journal, 162, 36

Welbanks, L., Madhusudhan, N., Allard, N. F., et al. 2019, The Astrophysical Journal, 887, L20

Welsh, W. F., Orosz, J. A., Seager, S., et al. 2010, The Astrophysical Journal, 713, L145

Williams, P. K. G., Charbonneau, D., Cooper, C. S., Showman, A. P., & Fortney, J. J. 2006, The Astrophysical Journal, 649, 1020

Wilson, R. F., Barclay, T., Powell, B. P., et al. 2023, The Astrophysical Journals, 269, 5

Winn, J. N. 2010, in Exoplanets, ed. S. Seager, 55–77

Winn, J. N. & Fabrycky, D. C. 2015, Annual Review of Astronomy and Astrophysics, 53, 409

Wittrock, J. M., Plavchan, P. P., Cale, B. L., et al. 2023, The Astronomical Journal, 166, 232

Wogan, N. F., Batalha, N. E., Zahnle, K. J., et al. 2024, The Astrophysical Journal, 963, L7

Wolszczan, A. & Frail, D. A. 1992, Nature, 355, 145

Wong, I., Kitzmann, D., Shporer, A., et al. 2021, The Astronomical Journal, 162, 127

Wong, I., Shporer, A., Daylan, T., et al. 2020a, The Astronomical Journal, 160, 155

Wong, I., Shporer, A., Kitzmann, D., et al. 2020b, The Astronomical Journal, 160, 88

Wright, E. L., Eisenhardt, P. R. M., Mainzer, A. K., et al. 2010, The Astronomical Journal, 140, 1868

Wright, J. T., Marcy, G. W., Howard, A. W., et al. 2012, The Astrophysical Journal, 753, 160

Wyttenbach, A., Mollière, P., Ehrenreich, D., et al. 2020, Astronomy and Astrophysics, 638, A87

Yahalomi, D. A., Kipping, D., Nesvorný, D., et al. 2024, Monthly Notices of the Royal Astronomical Society, 527, 620

Yan, F. & Henning, T. 2018, Nature Astronomy, 2, 714

Zieba, S., Zilinskas, M., Kreidberg, L., et al. 2022, Astronomy and Astrophysics, 664, A79

Zurlo, A., Goździewski, K., Lazzoni, C., et al. 2022, Astronomy and Astrophysics, 666, A133

Declaration of consent

on the basis of Article 18 of the PromR Phil.-nat. 19

Name/First Name:

Registration Number:

Study program:

Bachelor ☐ Master ☐ Dissertation ☐

Title of the thesis:

Supervisor:

I declare herewith that this thesis is my own work and that I have not used any sources other than those stated. I have indicated the adoption of quotations as well as thoughts taken from other authors as such in the thesis. I am aware that the Senate pursuant to Article 36 paragraph 1 litera r of the University Act of September 5th, 1996 and Article 69 of the University Statute of June 7th, 2011 is authorized to revoke the doctoral degree awarded on the basis of this thesis.
For the purposes of evaluation and verification of compliance with the declaration of originality and the regulations governing plagiarism, I hereby grant the University of Bern the right to process my personal data and to perform the acts of use this requires, in particular, to reproduce the written thesis and to store it permanently in a database, and to use said database, or to make said database available, to enable comparison with theses submitted by others.

Place/Date

Signature